



HAL
open science

Experimental, numerical and theoretical studies of rock salt as a host rock

Laura Blanco Martín

► **To cite this version:**

Laura Blanco Martín. Experimental, numerical and theoretical studies of rock salt as a host rock. Engineering Sciences [physics]. Sorbonne Université, 2023. tel-04125864

HAL Id: tel-04125864

<https://hal.science/tel-04125864>

Submitted on 12 Jun 2023

HAL is a multi-disciplinary open access archive for the deposit and dissemination of scientific research documents, whether they are published or not. The documents may come from teaching and research institutions in France or abroad, or from public or private research centers.

L'archive ouverte pluridisciplinaire **HAL**, est destinée au dépôt et à la diffusion de documents scientifiques de niveau recherche, publiés ou non, émanant des établissements d'enseignement et de recherche français ou étrangers, des laboratoires publics ou privés.



Distributed under a Creative Commons Attribution - NonCommercial - NoDerivatives 4.0 International License



Centre de
Géosciences



Sorbonne Université

Sciences de la Terre et de l'Univers

Habilitation à Diriger des Recherches

par

Laura BLANCO MARTÍN

Centre de Géosciences Mines Paris

Experimental, numerical and theoretical studies of rock salt as a host rock

Soutenue le 30 mai 2023 devant le jury composé de :

Philippe COSENZA	Professeur, Université de Poitiers	Rapporteur
Uwe DÜSTERLOH	Professeur, TU Clausthal	Rapporteur
Muriel GASC	Directrice de recherche, CEREMA	Rapporteuse
Roger GUÉRIN	Professeur, Sorbonne Université	Examineur
Ahmed ROUABHI	HDR, Mines Paris	Examineur

Abstract

Rock salt exhibits naturally very interesting properties for underground storage and disposal, such as ductility and very low permeability and porosity in the undisturbed state. The work that I present in this manuscript aims at improving current engineering practice in the design of underground structures in rock salt, which comprises three main steps: laboratory characterization, constitutive modeling and simulations at the facility scale, using well-established design criteria to evaluate the long-term feasibility of the excavations. The final goal of my research is to address society and industry challenges, such as the underground disposal of heat-generating nuclear waste and the underground storage of fluids and energy carriers in salt caverns. As shown through some applications, these challenges require the coupled study of different processes (thermal, mechanical, hydraulic).

The experimental work that I supervised has led to several guidelines for a better characterization of rock salt behaviour at the laboratory scale. Such guidelines concern various aspects such as samples preconditioning (*e.g.*, loading conditions, duration), further microscopic characterization (*e.g.*, brine content, grain size), and testing along different loading paths, covering the stress and temperature ranges expected *in situ* (*e.g.*, compression, extension, traction, low and high deviatoric levels).

Once the characterization is performed, and in order to determine a rheological parameter set from experimental laboratory data, it is necessary to consider heterogeneity in the analysis of the results. The first type of heterogeneity is due to the rough contact between the rock sample and the cell platens, and the second type, material heterogeneity, is due to the presence of impurities within the samples that have smaller dimensions than the representative volume element of the rock under investigation. Indeed, as I show in this work, assuming that the sample response is homogeneous is a simplification that could lead to an erroneous characterization of the material, and subsequently to an erroneous design of underground structures. This applies particularly to the dilatancy threshold, which is an important design criterion for excavations in rock salt. Volumetric strains are very small and very sensitive to the scale of measurement.

Most constitutive laws used in underground engineering are phenomenological, with parameters calibrated on the basis of laboratory work. Such laws have limited extrapolation capabilities. In this context, while it is in theory possible to cover at the laboratory scale the stress and temperature ranges expected in the field, the duration of the experiments is necessarily much shorter than the lifespan of the targeted underground facilities. This aspect is still unresolved.

Two main perspectives stem from this work. The first is related to the long-term, and to the need to reduce the uncertainties in the predictions by better understanding the physics underneath the observed response. The microscopic scale should be included further in standard engineering practice. The second is related to experimental thermo-hydro-mechanical coupling and to the need to better characterize flow within low-permeability rocks, such as rock salt.

Résumé

Le sel gemme est une roche ayant des caractéristiques très favorables pour le stockage souterrain, en particulier un comportement ductile, et de perméabilité et porosité très faibles dans l'état non endommagé. Le travail que je présente dans ce manuscrit se propose d'améliorer la démarche actuelle pour le dimensionnement des ouvrages souterrains dans les roches salines, qui comporte trois étapes principales : une caractérisation en laboratoire, une modélisation constitutive et des simulations numériques à l'échelle de l'ouvrage pour en évaluer la stabilité à long terme, moyennant l'utilisation de critères définissant des seuils de stabilité. Le but final de mes recherches est de répondre à des besoins sociétaux et industriels, tels que le stockage de déchets radioactifs exothermiques et le stockage souterrain de vecteurs énergétiques en lien avec la transition bas carbone. Comme les cas d'applications présentés le montrent, pour relever ces défis il est nécessaire de considérer des processus couplés (thermiques, mécaniques, hydrauliques).

Le travail expérimental que j'ai encadré a permis de proposer des recommandations pour la réalisation d'essais de caractérisation en laboratoire. Ces recommandations concernent plusieurs aspects tels que le préconditionnement des éprouvettes (*e.g.*, chargement, durée), une caractérisation microscopique plus approfondie (*e.g.*, teneur en saumure, taille des grains) et la réalisation d'essais selon des chemins de charge variés, couvrant la gamme de contraintes et températures *in situ* (*e.g.*, compression, extension, traction, faibles et fortes contraintes déviatoriques).

Une fois la roche caractérisée, et dans le but de déterminer un jeu de paramètres rhéologique, il est nécessaire d'analyser les résultats expérimentaux en tenant compte de l'hétérogénéité, qui peut être de deux types différents. Le premier type est dû au contact frottant entre l'éprouvette et les pistons qui appliquent la charge. Le deuxième type (hétérogénéité matérielle) est dû à la présence d'autres composants que le NaCl et doit être pris en compte lorsque les dimensions des éprouvettes sont plus petites que le volume élémentaire représentatif de la roche étudiée. Je montre que considérer que la réponse des éprouvettes est homogène est une simplification qui pourrait mener à une caractérisation erronée de la roche, et par conséquent à un dimensionnement erroné des ouvrages souterrains. Ceci est d'autant plus vrai pour le seuil dilatant, qui est un critère de dimensionnement très utilisé actuellement. En effet, les déformations volumiques sont très petites et très sensibles à l'échelle de la mesure.

La plupart des lois de comportement utilisées en ingénierie sont phénoménologiques, et leurs paramètres sont ajustés à partir des essais de laboratoire. L'extrapolation de ce type de loi est délicate. Dans ce contexte, même s'il est théoriquement possible d'étudier à l'échelle du laboratoire la gamme des contraintes et de température pertinente *in situ*, la durée des essais est forcément plus courte que les échelles de temps propres aux ouvrages souterrains. Cet aspect reste encore non résolu.

Deux perspectives principales découlent des travaux présentés. La première porte sur le comportement à long terme et sur la nécessité de réduire les incertitudes liées aux extrapolations

temporelles moyennant une étude plus approfondie des aspects physiques sous-jacents à la réponse observée. L'échelle microscopique devrait être davantage prise en compte dans les applications en ingénierie. La seconde porte sur le couplage thermo-hydro-mécanique expérimental et sur la nécessité de mieux comprendre l'écoulement dans des roches très peu perméables, telles que le sel gemme.

Contents

Abstract	ii
Résumé	iv
List of Figures	viii
List of Tables	xiv
1 Introduction	1
1.1 Rock salt as a host rock	1
1.2 Challenges imposed by the applications	3
2 Rheology	7
2.1 Physically-based and phenomenological laws	7
2.2 Temporal extrapolation	16
2.3 Experimental observations	20
2.3.1 Heterogeneity	20
2.3.2 Initial state of the samples	25
2.3.3 Reverse creep	28
2.3.4 Tensile response	30
3 Engineering applications	35
3.1 Laboratory characterization and design of underground structures	35
3.2 Salt cavern storage and energy transition	41
3.3 Disposal of heat-generating nuclear waste	55
4 Conclusions and perspectives	67
4.1 Towards more physics	69
4.2 THM coupling with experimental support	69
Bibliography	71
Appendix	85
A Curriculum Vitæ	87

B Selected Publications	97
B.1 Blanco-Martín et al. 2017	99
B.2 Blanco-Martín et al. 2015	107
B.3 Blanco-Martín et al. 2022	121
B.4 Azabou et al. 2021	135
B.5 Azabou et al. 2021	147

List of Figures

- 1.1 Strain-controlled test performed at $\dot{\epsilon}_{ax} = 10^{-5} \text{ s}^{-1}$, $P = 5 \text{ MPa}$ and ambient temperature. Strain hardening is observed beyond the dilatancy threshold, marked with a red dot on the left-hand side plot. This test was performed within the framework of the Citeph-20-2018 project (Blanco-Martín et al., 2021a). 2
- 1.2 Examples of heterogeneity during recent laboratory work on rock salt samples at the Centre for Geosciences and Geoengineering: (a) heterogeneity due to sample-piston friction (strain-controlled test at $\dot{\epsilon}_{ax} = 10^{-5} \text{ s}^{-1}$ and $P = 2 \text{ MPa}$); (b) three samples showing different levels of material heterogeneity. 4
- 1.3 Axial strain (in $\mu\text{m/m}$) during a unconfined test performed at the *Altaussee* mine (Austria) on a Hauterives salt sample (adapted from Bérest et al. (2022), compressive strains are negative). Small and intermediate loads are applied; such loads require specific settings in which temperature and relative humidity are extremeley constant. 5

- 2.1 Deformation-mechanism maps for natural rock salt: (a) from Munson & Dawson (1981) and (b) from Spiers & Carter (1996), grain size $d = 3 \text{ mm}$. Each labeled domain represents the conditions where the specified mechanism dominates. In the vertical axes, both σ'_{II} and σ refer to von Mises equivalent stress, and μ is the shear modulus (Lamé’s second parameter). 8
- 2.2 Creep rates as a function of the deviatoric stress (after Herchen et al. (2018)). Symbols correspond to experimental data and solid lines to predictions using the Günther-Salzer (GS) steady state creep law (Günther & Salzer, 2012). Note that $\sigma_{\text{eff}} = q$. . . 9
- 2.3 Confined creep test performed at $T = 50 \text{ }^\circ\text{C}$ and several deviatoric stress levels (Tijani et al., 2009): (a) experimental data (the enlarged view shows the three first loading stages); (b) computed strain rate (values displayed are greater than 10^{-18} s^{-1}). 10
- 2.4 Recent confined creep tests performed at $T = 50 \text{ }^\circ\text{C}$ and several deviatoric stress levels in the range $Q - P \in [0.5 - 20] \text{ MPa}$: (a) experimental data of three tests (the enlarged view shows the three first loading stages); (b) computed strain rate (values displayed are greater than 10^{-18} s^{-1}). The top row corresponds to Salt 1 and the two other rows correspond to Salt 2. All tests were conducted at Mines Paris (Blanco-Martín et al., 2021a). 11
- 2.5 Analysis of the creep tests in Figure 2.4 performed at $T = 50 \text{ }^\circ\text{C}$ and several deviatoric stress levels with the modified Lemaitre creep law, Eq. (2.5): (a) Salt 1 ; (b) Salt 2. 13

2.6	Comparison between experimental data (Figure 2.4) and model predictions with the modified Lemaitre creep law (Eq. (2.5)) using the parameters listed in Table 2.1: (a) Salt 1 ; (b) Salt 2. The model predictions are obtained using the in-house FEM code Phimef, in which I implemented the modified Lemaitre creep law.	14
2.7	Salt 1: fitting considering the range $0.5 \leq Q - P \leq 20$ MPa with Eqs. (2.5) and (2.3), or the reduced range $5 \leq Q - P \leq 20$ MPa with Eq. (2.3).	15
2.8	Salt 1: thirty-year prediction of a creep test at $T = 50$ °C with a parameter set obtained for $5 \leq Q - P \leq 20$ MPa (Eq. (2.3)) and a parameter set obtained for $0.5 \leq Q - P \leq 20$ MPa (Eq. (2.5)): (a) $Q - P = 10$ MPa; (b) $Q - P = 1$ MPa.	16
2.9	Salt 1: fitting of constant strain rate tests at $\dot{\epsilon}_{ax} = 10^{-6} \text{ s}^{-1}$ and ambient temperature with RTL2020 (equations of the volumetric part are detailed in Appendix B.4). All tests were conducted at Mines Paris (Blanco-Martín et al., 2022a).	17
2.10	Salt 1: fitting of constant strain rate tests at $\dot{\epsilon}_{ax} = 10^{-5} \text{ s}^{-1}$ and ambient temperature with RTL2020 (equations of the volumetric part are detailed in Appendix B.4). All tests were conducted at Mines Paris (Blanco-Martín et al., 2022a).	18
2.11	Salt 1: fitting of constant mean stress tests at $\dot{P} = -1$ MPa/d and ambient temperature with RTL2020 (equations of the volumetric part are detailed in Appendix B.4). All tests were conducted at Mines Paris (Blanco-Martín et al., 2022a).	18
2.12	Salt 1: fitting of multi-stage creep tests at ambient and higher temperatures with RTL2020 (volumetric strains are not available). All tests were conducted at Mines Paris (Blanco-Martín et al., 2022a).	19
2.13	Multi-scale acquisition to quantify heterogeneity during a laboratory test: (a) sketch of measuring devices and sample shape during a triaxial compression test —an initially cylindrical sample (black contours) evolves into a deformed cylinder assuming a perfectly smooth contact (homogeneous stress and strain fields, blue contour) or into a barrel-shaped sample assuming a completely rough contact (heterogeneous stress and strain fields, red contour); (b): exploratory set-up with 1 mm thick Viton bladder, strain gauges and extensometers; (c): exploratory set-up with 0.1 mm thick latex bladder, strain gauges and extensometers; (d): selected set-up with 0.1 mm thick latex bladder, circumferential extensometer and global axial LVDT (LVDT not visible in the picture).	22
2.14	Results of numerical strain-controlled isothermal tests at $P = 10$ MPa and $\dot{\epsilon}_{ax} = 10^{-5} \text{ s}^{-1}$, using the parameters in Table 2.3. Dashed lines correspond to a frictionless contact (all curves overlap), and solid lines to a fully frictional contact. Strains are shown at local, hybrid and global scales, assuming that the radial strain is equal to the hoop strain.	23
2.15	Experimental data at different scales. The trends observed in Figure 2.14 (fully frictional contact) are not systematic and reproduced qualitatively in cases (a) and (b), but not (c). In general, local data show more variability than global data (d).	24
2.16	Salt 2: results of strain-controlled tests during (a) the initial isotropic phase and (b) the deviatoric phase. All tests were conducted at Mines Paris (Blanco-Martín et al., 2022a).	26
2.17	Salt 3: analysis of a recent hydrostatic phase ($C = 12$ MPa, $Q - P = 0.2$ MPa, $T = 30$ °C) of some samples. The temperature is increased from ambient ($T_{\infty} = 20$ °C) to 30 °C after one day, inducing a fast elongation of the samples (average $\bar{\alpha}_{th} = 2.65 \cdot 10^{-5} \text{ K}^{-1}$). All tests were conducted at Mines Paris.	27

2.18	Salt 3: view of a salt sample (a) before and (b) after a three week-long hydrostatic phase at $C = 12$ MPa and $T = 30$ °C.	27
2.19	Salt 1: creep tests in which reverse creep was investigated (the enlarged views show the strain before and after the load drops). All tests were conducted at Mines Paris (Blanco-Martín et al., 2021a).	28
2.20	Salt 2: creep tests in which reverse creep was investigated (the enlarged views show the strain before and after the load drops). All tests were conducted at Mines Paris (Blanco-Martín et al., 2021a).	29
2.21	Salt 4: creep test in which reverse creep was investigated (the enlarged views show the strain before and after the load drops). All tests were conducted at Mines Paris (Blanco-Martín et al., 2021a).	29
2.22	Salt 1: reverse creep in unloading-reloading cycles of a strain-controlled test at $\dot{\epsilon}_{ax} = 10^{-6}$ s ⁻¹ , $P = 17$ MPa and ambient temperature: experimental data and analysis with RTL2020 for (a) $B = 0$ (reverse creep inactive) and (b) $B = 0.5$ (reverse creep active). The other parameters are listed in Table 2.2. All tests were conducted at Mines Paris (Blanco-Martín et al., 2021a).	30
2.23	Experimental investigation on the tensile response of rock salt at Mines Paris: (a) initial experimental set-up with strain gauges and LVDT sensors (in the case shown, the sample diameter is 65 mm); (b) unsatisfactory results (note that one of the horizontal strain gauges breaks short after 1 h, while the LVDT response is beyond noise only after 1.5 h [the third horizontal gauge did not work properly]).	32
2.24	Experimental investigation on the tensile response of rock salt at Mines Paris, combining DIC and strain gauges: (a) vertical [y] and (b) horizontal [x] displacements (in px) provided by DIC on one face of the sample, at the moment when the first fracture appeared, after about 6 h; (c) view of the face where strain gauges are used (note that out of the three vertical gauges, only the central one is working); (d) comparison between strain gauges and DIC before suspected start of gauges malfunctioning, short before 4 h (note that some differences are expected, as the two techniques are used on different faces of the sample).	33
3.1	Samples prepared for laboratory testing at Mines Paris showing important material heterogeneity: (a) cored within 7.5 m from each other.	35
3.1	Samples prepared for laboratory testing at Mines Paris showing important material heterogeneity: (b) cored within 1 m from each other.	36
3.2	Results of constant strain rate tests at $\dot{\epsilon}_{ax} = 2 \cdot 10^{-6}$ s ⁻¹ , ambient temperature and different confining pressures. The samples were cored within 1 m of each other. For each test, lines with symbols correspond to global measurements and lines without symbols correspond to local measurements. All tests were conducted at Mines Paris.	36
3.3	Results of a multi-stage creep test at $P = 10$ MPa and $T = 50$ °C. The test started with a one week-long isotropic phase at $C = 10$ MPa and $Q - P = 0.2$ MPa during which temperature was increased to 50 °C (not shown in the plot). The test was conducted at Mines Paris.	37
3.4	Fitting of the constant strain rate tests shown in Figure 3.2 with RTL2020. Global volumetric strains are considered.	38
3.5	Fitting of the constant strain rate tests shown in Figure 3.2 with RTL2020. Local volumetric strains are considered.	39

3.6	Fitting of the multi-stage creep test shown in Figure 3.3 with RTL2020.	39
3.7	Isovalues of $\dot{\zeta}_{vp} = 0$ at different times, obtained using the global parameter set (left plot) and the local parameter set (right plot) for the volumetric part, listed in Table 3.1.	40
3.8	Test at <i>Varangéville</i> : (a) plan view of the experimental niche, including location of the experimental chamber and the two slots; (b) view of the experimental chamber surrounded by the insulation cover (the height of the chamber is 2.23 m and the width of the walls [HD polyurethane] is 10 cm); (c) inside view of the chamber (floor fans are visible in the left-hand side, as well as acoustic emission devices on the floor).	42
3.9	Test at <i>Varangéville</i> : air temperature inside the chamber. The maximum value during cycles 1 and 3 is due to the use of an electric heater during the first week of warming.	44
3.10	Test at <i>Varangéville</i> : visible fractures developed during the different cooling stages.	45
3.11	Test at <i>Varangéville</i> : view of the 3D model used in the simulations (left) and enlarged views of the niche (top right) and the salt block (bottom right). The domain is discretized into 202,990 tetrahedral elements, having minimum and maximum sizes of respectively 0.05 m (test zone) and 72 m (far from the niche).	46
3.12	Test at <i>Varangéville</i> : location of temperature sensors in a local reference system. Note that the thermocouples define two main orthogonal profiles, which extend outside the chamber. Air temperature is measured by sensors identified <i>A52 – A54</i> . Pt100 sensors <i>T2-T5</i> are placed at different depths in a vertical borehole. Sensor <i>TF13</i> is a heat flux sensor.	48
3.13	Test at <i>Varangéville</i> : comparison between experimental data (symbols) and numerical results (lines) for temperature at several locations indicated in Figure 3.12.	49
3.14	Test at <i>Varangéville</i> : maximum principal stress (MPa) at the surface of the salt block (a) after excavation ($t=0$) and (b) before the beginning of the first cycle ($t=129$ d). The principal stresses at locations <i>P1-P5</i> (see Figure 3.10) are displayed (bottom color table).	50
3.15	Test at <i>Varangéville</i> : numerical results at the surface of the salt block during the first cooling stage. Left: maximum principal stress (MPa) (the bottom color table corresponds to the principal stresses at locations <i>P1-P5</i>). Right: temperature (°C).	51
3.16	Test at <i>Varangéville</i> : numerical results at the surface of the salt block during the first cooling stage. Left: maximum principal stress (MPa) (the bottom color table corresponds to the principal stresses at locations <i>P1-P5</i>). Right: temperature (°C).	52
3.17	Test at <i>Varangéville</i> : numerical results at the surface of the salt block at the end of the first cycle ($t=129+62=191$ d). Left: maximum principal stress (MPa) (the bottom color table corresponds to the principal stresses at locations <i>P1-P5</i>). Right: temperature (°C).	53
3.18	Test at <i>Varangéville</i> : evolution of the maximum principal stress during the first 12 h of cooling at three locations.	54
3.19	Test at <i>Varangéville</i> : maximum principal stress (MPa) on a vertical plane accross the chamber (plane $x=101.17$ m, between $y=17.3$ m and $y=20.9$ m), in the area where fractures were first observed. (a) $t=129$ d; (b) $t=129$ d+30 min; (c) $t=129$ d+40 min; (d) $t=129$ d+2 h; (e) $t=129$ d+6 h; (f) $t=129$ d+12 h; (g) $t=129$ d+28 d; (h) $t=129$ d+62 d.	54
3.20	TSDE: (a) cross-section of the Asse salt mine, indicating the location of the experiment; (b) schematic representation of the test area.	58

3.21	TSDE: plan view of the test drifts and monitoring cross-sections.	59
3.22	TSDE: views of the initial (non-deformed) mesh used in the geomechanics sub-problem. The main dimensions of the model are also shown.	60
3.23	TSDE: temperature evolution within the backfill and at the heater surface (section B) (a), and (b) within the host rock beneath the drift floor (section A).	62
3.24	TSDE: (a) drift closure in the heated area (section G1) and in the non-heated area (section E2); (b) backfill porosity in the same sections. The start of the heating phase is set as a reference time ($t = 0$), and also as a reference for drift closure. . . .	63
3.25	TSDE: host rock porosity around the drift area at three different moments of the THM run.	64
3.26	TSDE: reduced model used in the inversion (left) and results (right).	65

List of Tables

- 2.1 Parameters of the modified Lemaitre creep law (two power laws for the deviatoric stress dependence, Eq. (2.5)), derived from the creep tests in Figure 2.4 performed at $T = T_r = 50$ °C. The unit system is such that strain is in $\mu\text{m}/\text{m}$, stress in MPa, temperature in K and time in days. 14
- 2.2 Salt 1: RTL2020 parameter set that best fits simultaneously short- and long-term tests. The unit system is such that strain is in $\mu\text{m}/\text{m}$, stress in MPa, temperature in K and time in days. 20
- 2.3 RTL2020 parameter set used to investigate heterogeneity numerically. The unit system is such that strain is in $\mu\text{m}/\text{m}$, stress in MPa, temperature in K and time in days. 23
- 2.4 Load drops performed during creep tests to investigate reverse creep. 29

- 3.1 RTL2020 parameter set determined from laboratory tests (best fit for short- and long-term tests simultaneously). The unit system is such that strain is in $\mu\text{m}/\text{m}$, stress in MPa, temperature in K and time in days. 38
- 3.2 Test at *Varangéville*: material constants of the rock layers included in the model (ρ is mass density, C_p is heat capacity and λ is thermal conductivity). 47

Chapter 1

Introduction

1.1 Rock salt as a host rock

Rock salt, mainly NaCl, is formed by evaporation of seawater, followed by loading and recrystallization during further sedimentation. Pure rock salt has a polycrystalline structure, formed by a juxtaposition of halite crystals with limited quantities of fluids (mostly saturated brine). Fluids are present as intracrystalline inclusions and/or as intercrystalline fluids along the crystal boundaries, in the form of adsorbed thin films and island-channel networks (Rutter & Elliott, 1976; Boucher et al., 1979; Raj, 1982). Density of rock salt does not increase with burial, which makes salt layers less dense than the overlying strata. As a result, salt structures (such as diapirs) can be formed from initially horizontal layers depending on gravitational instabilities and the regional tectonic regime.

Rock salt exhibits naturally very low permeability and porosity in the undisturbed state. These two assets make rock salt very tight to fluid flow. In addition, rock salt has high thermal conductivity as compared to other shallow-crustal rock types, is a ductile rock and shows a tendency to sealing-healing when the conditions are propitious (brine availability, stress state, temperature). These main assets, combined with the large volumes available, make rock salt a potential candidate for underground storage and disposal. Two main techniques exist: salt caverns and drifts/boreholes. Solubility in water allows creation of salt caverns by leaching (or solution mining), which is a quite inexpensive technique. A well connects the ground surface to the cavern; such well is very similar to a typical well of the oil industry, and has initially two concentric spaces, one for injection of fresh water and another for withdrawal of the leached, saturated brine. Typically, cavern volumes range between 10^4 and 10^6 m³. Salt caverns have been used around the world since the 1940s to store liquid and gaseous hydrocarbons, and other substances such as hydrogen, compressed air, helium and chemical wastes. Today, there are about 2000 storage caverns worldwide, and this figure will increase rapidly in the next years because salt caverns will play an important role in the transition towards low-carbon energy; indeed, they offer relatively large volumes and high deliverability rates. Rock salt is also easy to mine and requires little reinforcement. In the USA, transuranic (low-level) nuclear waste is being disposed of since 1999 in the rooms of the Waste Isolation Pilot Plant (WIPP) in the Salado Formation (New Mexico), and, in Germany, low-level and intermediate-level radioactive wastes were stored in drifts of the Asse mine (1965-1978) and the Morsleben repository (1972-1998). Research for the disposal of heat-generating nuclear waste in saliniferous formations is ongoing in these two countries.

The use of rock salt as a disposal or a storage medium is based on extensive research performed

over the last 50 years, particularly at the laboratory scale but also at the field scale. An exhaustive literature review is out of the scope of this document. From a mechanical point of view, rock salt exhibits time-dependent, viscoplastic behaviour (creep) when it is subjected to deviatoric loadings. High temperatures enhance the creep of the rock. Many models have been developed in the past decades, including different features and different levels of complexity. They can be put in two main categories: physically-based (based on deformation mechanisms observed at the microscopic scale) and phenomenological (based on experiments, often at the macroscopic scale, without accounting for the physics underneath the observed response). Regardless of the physical or phenomenological nature of the model used, it should be noted that until the early 1990s, the viscoplastic response of rock salt was assumed to be purely deviatoric. Later on, non-elastic volumetric strains were taken into account, with a focus on non-elastic volume increase, or dilatancy. Dilatancy is related to the formation of micro-cracks and the subsequent development of flow paths (permeability and porosity increase). At the microscopic scale, dilatancy is thought to be due to plastic strain misfits between neighbouring crystals, which causes intercrystalline sliding and void opening. Dilatancy is much smaller than the corresponding deviatoric strains (see Figure 1.1 [note that unless otherwise specified, compressive strains and stresses are positive in laboratory data]) and does not —at least for moderate strains— induce softening, which explains why it was initially neglected.

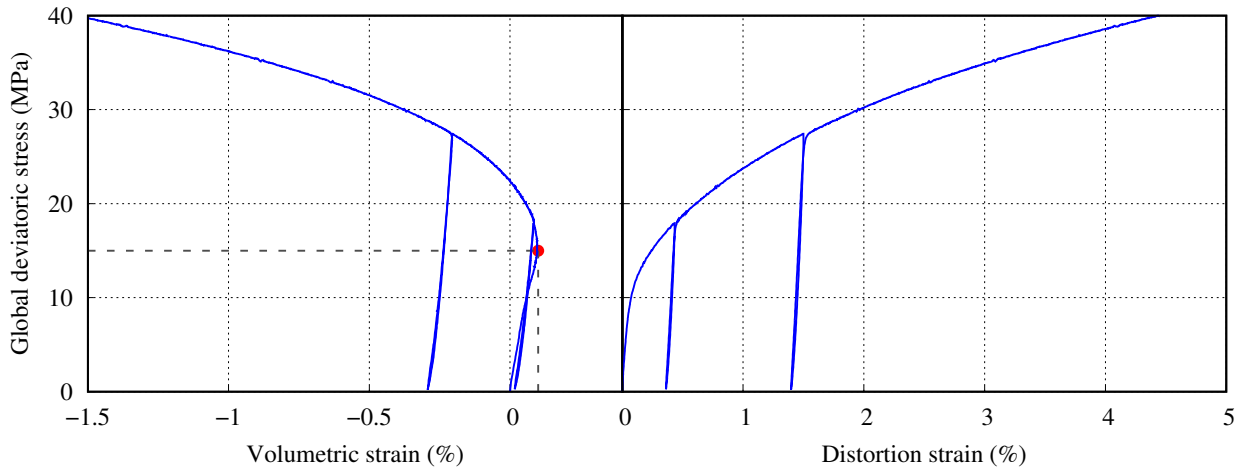


Figure 1.1. Strain-controlled test performed at $\dot{\epsilon}_{ax} = 10^{-5} \text{ s}^{-1}$, $P = 5 \text{ MPa}$ and ambient temperature. Strain hardening is observed beyond the dilatancy threshold, marked with a red dot on the left-hand side plot. This test was performed within the framework of the Citeph-20-2018 project (Blanco-Martín et al., 2021a).

Owing to the tightness loss that it implies, dilatancy has gained much attention over the last years, and many laboratory and field investigations have been performed, such as the EU BAMBUS project, experiments at WIPP, German & US/German joint projects, as well as extensive laboratory work, see for instance Peach (1991); Stormont & Daemen (1992); Thorel & Ghoreychi (1996); Cosenza et al. (1997); Stormont (1997); Popp & Kern (1998); Popp et al. (2001); Schulze et al. (2001); Bechthold et al. (2004); Alkan et al. (2007); Günther & Salzer (2012); Düsterloh et al. (2015); Roberts et al. (2015); Salzer et al. (2015); Azabou (2021). Likewise, dilatancy criteria have become very important in the design of underground structures (Hunsche, 1993; Van Sambeek et al., 1993; Staudtmeister & Rokahr, 1997; Heusermann et al., 2003; Hou, 2003; Labaune et al., 2018). To counteract dilatancy, healing/sealing processes have been observed under propitious

conditions (Wolters et al., 2012; Herchen et al., 2018), and several models include a healing/sealing component (*e.g.*, Lux/Wolters/Lerche, Günther/Salzer, CDM, Lubby-MCDF, see Hampel et al. (2015)).

Knowledge of salt processes in the context of engineering applications has undoubtedly improved over the years. For the last decade, I have performed research in the context of two main applications: disposal of heat-generating nuclear waste in drifts and energy storage in salt caverns. Conducting such research has allowed me to understand aspects that are currently unresolved, and to orientate my work to improve part of them, as I will introduce in the next section.

1.2 Challenges imposed by the applications

When designing underground facilities (in rock salt or any other formation), it is a common engineering practice to first characterize the rock behaviour at the laboratory scale. Then, constitutive laws are developed and fitted against the experimental data, and ultimately numerical simulations at the facility scale are conducted using the laws and parameters to evaluate the long-term feasibility and optimize the design. In this process, there are three important aspects: laboratory characterization, constitutive modeling and design criteria.

Laboratory characterization, when used to derive constitutive parameters and design criteria, is complex as heterogeneity needs to be taken into account, but is difficult to quantify. Friction between the cell pistons and the sample creates non-uniform stress and strain fields within the sample, and although it is topical in mechanical testing (Brady, 1971; Peng, 1971; Sheng et al., 1997; Shilko, 2002), it is difficult to quantify experimentally. The analysis of test results assuming a perfectly smooth or a completely rough contact provides two extreme cases. An example of this type of heterogeneity, obtained during a strain-controlled test on a salt sample, is displayed in Figure 1.2a (test under triaxial compression). Material heterogeneity is due to the presence of impurities (such as second phases or insolubles) within the samples, and can be identified through microscopic observations, scanning and, in the case of rock salt, dissolution. Material heterogeneity needs to be taken into account when the samples size—which is fixed by the drilling tools in the field and the testing devices in the laboratory—is smaller than the representative volume element (RVE) of the rock mass. Three examples of salt specimens showing different levels of material heterogeneity are shown in Figure 1.2b. Both types of heterogeneity might hinder a correct characterization of the rock material, particularly in the case of inelastic volumetric strains, which are very small (see Figure 1.1) and very sensitive to the scale of measurement; yet, dilatancy is an important design criterion, and needs to be evaluated accurately. Another aspect is the tensile response of rock salt, which has been less thoroughly researched than the compressive response, but is important, for instance, in the context of a fast temperature decrease related to high frequency cycling in salt caverns (Bérest et al., 2014). Performing direct tensile tests in rocks is technically difficult, and indirect tensile tests provide non-uniform strain and stress fields that need to be correctly interpreted for a proper characterization of the material. At the facility scale, decisions based on an improper laboratory characterization could be either too conservative or too optimistic.

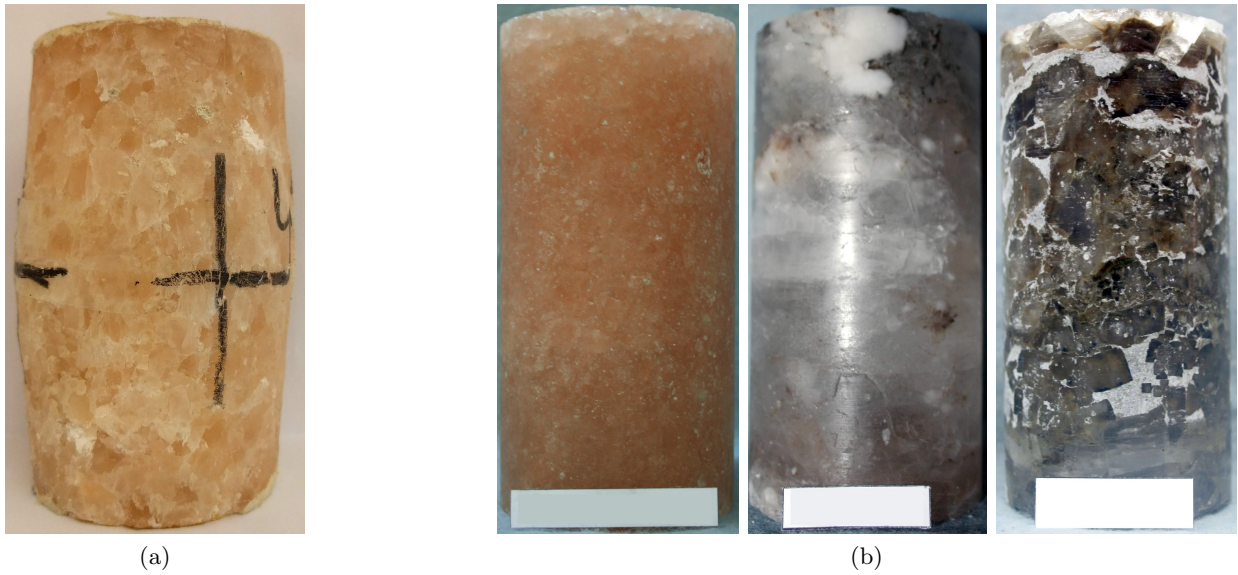


Figure 1.2. Examples of heterogeneity during recent laboratory work on rock salt samples at the Centre for Geosciences and Geoengineering: (a) heterogeneity due to sample-piston friction (strain-controlled test at $\dot{\epsilon}_{ax} = 10^{-5} \text{ s}^{-1}$ and $P = 2 \text{ MPa}$); (b) three samples showing different levels of material heterogeneity.

Most constitutive laws used in underground engineering are phenomenological. Therefore, laboratory characterization should include different loading paths in the stress, temperature and time domains, covering the ranges expected *in situ*. This, of course, can be theoretically achieved for stresses and temperature, but not for time, as the duration of experiments is limited compared to the lifespan of the facilities (performance analyses for the disposal of heat-generating nuclear waste often involve simulations covering $10^5 - 10^6$ years of post-closure). In addition to the temporal span, long-term applications usually require extrapolation to strain rates much slower than those typically investigated at the laboratory scale. Slow strain rates occur at low deviatoric stresses (and to a lesser extent, low temperatures), which are not only important in the long-term (nuclear waste post-closure, cavern abandonment), but also at shallow depths and far from the openings. Creep tests performed at low stress deviators are challenging because the measured strains are sensitive to small changes in temperature or relative humidity (smaller than typical regulation accuracy), and separation of the different effects is not straightforward (Bérest et al., 2019). In fact, the literature review shows that most creep tests have been performed using stress deviators greater than 5-8 MPa. Some tests at low and intermediate levels are available (*e.g.* Bérest et al. (2022); Tijani et al. (2009), see Figure 1.3), and although mostly unconfined, they suggest that extrapolation could underestimate the creep rate by several orders of magnitude. Therefore, to avoid extrapolation, creep tests should comprise stages at both low and high deviatoric stresses.

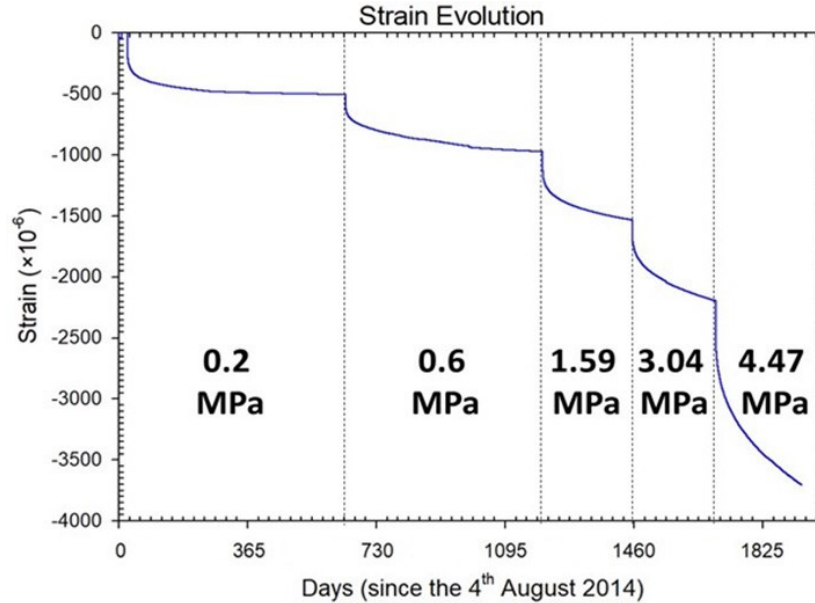


Figure 1.3. Axial strain (in $\mu\text{m}/\text{m}$) during a unconfined test performed at the *Altaussee* mine (Austria) on a Hauterives salt sample (adapted from Bérest et al. (2022), compressive strains are negative). Small and intermediate loads are applied; such loads require specific settings in which temperature and relative humidity are extremely constant.

In constitutive modeling and field-scale simulations, a common workaround to tackle temporal extrapolation is to recalibrate the laboratory-derived parameters on the basis of field observations over time. Nevertheless, field data are complex and often contain uncertainties that hinder an accurate quantification of the parameters (for instance, cavern sonar measurements are performed every 5-10 years and are accurate to about 4%, and their correct interpretation often requires to consider 3D effects among neighbouring caverns), and in any case the available time spans (a few decades) are not enough to avoid long-term extrapolation.

Laboratory characterization, constitutive modeling and design criteria have been thoroughly investigated since the 1970s at the Centre for Geosciences and Geoengineering of Mines Paris, see for instance Tijani et al. (1983); Hamami (1993); Merar (1999); Tijani (2008); Labaune (2018); Rouabhi (2019); Azabou (2021). The work presented in chapter 2 reflects recent efforts undertaken to improve those three aspects. The ultimate goal of improving such aspects is to address society and industry challenges, such as the underground disposal of heat-generating nuclear waste and the underground storage of fluids and energy carriers in salt caverns. In the first section of chapter 3, I illustrate the consequences of overlooking those aspects. Then, I present modeling work of a field test that aims to better understand high frequency cycling in salt caverns in the context of the transition to low-carbon energy. The last part of chapter 3 summarizes my postdoctoral research, in which I developed numerical tools and performed two-way coupled thermal-hydraulic-mechanical modeling in the context of nuclear waste disposal in saliferous formations. In chapter 4, I present the main conclusions of my research activities, as well as some perspectives for the next years.

Chapter 2

Rheology

2.1 Physically-based and phenomenological laws

The research on rock salt not only for storage purposes, but also for salt/brine production and for the understanding of halokinetic crustal processes, has led to extensive literature on rock salt rheology. As introduced in the first chapter, there are two main types of models: physically-based and phenomenological. The former are based on micro-mechanisms that control the creep deformation under given conditions (stress, temperature, brine availability . . .). For instance, at high deviatoric levels mechanisms of flow type, such as dislocation glide, cross-slip and climb dominate (Frost & Ashby, 1982). At low deviatoric levels and moderate to high temperatures diffusional mechanisms, such as pressure solution and dynamic recrystallisation, become important (Urai & Spiers, 2007). Most parameters involved in this type of model have a physical meaning, which eases their determination. Since the 1970s, deformation-mechanism maps have been developed to represent the stress and temperature conditions where a single mechanism dominates the (quasi-stationary) creep rate; the objective of such maps is to guide in the selection of a constitutive model for a particular application (Ashby, 1972; Munson & Dawson, 1981). Two examples are shown in Figure 2.1. It is interesting to mention that the dominant mechanisms at relevant conditions for most engineering applications are not fully understood. In fact, the flow of rock salt in nature tends to occur in the transition between the dislocation-dominated and the pressure solution-dominated fields (Spiers et al. (1990) and Figure 2.1).

Physically-based models may combine several micro-mechanisms to describe macroscopic rock salt behaviour. Examples of these models include Spiers&Carter, Ellis, Urai&Spiers, Wawersik&Zeuch (Wawersik & Zeuch, 1986; van Keken et al., 1993; Spiers & Carter, 1996; Urai & Spiers, 2007). In some cases, upscaling stresses and strains to the RVE in a self-consistent framework has been performed (micro-macro approach that accounts for the interactions between halite crystals, see for instance Pouya (2000); Zhu et al. (2015); Xu & Arson (2022)). It should be noted however that physically-based as well as micro-macro models often comprise phenomenological parameters that have to be calibrated on the basis of test results. In addition, physically-based models are often limited to steady state creep (whether a steady state is actually reached is still an open question within the salt mechanics community). Accepting this assumption, a complete reproduction of natural salt behaviour at the RVE scale would require a complex combination of mechanisms, which would be impractical for numerical simulations at the engineering scale.

In turn, phenomenological models attempt to reproduce the observed experimental response without examining the underlying physical processes. Their main advantages are that they re-

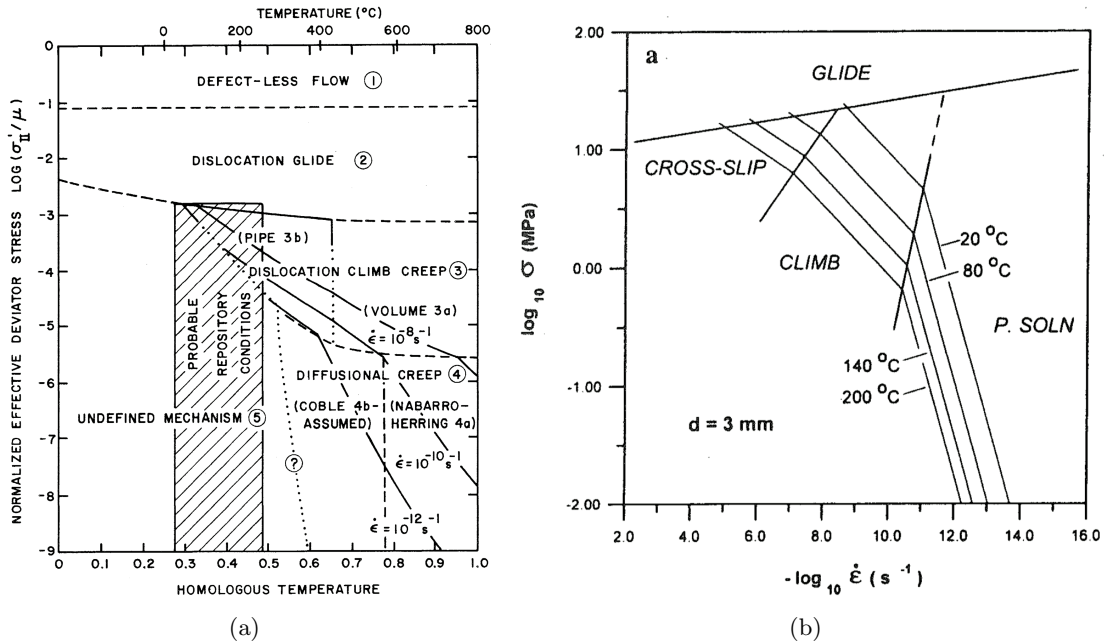


Figure 2.1. Deformation-mechanism maps for natural rock salt: (a) from Munson & Dawson (1981) and (b) from Spiers & Carter (1996), grain size $d = 3 \text{ mm}$. Each labeled domain represents the conditions where the specified mechanism dominates. In the vertical axes, both σ'_{II} and σ refer to von Mises equivalent stress, and μ is the shear modulus (Lamé’s second parameter).

produce an overall response at the RVE scale and are best suited for numerical simulations at the engineering scale; however, owing to the lack of physical basis, extrapolation is delicate. As explained in Tijani’s habilitation (Tijani, 2008), a unique phenomenological law exists for a given material; nevertheless, its complete determination would require to perform tests along all expected loading paths in the field, which is impractical. As a result, approximate laws are sought; this explains the vast number of phenomenological models developed over the years for rock salt, *e.g.*, Munson-Dawson, Cristescu, SUVIC, Günther-Salzer, Lux/Wolters/Lerche, Norton-Hoff, Lemaitre, RTL, Reedlunn (Tijani et al., 1983; Cristescu, 1993; Munson, 1997; Aubertin et al., 1999; Bérest et al., 2008; Günther & Salzer, 2012; Lux et al., 2018; Azabou et al., 2021c; Reedlunn, 2022). These laws include functional forms with various levels of complexity to account for different processes (*e.g.*, transient and stationary creep, damage, healing), and their parameters are fitted on experimental data, typically at the laboratory scale, with a parameter recalibration on field data when possible (*e.g.*, cavern volume loss over time, measurements at the WIPP and the Asse mine lasting several years). In my research, oriented towards engineering applications, I have focused so far on this type of law.

An example of extrapolation that is currently topical within the salt mechanics community is creep at low stress deviators. As mentioned in the first chapter, performing tests at low stress levels is difficult because it is very important to keep the test conditions (temperature, relative humidity, applied stresses) stable, so that the measured strain is not affected by experimental artefacts that could make the determination of the viscoplastic strain difficult and subject to hypotheses (for instance, if the ambient temperature fluctuates slightly, the temperature is not uniform within the sample, and the corresponding non-uniform thermo-elastic strains can be as high as the viscoplastic

strains). A few tests have been conducted in very specific settings, such as the *Altaussee* (Austria) and *Varangéville* (France) mines (Bérest et al., 2005, 2019), or a dedicated chamber in which temperature stability can be controlled to ± 0.01 K (Hunsche, 1984). These tests are original, but have limitations (uniaxial configuration, availability, feasibility/cost of the facilities). In general, tests are performed using high stress deviator levels (often in the range $5 \leq Q - P \leq 30$ MPa¹), corresponding to the conditions close to the excavated openings, and the results are extrapolated towards low stress deviators when numerical simulations at the facility scale are carried out (in the far field, the deviatoric stresses are low). Figure 2.2 shows experimental creep rates at the end of loading stages in the range $0.1 \leq Q - P \leq 40$ MPa, and suggests that the exponent of the classic power creep law changes from $n \approx 5 - 7$ at high stress levels to $n \approx 1$ at low stress levels, with a transition zone in the range $3 \leq Q - P \leq 8$ MPa.

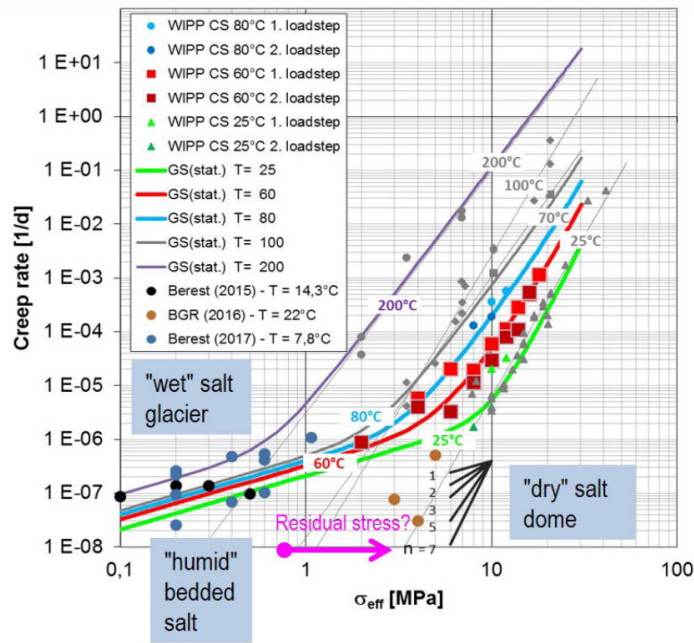


Figure 2.2. Creep rates as a function of the deviatoric stress (after Herchen et al. (2018)). Symbols correspond to experimental data and solid lines to predictions using the Günther-Salzer (GS) steady state creep law (Günther & Salzer, 2012). Note that $\sigma_{\text{eff}} = q$.

A first interpretation of this graph suggests that, if tests are performed under typical laboratory conditions and the results are extrapolated towards lower stress deviators, the quasi-stationary creep rates will be underestimated by several orders of magnitude, with potential impacts to the prediction of underground structures. Nevertheless, it should be noted that none of the displayed campaigns covers the whole stress range. Besides, it is not clear whether the rates correspond to

¹In this manuscript, Q is the applied axial stress during a test and P is the applied confining pressure. Assuming that the sample response is homogeneous, $C = \frac{Q+2P}{3}$ is the mean pressure and $D = |Q - P|$ is the stress deviator. However, when heterogeneities in the stress and strain fields arise, the local mean pressure and the local von Mises equivalent deviatoric stress should be computed using $p = -\frac{1}{3}\text{tr}(\underline{\underline{\sigma}})$ and $q = \sqrt{\frac{3}{2}}\|\underline{\underline{\sigma}}'\|$, respectively, where $\underline{\underline{\sigma}}$ is the Cauchy stress tensor and $\underline{\underline{\sigma}}' = \underline{\underline{\sigma}} - \frac{1}{3}\text{tr}(\underline{\underline{\sigma}})\underline{\underline{1}}$ is the deviatoric stress tensor. The third invariant is the Lode angle, defined as $\theta = \frac{1}{3}\arccos\left(\sqrt{6}\text{tr}\left(\underline{\underline{J}}^3\right)\right)$, with $\underline{\underline{J}} = \frac{\underline{\underline{\sigma}}'}{\|\underline{\underline{\sigma}}'\|}$.

truly stationary or to transient conditions (the data are analyzed with a stationary creep law). As it will be explained below, in the analysis the effect of the stress deviator can be separated from the effect of time, making the approach more powerful. From a microscopic point of view, the different response observed experimentally between high and low stress deviators is attributed to a change in dominant mechanism, see Figure 2.1: dislocation cross-slip and climb at high stress levels and pressure solution at low stress levels. Several phenomenological constitutive laws have been recently developed/adapted to account for this fact, and many modeling exercises have been performed (the reader is referred to the proceedings of SaltMechX for a wide range of examples).

The need to investigate further low stress deviators was highlighted in Tijani (2008). To avoid the limitations of uniaxial tests, short after Tijani et al. (2009) performed one confined creep test at $T = 50\text{ }^\circ\text{C}$ comprising several deviatoric stress levels: $Q - P = \{0.13, 0.5, 1, 2, 10\}$ MPa. The results are shown in Figure 2.3 (experimental data in the left-hand side plot and computed strain rates in the right-hand side plot). As it can be seen, a stationary state was not reached in any of the loading stages; nevertheless, this is not a limitation to study the influence of the stress deviator on the creep response, since it is possible to separate the effect of time from that of other variables such as the stress deviator or the temperature (details will be given below).

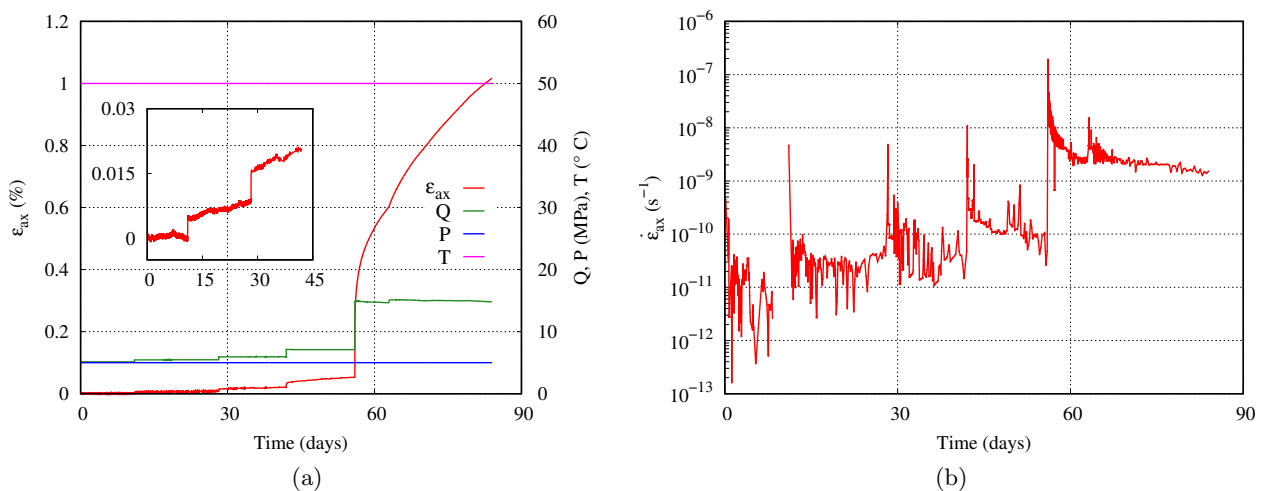


Figure 2.3. Confined creep test performed at $T = 50\text{ }^\circ\text{C}$ and several deviatoric stress levels (Tijani et al., 2009): (a) experimental data (the enlarged view shows the three first loading stages); (b) computed strain rate (values displayed are greater than 10^{-18} s^{-1}).

Tijani et al. (2009) performed only one test, and there was only one stage performed at high deviatoric stress. In order to gain more insight into this aspect, we have recently conducted additional confined creep tests at low and high stress deviator levels (project Citeph-20-2018, see Blanco-Martín et al. (2021a) and Blanco-Martín et al. (2022a) for details), and four other tests are underway in collaboration with a cavern operator. Three examples are discussed here, corresponding to two salt origins (hereafter Salt 1 and Salt 2). The results are shown in Figure 2.4. The three tests were conducted at $T = 50\text{ }^\circ\text{C}$ and comprised several loading levels, each of a duration of 3-4 weeks: $Q - P = \{0.5, 1, 2, 5, 10, 15, 20^2\}$ MPa. Again, as it can be inferred from the right-hand side plots, a stationary state was not reached in any of the loading stages, but this is not a limitation.

²The last loading level applies only to the test on the Salt 1 sample.

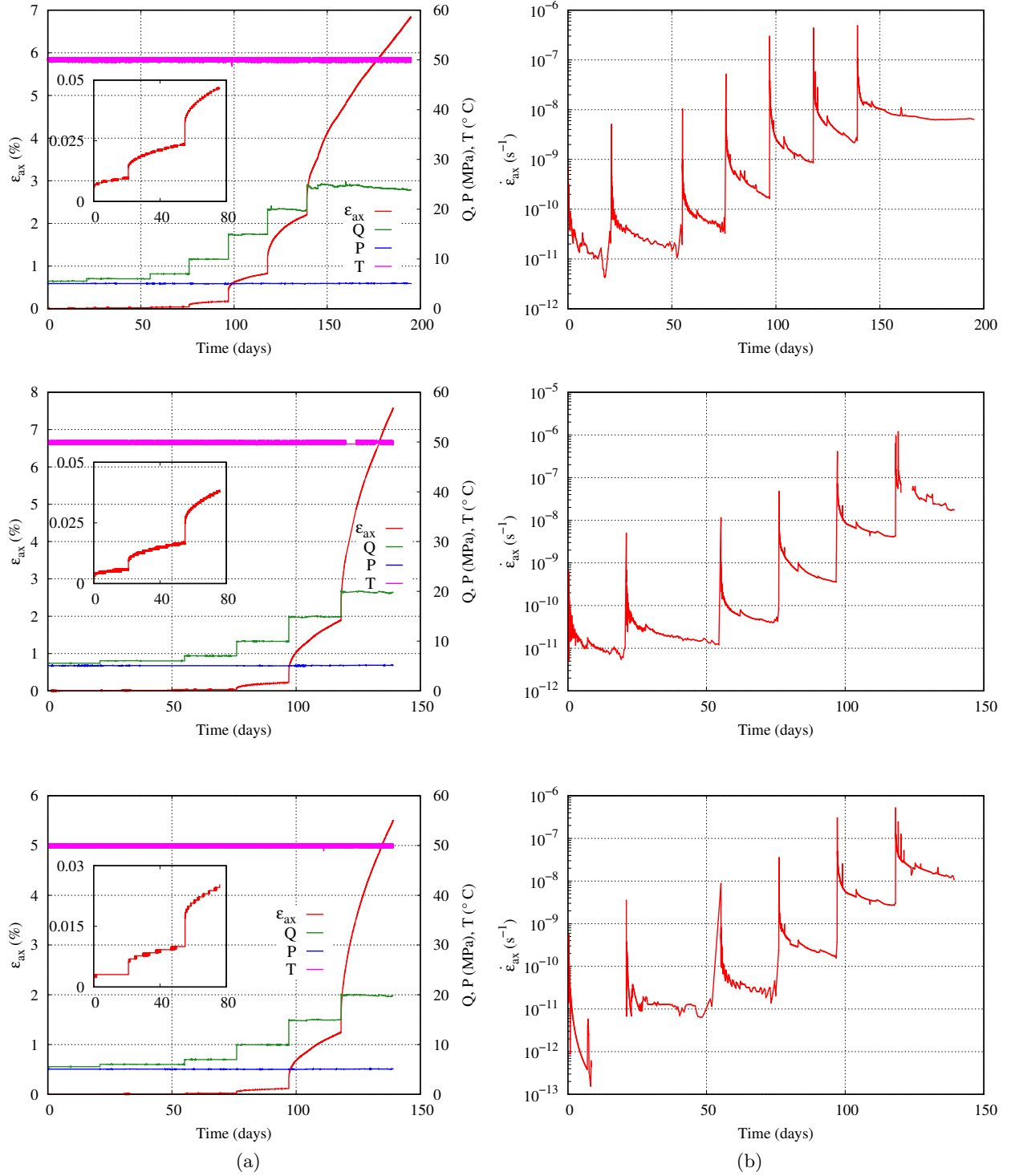


Figure 2.4. Recent confined creep tests performed at $T = 50 \text{ }^\circ\text{C}$ and several deviatoric stress levels in the range $Q - P \in [0.5 - 20] \text{ MPa}$: (a) experimental data of three tests (the enlarged view shows the three first loading stages); (b) computed strain rate (values displayed are greater than 10^{-18} s^{-1}). The top row corresponds to Salt 1 and the two other rows correspond to Salt 2. All tests were conducted at Mines Paris ([Blanco-Martín et al., 2021a](#)).

Results from these tests have been interpreted with the Lemaitre creep law (Tijani et al., 1983), which is the basis of the research on rock salt rheology at the Centre for Geosciences and Geoengineering of Mines Paris; nevertheless, other phenomenological laws could have been used, each having advantages and disadvantages (*e.g.*, assumptions on relevant processes, number of parameters, robustness of parameter identification, suitability of a parameter set to reproduce data under different loading paths and time scales ...)³. In the following, partition of the total strain rate tensor, $\underline{\dot{\epsilon}}$, into elastic, $\underline{\dot{\epsilon}}_{el}$, thermal, $\underline{\dot{\epsilon}}_{th}$ and viscoplastic, $\underline{\dot{\epsilon}}_{vp}$, parts is assumed:

$$\underline{\dot{\epsilon}} = \underline{\dot{\epsilon}}_{el} + \underline{\dot{\epsilon}}_{th} + \underline{\dot{\epsilon}}_{vp} \quad (2.1)$$

where $\underline{\dot{\epsilon}}_{el} = \frac{(1+\nu)}{E} \underline{\dot{\sigma}} - \frac{\nu}{E} \text{tr}(\underline{\dot{\sigma}}) \underline{\mathbb{1}}$ is the elastic strain rate tensor (E is the Young's modulus and ν the Poisson's ratio), $\underline{\dot{\epsilon}}_{th} = \alpha_{th} \underline{T} \underline{\mathbb{1}}$ is the thermal strain rate tensor (α_{th} is the linear thermal expansion coefficient), and the viscoplastic strain rate tensor is given by the Lemaitre constitutive law:

$$\underline{\dot{\epsilon}}_{vp} = \sqrt{\frac{3}{2}} \dot{\gamma}_{vp} \underline{J} \quad (2.2)$$

where $\dot{\gamma}_{vp} = \sqrt{2/3} \|\underline{\dot{\epsilon}}'_{vp}\|$ is the equivalent deviatoric viscoplastic strain rate (the deviatoric component of a tensor \underline{a} is denoted by $\underline{a}' = \underline{a} - \frac{1}{3} \text{tr}(\underline{a}) \underline{\mathbb{1}}$) and $\underline{J} = \frac{\underline{\sigma}'}{\|\underline{\sigma}'\|}$ is a unit tensor along the deviatoric flow direction. The evolution law of the hardening variable is defined by

$$\frac{d\gamma_{vp}^{1/\alpha}}{dt} = \left(\frac{q}{K(T)} \right)^{\beta/\alpha} \quad (2.3)$$

where $K(T) = k_r \exp(A_L \alpha/\beta (1/T - 1/T_r))$, T_r is the reference temperature, $0 < \alpha < 1$, and β , k_r and A_L are positive material parameters. From Eq.(2.3) it can be deduced that

$$\dot{\gamma}_{vp} = \psi_{vp}(\underline{\sigma}, T, \gamma_{vp}) = \alpha \exp\left(A_L \left(\frac{1}{T_r} - \frac{1}{T}\right)\right) \left(\frac{q}{k_r}\right)^{\beta/\alpha} \gamma_{vp}^{1-\frac{1}{\alpha}} \quad (2.4)$$

The above equation demonstrates that, under constant q and T , the Lemaitre creep law is purely transient. The analysis of the three tests with this law is displayed in Figure 2.5. The fitting procedure, adapted from P. Labaune's PhD work (Labaune, 2018), does not treat all parameters equally: a single pair (α, E) is determined for the whole test (α and E are constant throughout each test), and for each loading stage a value of $\gamma_{vp}^{1/\alpha}$ is determined, ensuring continuity between consecutive stages. Note that this procedure can only be applied if $\gamma_{vp}^{1/\alpha}$ is constant per loading stage, which is the case here (q and T are constant per stage). One main advantage of this fitting procedure is that the number of parameters to be fitted in each step is reduced, because two fittings are nested. Afterwards, an expression for $\gamma_{vp}^{1/\alpha}$ is sought. Creep tests performed over the years on salt samples from different origins, in the range $5 \leq Q - P \leq 30$ MPa, suggest that the expression in Eq. (2.3) (Lemaitre law) reproduces data satisfactorily. However, and particularly if the number of loading stages is reduced, other mathematical expressions could also yield satisfactory results.

³During my postdoctoral research at the Energy Geosciences Division of Lawrence Berkeley National Laboratory, I used other laws, mainly the Lux/Wolters creep law for natural salt developed at TU Clausthal and the cwipp creep law developed at Sandia National Laboratories to model crushed salt compaction in the context of nuclear waste disposal. These laws are not explained in this manuscript for brevity, but details can be found in, *e.g.*, Wolters et al. (2012); Lux et al. (2018); Blanco-Martín et al. (2016b); Itasca (2009); Sjaardema & Krieg (1987).

Here, the range $0.5 \leq Q - P \leq 20$ MPa is investigated. As it can be seen, the stress deviator dependency is different at high and low stress levels, and, as suggested by Tijani et al. (2009), it is best captured with a double power law:

$$\frac{d\gamma_{vp}^{1/\alpha}}{dt} = \exp\left(A_L\left(\frac{1}{T_r} - \frac{1}{T}\right)\right) \left(\left(\frac{q}{k_{r1}}\right)^{\beta_1} + \left(\frac{q}{k_{r2}}\right)^{\beta_2} \right)^{1/\alpha} \quad (2.5)$$

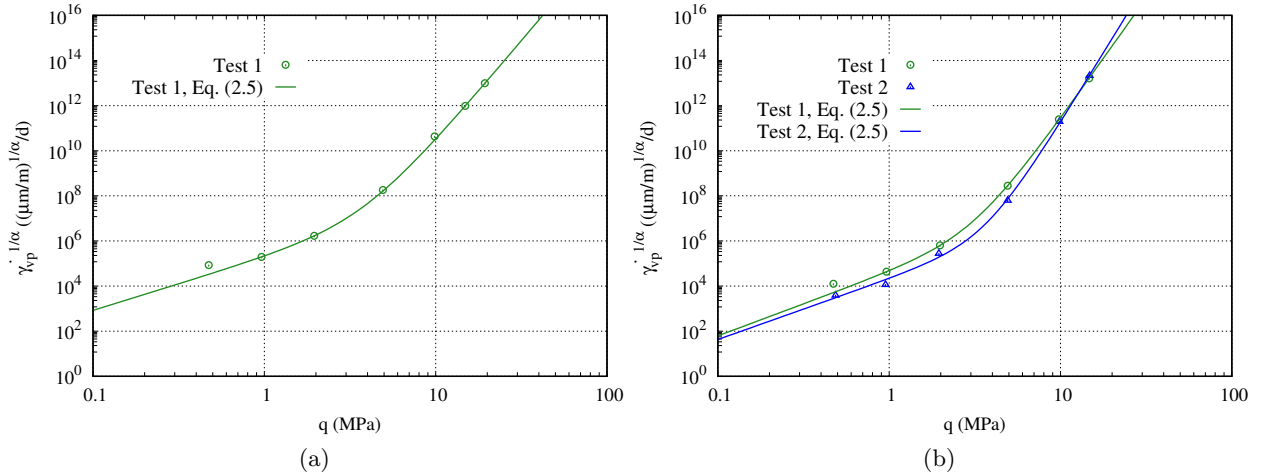


Figure 2.5. Analysis of the creep tests in Figure 2.4 performed at $T = 50$ °C and several deviatoric stress levels with the modified Lemaître creep law, Eq. (2.5): (a) Salt 1 ; (b) Salt 2.

Note that, for now, k_{r1} and k_{r2} are different, but the same temperature dependence is used for $K_1(T)$ and $K_2(T)$ (all tests have been conducted at the same temperature, so for consistency with Lemaître creep law, a single function of the temperature is used [as a perspective, in chapter 4 I propose to perform tests at several other temperatures; such tests and supplementary analyses will shed light on the temperature influence at low and high stress deviators]). Since two tests are available for Salt 2, a recalibration is performed simultaneously for both tests, taking the results shown above as the initial guess. The obtained parameters are listed in Table 2.1 and the comparison between model predictions and experimental data is shown in Figure 2.6. Note that here t_0 corresponds to the end of the isotropic phase —performed at $C = 17$ MPa and $D = 0.2$ MPa, with $Q > P$ — in order to include the initial elastic relaxation in the calculation of E (the isotropic phase is not illustrated in Figure 2.4, *i.e.*, there is an offset between the two Figures). The comparison is rather satisfactory both for low and high stress deviators (note that Salt 2 exhibits some scatter). For low stress levels, the exponent is close to 1. One could therefore infer that the exponent is about 1 for low stress levels. Notwithstanding, two important facts should be highlighted. First, if different loading paths are applied, the results cannot be extrapolated. As explained above, phenomenological models are only approximations of the true model, whose determination would require to test all relevant loading paths (here, we have only performed creep tests under constant P and T , and several stages of Q). Second, from a physical viewpoint the near-1 exponent at low stress levels is related to pressure solution creep, which requires the presence of intergranular brine; however, these samples have not been characterized at the microscopic scale, and no information is available on the brine content (recall that we are using a phenomenological approach, so it is not possible to conclude on the dominant deformation mechanisms).

Table 2.1. Parameters of the modified Lemaitre creep law (two power laws for the deviatoric stress dependence, Eq. (2.5)), derived from the creep tests in Figure 2.4 performed at $T = T_r = 50$ °C. The unit system is such that strain is in $\mu\text{m}/\text{m}$, stress in MPa, temperature in K and time in days.

	E	ν	α	k_{r1}	β_1	k_{r2}	β_2
Salt 1	8938	0.3	0.326	0.704	2.930	0.006	0.764
Salt 2	11739	0.3	0.340	1.216	3.950	0.044	0.951

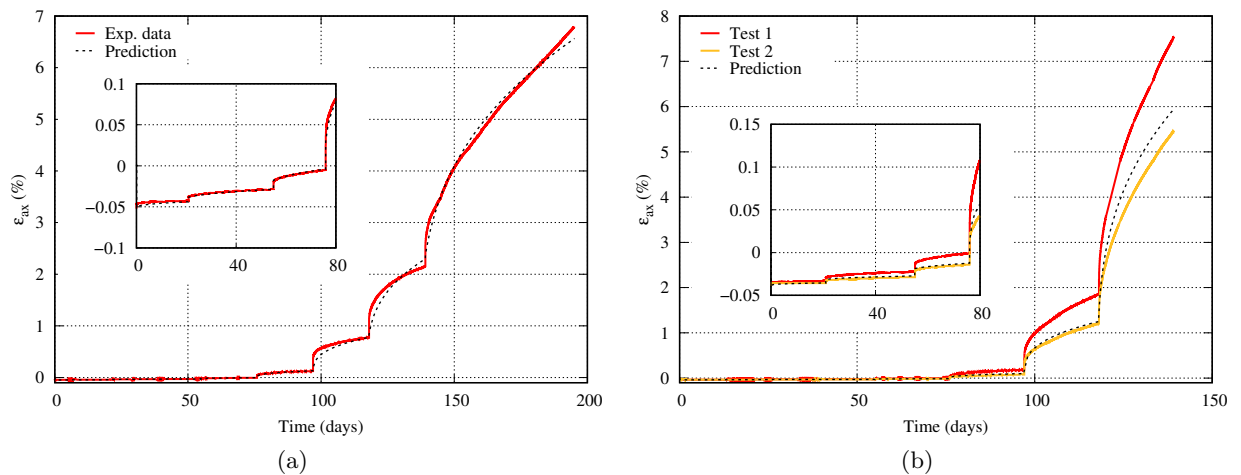


Figure 2.6. Comparison between experimental data (Figure 2.4) and model predictions with the modified Lemaitre creep law (Eq. (2.5)) using the parameters listed in Table 2.1: (a) Salt 1 ; (b) Salt 2. The model predictions are obtained using the in-house FEM code Phimef, in which I implemented the modified Lemaitre creep law.

Under these circumstances, the user should make sure that the selected model and parameters allow to simulate the target field application without extrapolation. For such purpose, consistently with Tijani (2008), the simulation results should be analyzed at different times and spatial zones and it should be verified that the computed strains, strain rates, stresses and temperatures lie within the experimental ranges that were used to infer the model and parameters. Even if this seems self-evident, it is not uncommon in engineering practice worldwide to extrapolate the material response beyond the range investigated at the laboratory scale (up to recently, $5 \leq Q - P \leq 30$ MPa because more importance was given to the near field). The tests shown above investigate the range $0.5 \leq Q - P \leq 20$ MPa, and suggest a different deviator dependence for low and high stress levels. In order to illustrate the consequences of extrapolating results obtained at high stress deviators towards low stress deviators, we now assume that the creep tests only comprised stages at high stress deviators (standard procedure up to recently). With only three or four stages, the classic Lemaitre law can be used, Eq. (2.3). Taking Salt 1 as an example, the fitting yields (note that E and α are those in Table 2.1): $\beta = 2.571$, $k_r = 0.443 \text{ MPa} \cdot \text{j}^{\alpha/\beta} (\mu\text{m}/\text{m})^{-1/\beta}$. Figure 2.7 compares the two fittings; as it can be seen, if only high stress deviators are considered, the extrapolation towards lower deviatoric levels underestimates $\gamma_{vp}^{1/\alpha}$ by several orders of magnitude. In fact, even if Eq. (2.3) is used for the whole experimental range, the differences between taking $0.5 \leq Q - P \leq 20$ MPa or $5 \leq Q - P \leq 20$ MPa are very large.

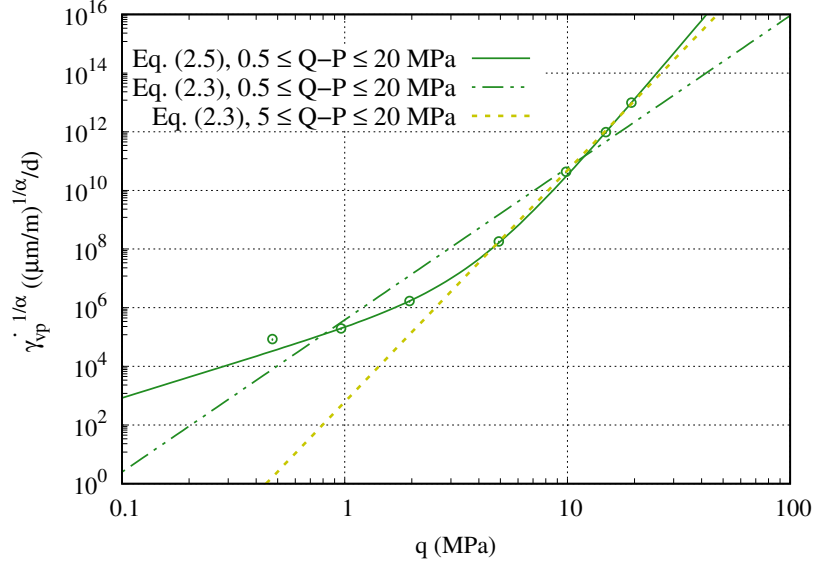


Figure 2.7. Salt 1: fitting considering the range $0.5 \leq Q - P \leq 20$ MPa with Eqs. (2.5) and (2.3), or the reduced range $5 \leq Q - P \leq 20$ MPa with Eq. (2.3).

Both models and parameter sets are now used to perform a 30-year prediction of a creep test under $T = 50$ °C. In one case, $Q - P = 1$ MPa, and in the other case, $Q - P = 10$ MPa. Figure 2.8 shows the results obtained. In fact, since there is only one loading stage, the relative error e between the two curves in each plot can be calculated as

$$e = 1 - \frac{\gamma_{vp,\text{single}}}{\gamma_{vp,\text{double}}} = 1 - \frac{\left(\frac{q}{k_r}\right)^\beta}{\left(\frac{q}{k_{r1}}\right)^{\beta_1} + \left(\frac{q}{k_{r2}}\right)^{\beta_2}} \quad (2.6)$$

yielding $e = -12.3\%$ for $Q - P = 10$ MPa and $e = 85.2\%$ for $Q - P = 1$ MPa. As it can be seen, the differences are noteworthy particularly for low stress levels. It should be noted however that the strains are quite small in that case. As a perspective, specific investigations should be performed for a particular site (depth, geometrical aspects, loading history, temperature, salt creep characteristics ...) to quantify the impact of each model and parameter set on the simulated response.

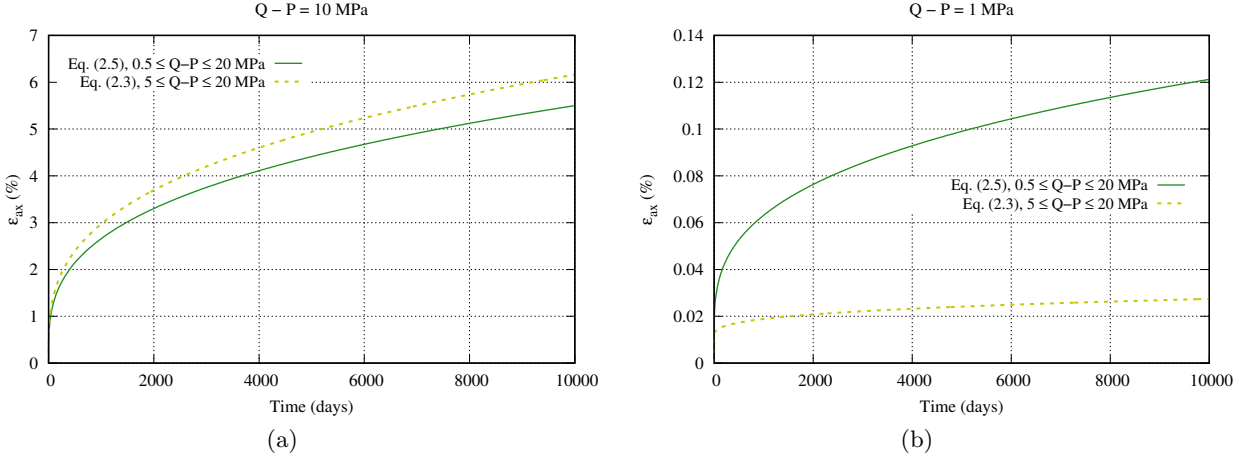


Figure 2.8. Salt 1: thirty-year prediction of a creep test at $T = 50$ °C with a parameter set obtained for $5 \leq Q - P \leq 20$ MPa (Eq. (2.3)) and a parameter set obtained for $0.5 \leq Q - P \leq 20$ MPa (Eq. (2.5)): (a) $Q - P = 10$ MPa; (b) $Q - P = 1$ MPa.

2.2 Temporal extrapolation

After focusing on the stress deviator in the previous section, here I focus on time, taking again the Lemaitre creep law as a reference to illustrate the main ideas. The Lemaitre creep law, originally developed for metals, is a transient law in which the viscoplastic strain rate reaches zero asymptotically if the deviatoric stress and the temperature are held constant (see Eq. (2.4), where $\alpha < 1$). Since its first use for rock salt in the 1970s, the Centre for Geosciences and Geoengineering of Mines Paris has introduced progressive improvements to this law and to the determination of its parameters⁴. In particular, because of the transient nature of the law, when laboratory results are extrapolated to longer periods of time (such as a cavern in operation during 40 or 50 years), the numerical predictions often underestimate the closure rate, impacting the estimations of, for instance, the volume of stored fluid. To overcome this limitation, in 2020 a second deviatoric transient component was added to improve the long-term predictions in the framework of M. Azabou’s PhD work (Azabou, 2021), that I co-supervised. This transient component is inspired from the transient part of the Munson-Dawson law (Munson, 1997), having a saturation strain and a characteristic time that are function of the stress deviator. Full details about RTL2020 (including the non-elastic volumetric component) are provided in Appendix B.4, and here only its mean features as regards the long-term are recalled. The equivalent deviatoric viscoplastic strain rate is now given by

$$\dot{\gamma}_{vp} = \dot{\gamma}_L + \dot{\gamma}_R \quad (2.7)$$

where $\dot{\gamma}_L$ corresponds to Eq. (2.4), but some parameters have been renamed:

$$\dot{\gamma}_L = \psi_L(\underline{\underline{\sigma}}, T, \gamma_L) = \alpha \exp\left(A_R \left(\frac{1}{T_r} - \frac{1}{T}\right)\right) \left(\frac{q}{A_2}\right)^{n_2} \gamma_L^{1-\frac{1}{\alpha}} \quad (2.8)$$

⁴Although not discussed here, in 2014 non-elastic viscoplastic strains were introduced in the framework of P. Labaune’s PhD work, and the law was renamed to RTL (Labaune et al., 2018; Labaune, 2018; Rouabhi, 2019). The viscoplastic strain rate tensor is expressed $\underline{\underline{\dot{\epsilon}}}_{vp} = \sqrt{\frac{3}{2}} \dot{\gamma}_{vp} \underline{\underline{I}} - \frac{1}{\sqrt{3}} \dot{\gamma}_{vp} \underline{\underline{I}}$, where $\underline{\underline{I}} = \frac{\underline{\underline{1}}}{\sqrt{3}}$.

The evolution law of the added component, $\dot{\gamma}_R$, is given by

$$\dot{\gamma}_R = \psi_R(\underline{\sigma}, T, \gamma_R) = \begin{cases} A(1 - \gamma_R/\bar{\gamma}_R)^n R(\underline{\sigma}, T) & \text{if } \gamma_R \leq \bar{\gamma}_R \\ -B(\gamma_R/\bar{\gamma}_R - 1)^m R(\underline{\sigma}, T) & \text{if } \gamma_R \geq \bar{\gamma}_R \end{cases} \quad (2.9)$$

where A and B are positive material parameters, $m > 1$, $n > 1$ and $\bar{\gamma}_R = (q/A_1)^{n_1}$ is the transient saturation strain (A_1 and n_1 are positive material parameters). As Eq. (2.9) shows, the second branch of $\dot{\gamma}_R$ allows to model inverse creep. As explained in Azabou et al. (2021c), $R(\underline{\sigma}, T)$ is taken to be equal to $\dot{\gamma}_L^{1/\alpha}$ to link the two components and to ensure that they yield contributions of the same order of magnitude.

Several laboratory campaigns have been successfully analyzed with RTL2020 (Azabou et al., 2021c). Here, a large campaign (≈ 50 tests) that I defined and oversaw with M. Azabou on Salt 1 is shown, including constant strain rate tests, constant mean stress tests (under triaxial compression and triaxial extension) and confined creep tests performed along different loading paths (constant mean pressure, constant deviatoric stress, constant confining pressure, triaxial compression, triaxial extension, different temperatures) and lasting up to 1 year. Table 2.2 lists the parameter set that best fits all tests simultaneously (a single set for all tests shown). Note that in this case, we perform a simultaneous fitting of short-term and long-term tests, and the elastic constants are deduced from unloading-reloading cycles during short-term tests. Figures 2.9-2.12 compare experimental results with model predictions. Overall, the comparison is deemed satisfactory.

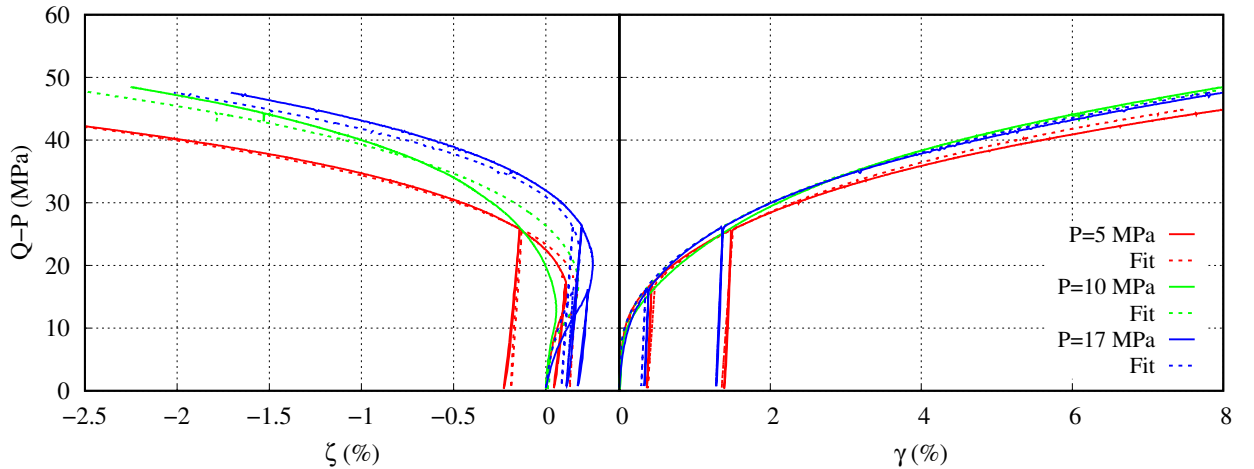


Figure 2.9. Salt 1: fitting of constant strain rate tests at $\dot{\epsilon}_{ax} = 10^{-6} \text{ s}^{-1}$ and ambient temperature with RTL2020 (equations of the volumetric part are detailed in Appendix B.4). All tests were conducted at Mines Paris (Blanco-Martín et al., 2022a).

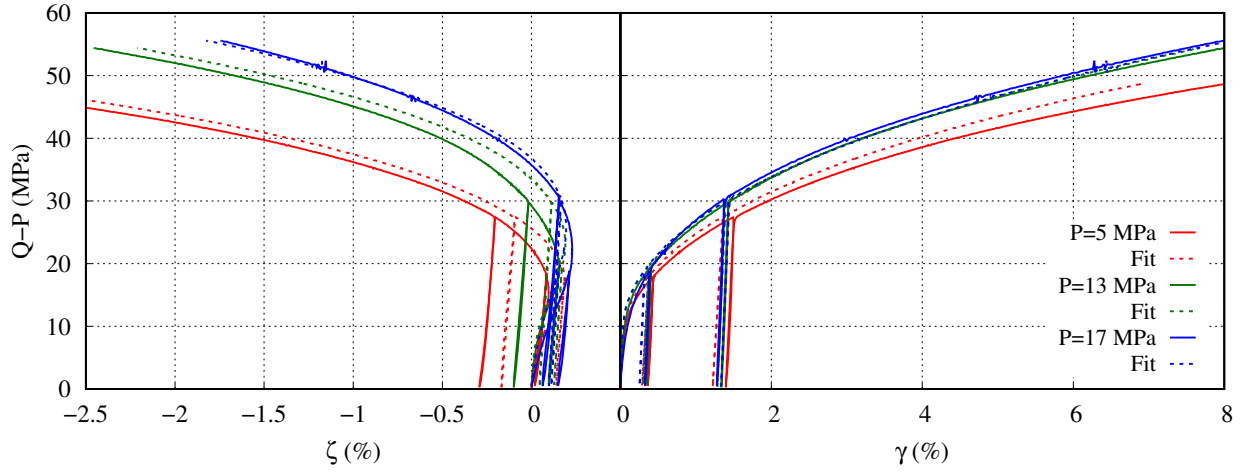


Figure 2.10. Salt 1: fitting of constant strain rate tests at $\dot{\epsilon}_{ax} = 10^{-5} \text{ s}^{-1}$ and ambient temperature with RTL2020 (equations of the volumetric part are detailed in Appendix B.4). All tests were conducted at Mines Paris (Blanco-Martín et al., 2022a).

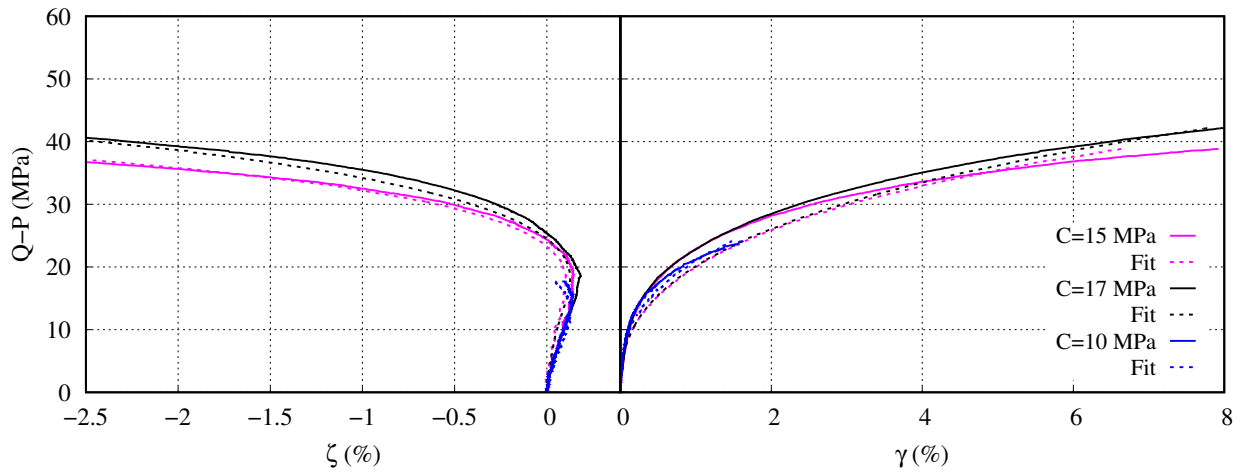


Figure 2.11. Salt 1: fitting of constant mean stress tests at $\dot{P} = -1 \text{ MPa/d}$ and ambient temperature with RTL2020 (equations of the volumetric part are detailed in Appendix B.4). All tests were conducted at Mines Paris (Blanco-Martín et al., 2022a).

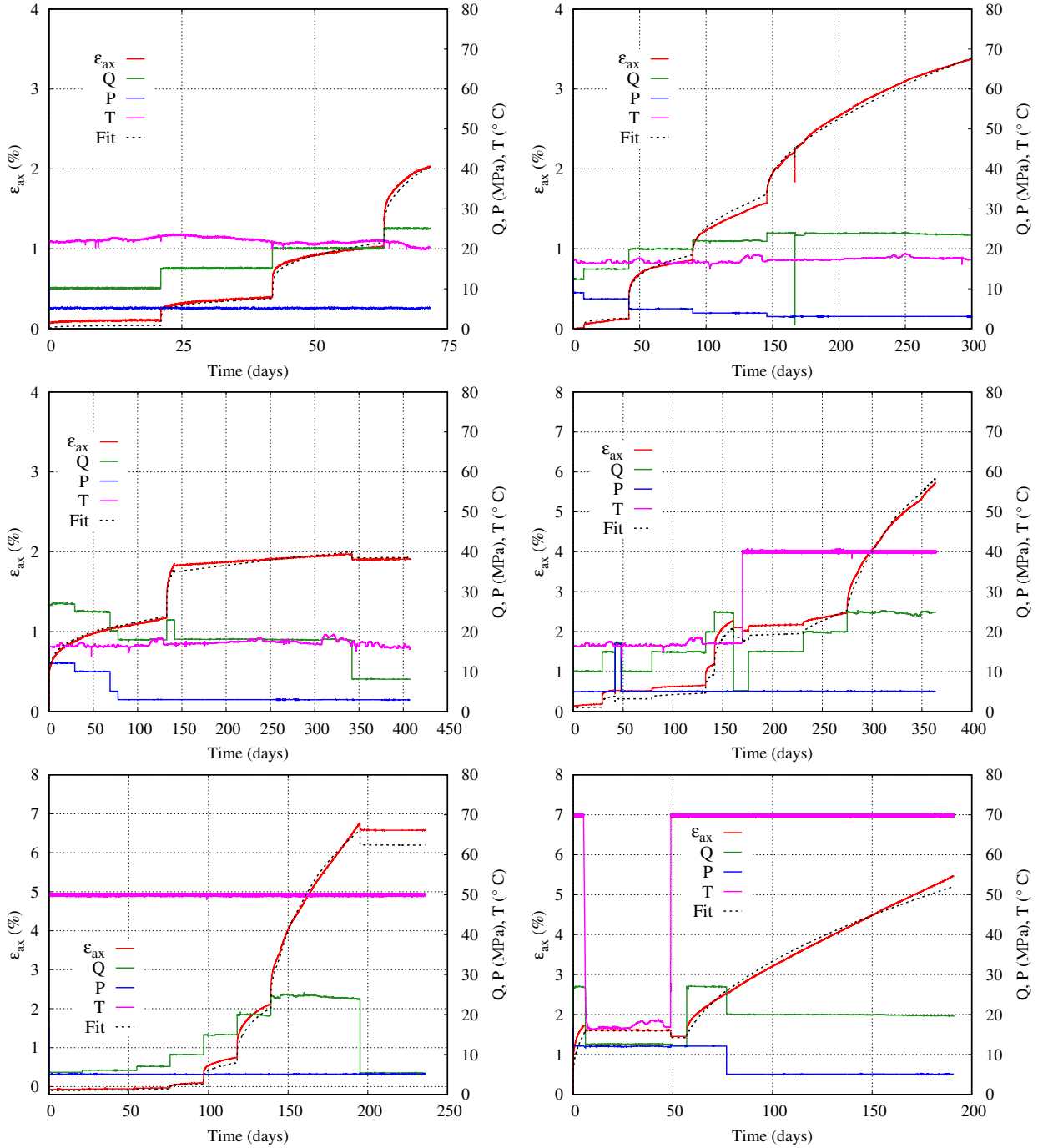


Figure 2.12. Salt 1: fitting of multi-stage creep tests at ambient and higher temperatures with RTL2020 (volumetric strains are not available). All tests were conducted at Mines Paris ([Blanco-Martín et al., 2022a](#)).

Using the parameters fitted on laboratory tests, [Azabou et al. \(2021c\)](#) showed that the long-term predictions (over 30 years) provided by RTL2020 lie between those of well-known purely transient (such as Lemaitre) and transient-steady state (such as Munson-Dawson) creep models, which are known to be optimistic and conservative in terms of convergence, respectively (see Figures 3-7 in

Appendix B.4). In fact, as shown in those figures, the three models can fit laboratory data along typical loading paths quite satisfactorily, but the long-term extrapolation with the laboratory-deduced parameter set yields quite different results. As for RTL2020, its capability to yield intermediate long-term predictions, together with the rather good comparison between laboratory data (along many different loading paths) and model predictions shown above, are encouraging. Notwithstanding, the long-term extrapolation capacity is not validated, and the considerations highlighted in the previous section about the limits of extrapolation should be kept in mind. As a perspective, RTL2020 should be confronted against *all* data available in a particular site (*i.e.*, depth, convergence, loading history, spatial constraints), covering several decades. Additionally, we are currently working on a robust parameter identification procedure, accounting for low and high stress deviator levels. It should be noted that in spite of the limitations of phenomenological laws with regard to temporal extrapolation, most physically-based models assume a steady state response. However, available data do not clearly show that, after a long enough period of time, the strain rate is actually constant. Besides, if the strain rate is constant, the deformation would be in theory active even at infinite time, which is not physically possible (disregarding damage and failure, a sample height cannot be reduced to zero, and in fact before that, repulsive forces between Na^+ and Cl^- in the crystalline structure would reduce the creep rate). In the next years, I will work on physical aspects that could help understand the long-term creep of rock salt, see chapter 4.

Table 2.2. Salt 1: RTL2020 parameter set that best fits simultaneously short- and long-term tests. The unit system is such that strain is in $\mu\text{m}/\text{m}$, stress in MPa, temperature in K and time in days.

E	ν	α_{th}			
22360	0.29	32.7			
α	A_2	n_2	A_R	T_r	
0.5	2.63	7.06	7870	289.55	
A	B	n	m	A_1	n_1
10	0.5	20.95	1.46	0.148	2.04
z	n_z	N_z	m_z	M_z	
0.61	1.12	0.009	2.67	0.79	

2.3 Experimental observations

2.3.1 Heterogeneity

As explained in the first chapter (section 1.2), there are two main sources of heterogeneity when testing rock samples at the laboratory. The first source is due to the contact between the cell pistons and the sample, which in practice is not frictionless. As a consequence of the end restraint on the sample, an initially cylindrical specimen evolves into a barrel-shaped one under triaxial compression, and into an hourglass-shaped one under triaxial extension (these shapes are amplified as the deformation increases). The second source, material heterogeneity, is due to the presence of impurities within the samples (or to a too small a number of large crystals), and needs to be taken into account when the samples size is smaller than the RVE of the rock mass. Indeed, natural variability leads to a lack of representativity if the samples size does not meet the required RVE of the studied rock. Heterogeneity results in strain and stress fields within the sample (*i.e.*, different strain and stress tensors at each material point), rather than in a uniform response (Tijani, 2008;

Rouabhi, 2019).

Heterogeneity can be quantified by the use of different measurement techniques, capturing the sample response at different spatial scales (the use of different techniques also helps mitigate possible malfunctions of part of the devices during an experiment). In addition, dissolution, microscopic observations and scanning are useful to quantify material heterogeneity (and also grain size distribution) of salt samples. Over the last years, we have worked on two experimental set-ups that allow us to measure the strains at three different scales. Local measurements are provided by strain gauges, typically 1 cm-long and placed at sample mid-height. Axial and circumferential gauges are used (one pair of each, diametrically opposed). In addition to providing local measurements, strain gauges are useful to compute the elastic constants during unloading-reloading cycles. Hybrid measurements are provided by the combination of a circumferential extensometer at sample mid-height with either an axial extensometer (hereafter referred to as *hybrid 1* technique) or the global axial displacement of the sample (hereafter referred to as *hybrid 2* technique). It should be noted that, while the interpretation of strain gauges measurements is straightforward (they are local), hybrid measurements need the assumption of a particular shape to be interpreted (as an illustration, the volumetric strain at a non-local scale can be computed using $(V-V_0)/V_0$, where V_0 is the initial volume of the cylindrical sample, and V is the sample current volume, which is often assumed to remain cylindrical with a radius deduced from the measurements of the circumferential extensometer)⁵. Global measurements are provided by the displaced volume of confining fluid and the global axial displacement of the sample; in this case, it is in theory possible to quantify the volume of the real, non-cylindrical sample. Figure 2.13 shows a sketch of the multi-scale acquisition system as well as some views of the experimental set-ups. Efforts have been made to tune and optimize these set-ups, and exploratory and selected configurations are shown in the Figure. For instance, different bladders, having different stiffness and thickness, have been tested in combination with the extensometers. Ideally, the measuring devices should embrace the sample movement without adding movement or perturbations of the non-sample components (pistons, jacket ...). It is well known that circumferential extensometers require flexible and thin bladders for accurate measurements. Notwithstanding, thin bladders might be penetrated by the pins of the axial extensometer, thereby cancelling the tightness function of the jacket (also, slippage of the axial extensometer is likely if the confining fluid infiltrates across the bladder, or if the device is not properly fixed on the sample). On the other hand, thick jackets could compromise not only the use of the circumferential extensometer, but also that of the axial extensometer, as a thicker jacket complicates the joint movement of the sample and the device. After testing several configurations, we have selected very thin (≈ 0.1 mm) latex membranes to be used with the circumferential extensometer, in combination with the global axial displacement of the sample, provided by a LVDT sensor (*hybrid 2* technique). Although some tests were successfully performed using the axial extensometer (*hybrid 1* technique), its installation and accurate use proved to introduce significant uncertainty. The simultaneous use of strain gauges and the *hybrid 2* technique was successful in several cases, but some improvements are required (particularly, tightness of the passage of the electrical wires). Moreover, as the use of extensometers requires larger cells, it is not possible to simultaneously use hybrid and global measurement techniques (the error associated with the global volume change is proportional to the volume of confining fluid [about 8 l in the cell that is big enough to host the extensometers]). Therefore, one of our experimental set-ups allows for local and global measurements, and the other set-up allows for local and hybrid measurements.

⁵Note that in these conditions, the volume of the real, non-cylindrical sample, is smaller than V (we assume that the non-uniform radius attains its maximum at sample mid-height).

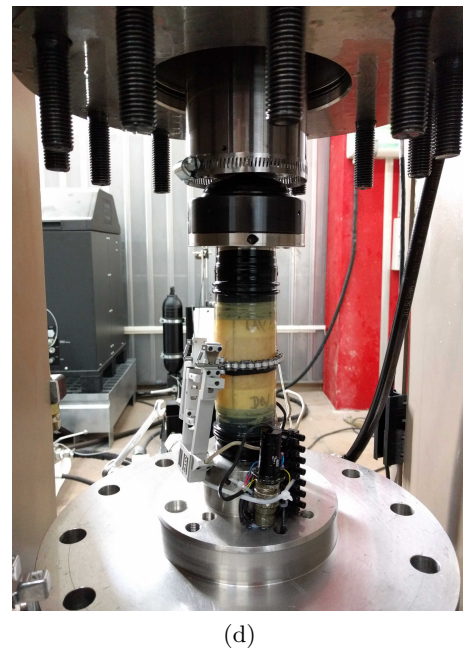
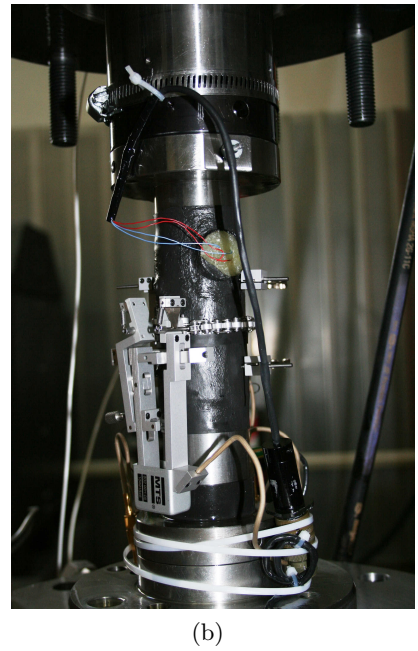
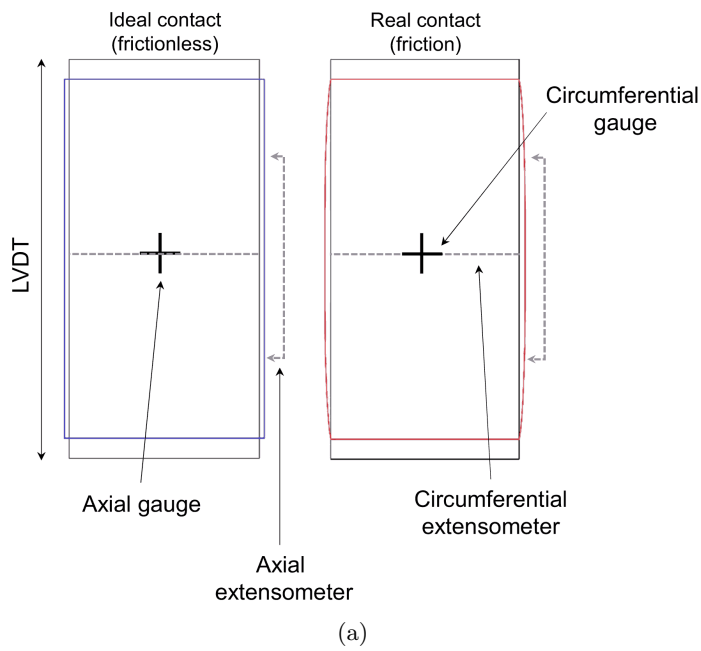


Figure 2.13. Multi-scale acquisition to quantify heterogeneity during a laboratory test: (a) sketch of measuring devices and sample shape during a triaxial compression test —an initially cylindrical sample (black contours) evolves into a deformed cylinder assuming a perfectly smooth contact (homogeneous stress and strain fields, blue contour) or into a barrel-shaped sample assuming a completely rough contact (heterogeneous stress and strain fields, red contour); (b): exploratory set-up with 1 mm thick Viton bladder, strain gauges and extensometers; (c): exploratory set-up with 0.1 mm thick latex bladder, strain gauges and extensometers; (d): selected set-up with 0.1 mm thick latex bladder, circumferential extensometer and global axial LVDT (LVDT not visible in the picture).

It should be noted that, in the absence of heterogeneity, all responses are theoretically identical, as shown in Figure 2.14. On the other hand, if heterogeneity is present, the responses are different as shown in the same Figure, assuming a fully frictional contact (numerical examples of material heterogeneity can be found in Azabou (2021)), and a real case of such heterogeneity will be illustrated in section 3.1, chapter 3). These numerical results prove that, for the worst case scenario (the area of the upper and lower faces of the sample remains constant during the test), the differences among spatial scales can be quite significant in terms of dilatancy threshold, which is an important criterion for the design of underground structures in rock salt (Labaune et al., 2018). As for the distortion component of strain, the Figure shows that the differences among spatial scales are less notorious, and in fact comparable to sample-to-sample variability. Note that these results are sensitive to the model and parameters, and for the illustrative purposes sought here, we have used the parameters listed in Table 2.3.

Table 2.3. RTL2020 parameter set used to investigate heterogeneity numerically. The unit system is such that strain is in $\mu\text{m}/\text{m}$, stress in MPa, temperature in K and time in days.

E	ν			
27610	0.32			
α	n_2	A_2	A_R	
0.29	7.59	0.128	0	
A				
0				
z	n_z	N_z	m_z	M_z
0.256	0.972	0.0012	2.378	0.334

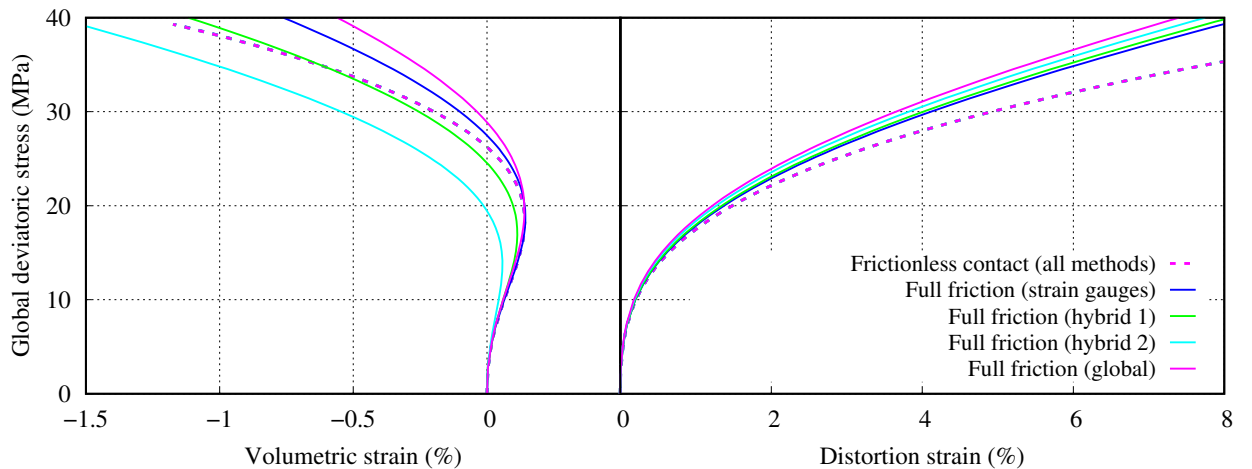


Figure 2.14. Results of numerical strain-controlled isothermal tests at $P = 10$ MPa and $\dot{\epsilon}_{ax} = 10^{-5} \text{ s}^{-1}$, using the parameters in Table 2.3. Dashed lines correspond to a frictionless contact (all curves overlap), and solid lines to a fully frictional contact. Strains are shown at local, hybrid and global scales, assuming that the radial strain is equal to the hoop strain.

Some recent experimental data are displayed in Figure 2.15 (attention is focused on the volumetric data, which are more sensitive to heterogeneity issues as discussed above). The tested

salt has average grain size of 5.5 mm (determined with the visual intercept method) and impurity content of 3.4%; both are rather low. Consistently with the numerical results displayed above, these data show significant differences among the dilatancy thresholds obtained at different spatial scales. On the other hand, while global data yield the largest dilatancy threshold (this is also observed in the numerical worst case scenario), a clear trend cannot be identified for local and hybrid measurements; this could be due to natural variability among samples, or to the difficulty to repeat a test twice (exact reproduction of the piston-sample contact, exact gauge/extensometer installation ...). Moreover, this Figure shows that, even for a relatively pure, not-too-coarse rock salt, local measurements can show significant variability among tests conducted under the same loading conditions. As expected, the more local the deformation, the higher the variability.

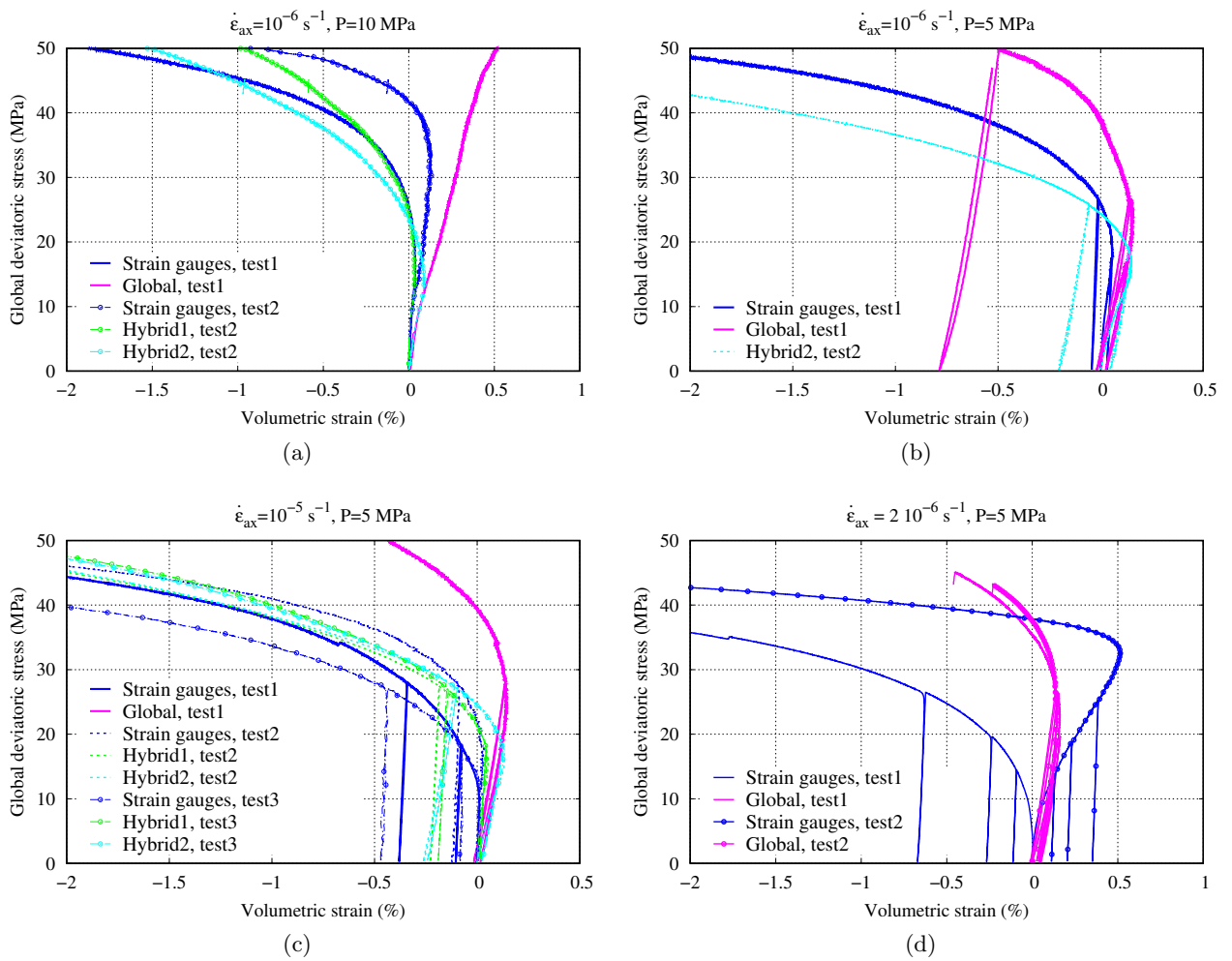


Figure 2.15. Experimental data at different scales. The trends observed in Figure 2.14 (fully frictional contact) are not systematic and reproduced qualitatively in cases (a) and (b), but not (c). In general, local data show more variability than global data (d).

When tests are performed at the laboratory scale to infer constitutive laws and parameters, heterogeneity must be considered. If sample-piston friction is present, the test results have to be analyzed numerically accounting for the contact between the sample and the cell platens (or,

in other words, accounting for the boundary conditions on the tested sample). This requires the combination of a numerical simulator with a software that provides inverse modeling capabilities. To reduce uncertainty experimentally, two solutions can be contemplated: using Teflon sheets between the sample and the platens or fixing the sample to the platens, so that the in-plane displacement on the top and bottom faces of the sample is zero. Our experience shows that the latter is easier to implement (very often, the sample and the piston have the same diameter, and therefore a perfectly smooth contact cannot be ensured after deformation starts).

If material heterogeneity is present, a methodology combining experimental and numerical work could be implemented, as described in detail in M. Azabou’s PhD work (Azabou, 2021) and in Appendix B.5: starting from tested, real non-representative samples, a virtual laboratory (or numerical twin) is used to reproduce the measured response and to determine the RVE size, on which the parameters of a constitutive law can be fitted. The consequences of using non-representative data on cavern design, as well as some more details on the proposed methodology, will be discussed in section 3.1.

2.3.2 Initial state of the samples

When rock material is removed from underground and converted into a sample some stress relaxation occurs, potentially inducing damage. Such damage should be healed before starting the intended tests at the laboratory, so that the sample is in a state close to the *in situ* conditions. In general, the preconditioning consists in a hydrostatic phase ($D \approx 0.2$ MPa, with $Q > P$) applied for several hours or a few days. When possible, the pressure and temperature applied should be close to those *in situ* at the coring depth. The analysis of this phase showed some interesting results, displayed in Figure 2.16 for a recent salt campaign in our laboratory (consistently with the previous discussions, we focus on the volumetric strains because they are much smaller than the axial strains, and important in terms of dilatancy). In this case, the isotropic phase is a few hours long, and consists in increasing the mean stress from 0 to 17 MPa at a rate of $\dot{C} = 5 \cdot 10^{-3}$ MPa/s. Then, the mean stress is reduced to 1 MPa at a rate of $-\dot{C}$, and subsequently the mean stress is increased again at \dot{C} to the target confining pressure of each test; at this point, the deviatoric phase starts (strain-controlled tests at $\dot{\epsilon}_{ax} = 2 \cdot 10^{-6}$ s $^{-1}$, ambient temperature and constant confining pressure). For each test shown, it can be seen that the volumetric strains measured during the hydrostatic phase (left plot) are not negligible compared to the values reached in the deviatoric phase (right plot, contractive part). The analysis of the unloading-reloading cycles yields similar elastic constants in both phases of each test, $E/(3(1-2\nu)) \approx 25.6$ GPa. Moreover, the plots suggest that, for each pair of repeated tests, the larger the scatter in the hydrostatic phase, the larger the differences observed in the deviatoric phase.

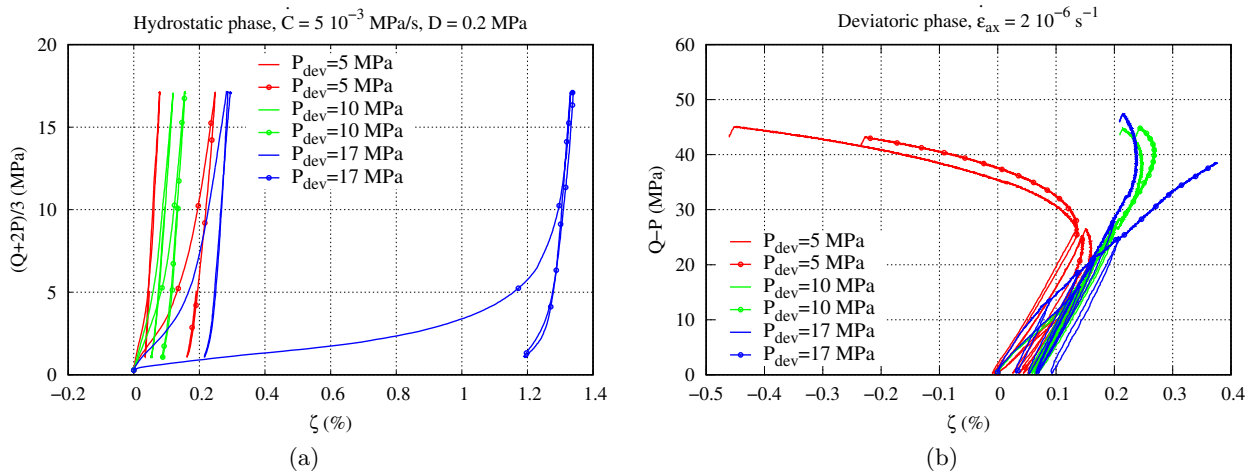


Figure 2.16. Salt 2: results of strain-controlled tests during (a) the initial isotropic phase and (b) the deviatoric phase. All tests were conducted at Mines Paris (Blanco-Martín et al., 2022a).

In terms of constitutive modeling, these results highlight the importance of the initial state of the samples and the uncertainties that may affect the strains, particularly when they are small; however, an accurate quantification is difficult. In this situation, some procedures can be defined to reduce bias. First, all tested samples within an experimental campaign should undergo the same preconditioning process regardless of the type of test to be conducted (creep, uniaxial, confined strain-controlled, constant mean pressure, tensile ...). Second, before starting the hydrostatic, preconditioning phase, a thin layer of saturated brine (prepared from the same salt material) should be applied to the outside of the samples prior to jacketing; the objective of this operation is to correct possible grain boundary drying during sample preparation, thereby favouring healing and restauration of the *in situ* state (Peach, 1991; Allemandou & Dusseault, 1993). Third, the preconditioning should be long enough to reduce the strain rate to near zero, so that the sample is brought close to the rock undisturbed state. Figure 2.17 shows results of a preconditioning phase performed recently on rock salt samples following these guidelines (3 week-long phase). The mean pressure and temperature are 12 MPa and 30 °C, respectively, corresponding to the *in situ* conditions at the coring depth. As it can be seen, the strain rate is reduced to near zero.

The samples were photographed before and after the hydrostatic phase, and some of them were also scanned in a tomograph. The analysis is ongoing within the framework of the ANR RockStorHy project (2021-2025), which involves partners from the Geosciences Department of Mines Paris, LMS (École Polytechnique), Navier laboratory (École des Ponts ParisTech), LAMPA laboratory (Angers Arts et Métiers ParisTech) and Brouard Consulting. Visually, it is clear that at least partially, some damage has been restored, see Figure 2.18. Propagation time of compressive waves consistently suggests at least partial compaction.

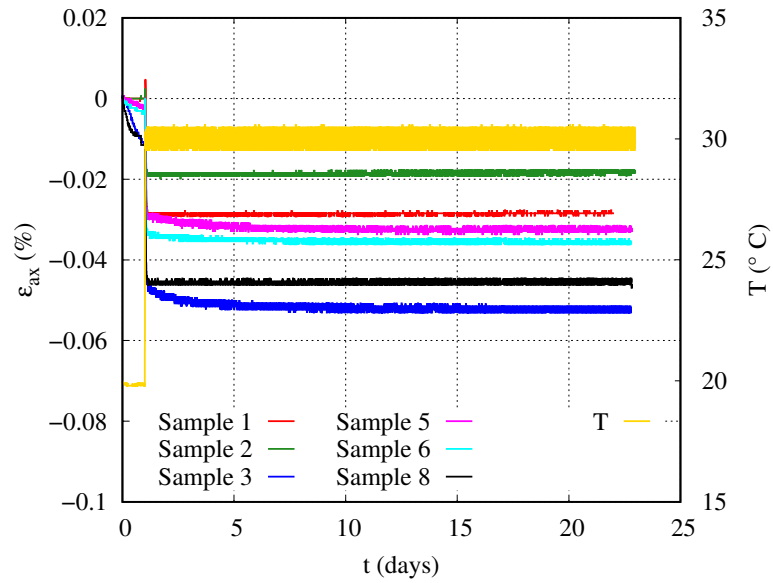


Figure 2.17. Salt 3: analysis of a recent hydrostatic phase ($C = 12$ MPa, $Q - P = 0.2$ MPa, $T = 30$ °C) of some samples. The temperature is increased from ambient ($T_{\infty} = 20$ °C) to 30 °C after one day, inducing a fast elongation of the samples (average $\bar{\alpha}_{th} = 2.65 \cdot 10^{-5}$ K $^{-1}$). All tests were conducted at Mines Paris.

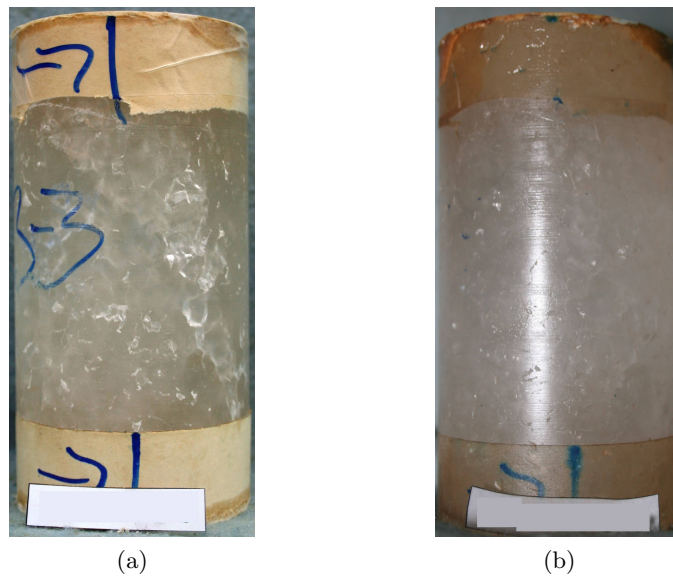


Figure 2.18. Salt 3: view of a salt sample (a) before and (b) after a three week-long hydrostatic phase at $C = 12$ MPa and $T = 30$ °C.

2.3.3 Reverse creep

Reverse creep is characterized by a transient change in the sign of the viscoplastic deviatoric strain rate. As noted above (Eq. (2.9)), from the perspective of constitutive modeling it occurs when the current transient strain is greater than the saturation transient strain, $\bar{\gamma}_R$, corresponding to the new loading conditions. In a creep test, it can be observed when, following a sudden decrease in the deviatoric stress, the height of a sample undergoing compression increases slightly for some time. However, previous work suggests that, to be observed, an important load drop must be applied: load drops (defined as $(D_1 - D_2)/D_1$, where D_1 and D_2 are the initial and final stress deviators, respectively) between 10 and 29% did not lead to observable reverse creep, either in uniaxial or confined creep tests, at 25 °C or higher temperatures (Senseny, 1981; Senseny & Fossum, 1996; Hunsche & Schulze, 1994; Hampel & Hunsche, 1999). On the other hand, load drops of 30% (Bérest et al., 2005) and 33% (Gharbi et al., 2020) did lead to measurable reverse creep (uniaxial creep tests under very small fluctuations of temperature and relative humidity). In an attempt to estimate the stress deviator D_2 below which reverse creep is observed, Hunsche (1984) performed an experimental program at elevated temperatures (100-140 °C) and estimated $D_2 \approx 0.7D_1$. The temperature did not seem to have a significant effect on D_2 ; notwithstanding, the lower the temperature, the longer the period during which the strain rate remained about zero prior to changing sign again.

We have investigated reverse creep during several recent creep tests. Figs. 2.19-2.21 show some examples for three different salts. As it can be seen, reverse creep was only clearly observed when the load drop was significant, which is consistent with the aforementioned laboratory work. Indeed, Salt 2, for which a significant number of load drops were performed, suggests that the required load drop to observe reverse creep is about 32%. Additionally, the plots show an important aspect: the amplitude of reverse creep is much smaller than the corresponding elastic drop. Table 2.4 details the characteristics of each of the load drops undertaken to investigate reverse creep.

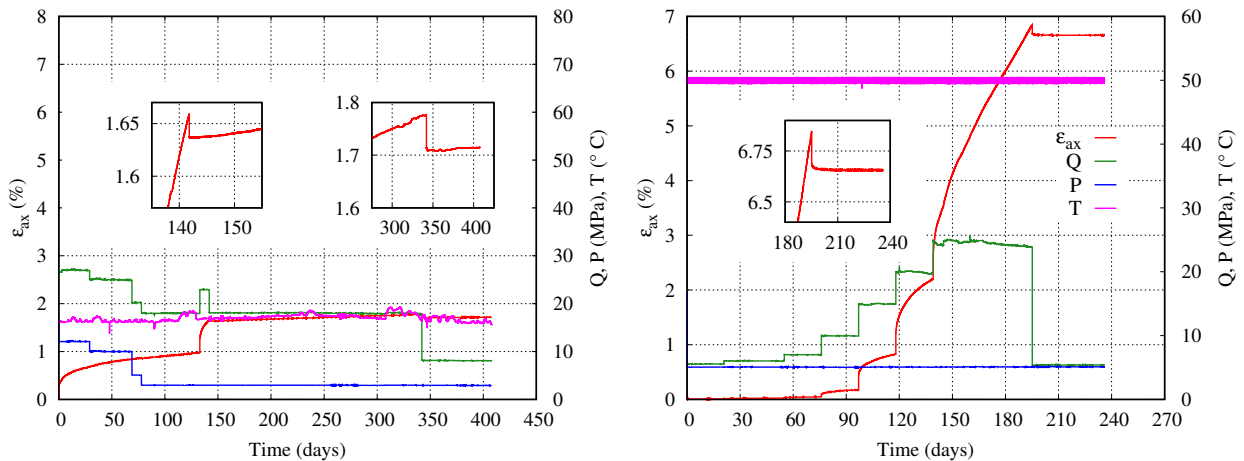


Figure 2.19. Salt 1: creep tests in which reverse creep was investigated (the enlarged views show the strain before and after the load drops). All tests were conducted at Mines Paris (Blanco-Martín et al., 2021a).

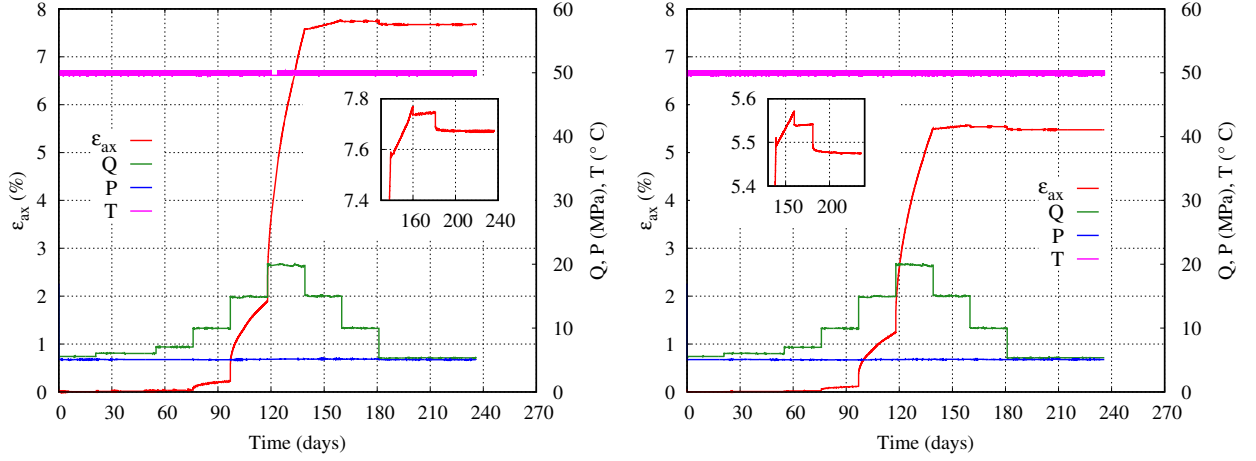


Figure 2.20. Salt 2: creep tests in which reverse creep was investigated (the enlarged views show the strain before and after the load drops). All tests were conducted at Mines Paris (Blanco-Martín et al., 2021a).

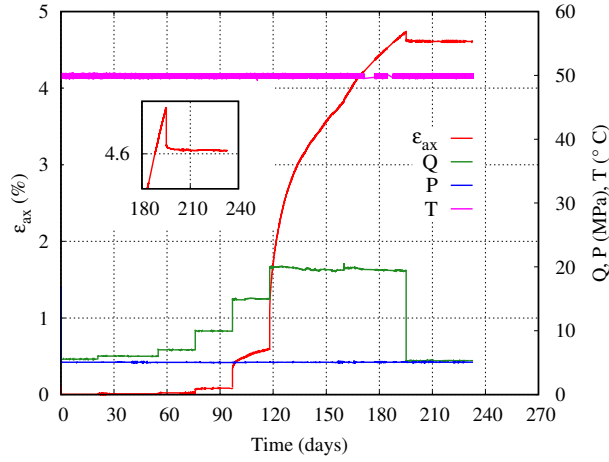


Figure 2.21. Salt 4: creep test in which reverse creep was investigated (the enlarged views show the strain before and after the load drops). All tests were conducted at Mines Paris (Blanco-Martín et al., 2021a).

Table 2.4. Load drops performed during creep tests to investigate reverse creep.

	Salt 1			Salt 2						Salt 4
	Test 1		Test 2	Test 1			Test 2			Test 1
	$t_1 = 147$ d	$t_2 = 347$ d	$t = 202$ d	$t_1 = 146$ d	$t_2 = 167$ d	$t_3 = 188$ d	$t_1 = 146$ d	$t_2 = 167$ d	$t_3 = 188$ d	$t = 202$ d
Q_1 (MPa)	23.01	17.80	23.89	19.80	15.03	9.96	19.87	15.07	9.95	19.40
Q_2 (MPa)	18	8.08	5.34	15.1	10	5.27	15.16	10	5.29	5.26
P (MPa)	2.98	2.98	5.12	5.13	5.13	5.13	5.11	5.11	5.11	5.07
$\frac{(D_1 - D_2)}{D_1}$ (%)	25	65.6	98.8	32	50.8	95.2	31.9	50.9	96.3	98.7
T (°C)	16.9	16.4	50	50	50	50	50	50	50	50
ε_{el}^{exp} ($\mu\text{m}/\text{m}$) ^a	223.3	569.9	1311.7	167.7	257.9	361.6	169	238.4	392.64	810.9
Observed?	Not clear ^b	Not clear ^b	Yes	Yes	Yes	Yes	No	Yes	Yes	Yes
Time to $\dot{\varepsilon} \approx 0$	-	-	31 d	2 h	2 d	28 d	-	2.5 d	28 d	21 d

^a: maximum instantaneous drop (upper bound for elastic drop); ^b: important T oscillations

Unloading-reloading cycles performed during the deviatoric phase of strain-controlled short-term tests (for the calculation of elastic constants) are characterized by a decrease-increase of the stress deviator. The analysis of these cycles shows that the path is not the same during unloading and reloading (slightly open hysteresis loops), something that can be captured with, for instance, Eq. (2.9). Figure 2.22 shows one example for Salt 1. Note that the hysteresis in the unloading-reloading cycles performed during the isotropic phase is much smaller (see, for instance, the left plot in Figure 2.16). Furthermore, as compared to the sudden load drops applied during creep tests, in this case the load drop is progressive, and thus more representative of field applications (disregarding failure). The analysis of unloading-reloading cycles with the RTL2020 model is shown in the Figure with $B = 0$ and $B = 0.5$ (the other parameters are listed in Table 2.2). As it can be seen, when $B = 0.5$ the prediction of the test is quite satisfactory.

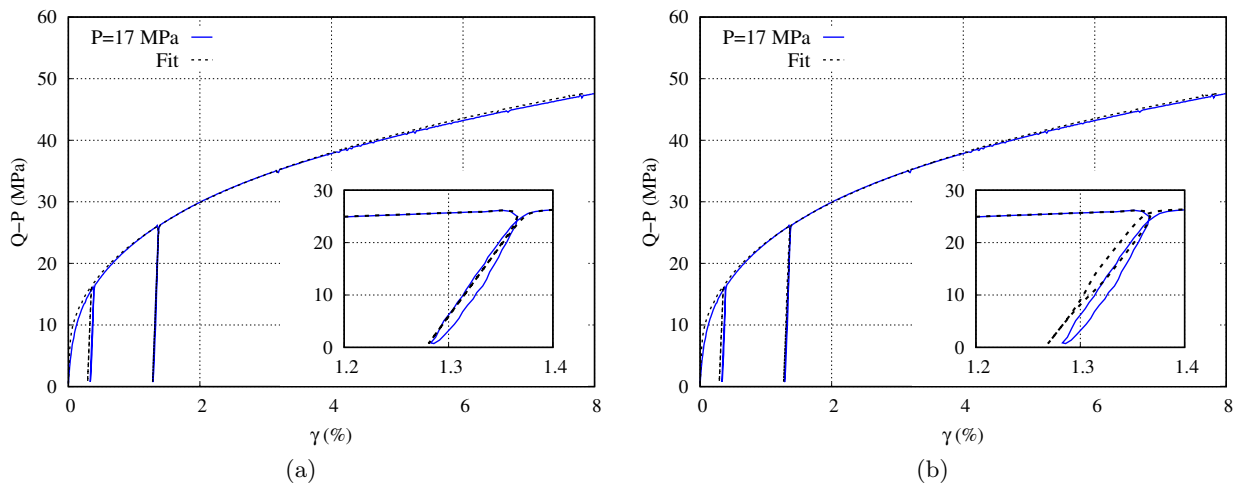


Figure 2.22. Salt 1: reverse creep in unloading-reloading cycles of a strain-controlled test at $\dot{\epsilon}_{ax} = 10^{-6} \text{ s}^{-1}$, $P = 17 \text{ MPa}$ and ambient temperature: experimental data and analysis with RTL2020 for (a) $B = 0$ (reverse creep inactive) and (b) $B = 0.5$ (reverse creep active). The other parameters are listed in Table 2.2. All tests were conducted at Mines Paris (Blanco-Martín et al., 2021a).

At the field scale, reverse creep could be active when the stress deviator decreases (for instance, during the injection phase in a salt cavern). However, an accurate quantification is difficult because the closure rate is affected by several other phenomena, such as temperature changes, stress redistributions around the openings or additional dissolution in a brine-filled cavern (Bérest & Brouard, 2015; Bérest et al., 2017). Nevertheless, as suggested by previous work and the experiments shown above, the impact of reverse creep is expected to be small (smaller than the elastic strain corresponding to the load drop).

2.3.4 Tensile response

Rocks exhibit lower strength under tensile than under compressive states of stress. Rock salt is no exception, with typical apparent strength values obtained during indirect Brazilian tests in the range 1-4 MPa. Similarly to the compressive behaviour, tensile behaviour of rock salt is time-dependent. In the recent years, two scenarios where tensile stresses may be active have been investigated by

the salt mechanics community: that of a rapid depressurization in a salt cavern (Bérest et al., 2012, 2014; Zapf et al., 2012; Hévin et al., 2017), and that of intergranular (pore) pressure increase above the least compressive principal stress, also called fluid infiltration (Fokker, 1995; Popp & Minkley, 2010; Wolters et al., 2012). Apart from these scenarios, which are explained in more detail in sections 3.2 and 3.3 respectively, there might be other cases in which tensile stresses could develop (*e.g.*, stress redistribution around an opening), and it is important to be able to understand and to model the behavior of rock salt under such conditions.

Over the last years, we have attempted to better characterize the time-dependent tensile response of rock salt. For such purpose, we have conducted Brazilian tests on instrumented salt samples, and we have analyzed the experimental data through numerical modeling (the analysis of tensile tests, whether direct or indirect, is not straightforward due to the heterogeneity of the stress and the strain fields and the influence of the boundary conditions, and therefore numerical simulations are required). We have selected Brazilian tests because as compared to direct tensile tests, they are easier to perform, less time-consuming, less prone to invalidity (in direct tests, failure often occurs at the bonded or clamped ends) and they reduce the likelihood of alignment problems, which could trigger bending and torsion of the samples. Nevertheless, for the results to be valid, failure should initiate in the region of tensile stresses, rather than at the platen-sample contacts (Hudson et al., 1972; Liu et al., 2022). As the literature review shows, it is still a challenging task to characterize the tensile behaviour of rock samples.

The initial set-up developed consisted of the combination of strain gauges and LVDT sensors, see Figure 2.23. One horizontal and one vertical 1 cm-long gauges were placed at the center of the sample, and two additional horizontal gauges were placed along the horizontal and vertical diameters, at $r = R/2$ (R is the sample radius, here 65 or 100 mm). Both faces of the sample were instrumented. Two LVDTs were placed at the limits of the horizontal diameter of the sample to measure horizontal expansion. A third LVDT, mounted on the loading frame, measured the vertical compression of the sample. The tests were strain-controlled, some of them at $\dot{\epsilon}_{ax} = 5 \mu\text{m}/\text{m}/\text{min}$ and others at $\dot{\epsilon}_{ax} = 50 \mu\text{m}/\text{m}/\text{min}$. It was expected that the combination of the LVDTs and the strain gauges could be used to characterize the strain development within the sample. Nevertheless, experiments performed on different rock salt samples, of different size and under different axial strain rates, proved that there was always a discontinuity in the data: the strain gauges failed at an early stage, before any significant horizontal displacement would be captured by the LVDT sensors, see right plot in Figure 2.23.

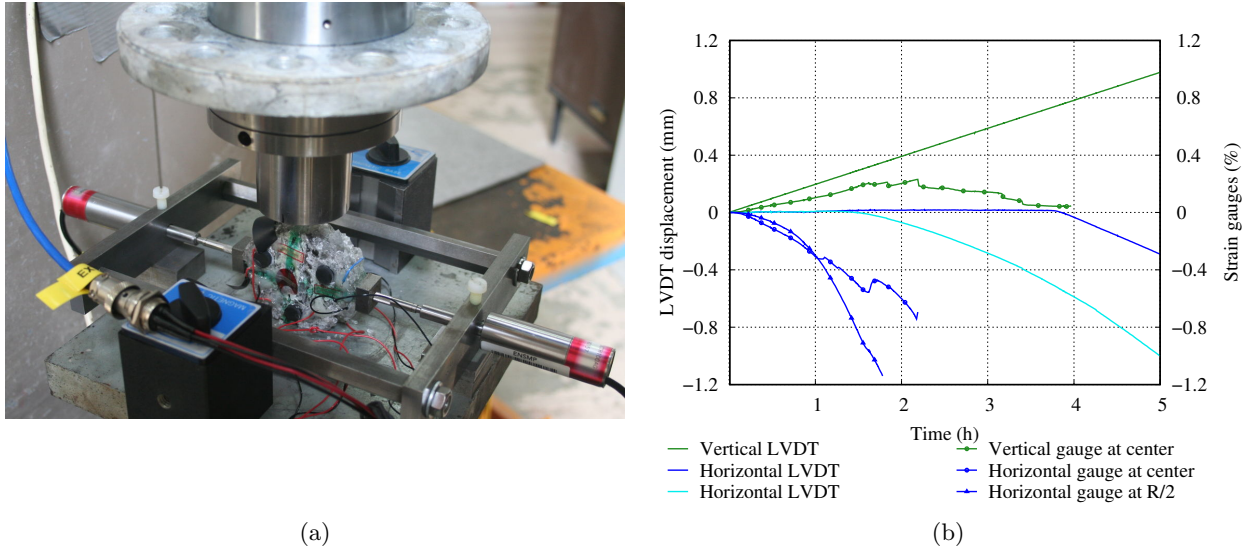


Figure 2.23. Experimental investigation on the tensile response of rock salt at Mines Paris: (a) initial experimental set-up with strain gauges and LVDT sensors (in the case shown, the sample diameter is 65 mm); (b) unsatisfactory results (note that one of the horizontal strain gauges breaks short after 1 h, while the LVDT response is beyond noise only after 1.5 h [the third horizontal gauge did not work properly]).

Recently, we have improved the data acquisition system using digital image correlation (DIC) (Pan et al., 2009; Sutton et al., 2016; Aliabadian et al., 2019a,b). This technique has several advantages, such as the determination of the strain field all over the sample rather than at discrete locations, the possibility to identify crack initiation location and failure patterns, its easy implementation, its reduced cost, its non-destructive nature and its flexibility (frequency of image acquisition, ease of configuration changes . . .). In the new experimental set-up, DIC is used on one face of the sample, and on the other face, several strain gauges are placed, see Figure 2.24. We have first calibrated the DIC technique (points to track, size of the grid and of the correlation window, algorithm for flow calculation, termination criteria, method [if any] to interpolate the displacement field), and we have compared strain gauges and DIC data before failure of the gauges. As the Figure shows, the comparison is quite satisfactory and provides confidence to use DIC-derived data after failure of the strain gauges (note that some differences between DIC and strain gauges measurements are expected, as they are taken on two different faces of the sample). Although DIC proves to be reliable, it is recommended to use strain gauges on one face of the sample whenever possible, in order to be able to compare both techniques and to calibrate the DIC parameters. The Brazilian test shown was performed on a sample having a diameter of 100 mm (thickness of 50 mm) at an axial strain rate of $\dot{\epsilon}_{ax} = 60 \mu\text{m}/\text{m}/\text{min}$. A picture was taken every 2 min, and it was verified that failure initiated in the central region, where maximum tensile stresses occur. Moreover, as recommended by previous investigations in the literature, a pair of cushions was used to increase the contact area between the platens and the sample.

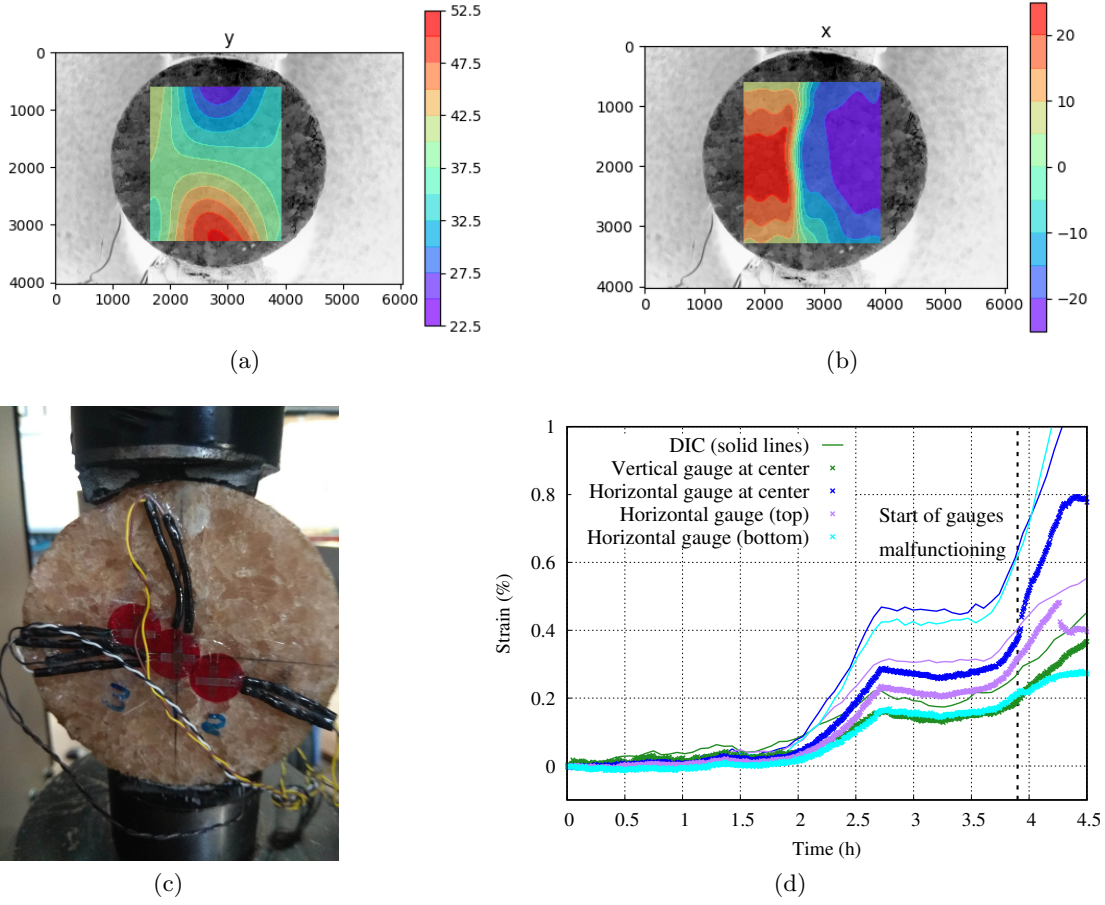


Figure 2.24. Experimental investigation on the tensile response of rock salt at Mines Paris, combining DIC and strain gauges: (a) vertical [y] and (b) horizontal [x] displacements (in px) provided by DIC on one face of the sample, at the moment when the first fracture appeared, after about 6 h; (c) view of the face where strain gauges are used (note that out of the three vertical gauges, only the central one is working); (d) comparison between strain gauges and DIC before suspected start of gauges malfunctioning, short before 4 h (note that some differences are expected, as the two techniques are used on different faces of the sample).

Following the multi-potential approach on which RTL2020 is based, [Labaune \(2018\)](#) presented a viscoplastic tensile component for this law, which reads⁶

$$\underline{\dot{\underline{\epsilon}}}_{vp}^t = \dot{\lambda}_t \partial_{\underline{\underline{\sigma}}} G \quad (2.10)$$

where $G(\underline{\underline{\sigma}}) = \left(\sum_{i=1}^3 \langle \sigma_i \rangle^d \right)^{1/d}$ (G is the d -norm of $\underline{\underline{\sigma}}$, and parameter $d \geq 1$ controls the shape of the potential $G(\underline{\underline{\sigma}})$). Note that $\underline{\dot{\underline{\epsilon}}}_{vp}^t$ has a deviatoric component and a volumetric component (details are given in [Labaune \(2018\)](#) and [Azabou et al. \(2021a\)](#)). The positive multiplier $\dot{\lambda}$ is

⁶Note that for the compressive part, $\underline{\dot{\underline{\epsilon}}}_{vp}^c = \dot{\lambda}_\gamma \partial_{\underline{\underline{\sigma}}} P_\gamma + \dot{\lambda}_{\zeta_c} \partial_{\underline{\underline{\sigma}}} P_{\zeta_c} + \dot{\lambda}_{\zeta_d} \partial_{\underline{\underline{\sigma}}} P_{\zeta_d}$, where γ stands for distortion, ζ_c for contractancy and ζ_d for dilatancy. The multipliers are respectively $\dot{\lambda}_{vp}^c$, $\langle \dot{\lambda}_{vp}^c \rangle$ and $\langle -\dot{\lambda}_{vp}^c \rangle$. The potentials are respectively q , p and $-p$.

defined by

$$\dot{\lambda}_t = \Lambda \left(\left\langle \frac{G(\underline{\underline{\sigma}}) - R_t}{S} \right\rangle \exp(\omega \lambda_t) \right)^s \quad (2.11)$$

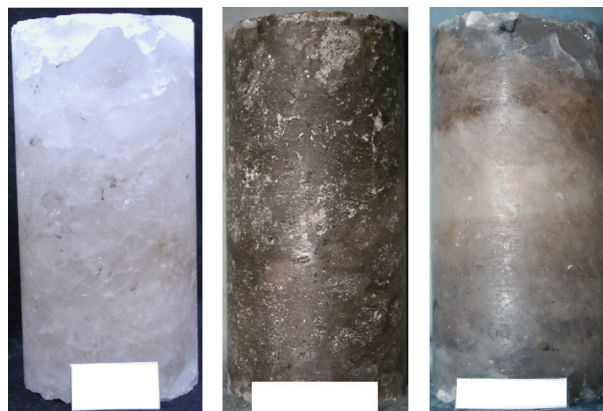
where Λ , R_t , S , s and ω are positive material parameters (R_t is the tensile strength, taken to be zero for consistency with the compressive component of RTL, in which rock salt is assumed to have zero cohesion and hence creep for $q > 0$). We are currently conducting FEM simulations of the tests performed combining DIC and strain gauges to estimate a parameter set for the tensile component of RTL2020. The results are encouraging, but we need to analyze further the non-homogeneous response of the samples and the applied boundary conditions (this is a perspective for the next years as mentioned in chapter 4).

Chapter 3

Engineering applications

3.1 Laboratory characterization and design of underground structures

It has been explained in the previous chapters that material heterogeneity leads to a wide range of RVEs among different rock origins. Ideally, laboratory work should be performed on samples that meet the RVE size; however, this is impractical as the drilling equipment in the field and the experimental devices in the laboratory cannot be adapted easily to different sample sizes. In order to illustrate the effects of specimen representativity and material heterogeneity on the characterization of the behavior of rock salt at the laboratory scale, I show results of an experimental campaign conducted at the Centre for Geosciences and Geoengineering of Mines Paris. The tested samples have a diameter of 65 mm and a height of 130 mm. They contain impurities visible to the naked eye, up to cm size. The top image in Figure 3.1 shows three of the tested samples, cored within 7.5 m from each other. Differences could be attributed to the presence of different facies; however, in the bottom image, three samples cored within 1 m from each other are shown, proving that material heterogeneity is important. X-ray diffraction of the insoluble part revealed 12% anhydrite, 2.3% calcite, 0.5% illite, 0.3% quartz and 0.3% dolomite (% of total mass).



(a)

Figure 3.1. Samples prepared for laboratory testing at Mines Paris showing important material heterogeneity: (a) cored within 7.5 m from each other.



(b)

Figure 3.1. Samples prepared for laboratory testing at Mines Paris showing important material heterogeneity: (b) cored within 1 m from each other.

Sixteen strain-controlled compression tests and twelve creep tests were conducted on samples cored at depths between 1224 and 1472 m. The short-term tests were performed at ambient temperature and under constant axial strain rate ($\dot{\epsilon}_{ax} = 2 \cdot 10^{-6} \text{ s}^{-1}$). The confining pressure was kept constant during each test; four values were applied to different samples: $P = \{5, 10, 17, 20\}$ MPa. When possible, the same loading conditions were applied to samples from the same and different facies to evaluate repeatability and material heterogeneity. Creep tests were performed at temperatures between 50 and 70 °C, with stress deviators up to 15 MPa. Several loading stages were applied to each sample, at increasing and decreasing values of stress deviator. While during strain-controlled tests the sample response was measured at local and global scales (see section 2.3.1), only global axial displacements are available for creep tests. Some typical results are shown in Figures 3.2-3.3. As it can be seen, there is significant scattering among tests that were conducted under equivalent conditions but using different samples.

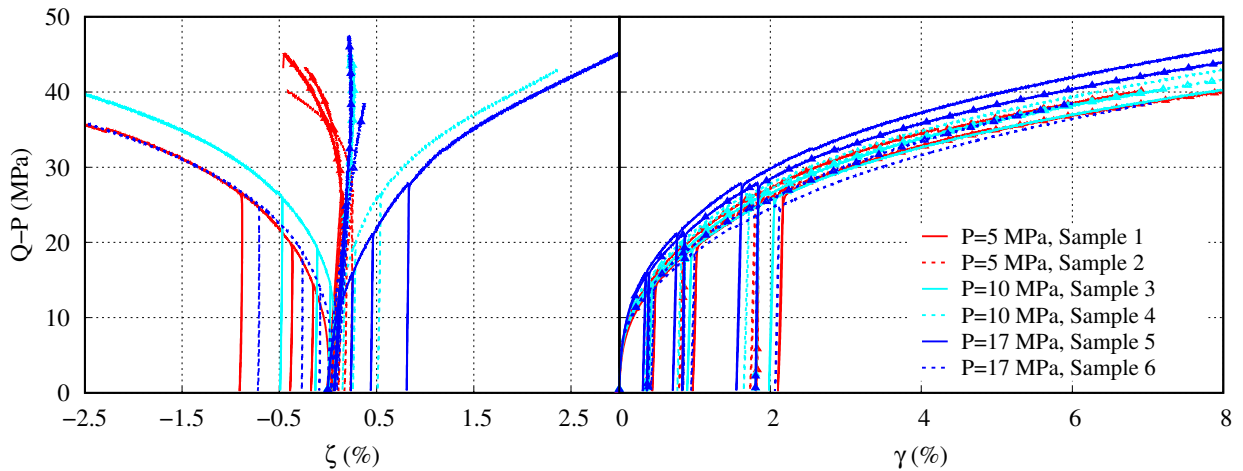


Figure 3.2. Results of constant strain rate tests at $\dot{\epsilon}_{ax} = 2 \cdot 10^{-6} \text{ s}^{-1}$, ambient temperature and different confining pressures. The samples were cored within 1 m of each other. For each test, lines with symbols correspond to global measurements and lines without symbols correspond to local measurements. All tests were conducted at Mines Paris.

The analysis of Figure 3.2 reveals that, for a given sample, the volumetric response measured using local and global techniques can be very different (for instance, in one of the tests performed at $P = 10$ MPa [sample 4, dashed lines], the local measurements suggest that the sample remained within the contracting domain throughout the test, whereas the global measurements indicate a switch to the dilation domain at a stress deviator of about 40 MPa). Disregarding malfunctions of the measuring devices, these differences exceed the limits of natural variability and are related to some kind of heterogeneity. The differences in the measurements are particularly important for the volumetric strains, given their small values as compared to the distortion strains (note that differences between global and local deviatoric data are within natural variability and/or experimental error limits); yet, the volumetric strains are particularly important because the dilatancy threshold is used as a criterion for the design of underground facilities, such as salt caverns (Labaune et al., 2018).

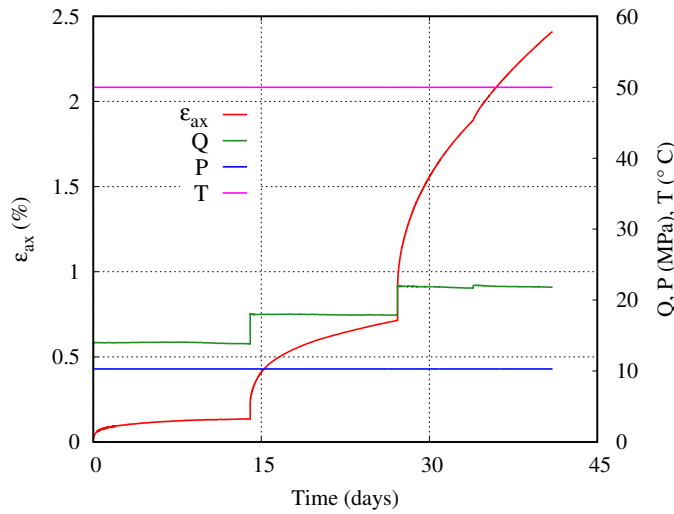


Figure 3.3. Results of a multi-stage creep test at $P = 10$ MPa and $T = 50$ °C. The test started with a one week-long isotropic phase at $C = 10$ MPa and $Q - P = 0.2$ MPa during which temperature was increased to 50 °C (not shown in the plot). The test was conducted at Mines Paris.

There could be several explanations to the observed anomalies. The first one is related to heterogeneity induced by the end restraints on the sample. However, as investigated in Rouabhi et al. (2019), this explanation alone is not sufficient to explain the observed results. Another possible explanation is material heterogeneity: depending on the placement of the strain gauges with respect to the heterogeneities, their response could be very different from the global measurements (Azabou et al., 2021a). This suggests that the samples may not be representative of the salt rock mass under investigation, as their size seems to be smaller than the RVE.

In the following, we will disregard the anomalies discussed above and we will apply the classic design methodology, which, as explained in the first chapter (section 1.2), combines laboratory work, constitutive modeling and design criteria. This situation could correspond to a case where only one measurement technique is available (*i.e.*, global or local), or to a case where several measurement techniques are available, but the observed anomalies are disregarded for lack of an available methodology to tackle material heterogeneity. This work was presented in the last Saltmech conference (Blanco-Martín et al., 2022b).

Analysis of the experimental results is performed with a phenomenological creep law, here taken to be RTL2020, which includes dilatancy at the rheological level (details can be found in Appendix B.4). For the illustrative purposes sought here, we focus on the volumetric part given that remarkable differences were found experimentally between local and global measurements (Figure 3.2). We perform two separate calibrations for the volumetric strains: one is based on local data (disregarding anomalous trends [samples 4 and 5], which one could be tempted to attribute to malfunctions of the measuring devices), and the other one is based on global data. For the deviatoric part, as well as for creep tests, we only consider global measurements. A single parameter set is determined simultaneously for short- and long-term tests, listed in Table 3.1. Figures 3.4-3.6 compare experimental and fitted results for the tests displayed in Figures 3.2-3.3. The use of a single set for all tests explains the misfit observed individually for some cases; however, overall the fitting is deemed satisfactory. In particular, it is possible to find two parameter sets for the volumetric part, one for the local measurements and one for the global measurements.

Table 3.1. RTL2020 parameter set determined from laboratory tests (best fit for short- and long-term tests simultaneously). The unit system is such that strain is in $\mu\text{m}/\text{m}$, stress in MPa, temperature in K and time in days.

E	ν	α_{th}			
31200	0.30	29.1			
α	A_2	n_2	A_R	T_r	
0.46	0.63	5.88	4809.54	289.55	
A	B	n	m	A_1	n_1
146.41	$2.13 \cdot 10^{-9}$	2.99	3.48	0.29	2.11
z_{glo}	$n_{z,glo}$	$N_{z,glo}$	$m_{z,glo}$	$M_{z,glo}$	
0.11	2.34	0.24	4.99	2.80	
z_{loc}	$n_{z,loc}$	$N_{z,loc}$	$m_{z,loc}$	$M_{z,loc}$	
0.50	2.48	2.23	1.23	0.05	

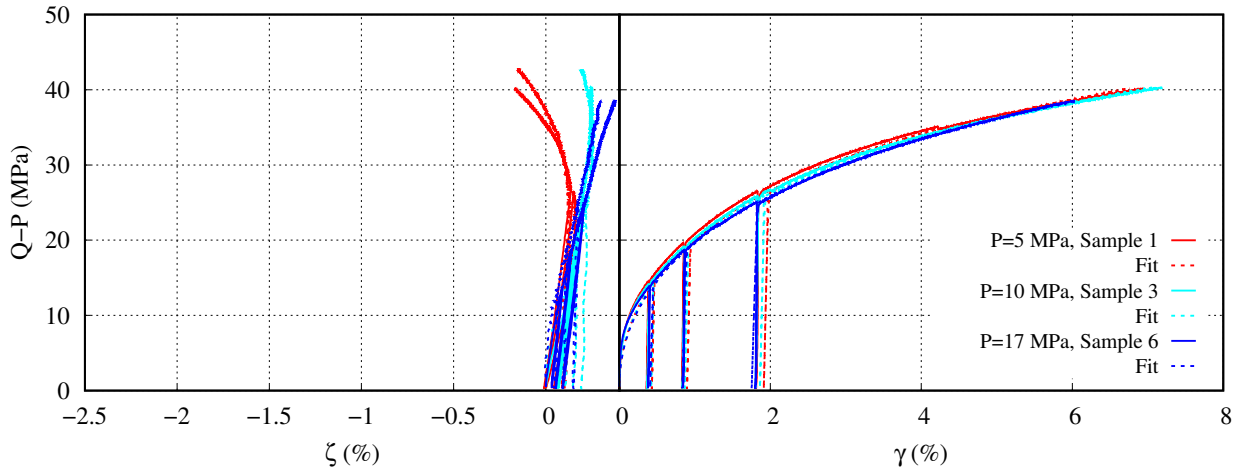


Figure 3.4. Fitting of the constant strain rate tests shown in Figure 3.2 with RTL2020. Global volumetric strains are considered.

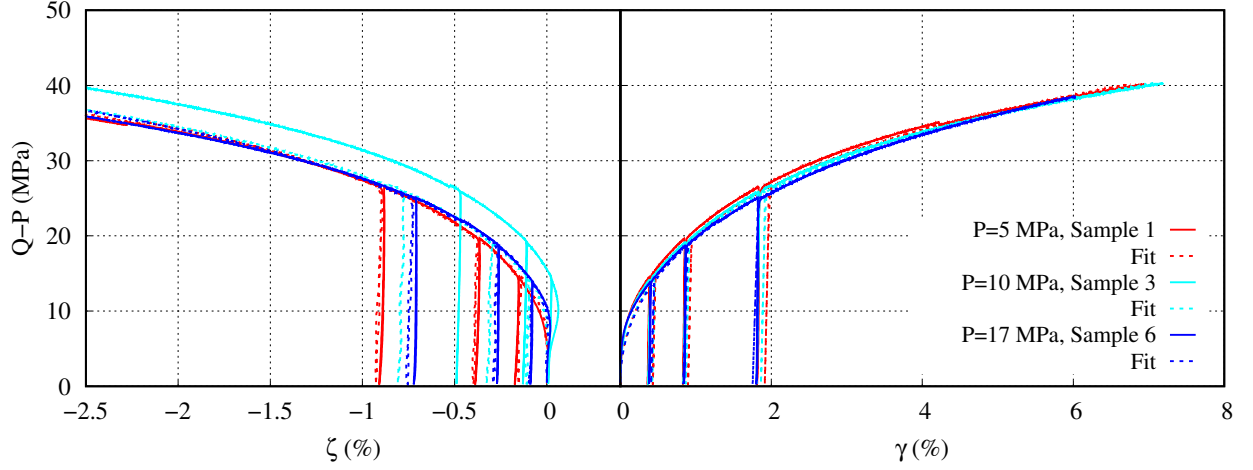


Figure 3.5. Fitting of the constant strain rate tests shown in Figure 3.2 with RTL2020. Local volumetric strains are considered.

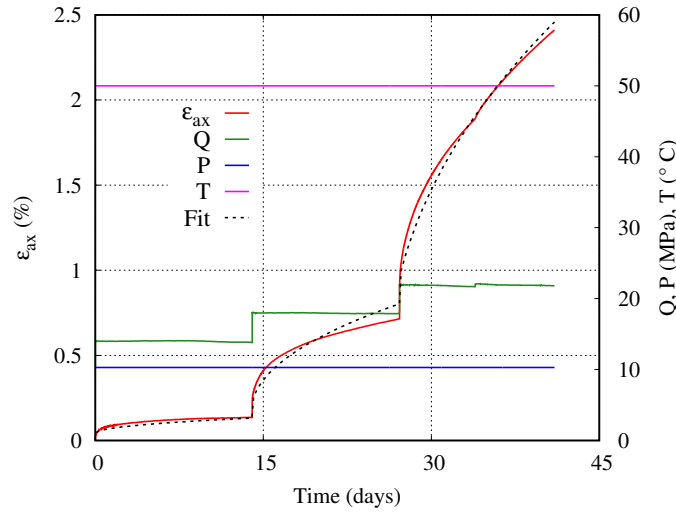


Figure 3.6. Fitting of the multi-stage creep test shown in Figure 3.3 with RTL2020.

As the next step, we perform numerical simulations for seasonal storage of CH_4 in an isolated salt cavern. The behaviour of the rock mass is modeled with RTL2020 and the parameters listed above. The initial cavern volume is 191000 m^3 . The sump, filled with brine, represents about 43000 m^3 . The cavern is 145 m high, and its top is at a depth of 1430 m (its profile can be seen in Figure 3.7). Two FEM axisymmetric simulations are performed including the leaching (3 years) and debrining (3 months) phases, followed by 40 years of cycling. During these stages, the boundary condition at the cavern wall changes from geostatic to halmostatic (leaching), then to the debrining pressure (20 MPa), and during the cycles, it oscillates between $P_{max} = 24 \text{ MPa}$ and $P_{min} = 12 \text{ MPa}$. The simulations differ in the parameter set used for the volumetric part: one simulation uses the local set, and the other uses the global set (both sets are listed in Table 3.1). For the purposes sought here, an isothermal calculation is sufficient. Figure 3.7 shows the isovalues of $\dot{\zeta}_{vp} = 0$ (dilatancy threshold) at different times obtained in the two simulations. As it can be seen, the global parameter set predicts a smaller extent of the dilatancy zone than the local set:

while the maximum width of such zone is 25 m in the former case, it is 150 m in the latter. In both cases, during the cycling phase the extent of the dilatancy zone around the cavern increases rapidly initially and then tends to stabilize over time, which is beneficial from a design perspective. However, the local parameter set predicts an important extent of the dilatancy zone during the leaching phase. The differences obtained in these simulations are important for cavern design (*e.g.*, feasibility of storage, spacing between caverns), and show the importance of accurate laboratory measurements and rock characterization to avoid both conservative and optimistic designs.

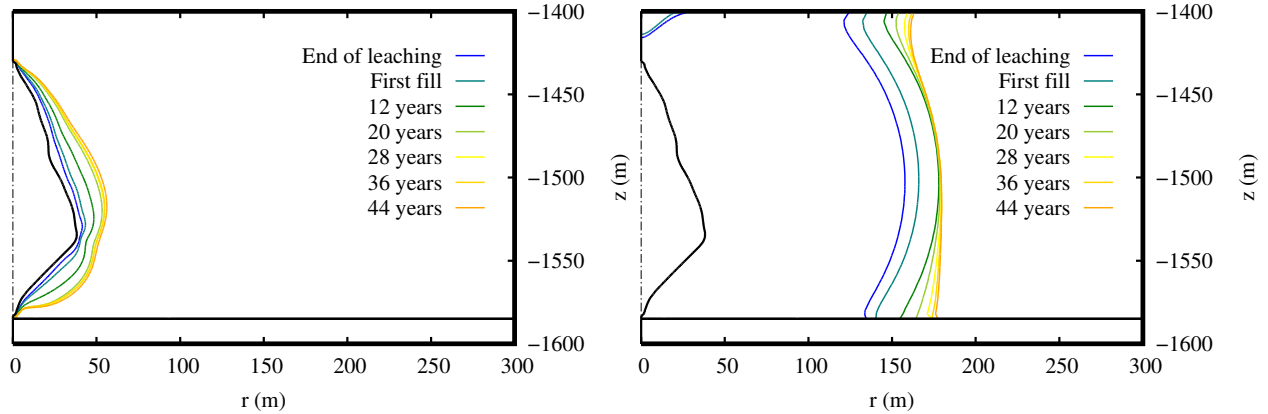


Figure 3.7. Isovalues of $\dot{\zeta}_{vp} = 0$ at different times, obtained using the global parameter set (left plot) and the local parameter set (right plot) for the volumetric part, listed in Table 3.1.

In order to overcome representativity issues if the RVE cannot be tested in the laboratory, [Azabou \(2021\)](#) proposed a methodology that combines experimental and numerical work. The main steps of such methodology are as follows:

1. Perform laboratory tests on non-representative specimens, such as those shown in Figure 3.1;
2. Numerically model the structure (size and insolubles distribution) of a non representative specimen as a two-phase material (pure halite and insolubles);
3. Fit the parameters for each phase on the experimental results. For this step, it is necessary to use a constitutive law in which dilatancy results from the activation of a tensile mechanism (due to the presence of heterogeneities, which have different properties than the halite phase), such as RTL2020 (see Appendix B.5);
4. Increase sample size in a virtual laboratory (or numerical twin) until the RVE is found. Two alternatives exist, discussed in [Azabou et al. \(2021a\)](#) and [Azabou et al. \(2021b\)](#): either the insolubles are accounted for explicitly or implicitly, using leveled Gaussian random fields. Both approaches are equivalent, and the latter is less computational intensive;
5. Once the RVE is found, fit a phenomenological law (such as RTL2020) on the numerical results obtained, assuming that the sample response is homogeneous; therefore, the tensile mechanism of the law should not be active, as dilatancy should be accounted for at the constitutive level, resulting from non-elastic volume increase under uniform, compressive stresses;

6. Use this law and fitted parameters in the previous step to investigate structures of size \gg RVE.

Further details about this methodology can be found in Appendix B.5, together with one illustrative, academic example (particularly, Figures 13 and 14). We hope to have some funding and access to field data in the next years to test and verify the approach. M. Azabou presented this work in the SMRI 2022 Fall Technical Meeting (Azabou et al., 2022), and some preliminary results using the explicit method in the ARMA 2020 symposium (Azabou et al., 2020).

3.2 Salt cavern storage and energy transition

Leached salt caverns have been used since the 1940s to store (or dispose of) fluids underground (Bays, 1962; Hoather & Challinor, 1994; Thoms & Gehle, 2000; Gillhaus, 2007). Among the stored fluids, hydrocarbons (oil, natural gas) have dominated in the storage facilities worldwide. Apart from strategic storage, these fluids are typically injected when the demand is low (summer) and withdrawn when the demand is high (winter); in such scenario, caverns undergo yearly cycles during which the stress state and the temperature change at the cavern wall and the surrounding rock. The mechanical stability and hydraulic tightness of salt caverns for hydrocarbon storage have been widely investigated, *e.g.*, Staudtmeister & Rokahr (1997); Staudtmesiter & Schmidt (2000); Sobolik & Ehgartner (2007); Wolters et al. (2012); Costa et al. (2015); Minkley et al. (2015); Serbin et al. (2015). Since temperature changes are small for low injection/withdrawal rates, thermal effects do not propagate far from the cavern wall and are often neglected (Heusermann et al., 2003).

In the recent years, the liberalization of energy markets and the use of the underground to foster renewable energy penetration in the energy matrix have brought about new scenarios in which new fluids and operating conditions are encountered (Khaledi et al., 2016)¹. A move towards high-frequency cycles (*i.e.*, weeks, days or even less) has been observed for natural gas and hydrogen (Brouard et al., 2012; Ozarslan, 2012). These operating conditions need to be thoroughly investigated because in the case of a rapid depressurization, the gas cools down quickly and heat transfer with the surrounding host rock is limited. Thermal contraction of the rock occurs, which can lead to the onset of tensile stresses. Since the apparent tensile strength of rock salt is quite small (see section 2.3.4), tensile stresses must be managed (better avoided) to preserve the barrier integrity of the salt rock mass. Some numerical studies suggest that tensile stresses induced by rapid cooling are transient by nature, and also that the depth of penetration of possible thermally-induced fractures is small; consequently, cavern integrity is unlikely to be threatened (Karimi-Jafari et al., 2011; Brouard et al., 2012; Djizanne et al., 2012; Pellizzaro et al., 2012; Bérest et al., 2014; Sicsic & Bérest, 2014). Since salt caverns are not accessible, experimental evidence that could support or contradict the numerical predictions is limited (Bérest et al., 2012; Zapf et al., 2012), and as a result a sound conclusion has not yet been reached. In order to gain more insight, the Solution Mining Research Institute (SMRI) launched a research program to further investigate the effects of high frequency cycling on the integrity of rock salt.

¹Although not discussed in this manuscript, in the context of the transition to low-carbon energy I investigated storage of O₂ and CO₂ in salt caverns (Blanco-Martín et al., 2021b). Such storage would be needed in processes such as electrolysis-methanation-oxyfuel (EMO, or Power-to-Gas-Oxyfuel), which could work in a closed loop for the fluids supply. Storage of O₂ and CO₂ in salt caverns has not been implemented to date, and it was necessary to perform a preliminary assessment of cavern stability accounting for the thermodynamics of the fluids involved, and to investigate different storage configurations (in particular, independent *vs.* combined storage of O₂ and CO₂).

In the context of the SMRI research program, a thermo-mechanical test was performed in the *Varangéville* salt mine in North-Eastern France. This unique test consisted of three cooling-warming cycles followed by two cooling stages applied to a salt surface of 10 m^2 . The cooling was applied rapidly ($\Delta T = -20 \text{ }^\circ\text{C}$ in about 8 h), and monitoring of the test was extensive to allow investigating the thermo-mechanical response of the rock, including possible fracture creation and propagation. An international team was reunited to conduct the test: researchers from Armines/Mines Paris, IUB-Leibniz Universität Hanover, Ineris, Storengy and *Compagnie des Salins du Midi et des Salines de l'Est* took part in the effort. A complete description of the experiment can be found in Hévin et al. (2016). Here, I will present my contribution, which consisted in thermo-mechanical modeling of the experiment performed after the test to help interpret the experimental data and to evaluate the capabilities of the numerical tools commonly used in cavern design to reproduce the test results, and in particular, the location, orientation and timing of the first fracture. Full details can be found in Blanco-Martín et al. (2018a).

At *Varangéville*, the salt layer sits above a marl layer and underneath a sandstone-marl layer. For the purposes of the experiment, a dead-end gallery (niche) was excavated at a depth of about 120 m, with dimensions $17.5 \times 12 \times 4.5 \text{ m}^3$ (length, width, height). To perform the test, a $13 \times 12 \times 1.3 \text{ m}^3$ salt slab was left unexcavated at the floor of the niche. The distance from the top surface of the salt block to the salt-marl contact is about 1.5 m.

In order to isolate the effects of rapid cooling on the stress state, the influence of the *in situ* stress field was minimized. For this purpose, two vertical slots were cut parallel to the niche axis, at a distance of 1.1 m and 0.7 m from the West and East walls, respectively. The slots were 0.1 m wide and 1.5 m high, and were backfilled prior to the test to prevent heat convection. Thanks to the slots, the salt block is free at four surfaces: top, front and two sides. Figure 3.8a shows a plan view of the experimental niche.

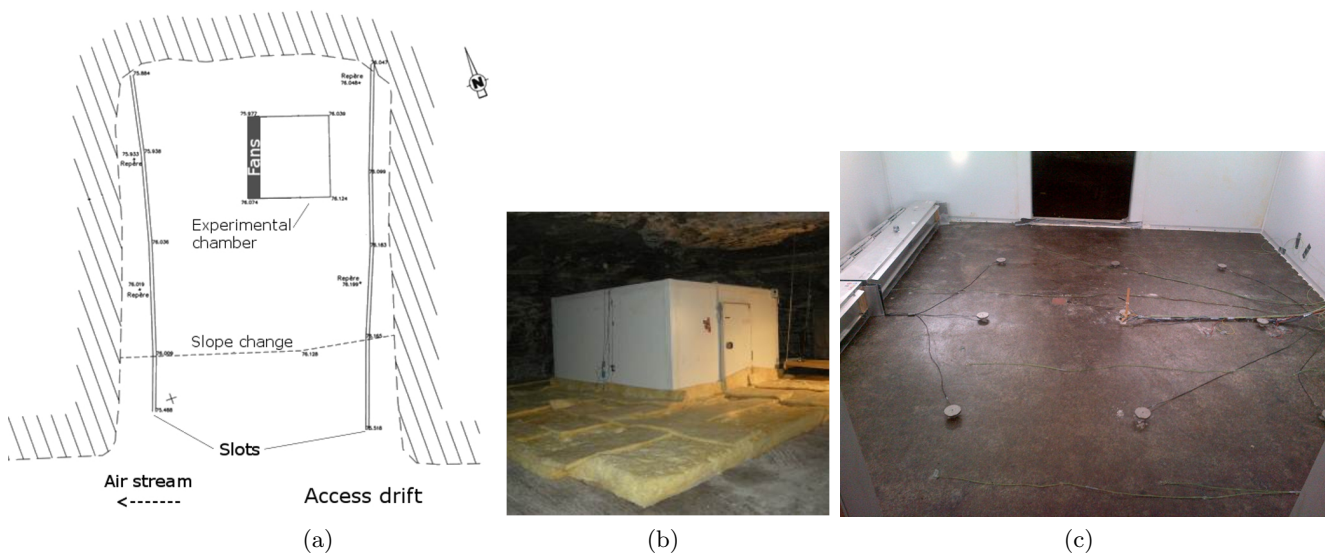


Figure 3.8. Test at *Varangéville*: (a) plan view of the experimental niche, including location of the experimental chamber and the two slots; (b) view of the experimental chamber surrounded by the insulation cover (the height of the chamber is 2.23 m and the width of the walls [HD polyurethane] is 10 cm); (c) inside view of the chamber (floor fans are visible in the left-hand side, as well as acoustic emission devices on the floor).

After excavation, the block was analyzed to identify possible cracks caused by the niche excavation or related to the salt structure (desiccation cracks, etc). Based on this analysis, it was decided to conduct the experiment in the rear part of the slab, close to the niche end. A square surface of 10 m² was conditioned on top of the salt block to perform the test. The experimental surface can be seen in Figure 3.8a. On this surface, an experimental chamber was built; it allowed cooling the salt surface and the underlying salt rock mass. Figure 3.8b shows an outside view of the chamber and Figure 3.8c shows a view of the inside with some equipment (details will be given below). The chamber was designed so that a temperature drop of 40 °C could be applied to the salt surface (from the ambient temperature to about -25 °C). The cooling device consists of a 7.5 kW refrigeration unit that cools down the air inside the chamber. In order to keep the niche temperature as constant as possible, the compressor was placed in the access gallery, next to the niche entrance. The mine is ventilated, and temperature is about constant in the drifts (14.5 °C approximately at a depth of 120 m, corresponding to the geothermal gradient).

To ensure a uniform cold production inside the chamber, the cold air was blown through an evaporating system placed in the ceiling along the right (East) wall of the room. To reduce heat losses below the walls and through the rock mass outside the chamber, a 20 cm thick rockwool insulation cover was placed on the salt floor around the chamber during the cooling stages. The insulation cover is displayed in Figure 3.8b. The optimal distance from the chamber that should be insulated was estimated numerically to be about 2.5 m (Hévin et al., 2017). This way, the energy required to cool down the salt surface is reduced by 30%, yielding 150 W/m².

In order to enhance the convective flux inside the chamber (and therefore, the transfer of thermal energy with the rock), eight fans were placed on the floor next to the left wall (nominal range of 9.5 m/s); they can be seen in Figure 3.8c. The air speed is thereby increased, which increases the heat transfer coefficient between the air and the salt surface.

During the experiment, three cooling-warming cycles were performed, followed by two additional cooling phases. For each of the cycles, the cold air flow was applied for 28 days and the average temperature of the salt surface decreased to about -6 °C. Then, the air flow was stopped for at least six weeks so that temperature inside the chamber and in the salt block could equilibrate with the mine temperature (to facilitate warming, the insulation cover was removed during the warming periods). The last two stages consisted in cooling the salt surface down to temperatures of -6 °C and -25 °C for a time period of 14 and 21 days, respectively. They were conducted to investigate the effects of a further decrease in temperature on the stress state and on the onset and propagation of possible cracks. Figure 3.9 displays the loading history (measured air temperature in the chamber over time). As the Figure shows, during each cycle the air temperature reached -8.5 °C (-27 °C for the last stage) in a very short time (about 8 h). Likewise, the temperature rise was very fast during the warming phases, although about three times slower than the cooling rate. At the end of the first four cooling stages, the air temperature reached -9 °C (-27.6 °C for the fifth stage).

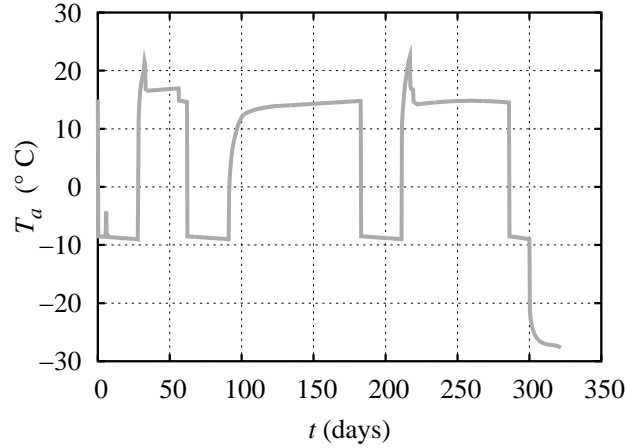


Figure 3.9. Test at *Varangéville*: air temperature inside the chamber. The maximum value during cycles 1 and 3 is due to the use of an electric heater during the first week of warming.

An extensive measurement program was defined to get as much insight as possible (Hévin et al., 2016). Temperature sensors (Pt100 and thermocouples) were installed at different locations inside the chamber and outside the chamber below the insulation cover. Inside the chamber, they were placed at the salt surface, at 1 cm depth and in a vertical borehole drilled at the center of the room, allowing to sample temperature as deep as 80 cm. Outside the chamber, the sensors were placed at a depth of 1 cm. The heat flux between the air and the salt surface was also measured, using a flux sensor placed on the floor, in the central part of the chamber. Strain gauges were placed on the salt surface and in the central borehole. An ultrasonic network was also set up, comprising 5 emitters and 12 receivers (see Figure 3.8c). To get three-dimensional gridding, the receivers were placed on the salt surface and underneath; for this purpose, 4 inclined boreholes were drilled from outside the chamber to a depth of 60 cm below the test surface. An imaging system was also set up; it allowed tracking the formation and propagation of possible fractures. Four digital cameras (resolution of 3 px/mm) attached to the ceiling of the room covered the entire floor of the chamber. A rotating infrared camera was also placed at the ceiling to track the room surface temperature. All these techniques allowed for a full characterization of possible fractures: time of creation, location and orientation, size, number, etc.

During the first cycle, a macro-fracture was visible after about six hours of cooling. It was located perpendicular to the air flow, about one meter from the fans (area with coldest temperature), and extended rapidly along more than one meter. At the end of the first cycle, the crack aperture was less than 1 mm (measured with dial gauges). In addition to this macro-crack, many micro-cracks (imperceptible to the naked eye) were present over the entire surface at that time. They were closed and shallow in appearance. In subsequent cycles, pre-existing fractures reopened and spread. Additionally, new cracks were created. Therefore, a fracture network developed progressively during the cycles; however, it should be noted that the extension of the cracks decreased with the number of cycles. Measurements from acoustic emission are consistent with the images interpretation (Balland et al., 2018): the number of events reduced from one cycle to the next, with the first cycle producing 2-3 more events than the rest. Figure 3.10 shows the visible fractures developed throughout the experiment. It can be seen how these fractures tend to join over time. At the end of the test, the maximum crack width was 1-1.2 mm. The analysis of the last cooling stage shows that a

further temperature decrease increases the width of crack opening and enhances the creation of new fractures.

Modeling was performed after the test. In order to ensure cavern integrity, fractures should be avoided, so we focus on the conditions under which fractures could appear (rather than fracture propagation), for which a continuum modeling approach is justified (knowledge about the critical zones is sufficient at the design stage). It should be noted that in those cases in which fracture propagation is important, a continuum modeling approach should be coupled with a numerical method that allows fracture evolution, such as the extended finite element method (XFEM) (Moës et al., 1999). Proper modeling of the experiment requires coupling between different processes, particularly thermal and mechanical. Indeed, hydraulic processes are less important in the current case because the intercrystalline space of rock salt, although very small, is filled with saturated brine, whose freezing point is about $-21\text{ }^{\circ}\text{C}$. The governing equations of the thermo-mechanical problem are the balance laws of momentum and thermal energy.

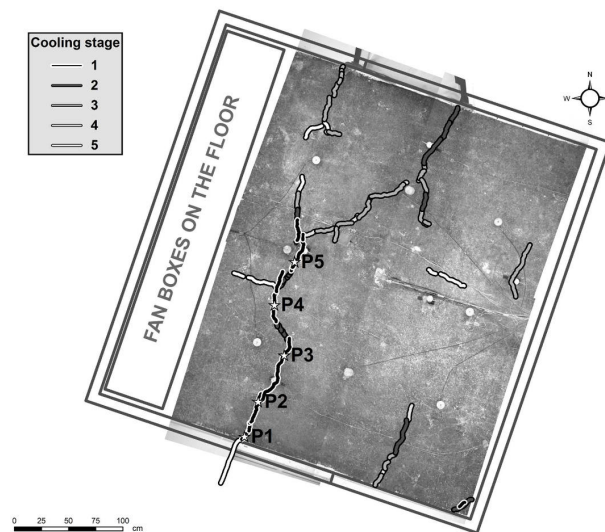


Figure 3.10. Test at *Varangéville*: visible fractures developed during the different cooling stages.

In a first step, the temperature field is computed in space and time, and then thermo-mechanical modeling is performed (one-way coupling from heat flow to geomechanics, justified here because the strains measured during the test are small). Both simulations model the same domain, displayed in Figure 3.11. It extends 200 m along each axis, and it starts at the ground surface. Three horizontal layers are defined from the top: a 40 m thick sandstone-marl layer, a 80 m thick salt layer and a 80 m thick marl layer. The access drift and the experimental niche are at a depth of 119.8 m, 20 cm above the salt-marl contact. Note that in agreement with the experiment, the two slots created parallel to the niche axis reach the salt-marl contact in the model.

In the thermal simulation, temperature is held constant at all outer planes ($x=0$, $x=200$ m, $y=0$, $y=200$ m, $z=-200$ m, $z=0$). It has been verified that the thermal perturbation induced by the experiment does not reach these planes. The initial temperature is $14.5\text{ }^{\circ}\text{C}$ in the whole domain (this simplification is justified due to the limited extent of the thermal perturbation as will be shown below), and the evolution of the air temperature, T_a , is given in Figure 3.9. Heat transfer between the air and the salt surface is taken into account using Newton's law of cooling, defined as

$$\vec{\psi} \cdot \vec{n} = h(T - T_a) \quad (3.1)$$

where \vec{n} is the outward-pointing unit normal vector and h is the heat transfer coefficient. The heat transfer coefficients have been determined inside and outside the chamber, during the cooling and the warming periods (Hévin et al., 2016). They are function of the air speed, independent of temperature, and their values have been confirmed by measurements of the heat flux and the temperature difference between the air and the salt surface. The regular value is $h=10 \text{ W/m}^2/\text{K}$, but heat transfer is modified at some locations and periods. In particular, during cooling $h=22 \text{ W/m}^2/\text{K}$ below the fans, and $h = 3.8x^2 - 21.96x + 50.56 \text{ W/m}^2/\text{K}$ elsewhere in the chamber (x is a local coordinate system with origin at the chamber lower left corner, see Figure 3.12). Below the insulation cover, $h=0.2 \text{ W/m}^2/\text{K}$ and in the backfilled slots, $h=2 \text{ W/m}^2/\text{K}$.

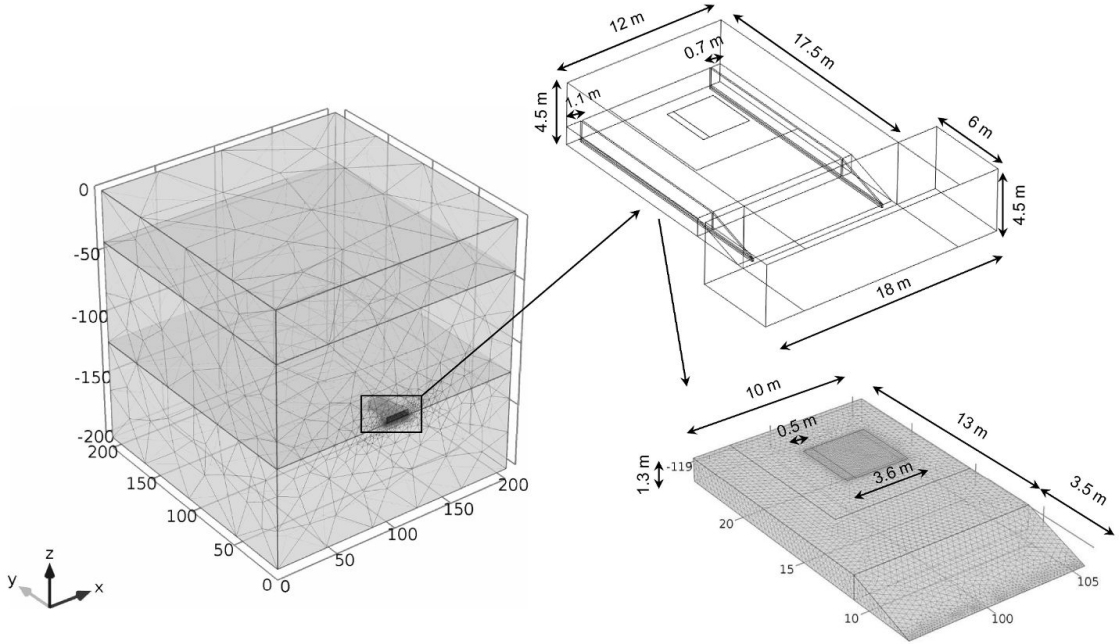


Figure 3.11. Test at *Varangéville*: view of the 3D model used in the simulations (left) and enlarged views of the niche (top right) and the salt block (bottom right). The domain is discretized into 202,990 tetrahedral elements, having minimum and maximum sizes of respectively 0.05 m (test zone) and 72 m (far from the niche).

As for geomechanics, the displacement normal to the vertical and bottom planes is blocked, and the $z=0$ plane is not constrained. Similarly to the thermal problem, it has been verified that the constrained boundaries are far enough and not affected by the processes induced by the experiment. The initial stress field is isotropic, equal to the lithostatic stress magnitude (hereafter, compressive strains are stresses are negative).

Table 3.2 lists thermo-mechanical properties of each layer. The marl and sandstone-marl layers are assumed to behave elastically, and the time-dependent behavior of rock salt is described by the Lemaitre creep law (Eq. 2.3), with parameters obtained from creep tests performed at ambient temperature ($T_r=27 \text{ }^\circ\text{C}$) at Mines Paris on salt samples from the *Varangéville* mine.

Table 3.2. Test at *Varangéville*: material constants of the rock layers included in the model (ρ is mass density, C_p is heat capacity and λ is thermal conductivity).

Parameter (unit)	Sandstone-marl layer	Salt layer	Marl layer
Thermo-physical parameters			
ρ (kg/m ³)	2500	2200	2300
C_p (J/kg/K)	850	850	900
λ (W/m/K)	2.5	6.8	2.9
Thermo-elastic parameters			
α_{th} (K ⁻¹)	$1.5 \cdot 10^{-5}$	$3 \cdot 10^{-5}$	$1.5 \cdot 10^{-5}$
E (GPa)	15	25	15
ν (-)	0.25	0.25	0.2
Viscoplastic parameters (unit system is MPa, K, days, $\mu\text{m}/\text{m}$)			
α	-	0.303	-
β	-	3.4	-
k	-	1.5	-
A_L	-	8250.78	-

The thermal simulation covers the test duration, that in total was 322 days (three cycles and two subsequent cooling periods, see Figure 3.9). This simulation is performed using the FEM code COMSOL Multiphysics (COMSOL AB, 2013). The geomechanical simulation, performed with the FEM code VIPLEF3D (Tijani, 1996), starts with the excavation of the drift, the niche and the two slots, assumed instantaneous and isothermal. This step is necessary to recalculate the stress field around the openings, and particularly in the salt block. Then, the elapsed time between the excavation and the beginning of the test is modeled (129 days), also in isothermal conditions. Finally, the test itself is modeled (thermo-mechanical coupling). The total modeled time in geomechanics is therefore 451 days.

The temperature field computed over time compares well with experimental data. Figure 3.12 shows the location of the temperature sensors inside and outside the chamber, and Figure 3.13 compares experimental and numerical temperatures for some sensors. Note that after the first cooling stage, values of surface thermocouples appeared to be very noisy and it was decided to place them at a depth of 1 cm (except for sensor *S31*, which was located under the ventilation box). As it can be seen, the surface temperature inside the chamber is not uniform, but increases at further distances from the fans. Moreover, the length of the cooling phases allows temperature changes well below the salt surface and also beyond the chamber (this was actually a design requirement of the experiment). As Figure 3.13 shows, negative temperatures are reached 80 cm below the salt surface in the second and subsequent cycles (sensor *T5*). Outside the chamber, the temperature of the salt surface is clearly affected by the experiment, and as expected the temperature gradient decreases at greater distances from the walls of the chamber.

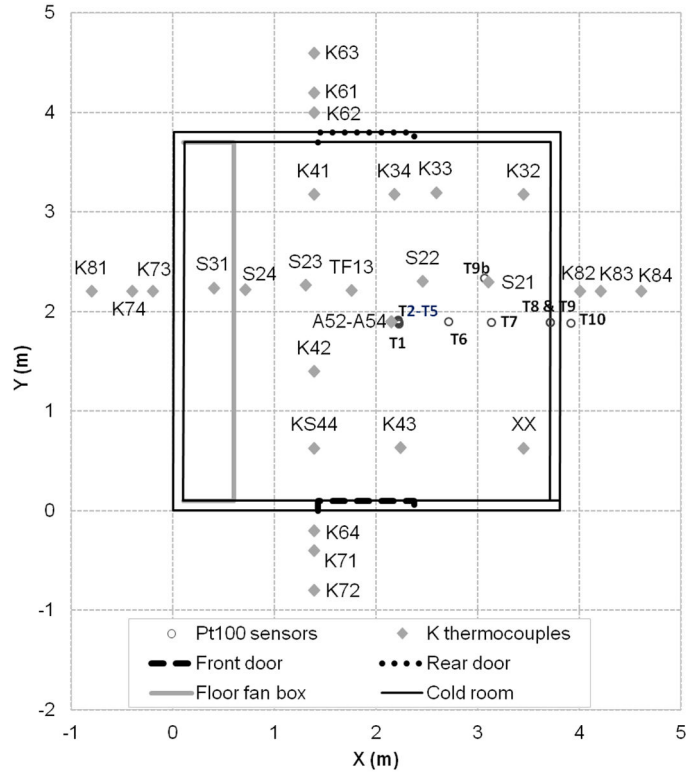


Figure 3.12. Test at *Varangéville*: location of temperature sensors in a local reference system.

Note that the thermocouples define two main orthogonal profiles, which extend outside the chamber. Air temperature is measured by sensors identified *A52 – A54*. Pt100 sensors *T2-T5* are placed at different depths in a vertical borehole. Sensor *TF13* is a heat flux sensor.

Overall, temperature measurements inside the chamber show similar distributions for the first four cooling periods, and more particularly for periods 2-4. This suggests that the thermal loading on the rock salt was about the same during the cycles, and that the fractures created did not affect significantly the temperature field (note however that fracture aperture remained small, around 1-1.2 mm).

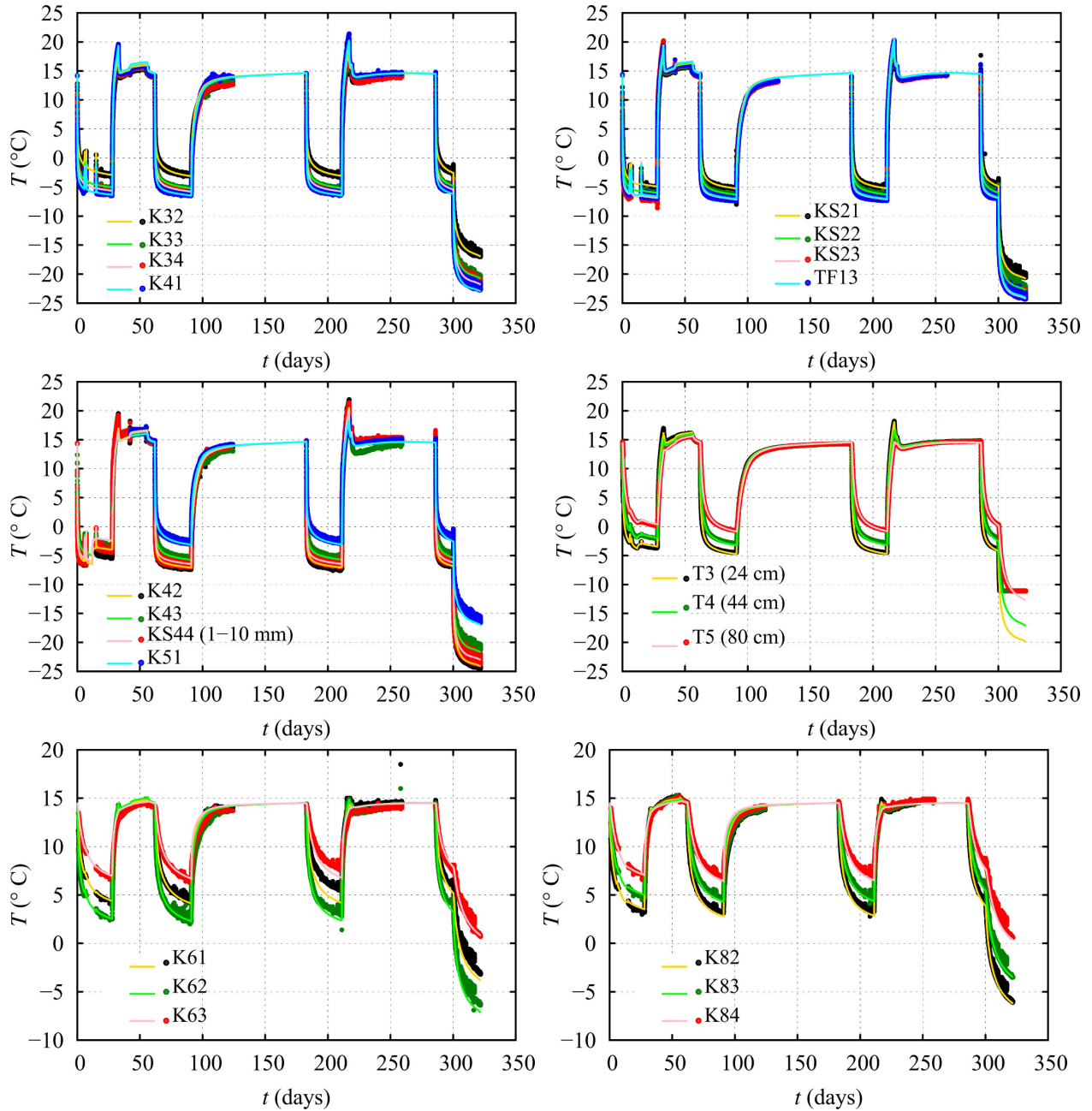


Figure 3.13. Test at *Varangéville*: comparison between experimental data (symbols) and numerical results (lines) for temperature at several locations indicated in Figure 3.12.

Regarding thermo-mechanical modeling, we first highlight that, owing to the use of a continuum modeling approach, the following analysis focuses on the first cycle, and particularly, the conditions that lead to the creation of the first fracture. Figure 3.14a shows the maximum (*i.e.*, least compressive) principal stress σ_1 at the surface of the salt block ($z=-118.5$ m) after excavation. As it can be seen, the maximum principal stress is 2.76 MPa. This value is reached in the two small blocks left at both sides of the experimental block after cutting the slots, and is due to local effects induced by the free surfaces (some damage was observed in these zones before the test). On the

surface of the experimental block, the stresses do not exceed 1.5 MPa. The maximum principal stress at $t=129$ d (*i.e.*, before the beginning of the test) is shown in Figure 3.14b. The comparison between the two Figures shows that there has been some relaxation due to the creep of the rock salt. On the test surface, after 129 days the maximum principal stress peaks at 1.3 MPa.

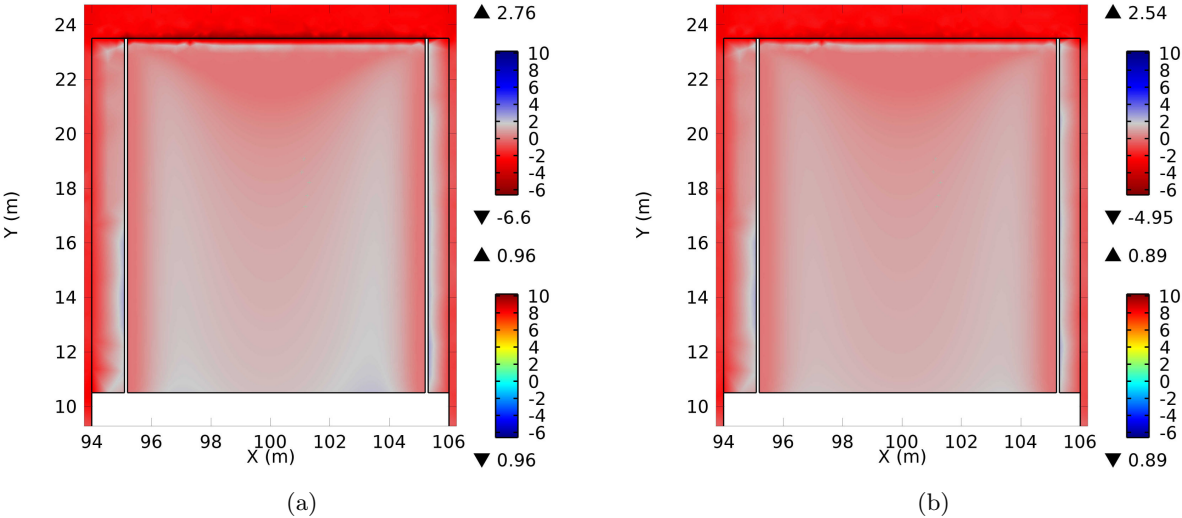


Figure 3.14. Test at *Varangéville*: maximum principal stress (MPa) at the surface of the salt block (a) after excavation ($t=0$) and (b) before the beginning of the first cycle ($t=129$ d). The principal stresses at locations $P1-P5$ (see Figure 3.10) are displayed (bottom color table).

Figures 3.15 and 3.16 show the maximum principal stress and the temperature at different moments of the first cooling stage. Note that the temperature profile at $t=129+28$ d (cooler temperatures close to the rear door of the chamber) is due to the fact that the fans in the front area stopped working at $t=129+12$ d, and were not repaired until the first warming period. From the plots shown, it can be seen that as temperature decreases the stress state becomes more tensile. Since these modeling results have been obtained with a continuum approach, they are less accurate after the onset of fracturing; nevertheless, the computed stresses suggest that the emplacement and orientation of fracture initialization are fairly well reproduced numerically. Indeed, the first fracture was observed during the experiment at location $P3$ in Figure 3.10, and the computed results displayed in Figures 3.15 and 3.16 show maximum stress values in this zone. Likewise, the orientation of the least compressive stress shown in these Figures is consistent with the orientation of the main fracture in Figure 3.10.

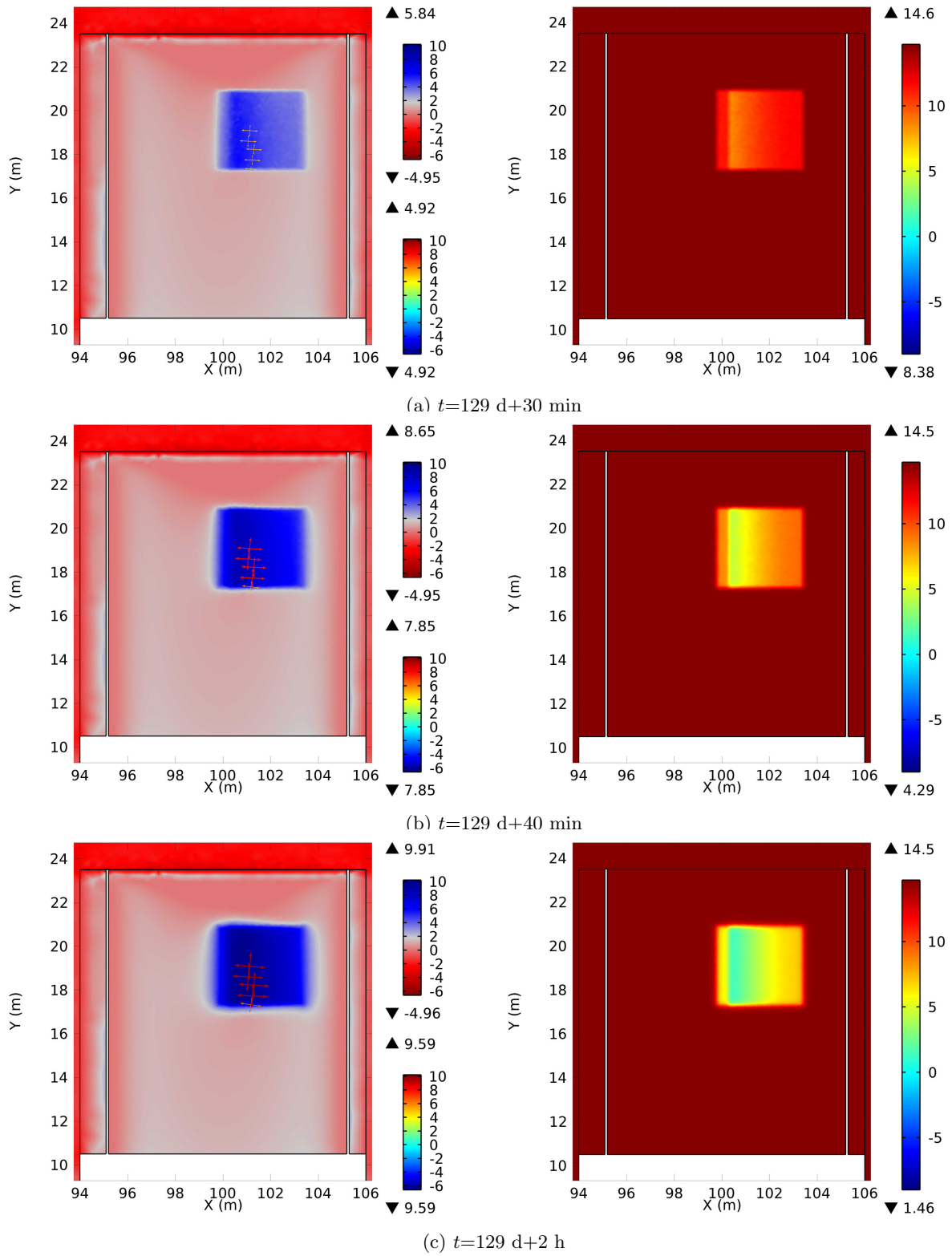


Figure 3.15. Test at *Varangéville*: numerical results at the surface of the salt block during the first cooling stage. Left: maximum principal stress (MPa) (the bottom color table corresponds to the principal stresses at locations $P1$ - $P5$). Right: temperature ($^{\circ}\text{C}$).

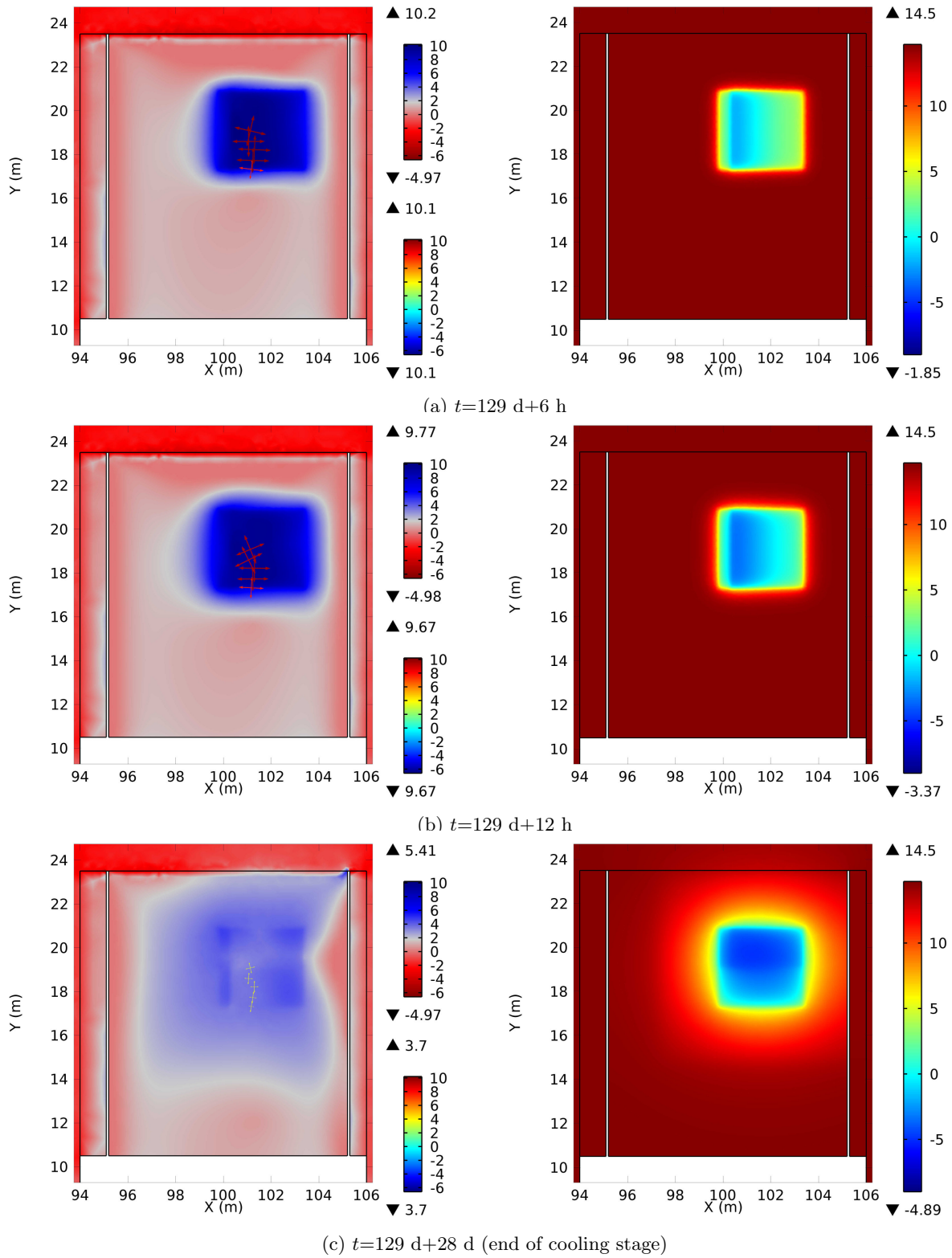


Figure 3.16. Test at *Varangéville*: numerical results at the surface of the salt block during the first cooling stage. Left: maximum principal stress (MPa) (the bottom color table corresponds to the principal stresses at locations $P1$ - $P5$). Right: temperature ($^{\circ}\text{C}$).

We highlight that the main factor affecting the thermal stress is the linear thermal expansion coefficient, α_{th} . Indeed, given the short time in which fractures develop, time-dependent processes

play a secondary role in this case. As Figure 3.15 shows, after 30 minutes of cooling the temperature in the area where the first fracture was observed is about 9 °C, and the least compressive stress is about 8 MPa; this value is consistent with the stress change estimated using $-\alpha_{th}E\Delta T/(1-2\nu)$.

The results at the end of the first cycle are shown in Figure 3.17. As it can be seen, the temperature has come back to the initial value (14.5 °C), but a slight difference is observed in the stresses, due to the non-elastic response of the rock salt.

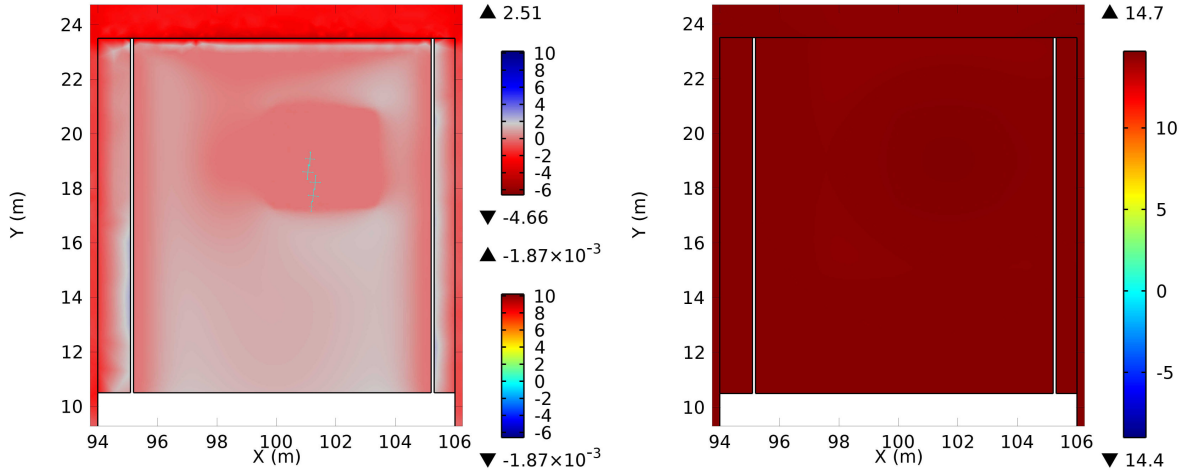


Figure 3.17. Test at *Varangéville*: numerical results at the surface of the salt block at the end of the first cycle ($t=129+62=191$ d). Left: maximum principal stress (MPa) (the bottom color table corresponds to the principal stresses at locations $P1-P5$). Right: temperature (°C).

Figure 3.18 displays the maximum principal stress at three locations during the first 12 hours of cooling: $P3$ (surface of block), a point 50 cm below $P3$ and a point 1 m below $P3$. The air temperature inside the chamber is also plotted. Note that below the salt surface, the maximum principal stress decreases initially due to the stress redistribution imposed by the compatibility requirement. Assuming that the apparent tensile strength of the rock salt is 1.5 MPa, these numerical results suggest that such strength at location $P3$ was reached after about 8 minutes of cooling, and after about 10 hours 50 cm below $P3$. During the experiment, the first fracture was visible at $P3$ after about 6 hours, which suggests its creation started at an earlier time. Taking into account the sensitivity of the results to parameters such as the thermal expansion coefficient of the rock salt or the Young's modulus of the underlying marl layer, the predicted timing of fracture creation can be considered satisfactory.

Finally, Figure 3.19 displays the maximum principal stress on a vertical plane across the chamber (plane $x=101.17$ m, which intersects the fracture visible during the first cycle), at the times displayed in Figures 3.14b-3.17. Although during the first hours large tensile stresses concentrate in the upper part of the block (first 80 cm), at the end of the first cooling phase large tensile stresses are predicted deeper than 1 m from the top of the salt block (due to propagation of cooling), which is in agreement with the observed depth of penetration of the main fracture. Overall, from Figures 3.14-3.19, it can be concluded that the modeling results reproduce the location, orientation, timing and depth of penetration of the first fracture quite satisfactorily.

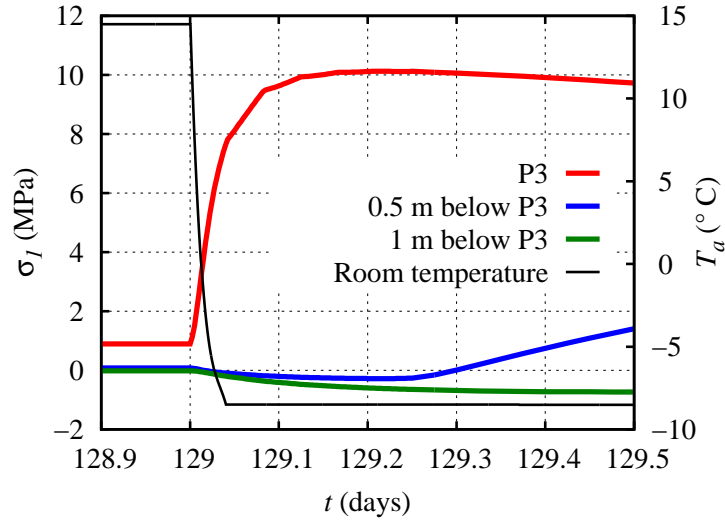


Figure 3.18. Test at *Varangéville*: evolution of the maximum principal stress during the first 12 h of cooling at three locations.

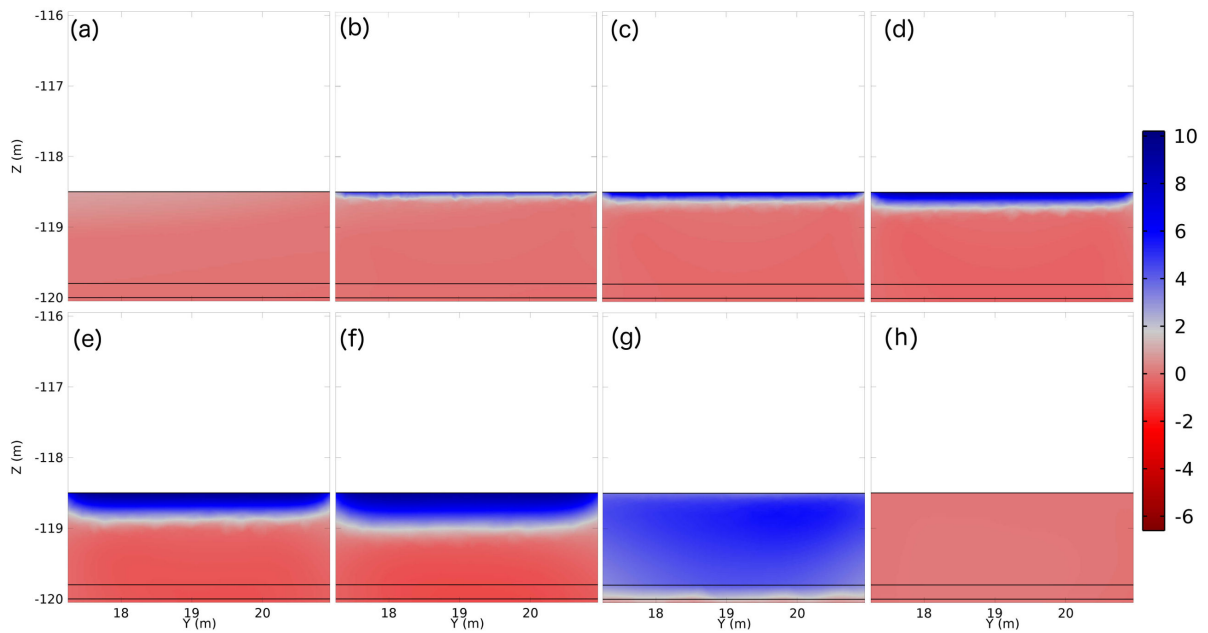


Figure 3.19. Test at *Varangéville*: maximum principal stress (MPa) on a vertical plane across the chamber (plane $x=101.17$ m, between $y=17.3$ m and $y=20.9$ m), in the area where fractures were first observed. (a) $t=129$ d; (b) $t=129$ d+30 min; (c) $t=129$ d+40 min; (d) $t=129$ d+2 h; (e) $t=129$ d+6 h; (f) $t=129$ d+12 h; (g) $t=129$ d+28 d; (h) $t=129$ d+62 d.

It should be noted that the test was conducted under particular conditions that did not aim at reproducing a salt storage cavern, but rather, at verifying whether a rapid temperature drop could lead to fracturing. In this context, the test specifications required that fracturing be favored as much as possible. To comply with these specifications, the initial stress state in the salt block

was minimized by additionally cutting the two slots. This way, any thermally-induced tensile stress would only be balanced by the very low *in situ* stresses, thereby facilitating fracturing (*i.e.*, this is a conservative scenario). Moreover, the applied cooling rate was high enough to favor the onset of fractures. Indeed, as the cooling rate increases heat transfer with the surrounding rock is much more limited, and large temperature changes concentrate close to the cooled surface, thereby favoring the creation of fractures.

Similarly, the test specifications required that temperature changes extend well beyond the test surface. To meet this requirement, cooling was maintained for 28 days during each cycle, whereas in a salt cavern undergoing high frequency cycling, the withdrawal phase is much shorter. This leads to a conservative scenario as well.

The test demonstrated that tensile fracturing induced by rapid cooling is possible. However, despite the rather extreme scenario tested (very low initial stresses, aggressive cooling rate, long cooling periods), the depth of penetration of the fractures remained limited (<2 m) through the cooling stages, which, given the size of a storage cavern, suggests that the effects of thermally-induced fractures are quite restricted (areas likely to be more sensitive are around the well or those with irregular shapes). Nevertheless, to stay on the safe side the existing design criteria and operational conditions should be adapted to minimize the effects of rapid depressurizations.

Finally, during this test, the rock salt was subjected to low (and negative) temperatures —a domain that is rarely investigated, but that is important in the context of high frequency cycling. In the modeling presented, temperature effects are extrapolated from the domain usually studied in laboratory tests ($T \geq 20$ °C). There is currently no sound evidence that the viscoplastic behavior of rock salt is the same for high and low (even negative) temperatures. As a perspective, research should be conducted on this matter to gain more insight, see chapter 4.

3.3 Disposal of heat-generating nuclear waste

Rock salt is being considered in the United States and Germany as a disposal medium for heat-generating nuclear waste. In a generic scenario with in-drift emplacement of the waste packages, the backfill consists of crushed (run-of-mine) salt, which gets progressively compacted as the natural salt creeps. Once the reconsolidation process is over, it is expected that the backfill will provide a geotechnical barrier, thereby reinforcing the natural (or geological) barrier function of the host rock. In this context, the ultimate goal of a research about disposal of heat-generating nuclear waste in salt is to evaluate the long-term integrity of the geological (host rock) barrier, as well as the development and long-term integrity of the geotechnical (backfill) barrier. Indeed, in the unfavorable event of a radionuclide release from the waste packages, these barriers are essential to prevent the escape and the transport of undesired fluids into the biosphere.

As for the natural salt, it is well known that its initial tightness (very low permeability and porosity) could be affected by processes that take place at different stages during the lifetime of a repository (Stormont & Daemen, 1992; Peach & Spiers, 1996; Hunsche & Hampel, 1999; Schulze et al., 2001; Hou, 2003). First, the development of an excavation damaged zone (EDZ) around the mined openings represents a potential risk because preferential flow pathways could be created; such development is related to the dilatancy threshold, and is sometimes referred to as thermo-mechanical damage (Minkley & Popp, 2010; Wolters et al., 2012). Second, a pore pressure-driven percolation process (fluid infiltration) can take place if the pore pressure locally exceeds the least compressive principal stress. Several factors can result in fluid infiltration: thermal pressurization within the rock (due to thermal expansion of pore fluids that cannot escape in a very

low permeability medium —this is particularly true when the pore space is mostly occupied by low compressibility fluids, such as water or brine), convergence-induced pore pressure increase (for instance, within the backfill), and gas generation from the waste packages, among others. Should thermo-mechanical damage or fluid infiltration occur, the initial, near-zero permeability of the host rock would be superseded by an increased, secondary permeability (Wieczorek et al., 2012; Wolters et al., 2012). These perturbations, however, are generally not persistent in a plastic medium such as rock salt. Once the thermal and stress regime become favorable, and with sufficient amounts of brine, it is expected that healing processes will operate, helping bond fracture surfaces and close micro-fractures (Hansen, 2008; Popp et al., 2012; Wolters et al., 2012). Additionally, local widening of grain boundaries caused by percolation of pore fluids is expected to cease as the pore pressure decreases below the least compressive principal stress (Wolters et al., 2012). Damage, healing and percolation processes within natural salt have been studied at the laboratory scale and have been included in phenomenological constitutive relationships, *e.g.*, Wolters et al. (2012); Hampel et al. (2013). They have also been observed in various field studies (Wieczorek & Schwarzieneck, 2001; Hou, 2003; Bechthold et al., 2004; Popp & Minkley, 2010).

The reconsolidation process of the crushed salt used for backfilling has also been studied in the past years, and several time-dependent compaction models have been proposed, *e.g.*, Sjaardema & Krieg (1987); Callahan et al. (1991); Olivella & Gens (2002). The initial porosity of the backfill is about 30-40%, and values smaller than 10% are expected in the long-term. As compaction takes place, triggered by the closure of the excavations due to the creep of the host rock, the mechanical and flow properties of the crushed salt evolve towards those of the natural salt, helping encapsulate the waste. In particular, permeability decreases several orders of magnitude, the thermal conductivity increases and so do the elastic moduli (Callahan et al., 1991; Bechthold et al., 1999, 2004; Hurtado et al., 1997; Wieczorek et al., 2012). Experimental studies have shown that the compaction rate increases with the moisture content (Popp & Salzer, 2012). On the other hand, the reconsolidation process at the high temperatures associated with exothermic nuclear waste would benefit from further investigation (Carter et al., 2011). Moreover, the compaction behavior at porosities lower than 5–10% is not currently well understood, and data in this range are scarce (Kröhn et al., 2012).

Overall, in order to evaluate the safety of the geological and geotechnical barriers, thermal, hydraulic and mechanical (and chemical) processes need to be considered. These processes interact and influence each other in a complex manner. In addition, they do not necessarily have the same spatial and temporal scales; therefore, numerical modeling based on suitable tools as well as on state-of-the-art and physically-based knowledge is needed (Tsang et al., 2009). Several modeling studies on the disposal of heat-generating nuclear waste in saliniferous formations have been reported in the literature, *e.g.*, Lowe & Knowles (1989); Munson et al. (1990); Pudewills et al. (1995); Bechthold et al. (2004); Javeri & Baltes (2008); Stone et al. (2010); Clayton et al. (2012); Lerch et al. (2012); Argüello & Rath (2013); Hampel et al. (2013); Kock et al. (2013). Nevertheless, the majority of these studies do not consider simultaneously important thermal, hydraulic and mechanical processes in the different barriers. As a postdoc, I sought to improve the understanding of the long-term integrity of the natural salt and the crushed salt backfill by considering coupled thermal–hydraulic–mechanical (THM) processes. For such purpose, I used the TOUGH-FLAC sequential simulator for flow and geomechanics (Rutqvist & Tsang, 2003). In this sequential simulator, the multiphase, multicomponent and non-isothermal sub-problem is solved by the integral finite difference software TOUGH2 (Pruess et al., 2012) and the geomechanics sub-problem is solved by the finite difference software FLAC^{3D} (Itasca, 2009). TOUGH2 includes several equation-of-

state (EOS) modules for different pure substances and mixtures, and FLAC^{3D} includes several viscoplastic rheological models. TOUGH-FLAC is based on the fixed-stress split sequential method to couple flow and geomechanics (Kim et al., 2011b) and in order to use it to investigate the long-term integrity of the barriers, I adapted it to deal with finite strains and with time-dependent mechanical response. The details of the modifications that I introduced, as well as some verifications cases, are presented in Blanco-Martín et al. (2017) (Appendix B.1). While FLAC^{3D} provides a capability for large strains, TOUGH2 does not. Therefore, in order to extend TOUGH-FLAC into the finite strain framework and into viscoplasticity, I had to (i) adapt TOUGH2 to account for finite strains from the geomechanics sub-problem, and (ii) adapt the coupling between the two codes. TOUGH-FLAC is two-way coupled, but one-way coupling is possible as well. Note that as compared to the case investigated in section 3.2, here two-way coupling is required to avoid overlooking important processes (some examples are shown in Appendix B.2), and obviously there are additional equations for the mass balances (one equation per component; such equations are Eqs. (3-4) and (6) in Appendix B.1). In the context of disposal of heat-generating nuclear waste in salt, some particularities were needed in the simulator (material-specific evolution of flow and mechanical properties, based on experimental evidence as well as on theoretical considerations), detailed in Appendix B.2 and illustrated through the long-term performance of a generic repository covering 100,000 years of post-closure. Over the years, I introduced additional improvements to the simulator, such as the use of an updated version of an EOS, EWASG, that considers halite solubility constraints (in the initial version I used EOS3, which considers air and water but not salt), see Blanco-Martín et al. (2018b)². As an illustration, such improvements allowed to model the effects of diffusion and capillary forces gradients within the crushed salt. In addition, I benchmarked the augmented simulator against a sequential THM simulator developed at TU Clausthal, based on the same software, but using the undrained split sequential method (Kim et al., 2011a). We performed several simulations of a generic salt repository with in-drift emplacement of the waste packages and obtained quite satisfactory results (Blanco-Martín et al., 2014, 2015c).

Here, I will focus on the modeling of the *Thermal Simulation for Drift Emplacement* (TSDE) test. Full details can be found in Blanco-Martín et al. (2016b), and here only some features are discussed. This test benefited from extensive monitoring and allows for additional validation of the developed numerical tools. In addition to confrontation against experimental data, the numerical results were benchmarked against TU Clausthal results (benchmark and code-to-code verification). This way, the capabilities of the two simulators to predict relevant processes and phenomena can be evaluated, provided that the measurements are correct. This is a fundamental (although preliminary) step to evaluate the suitability of the simulators to study the long-term performance of an underground repository for nuclear waste in rock salt geological formations. Modeling of this test was also an opportunity to calibrate creep parameters of the natural salt host rock and of the backfill that were either unavailable or difficult to study at laboratory-scale (Blanco-Martín et al., 2016b).

The TSDE experiment was a large-scale underground heater test designed to represent reference repository conditions for heat-generating nuclear waste in salt-based systems. It was conducted in

²I also implemented the coupling between iTOUGH2 and FLAC^{3D} to perform numerical inversions using a coupled THM forward model (Blanco-Martín et al., 2016a) (iTROUGH2, developed at LBNL as well, provides inverse modeling capabilities for TOUGH2 and other code suites (Finsterle, 2007)). I also worked on the coupling between Pylith and TOUGH2, which is presented in Appendix B.3 (Blanco-Martín et al., 2022c), motivated by the need to yield more accurate estimations of possible induced seismicity. Furthermore, in the context of an application related to the production of non-conventional oil, I introduced three-phase relationships for relative permeability and capillary pressure into an EOS8, allowing to compute better flow estimates (Blanco-Martín et al., 2015b).

the Asse salt mine in Germany in the 1990s to support the development of the in-drift emplacement concept with multiple barriers (Bechthold et al., 1999, 2004). According to this concept, waste packages containing fuel assemblies are placed on the floor of horizontal drifts, which are subsequently backfilled with crushed salt. The natural salt host rock is the most important barrier, and secondary barriers are provided by the waste packages and the reconsolidated crushed salt backfill. One significant aspect of the TSDE experiment is that it was extensively monitored, using several observation and access drifts, as well as more than 200 boreholes for instrumentation, with sensors scanned every 12 h. The extensive measurement program included temperature, drift closure, rock deformation, stress evolution and gas generation and transport, among others. Some measuring devices were specially designed for this experiment. Therefore, in addition to evaluating the feasibility of the in-drift emplacement concept, the TSDE experiment provided a vast database on relevant phenomena and processes regarding the host rock, the backfill and also the waste packages. Subsequent analysis of the observations led to an improved understanding of the behavior of the host rock and the backfill under reference repository conditions for heat-generating nuclear waste, as well as to the development and improvement of constitutive models and computer codes required to predict the aforementioned relevant phenomena and processes.

In the TSDE experiment, six electrical heaters were placed in two parallel drifts excavated for the purposes of the experiment in the 800 m level of the Asse mine, in the North-Eastern part of the salt dome. The drifts were excavated in a relatively undisturbed area (Stassfurt Halite of the Zechstein series), and three heaters were emplaced in the central part of each drift. Figure 3.20 shows a cross-section of the Asse salt mine marking the location of the TSDE experiment as well as a view of the two test drifts. Some observation drifts (750 m level) and boreholes can also be seen in the Figure.

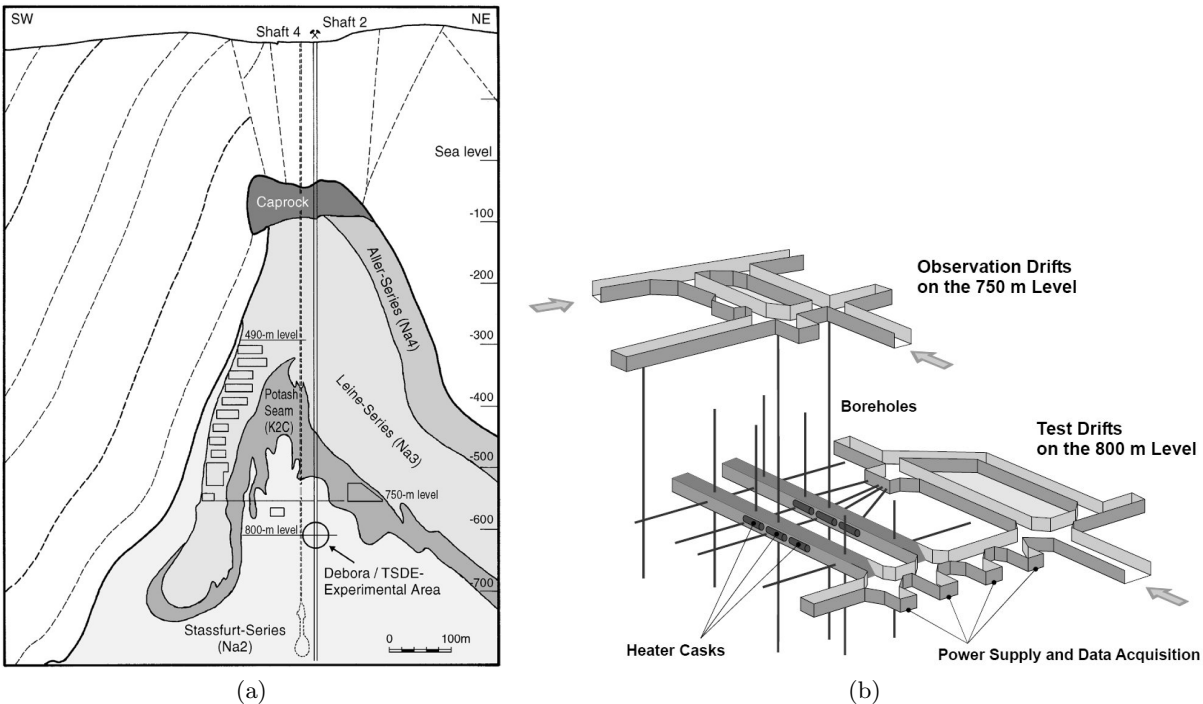


Figure 3.20. TSDE: (a) cross-section of the Asse salt mine, indicating the location of the experiment; (b) schematic representation of the test area.

The dimensions of the drifts, as well as the heat capacity of the electrical heaters, were selected to match the preliminary layout of the in-drift emplacement concept; therefore, the test represented a portion of a typical repository emplacement panel. The heaters were 5.5 m long, had a diameter of 1.6 m and were separated by 3 m along the drift axis. They weighted about 65 t and were designed to host 8 pressurized water reactor (PWR) assemblies. The drifts were about 4.5 m wide and 3.5 m high, and had a length of 77 m. A 10 m wide pillar lay between them. The heaters were emplaced 1.4 years after excavation. Immediately after the emplacement of the heaters, the drifts were backfilled using crushed salt, sieved to retain grain sizes smaller than 45 mm. The heaters were switched on in September 1990, and a constant heat load of 6.4 kW was applied to each heater until February 1999, when the heaters were switched off. The measuring instruments were installed in twenty monitoring cross-sections, not only in the heated area, but also in the non-heated area of the two drifts, see Figure 3.21.

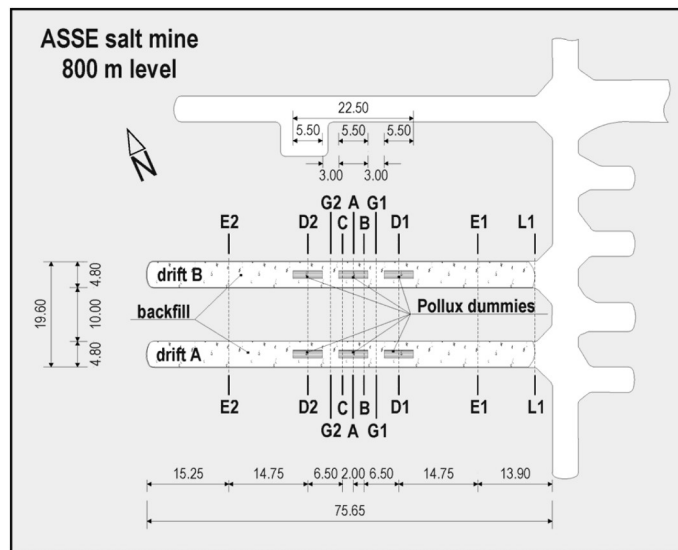


Figure 3.21. TSDE: plan view of the test drifts and monitoring cross-sections.

According to the geometry of the experiment, a 3D model of half of one drift was prepared with two symmetry planes: one at $X = 0$ (across the pillar between the two test drifts) and one at $Y = 0$ (across the central cross-section of the drifts). A 3D configuration is necessary for the computation of the temperature field; moreover, local effects between heaters cannot be captured in a 2D plane strain approximation. The model is 100 m wide, 200 m high and 38.5 m deep. Figure 3.22 shows some views of the initial (*i.e.*, non-deformed) discretization used in geomechanics (a Voronoi partition was used in the flow sub-problem). The mesh has 85870 elements. All external planes are no-flow boundaries (an exception exists, see comment below regarding the drift). Additionally, the displacement is blocked in the normal direction to those planes.

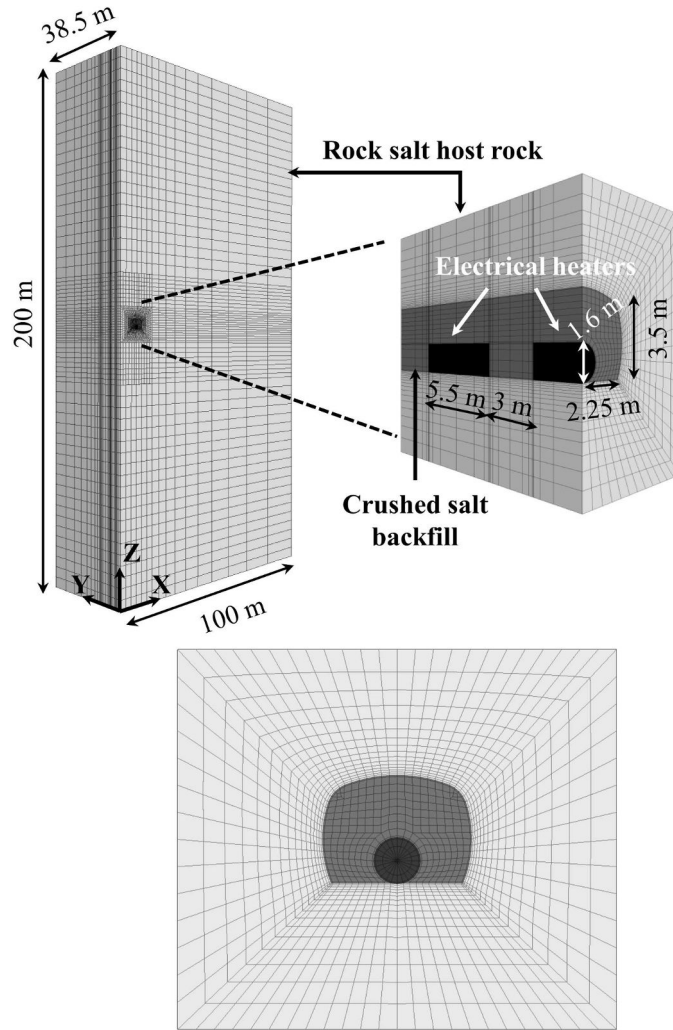


Figure 3.22. TSDE: views of the initial (non-deformed) mesh used in the geomechanics sub-problem. The main dimensions of the model are also shown.

Based on available information (Bechthold et al., 1999), we assign an initial (isotropic) stress field of -12 MPa to the host rock. The initial pore pressure within the host rock is lithostatic, and the initial temperature is 36.4 °C. The flow and mechanical parameters used for the heaters, the crushed salt and the natural salt are detailed in Blanco-Martín et al. (2016b), section 2.2. From the flow point of view, two-phase flow of water and air, as well as heat flow, are modeled using EOS3 of TOUGH2 (advective and diffusive mass transport and conductive and convective heat transport). The mechanical response of the natural salt is described using the Lux/Wolters constitutive model (Wolters et al., 2012), and for the crushed salt a modified version of the cwipp model implemented in $FLAC^{3D}$ has been used, in which density honors the volumetric strain evolution (Itasca, 2009; Blanco-Martín et al., 2015a).

The modeling sequence is as follows. First, initial equilibrium and drift excavation are modeled. The excavation is assumed instantaneous, and flow during this stage is disregarded. The coupled THM simulations include two parts: (1) the open drift phase, before the emplacement of the electrical heaters and subsequent backfilling of the drifts (1.4 year), and (2) the experiment itself

(heating), which lasted 8 years and 5 months. During the open drift phase, the heaters and backfill are deactivated and the pore pressure is kept constant within the drift at 0.1 MPa. During this phase, the temperature remains approximately constant. The main purpose of modeling this phase is to investigate the mechanical response of the natural salt host rock, including the EDZ. After 1.4 years, the heaters and backfill are activated. The initial porosity of the backfill is 35%, and the initial pore pressure and temperature within the drift are 0.1 MPa and 36.4 °C, respectively. In accordance to the situation sketched in Figure 3.21, the extremity of the drift at $Y = 38.5$ m is kept hydraulically open at the atmospheric pressure as a boundary condition during the heating phase. This leads to the effect that the pore pressure increase within the crushed salt induced by its compaction as well as by the heating of the included pore fluid is accompanied by a pore pressure decrease induced by an outflow of fluid at the open drift end. Therefore, pore pressure cannot increase very much within the drift. Additionally, the drift temperature at this extremity is held at 36.4 °C. Both during the open drift and heating phases, the mesh used in the flow sub-problem is progressively updated as the mesh used in the geomechanics sub-problem deforms. Depending on the criterion chosen to update the mesh, this operation is performed up to 50 times during the simulation.

The temperature evolution within the backfill (section B) and at the heater surface is displayed in Figure 3.23a. At the heater cask surface, the temperature reached 210 °C five months after the beginning of heating, and it decreased thereafter as the thermal conductivity of the backfill increased (due to compaction, *cf.* Eqs. (2-3) and (7) in Blanco-Martín et al. (2016b)), which facilitated the heat flow. The temperature increase was more gradual within the backfill, and significant temperature gradients were measured due to non-uniform compaction, which yields non-uniform thermal conductivity. After about 5 years, temperatures in the heater cask area approached a constant value (160–180 °C at the heater surface), while they continued to increase within the backfill at farther distances from the heater. The temperature within the rock in the heated area (section A) is displayed in Figure 3.23b. Heat transfer towards the salt rock mass occurs both by direct contact between the heater cask and the drift floor (heated area only), and also through the backfill. As expected, temperature decreases with the increase in depth. Temperatures approach a constant value after about 5 years (equilibrium between heat generation and propagation). As both Figures show, numerical results from the two simulators are in very good agreement with each other and they reproduce the measurements closely, with highest error at the heater cask surface.

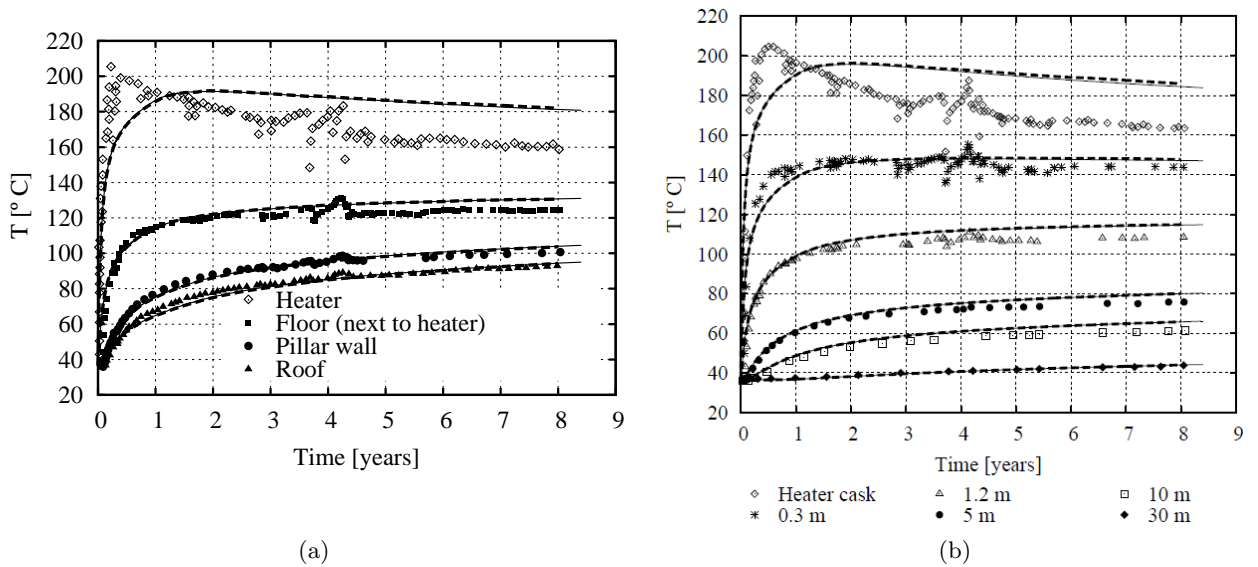


Figure 3.23. TSDE: temperature evolution within the backfill and at the heater surface (section B) (a), and (b) within the host rock beneath the drift floor (section A).

The drift closure over time is displayed in Figure 3.24a, for the heated (section G1) and non-heated (section E2) areas. Drift closure is calculated from horizontal and vertical convergence data. Both the open drift and heating phases of the experiment are included in the plot. As the Figure shows, the absolute value of the closure rate in the heated area increased significantly (factor of about 12) once heating started. High rates lasted about three months. On the other hand, the closure rate did not change noticeably in the non-heated area when the heaters were turned on. In the heated area, the absolute value of the closure rate decreased progressively over time due to the compaction of the backfill. Indeed, as compaction moves forward, the backfill densifies, stiffens and provides increased mechanical support against the drift walls, thereby reducing the drift closure rate. On the other hand, in the non-heated area the drift closure rate changed smoothly, and during the last five years of heating the vertical and horizontal closure rates were (in absolute value), respectively, 0.26–0.50% per year and 0.26–0.30% per year (values close to those of the open drift phase). In the heated area, they stabilized at 0.5% per year (vertical) and 0.4% per year (horizontal). As the Figure shows, results obtained by the two simulators are very similar. Moreover, they fall within the range of experimental measurements. We note that in agreement with experimental evidence from the post-test dismantling phase (Bechthold et al., 1999), drift closure rates (in absolute value) are higher at the pillar side of the drift due to higher temperatures at this sidewall. Also, due to the flat floor and the arch-shaped roof, vertical displacement is higher at the floor (uplift).

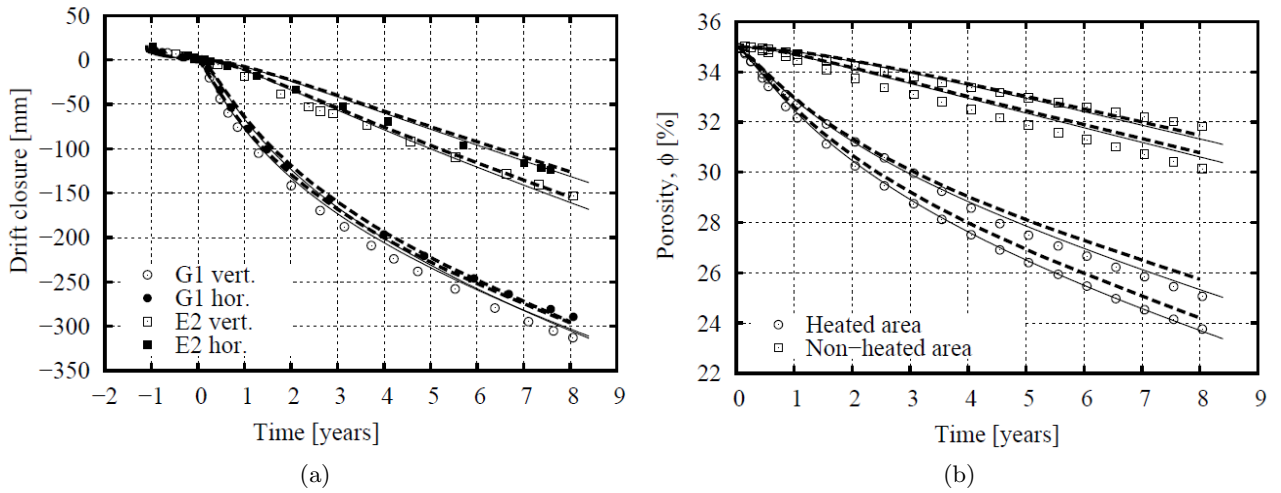


Figure 3.24. TSDE: (a) drift closure in the heated area (section G1) and in the non-heated area (section E2); (b) backfill porosity in the same sections. The start of the heating phase is set as a reference time ($t = 0$), and also as a reference for drift closure.

The evolution of backfill porosity in the same sections is displayed in Figure 3.24b. In fact, since backfill porosity was not directly measured during the test, the experimental values displayed were recalculated from experimental drift closure measurements, yielding an average porosity within a cross-section. For this reason, the comparison between data and numerical results for porosity is only approximate. Since high temperature gradients develop within the backfill (see Figure 3.23a), drift closure rates are not uniform; as a result, significant porosity gradients within the backfill are likely, even within a cross-section (heterogeneous compaction). As the Figure shows, during the heating period the average porosity reduced from 35% to 24–25.5% in the heated area, and from 35% to 30–32% in the non-heated area. Therefore, the compaction of the backfill was partial during the test. Using the porosities displayed, maximum values of thermal conductivity reached after 8 years were around 1.5 W/m/K (the initial thermal conductivity was 0.8 W/m/K).

Figure 3.25 shows the computed porosity profile within the host rock at the drift contour, at three different times: at the end of the open drift phase, after 4 years of heating, and at the end of the heating phase. As the contours show, porosity increases during heating, particularly in the heated area, and decreases over time as compaction takes place (development of mechanical support against the drift wall). Since compaction is faster in the heated area, in this zone host rock porosity at the end of the test has decreased more than in the non-heated area.

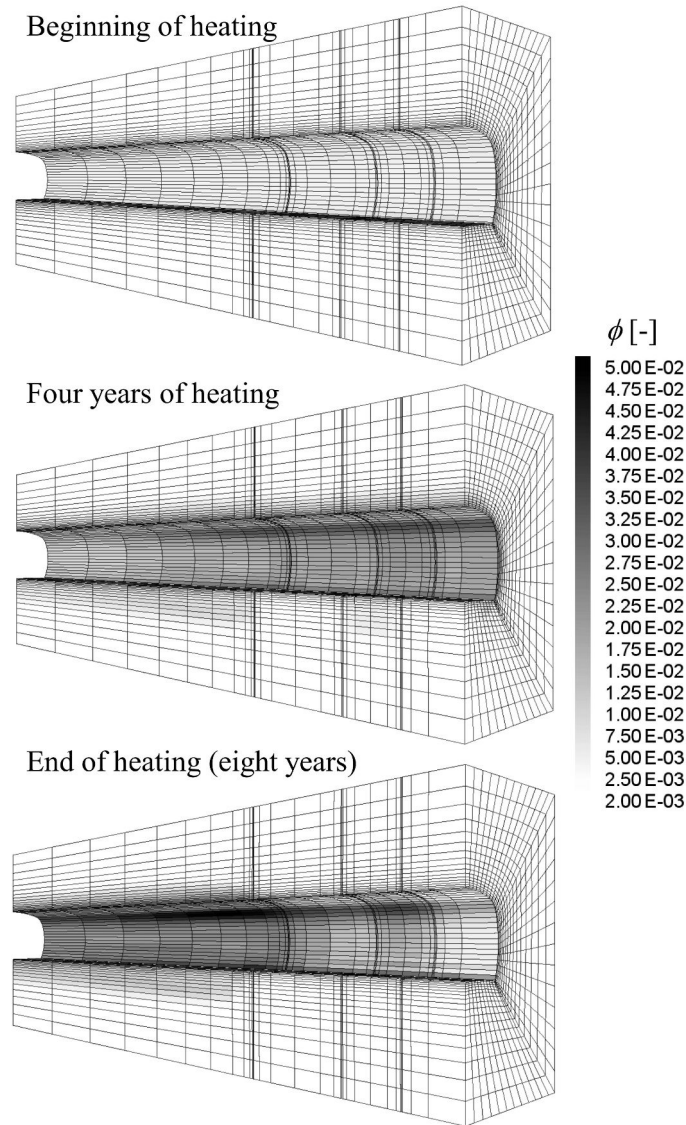


Figure 3.25. TSDE: host rock porosity around the drift area at three different moments of the THM run.

Overall, the numerical results obtained by the two simulators are in very good agreement with each other, which leads to a code-to-code verification and to a successful benchmark exercise. The accuracy of the numerical tools is tested by direct comparison between measurements and simulation results. In terms of temperature, rock deformation and drift closure, our results are in quite good agreement with available experimental data from the test. Regarding backfill compaction and associated setting (*i.e.*, stress increase), drift closure data from the experiment have been used to calibrate parameters of the cwipp model (compaction part). For this purpose, we have used a reduced model derived from the full 3D one, consisting only of the crushed salt and the electrical heaters, and we have applied the measured drift closure rate during the heating period as a boundary condition (different rates along the heated and non-heated areas, see Figure 3.26 and details in Blanco-Martín et al. (2016b)). Through inverse modeling, we have estimated a

parameter set. This preliminary approach has been selected due to the limited amount of available data regarding crushed salt compaction, in particular at high temperatures. The parameter set obtained has been subsequently used to model the TSDE experiment, and the results are more satisfactory than before the inversion. In order to test the suitability of the current parameter set for other scenarios, we have modeled an oedometer test conducted on crushed salt from one of the TSDE drifts. The results show some discrepancies, which should be investigated further (validity of the reduced order model, need to further develop the cwipp model ...).

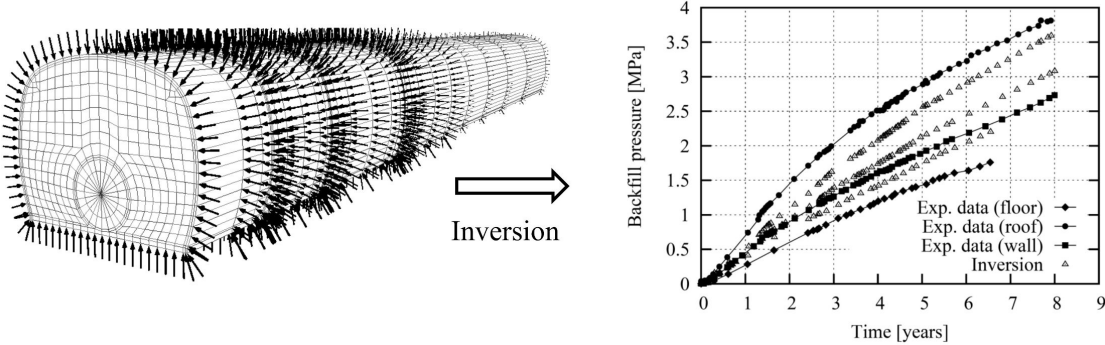


Figure 3.26. TSDE: reduced model used in the inversion (left) and results (right).

Further investigation of certain aspects is necessary, such as backfill compaction and long-term response of the natural and geotechnical barriers. The results shown in this section are promising, and the simulators presented should be updated as the understanding of such aspects moves forward. In the case of TOUGH-FLAC, H. Tounsi, a former PhD student at the geomechanics team of the Centre for Geosciences and Geoengineering, is currently a postdoc at the Energy Geosciences Division of LBNL, further developing and testing the simulator (Tounsi et al., 2022).

Chapter 4

Conclusions and perspectives

This document shows an overview of my research activities on rock salt. My research work aims at improving current knowledge on the behaviour of salt-based materials to tackle challenges that affect both society and industry, such as the underground disposal of heat-generating nuclear waste and the underground storage of fluids and energy carriers in salt caverns. Over the last ten years, I have acquired experimental, numerical and theoretical skills; such skills are interdependent, and since they allow for a broader perception of the problem to solve, I plan to develop and combine them further in the years to come. Moreover, they fit perfectly into the research and teaching activities within the geomechanics team of the Centre for Geosciences and Geoengineering of Mines Paris. In addition, the balance between public and private projects to which I contribute, combined with the academic collaborations that I seek to develop and preserve over time, are consistent with the teaching and research roadmap at Mines Paris, whose motto is “theory and practice”.

The experimental work has shown that, in order to characterize rock salt behavior for engineering applications following standard practice (*i.e.*, tests on decimetric-scale samples, use of phenomenological laws), heterogeneity must be considered. For that purpose, several measurement techniques, capturing the sample response at different scales, are necessary. If the heterogeneity induced by the end restraints on the sample is important, numerical inversions taking into account the contact between the sample and the pistons should be performed to determine a rheological parameter set, instead of assuming that the sample response is homogeneous. If material heterogeneity is important, the methodology proposed could be applied, which combines experimental work and simulations in a numerical twin, allowing to determine the RVE of the tested rock, and subsequently a rheological parameter set. Both cases of heterogeneity are in fact combined, as in general the sample response is affected by the characteristics of the contact between sample and platens, and rock salt often contains impurities of different nature. In both cases, intensive numerical computations are required, the computational cost being significant in the case of material heterogeneity. Assuming that the sample response is homogeneous is a simplification that could lead to an erroneous characterization of the material, and subsequently to an erroneous design of underground structures.

In addition, the experimental work performed leads to some guidelines for the characterization of rock salt. First, the same preconditioning should be applied to all rock samples within a campaign. Such preconditioning consists in a hydrostatic phase performed (when possible) under the relevant stress and temperature conditions at the coring depth, with sufficient duration to allow for a (quasi-)restoration of the *in situ* state. For such purpose, a thin layer of saturated brine, prepared from the same rock salt, should be applied to the surfaces of the samples prior to the hydrostatic phase

(to correct possible drying), and the evolution of the strain over time should be monitored.

Second, it is important to characterize the rock salt under investigation in a way that helps interpret experimental results. For instance, in addition to common petrophysical measurements, an estimation of the intercrystalline brine would be beneficial, and so would be an estimation of the grain size. Such estimations would help examine the importance of fluid-assisted deformation mechanisms. The best way to quantify these features is through microscopic observations (*e.g.*, SEM/EDS and reflected light), but these techniques are not always available; in that case, an estimation can be obtained as follows. The water content can be evaluated by drying a small amount of material at high temperature, and by performing several mass balances over time. Afterwards, the sample could be ground finely and dried again, to determine whether intracrystalline brine is also present. The grain size can be roughly estimated using the intercept method. Likewise, in order to examine the weight of other deformation mechanisms, it would be beneficial to investigate the presence and size of subgrains, as well as the density of dislocations; for such purposes, microscopic observations are required.

Third, it is important to characterize the mechanical behaviour of rock salt both under low and high stress deviators. It has been shown that extrapolation of results obtained at stress deviators larger than 5 MPa to smaller values underestimates the creep rate by several orders of magnitude. In the last years, we have performed several confined creep tests covering the range $0.13 \leq Q - P \leq 20$ MPa in salt samples from different geographical origins, and new tests will be launched soon (ANR project RockStorHy). In addition, some samples have been or are being tested in the *Altaussee* and *Varangéville* salt mines under low and intermediate stress deviators, and a cross-check creep test in the laboratory is about to start under conditions similar to those at *Altaussee* ($T = 8$ °C, 68%RH, $P = 0.1$ MPa [confined]). The target of this test is to make sure that the results at our laboratory and at the mines are comparable, so that all test results can be combined to infer a constitutive law covering the relevant stress range for field applications. The conditions in the mines are ideal to test low stress levels (very constant temperature and humidity, and reduced cost as compared to a laboratory test), but it is important to ensure that the test conditions reproduce the field situation (in particular, it would be more suitable if the samples were undrained and confined).

Fourth, from a phenomenological point of view, it is important to characterize the behaviour of rock salt along different loading paths, covering the ranges expected *in situ*. This guideline embraces number 3, but is broader: in addition to several temperatures (at low and high stress levels), compressive as well as tensile states of stress should be investigated further, and also true triaxial conditions. It has been shown that digital image correlation is a promising technique to characterize the tensile response during Brazilian tests, and I plan to examine this technique more deeply, combined with numerical modeling. Besides, although not shown in this manuscript, we have recently performed creep tests under triaxial extension, and modeling of different loading paths is underway to validate the rheological developments.

These guidelines, combined with improved experimental procedures (for instance, we are currently working on the use of tighter membranes and long-lasting strain gauges), should lead to a better characterization of the material. However, the temporal extrapolation is still unresolved. This aspect, and some perspectives on THM coupling, are presented in the next two sections.

4.1 Towards more physics

Rock salt is a viscoplastic material and as a result, even if laboratory characterization includes different loading paths in the stress and temperature domains —covering the ranges expected *in situ*— temporal extrapolation is unavoidable. The long-term performance assessment of a nuclear waste repository or an abandoned cavern relies on temporal extrapolation of the observed, short-term response, reflecting the importance of this aspect. It should be noted that the effect of time has to be separated from the effect of other variables (stress, temperature, internal variables). Whether steady state is truly reached is still an open question within the salt mechanics community. Field data, putting uncertainties aside, are not available over long enough periods of time to solve this important concern. In my opinion, the long-term extrapolation should be performed on the basis of the dominant deformation mechanisms, or, in other words, on the basis of the physics underneath the observed response. The microscopic scale should be included further in the standard engineering practice (mostly phenomenological), and in the next years I would like to explore this field, first through national and international collaborations with well-known experts, and then, possibly, through skills development within our laboratory. The ANR project RockStorHy as well as some informal international collaborations are valuable starting points. I will also explore available data on natural laboratories —such as salt domes and salt glaciers— as they could provide additional information on long-term creep.

4.2 THM coupling with experimental support

THM coupled processes in rock salt are relevant in many scenarios involving nuclear waste disposal and cavern storage, even if the pressure and temperature ranges are not the same. Throughout this manuscript, the characterization of the material has been mainly approached from the thermo-mechanical perspective. Rock salt permeability is near zero in the undisturbed state, and accurate permeability measurements are scarce. Over the years, two main techniques for permeability measurements have raised attention: transient pulse decay on cylindrical samples (Zhang, 2021), and flow between two concentric spaces at different pressures in a spherical sample (Bérest et al., 2001). The latter was developed to avoid well-known boundary effects of the former (lateral leakage between the sample and the jacket that could lead to misinterpretation of the results); however, while it worked satisfactorily with brine (the fluid pressure was increased purposely beyond the least compressive principal stress [the target was to evaluate well closure and cavern abandonment]), gas measurements proved to be difficult (in this case the fluid pressure was smaller than the infiltration threshold, and the flow rates were exceedingly small). A new experimental set-up has been recently designed by our geomechanics team to characterize the gas flow within a low-permeability sample. Flow tests will be coupled with thermo-mechanical tests at different levels of damage. The interest both from academic and industrial partners is evident, as this set-up will be soon be used in a ANR project, a InterCarnot project, and a new Citeph project. I am involved in the tuning and future use of this set-up, and attention will be focused on hydrogen (having high mobility), which is relevant both in salt cavern storage within the framework of the energy transition, and in nuclear waste disposal (H_2 is released in case of corrosion of the waste packages). Different salt origins, containing different amounts of impurities, will be investigated, and the experimental results will support numerical modeling at the sample scale, and simulations of different storage scenarios at the facility scale.

Bibliography

- Aliabadian, Z., Zhao, G.-F., & Russell, A. R. (2019a). Crack development in transversely isotropic sandstone discs subjected to brazilian tests observed using digital image correlation. *International Journal of Rock Mechanics and Mining Sciences*, *119*, 211–221. doi:[10.1016/j.ijrmms.2019.04.004](https://doi.org/10.1016/j.ijrmms.2019.04.004).
- Aliabadian, Z., Zhao, G.-F., & Russell, A. R. (2019b). Failure, crack initiation and the tensile strength of transversely isotropic rock using the brazilian test. *International Journal of Rock Mechanics and Mining Sciences*, *122*, 104073. doi:[10.1016/j.ijrmms.2019.104073](https://doi.org/10.1016/j.ijrmms.2019.104073).
- Alkan, H., Cinar, Y., & Pusch, G. (2007). Rock salt dilatancy boundary from combined acoustic emission and triaxial compression tests. *International Journal of Rock Mechanics and Mining Sciences*, *44*, 108–119. doi:[10.1016/j.ijrmms.2006.05.003](https://doi.org/10.1016/j.ijrmms.2006.05.003).
- Allemandou, X., & Dusseault, M. (1993). Procedures for cyclic creep testing of salt rock, results and discussion. In *3rd Conference Mechanical Behavior of Salt (Saltmech III)* (pp. 207–218). Palaiseau, France.
- Argüello, J., & Rath, J. (2013). Revisiting the 1980’s WIPP Room D and B in-situ experiments: Performing thermo-mechanical simulations of rock salt using a state-of-the-art code suite. In *4th US Rock Mechanics/Geomechanics Symposium* (ARMA 13-370). San Francisco, CA, United States.
- Ashby, M. (1972). A first report on deformation-mechanism maps. *Acta Metallurgica*, *20*, 887–897. doi:[10.1016/0001-6160\(72\)90082-X](https://doi.org/10.1016/0001-6160(72)90082-X).
- Aubertin, M., Yahya, O. M. L., & Julien, M. (1999). Modeling mixed hardening of alkali halides with a modified version of an internal state variables model. *International Journal of Plasticity*, *15*, 1067 – 1088.
- Azabou, M. (2021). *Modélisation et prédiction du comportement macroscopique du sel gemme dans le contexte du stockage souterrain*. Ph.D. thesis École des Mines de Paris.
- Azabou, M., Rouabhi, A., & Blanco-Martín, L. (2021a). Effect of insoluble materials on the volumetric behavior of rock salt. *Journal of Rock Mechanics and Geotechnical Engineering*, *13*, 84–97. doi:[10.1016/j.jrmge.2020.06.007](https://doi.org/10.1016/j.jrmge.2020.06.007).
- Azabou, M., Rouabhi, A., & Blanco-Martín, L. (2021b). On the Representativity of Rock Salt Specimens During Laboratory Tests. *Rock Mechanics and Rock Engineering*, *55*, 2679–2692. doi:[10.1007/s00603-021-02590-0](https://doi.org/10.1007/s00603-021-02590-0).

- Azabou, M., Rouabhi, A., Blanco-Martín, L., Hadj-Hassen, F., Karimi-Jafari, M., & Hévin, G. (2021c). Rock salt behavior: From laboratory experiments to pertinent long-term predictions. *International Journal of Rock Mechanics and Mining Sciences*, *142*, 104588. doi:[10.1016/j.ijrmms.2020.104588](https://doi.org/10.1016/j.ijrmms.2020.104588).
- Azabou, M., Rouabhi, A., Blanco-Martín, L., & Hévin, G. (2022). Effect of impurities in rock salt samples on laboratory tests - consequences on rock mass representativity. In *SMRI Fall Technical Conference* (pp. 1–17). Chester, United Kingdom.
- Azabou, M., Rouabhi, A., Blanco-Martín, L., Tijani, M., & Hadj-Hassen, F. (2020). On the effect of insoluble materials on rock salt dilatancy. In *54th US Rock Mechanics/Geomechanics Symposium* (ARMA 20-1429). Golden, CO, United States.
- Balland, C., Billiotte, J., Tessier, B., Raingeard, A., Hertz, E., Hévin, G., Tribout, D., Thelier, N., Hadj-Hassen, F., Charnavel, Y., & Bigarré, P. (2018). Acoustic monitoring of a thermo-mechanical test simulating withdrawal in a gas storage salt cavern. *International Journal of Rock Mechanics and Mining Sciences*, *111*, 21–32. doi:[10.1016/j.ijrmms.2018.07.023](https://doi.org/10.1016/j.ijrmms.2018.07.023).
- Bays, C. (1962). Use of salt solution cavities for underground storage. In Bersticker, Hoekstra, & Hall (Eds.), *1st World Salt Symposium* (pp. 564–578). Cleveland, OH, United States.
- Bechthold, W., Rothfuchs, T., Poley, A., Ghoreychi, M., Heusermann, S., Gens, A., & Olivella, S. (1999). *Backfilling and sealing of underground repositories for radioactive waste in salt, Phase I (BAMBUS project)*. Technical report EUR 19124 EN Nuclear Science and Technology Commission of the European Communities.
- Bechthold, W., Smailos, E., Heusermann, S., Bollingerfehr, W., Bazargan-Sabet, B., Rothfuchs, T., Kamlot, P., Grupa, J., Olivella, S., & Hansen, F. (2004). *Backfilling and sealing of underground repositories for radioactive waste in salt, Phase II (BAMBUS project)*. Technical report EUR 20621 EN Nuclear Science and Technology Commission of the European Communities.
- Bérest, P., Blum, P., Charpentier, J.-P., Gharbi, H., & Valès, F. (2005). Very slow creep tests on rock samples. *International Journal of Rock Mechanics and Mining Sciences*, *42*, 569–576. doi:[10.1016/j.ijrmms.2005.02.003](https://doi.org/10.1016/j.ijrmms.2005.02.003).
- Bérest, P., & Brouard, B. (2015). Rheological and geometrical reverse creep in salt caverns. In Roberts, Mellegard, & Hansen (Eds.), *8th Conference Mechanical Behavior of Salt (Saltmech VIII)* (pp. 199–208). Rapid City, SD, United States.
- Bérest, P., Brouard, B., & de Greef, V. (2001). *Salt Permeability Testing. The Influence of Permeability and stress on Hollow Salt Samples*. Report SMRI-2008-1 LMS, École Polytechnique, France (prepared for SMRI).
- Bérest, P., Brouard, B., Djakeun-Djizanne, H., & Hévin, G. (2014). Thermomechanical effects of a rapid depressurization in a gas cavern. *Acta Geotechnica*, *9*, 181–186. doi:[10.1007/s11440-013-0233-8](https://doi.org/10.1007/s11440-013-0233-8).
- Bérest, P., Djizanne, H., Brouard, B., & Hévin, G. (2012). Rapid depressurizations: can they lead to irreversible damage ? In *SMRI Spring Technical Conference*. Regina, SK, Canada.

- Bérest, P., Gharbi, H., Blanco-Martín, L., Brouard, B., Brückner, D., DeVries, K., Hévin, G., Hofer, G., Spiers, C. J., & Urai, J. L. (2022). Salt creep: transition between the low and high stress domains. *Rock Mechanics and Rock Engineering*, submitted.
- Bérest, P., Gharbi, H., Brouard, B., Brückner, D., DeVries, K., Hévin, G., Hofer, G., Spiers, C. J., & Urai, J. L. (2019). Very slow creep tests on salt samples. *Rock Mechanics and Rock Engineering*, 52, 2917–2934. doi:[10.1007/s00603-019-01778-9](https://doi.org/10.1007/s00603-019-01778-9).
- Bérest, P., Karimi-Jafari, M., & Brouard, B. (2008). Comportement mécanique à très long terme des mines et cavernes dans le sel gemme: loi de Norton-Hoff ou loi de Lemaître? *Revue Française de Géotechnique*, 124, 45–59. doi:[10.1051/geotech/2008124045](https://doi.org/10.1051/geotech/2008124045).
- Bérest, P., Karimi-Jafari, M., & Brouard, B. (2017). Geometrical versus rheological transient creep closure in a salt cavern. *Comptes Rendus Mécanique*, 345, 735–741. doi:[10.1016/j.crme.2017.09.002](https://doi.org/10.1016/j.crme.2017.09.002).
- Blanco-Martín, L., Azabou, M., Rouabhi, A., & Hadj-Hassen, F. (2021a). *Maîtriser le comportement géomécanique du sel pour optimiser le stockage de gaz en cavités salines*. Technical Report Citeph-20-2018 Centre de Géosciences Mines Paris.
- Blanco-Martín, L., Azabou, M., Rouabhi, A., & Hadj-Hassen, F. (2022a). Phenomenological behavior of rock salt: observations from laboratory work. *International Journal of Rock Mechanics and Mining Sciences*, submitted.
- Blanco-Martín, L., Azabou, M., Rouabhi, A., Hadj-Hassen, F., & Hévin, G. (2022b). Insights from an experimental campaign on rock salt and implications at the cavern scale. In de Bresser, Drury, Fokker, Gazzani, Hanx, Niemeijer, & Spiers (Eds.), *10th Conference Mechanical Behavior of Salt (Saltmech X)* (pp. 119–129). Utrecht, The Netherlands.
- Blanco-Martín, L., Jahangir, E., Rinaldi, A. P., & Rutqvist, J. (2022c). Evaluation of possible reactivation of undetected faults during CO₂ injection. *International Journal of Greenhouse Gas Control*, 121, 103794. doi:[10.1016/j.ijggc.2022.103794](https://doi.org/10.1016/j.ijggc.2022.103794).
- Blanco-Martín, L., Rouabhi, A., Billiotte, J., Hadj-Hassen, F., Tessier, B., Hévin, G., Bolland, C., & Hertz, E. (2018a). Experimental and numerical investigation into rapid cooling of rock salt related to high frequency cycling of storage caverns. *International Journal of Rock Mechanics and Mining Sciences*, 102, 120–130. doi:[10.1016/j.ijrmms.2018.01.008](https://doi.org/10.1016/j.ijrmms.2018.01.008).
- Blanco-Martín, L., Rouabhi, A., & Hadj-Hassen, F. (2021b). Use of salt caverns in the energy transition: Application to Power-to-Gas-Oxyfuel. *Journal of Energy Storage*, 44, 103333. doi:[10.1016/j.est.2021.103333](https://doi.org/10.1016/j.est.2021.103333).
- Blanco-Martín, L., Rutqvist, J., Battistelli, A., & Birkholzer, J. T. (2018b). Coupled processes modeling in rock salt and crushed salt including halite solubility constraints: Application to disposal of heat-generating nuclear waste. *Transport in Porous Media*, 124, 159–182. doi:[10.1007/s11242-018-1057-7](https://doi.org/10.1007/s11242-018-1057-7).
- Blanco-Martín, L., Rutqvist, J., & Birkholzer, J. T. (2015a). Long-term modeling of the thermal-hydraulic-mechanical response of a generic salt repository for heat-generating nuclear waste. *Engineering Geology*, 193, 198–211. doi:[10.1016/j.enggeo.2015.04.014](https://doi.org/10.1016/j.enggeo.2015.04.014).

- Blanco-Martín, L., Rutqvist, J., & Birkholzer, J. T. (2017). Extension of TOUGH-FLAC to the finite strain framework. *Computers & Geosciences*, *108*, 64–71. doi:[10.1016/j.cageo.2016.10.015](https://doi.org/10.1016/j.cageo.2016.10.015).
- Blanco-Martín, L., Rutqvist, J., Birkholzer, J. T., Wolters, R., Rutenberg, M., Zhao, J., & Lux, K.-H. (2014). Comparison of two modeling procedures to evaluate thermal-hydraulic-mechanical processes in a generic salt repository for high-level nuclear waste. In *48th US Rock Mechanics/Geomechanics Symposium* (ARMA 14-7411). Minneapolis, MN, United States.
- Blanco-Martín, L., Rutqvist, J., Doughty, C., Zhang, Y., Finsterle, S., & Oldenburg, C. M. (2015b). iTOUGH2-FLAC modeling of thermal-hydraulic-mechanical processes related to steam-assisted heavy oil recovery from diatomite. In *TOUGH Symposium 2015*. Berkeley, CA, United States.
- Blanco-Martín, L., Rutqvist, J., Doughty, C., Zhang, Y., Finsterle, S., & Oldenburg, C. M. (2016a). Coupled geomechanics and flow modeling of thermally induced compaction in heavy oil diatomite reservoirs under cyclic steaming. *Journal of Petroleum Science and Engineering*, *147*, 474–484. doi:[10.1016/j.petrol.2016.09.002](https://doi.org/10.1016/j.petrol.2016.09.002).
- Blanco-Martín, L., Wolters, R., Rutqvist, J., Lux, K.-H., & Birkholzer, J. T. (2015c). Comparison of two simulators to investigate thermal-hydraulic-mechanical processes related to nuclear waste isolation in saliferous formations. *Computers and Geotechnics*, *66*, 219–229. doi:[10.1016/j.compgeo.2015.01.021](https://doi.org/10.1016/j.compgeo.2015.01.021).
- Blanco-Martín, L., Wolters, R., Rutqvist, J., Lux, K.-H., & Birkholzer, J. T. (2016b). Thermal-hydraulic-mechanical modeling of a large-scale heater test to investigate rock salt and crushed salt behavior under repository conditions for heat-generating nuclear waste. *Computers and Geotechnics*, *77*, 120–133. doi:[10.1016/j.compgeo.2016.04.008](https://doi.org/10.1016/j.compgeo.2016.04.008).
- Boucher, M., Boulanger, D., Saintives, J., & Kuntz, P. (1979). Lacunae and inclusions in the halite from valence and bresse saliniferous basins. In *5th Symposium on Salt* (pp. 21–30). The Northern Ohio Geological Society.
- Brady, B. (1971). An exact solution to the radially end-constrained circular cylinder under triaxial loading. *International Journal of Rock Mechanics and Mining Sciences & Geomechanics Abstracts*, *8*, 165–178. doi:[10.1016/0148-9062\(71\)90007-6](https://doi.org/10.1016/0148-9062(71)90007-6).
- Brouard, B., Bérest, P., Djizanne, H., & Frangi, A. (2012). Mechanical stability of a salt cavern submitted to high-frequency cycles. In Bérest, Ghoreychi, Hadj-Hassen, & Tijani (Eds.), *7th Conference Mechanical Behavior of Salt (Saltmech VII)* (pp. 381–389). Paris, France.
- Callahan, G., Mellegard, K., & Hansen, F. (1991). *Constitutive behavior of reconsolidating crushed salt*. Report SAND-98-0179C RE/SPEC (Prepared for US DOE), Rapid City, SD, United States.
- Carter, J., Hansen, F., Kehrman, R., & Hayes, T. (2011). *A generic salt repository for disposal of waste from a spent nuclear fuel recycle facility*. Report SRNL-RP-2011-00149Rev0 Savannah River National Laboratory, Aiken, SC, United States.

- Clayton, D. J., Bean, J., Argüello Jr, J., Hardin, E., & Hansen, F. (2012). Thermal-mechanical modeling of a generic high-level waste salt repository. In *7th Conference Mechanical Behavior of Salt (Saltmech VII)* (pp. 427–432). Paris, France.
- COMSOL AB (2013). *COMSOL Multiphysics Reference Manual, v4.4*.
- Cosenza, P., Ghoreychi, M., & Bazargan-Sabet, B. (1997). In situ permeability measurement in salt (in French). *Revue Française de Géotechnique*, 79, 73–83. doi:[10.1051/geotech/1997079073](https://doi.org/10.1051/geotech/1997079073).
- Costa, A., Costa, P., Amaral, C., & Poiate Jr., E. (2015). Computer modeling applied in the design of salt caverns for natural gas storage. In Roberts, Mellegard, & Hansen (Eds.), *8th Conference Mechanical Behavior of Salt (Saltmech VIII)* (pp. 265–271). Rapid City, SD, United States.
- Cristescu, N. (1993). A general constitutive equation for transient and stationary creep of rock salt. *International Journal of Rock Mechanics and Mining Sciences & Geomechanics Abstracts*, 30, 125 – 140. doi:[10.1016/0148-9062\(93\)90705-I](https://doi.org/10.1016/0148-9062(93)90705-I).
- Djizanne, H., Bérest, P., & Brouard, B. (2012). Tensile effective stresses in hydrocarbon storage caverns. In *Proceedings SMRI Fall Meeting*. Bremen, Germany.
- Düsterloh, U., Herchen, K., Lux, K.-H., Salzer, K., Günther, R.-G., Minkley, W., Hampel, A., Argüello, J., & Hansen, F. (2015). Joint Project III on the comparison of constitutive models for the mechanical behavior of rock salt III. Extensive laboratory test program with argillaceous salt from WIPP and comparison of test results. In Roberts, Mellegard, & Hansen (Eds.), *8th Conference Mechanical Behavior of Salt (Saltmech VIII)* (pp. 13–21). Rapid City, SD, United States.
- Finsterle, F. (2007). *iTOUGH2 User's Guide*. Report LBNL-40040 Lawrence Berkeley National Laboratory. URL: <https://itough2.lbl.gov/itough2-users-guide/>.
- Fokker, P. (1995). *The behaviour of salt and salt caverns*. Ph.D. thesis TU Delft.
- Frost, H., & Ashby, M. (1982). *Deformation-mechanism Maps*. New York: Pergamon Press.
- Gharbi, H., Bérest, P., Blanco-Martín, L., & Brouard, B. (2020). Determining upper and lower bounds for steady state strain rate during a creep test on a salt sample. *International Journal of Rock Mechanics and Mining Sciences*, 134, 104452. doi:[10.1016/j.ijrmms.2020.104452](https://doi.org/10.1016/j.ijrmms.2020.104452).
- Gillhaus, A. (2007). Natural gas storage in salt caverns - present status, developments and future trends in Europe. In *Proceedings SMRI Fall Meeting*. Basel, Switzerland.
- Günther, R.-G., & Salzer, K. (2012). Advanced strain-hardening approach: a powerful creep model for rock salt with dilatancy, strength and healing. In Bérest, Ghoreychi, Hadj-Hassen, & Tijani (Eds.), *7th Conference Mechanical Behavior of Salt (Saltmech VII)* (pp. 13–22). Paris, France.
- Hamami, M. (1993). *Rhéologie du sel gemme: application à la conception des dépôts souterrains des déchets nucléaires*. Ph.D. thesis École des Mines de Paris.
- Hampel, A., Günther, R.-M., Salzer, K., Minkley, W., Pudewills, A., Yildirim, S., Rokahr, R., Missal, A. G. C., Stahlmann, J., Herchen, K., & Lux, K.-H. (2015). Joint project III on the comparison of constitutive models for the mechanical behavior of rock salt, I. Overview and

- results from model calculations of healing of rock salt. In Roberts, Mellegard, & Hansen (Eds.), *8th Conference Mechanical Behavior of Salt (Saltmech VIII)* (pp. 349–359). Rapid City, SD, United States.
- Hampel, A., Hansen, F., Salzer, K., Minkley, W., Lux, K.-H., Herchen, K., Pudewills, A., Yildirim, S., Staudtmeister, K., Rokahr, R. et al. (2013). Benchmark Calculations of the Thermo-Mechanical Behavior of Rock Salt—Results from a US-German Joint Project. In *47th US Rock Mechanics/Geomechanics Symposium* (ARMA 13-456). San Francisco, CA, United States.
- Hampel, A., & Hunsche, U. (1999). Extrapolation of creep of rock salt with the composite model. In Cristescu, Reginald Hardy Jr, & Simionescu (Eds.), *5th Conference Mechanical Behavior of Salt (Saltmech V)* (pp. 193–207). Bucharest, Romania.
- Hansen, F. D. (2008). Disturbed Rock Zone Geomechanics at the Waste Isolation Pilot Plant. *International Journal of Geomechanics*, *8*, 30–38. doi:[10.1061/\(ASCE\)1532-3641\(2008\)8:1\(30\)](https://doi.org/10.1061/(ASCE)1532-3641(2008)8:1(30)).
- Herchen, K., Popp, T., Düsterloh, U., Lux, K.-H., Salzer, K., Lüdeling, C., Günther, R.-G., Rölke, C., Minkley, W., Hampel, A., Yildirim, S., Staudtmeister, K., Gährken, A., Stahlmann, J., Reedlunn, B., & Hansen, F. (2018). WEIMOS: Laboratory Investigations of Damage Reduction and Creep at Small Deviatoric Stresses in Rock Salt. In Fahland, Hammer, Hansen, Heusermann, Lux, & Minkley (Eds.), *9th Conference Mechanical Behavior of Salt (Saltmech IX)* (pp. 175–192). Hanover, Germany.
- Heusermann, S., Rolfs, O., & Schmidt, U. (2003). Nonlinear finite-element analysis of solution mined storage caverns in rock salt using the LUBBY2 constitutive model. *Computers & Structures*, *81*, 629 – 638. doi:[10.1016/S0045-7949\(02\)00415-7](https://doi.org/10.1016/S0045-7949(02)00415-7).
- Hévin, G., Baland, C., Billiotte, J., Tessier, B., Hadj-Hassen, F., Rouabhi, A., Blanco-Martín, L., Bonnard, C., Staudtmeister, K., Leuger, B., Zapf, D., Hertz, E., Tribout, D., & Thelier, N. (2016). *Perform a Thermo-mechanical Test in a Salt Mine*. Technical Report RR2016-1 SMRI.
- Hévin, G., Baland, C., Billiotte, J., Tessier, F., Hadj-Hassen, F., Rouabhi, A., Blanco-Martín, L., Staudtmeister, K., Leuger, B., Zapf, D., Hertz, E., Tribout, D., & Thelier, N. (2017). Expérience de fissuration thermique dans une mine de sel. In M. Gasc-Barbier, V. Merrien-Soukatchoff, & P. Bérest (Eds.), *Manuel de mécanique des roches. Tome V - Thermomécanique des roches* (pp. 415–427). Presses des mines.
- Hoather, H., & Challinor, D. (1994). The use of salt cavities for the disposal of waste. In *Proceedings SMRI Fall Meeting*. Hanover, Germany.
- Hou, Z. (2003). Mechanical and hydraulic behavior of rock salt in the excavation disturbed zone around underground facilities. *International Journal of Rock Mechanics and Mining Sciences*, *40*, 725–738. doi:[10.1016/S1365-1609\(03\)00064-9](https://doi.org/10.1016/S1365-1609(03)00064-9).
- Hudson, J., Brown, E., & Rummel, F. (1972). The controlled failure of rock discs and rings loaded in diametral compression. *International Journal of Rock Mechanics and Mining Sciences & Geomechanics Abstracts*, *9*, 241–248. doi:[10.1016/0148-9062\(72\)90025-3](https://doi.org/10.1016/0148-9062(72)90025-3).

- Hunsche, U. (1984). Measurement of creep in rock salt at small strain rates. In Reginald Hardy Jr., & Langer (Eds.), *2nd Conference Mechanical Behavior of Salt (Saltmech II)* (pp. 187–196). Hanover, Germany.
- Hunsche, U. (1993). Failure behaviour of rock salt underground cavities. In *7th Symposium on Salt* (pp. 59–65 (vol. 1)).
- Hunsche, U., & Hampel, A. (1999). Rock salt — the mechanical properties of the host rock material for a radioactive waste repository. *Engineering Geology*, *52*, 271–291. doi:[10.1016/S0013-7952\(99\)00011-3](https://doi.org/10.1016/S0013-7952(99)00011-3).
- Hunsche, U., & Schulze, O. (1994). Das Kriechverhalten von Steinsalz. *Kali & Steinsalz*, *11*, 238–255.
- Hurtado, L. D., Knowles, M. K., Kelley, V. A., Jones, T. L., Ogintz, J. B., & Pfeifle, T. W. (1997). *WIPP shaft seal system parameters recommended to support compliance calculations*. Report SAND-97-1287 Sandia National Laboratories Albuquerque, NM, United States. doi:[10.2172/563218](https://doi.org/10.2172/563218).
- Itasca (2009). *FLAC^{3D} (Fast Lagrangian Analysis of Continua in 3 Dimensions, v4)*. Itasca Consulting Group, Minneapolis, MN, United States.
- Javeri, V., & Baltes, B. (2008). Three dimensional analyses of combined gas, heat and nuclide transport in a repository considering thermo-hydro-geo-mechanical processes. In *12th International Conference on Computer Methods and Advances in Geomechanics IACMAG* (p. 1264 – 1271). Goa, India.
- Karimi-Jafari, M., Gatelier, N., Brouard, B., Bérest, P., & Djizanne, H. (2011). Multi-cycle storage in salt caverns. In *Proceedings SMRI Fall Meeting*. York, United Kingdom.
- Khaledi, K., Mahmoudi, E., Datcheva, M., & Schanz, T. (2016). Analysis of compressed air storage caverns in rock salt considering thermo-mechanical cyclic loading. *Environmental Earth Sciences*, *75*. doi:[10.1007/s12665-016-5970-1](https://doi.org/10.1007/s12665-016-5970-1).
- Kim, J., Tchelepi, H., & Juanes, R. (2011a). Stability and convergence of sequential methods for coupled flow and geomechanics: Drained and undrained splits. *Computer Methods in Applied Mechanics and Engineering*, *200*, 2094–2116. doi:[10.1016/j.cma.2011.02.011](https://doi.org/10.1016/j.cma.2011.02.011).
- Kim, J., Tchelepi, H., & Juanes, R. (2011b). Stability and convergence of sequential methods for coupled flow and geomechanics: Fixed-stress and fixed-strain splits. *Computer Methods in Applied Mechanics and Engineering*, *200*, 1591–1606. doi:[10.1016/j.cma.2010.12.022](https://doi.org/10.1016/j.cma.2010.12.022).
- Kock, I., Larue, J., Fischer, H., Frieling, G., Navarro, M., & Seher, H. (2013). Results from one and two phase fluid flow calculations within the Preliminary Safety Analysis of the Gorleben Site–13310. In *WM2013 Conference*. Phoenix, AZ, United States.
- Kröhn, K., Zhang, C., Wolf, J., Stührenberg, D., Jobmann, M., von Borstel, L., & Lerch, C. (2012). The compaction behaviour of salt backfill at low porosities. In *7th Conference Mechanical Behavior of Salt (Saltmech VII)* (pp. 155–162). Paris, France.
- Labaune, P. (2018). *Comportement thermomécanique du sel gemme : Application au dimensionnement des cavités*. Ph.D. thesis École des Mines de Paris.

- Labaune, P., Rouabhi, A., Tijani, M., Blanco-Martín, L., & You, T. (2018). Dilatancy criteria for salt cavern design: A comparison between stress- and strain-based approaches. *Rock Mechanics and Rock Engineering*, *51*, 599–611. doi:[10.1007/s00603-017-1338-4](https://doi.org/10.1007/s00603-017-1338-4).
- Lerch, C., Bollingerfehr, W., Filbert, W., & Zhang, Q. (2012). Thermo-mechanical analyses for evaluating a HLW-repository concept. In *7th Conference Mechanical Behavior of Salt (Saltmech VII)* (pp. 433–442). Paris, France.
- Liu, J., Lyu, C., Lu, G., Shi, X., Li, H., Liang, C., & Deng, C. (2022). Evaluating a new method for direct testing of rock tensile strength. *International Journal of Rock Mechanics and Mining Sciences*, *160*, 105258. doi:[10.1016/j.ijrmms.2022.105258](https://doi.org/10.1016/j.ijrmms.2022.105258).
- Lowe, M., & Knowles, N. (1989). *COSA II further benchmark exercises to compare geomechanical computer codes for salt*. Report EUR 12135 EN Commission of the European Communities.
- Lux, K.-H., Lerche, S., & Dyogtyev, O. (2018). Intense damage processes in salt rocks – a new approach for laboratory investigations, physical modelling and numerical simulation. In Fahland, Hammer, Hansen, Heusermann, Lux, & Minkley (Eds.), *9th Conference Mechanical Behavior of Salt (Saltmech IX)* (pp. 47–67). Hanover, Germany.
- Merar, J. (1999). *Élaboration d'une loi de comportement pour le sel gemme*. Ph.D. thesis École des Mines de Paris.
- Minkley, W., Knauth, M., Fabig, T., & Farag, N. (2015). Stability and integrity of salt caverns under consideration of hydro-mechanical loading. In Roberts, Mellegard, & Hansen (Eds.), *8th Conference Mechanical Behavior of Salt (Saltmech VIII)* (pp. 217–227). Rapid City, SD, United States.
- Minkley, W., & Popp, T. (2010). Final Disposal in Rock Salt-Geomechanical Assessment of the Barrier Integrity. In *44th US Rock Mechanics/Geomechanics Symposium* (ARMA 10-492). Salt Lake City, UT, United States.
- Moës, N., Dolbow, J., & Belytschko, T. (1999). A Finite element method for crack growth without remeshing. *International Journal for Numerical Methods in Engineering*, *46*, 131–150. doi:[10.1002/\(SICI\)1097-0207\(19990910\)46:1<131::AID-NME726>3.0.CO;2-J](https://doi.org/10.1002/(SICI)1097-0207(19990910)46:1<131::AID-NME726>3.0.CO;2-J).
- Munson, D. (1997). Constitutive model of creep in rock salt applied to underground room closure. *International Journal of Rock Mechanics and Mining Sciences*, *34*, 233 – 247. doi:[10.1016/S0148-9062\(96\)00047-2](https://doi.org/10.1016/S0148-9062(96)00047-2).
- Munson, D., DeVries, K., & Callahan, G. (1990). Comparison of calculations and in situ results for a large, heated test room at the Waste Isolation Pilot Plant (WIPP). In *31st US Symposium on Rock Mechanics* (p. 389 – 396). Golden, CO, United States.
- Munson, D. E., & Dawson, P. R. (1981). Salt constitutive modeling using mechanism maps. In Reginald Hardy Jr., & M. Langer (Eds.), *1st Conference Mechanical Behavior of Salt (Saltmech I)* (pp. 717–737). University Park, PA, United States.
- Olivella, S., & Gens, A. (2002). A constitutive model for crushed salt. *International Journal for Numerical and Analytical Methods in Geomechanics*, *26*, 719–746. doi:[10.1002/nag.220](https://doi.org/10.1002/nag.220).

- Ozarslan, A. (2012). Large-scale hydrogen energy storage in salt caverns. *International Journal of Hydrogen Energy*, 37, 14265 – 14277. doi:[10.1016/j.ijhydene.2012.07.111](https://doi.org/10.1016/j.ijhydene.2012.07.111).
- Pan, B., Qian, K., Xie, H., & Asundi, A. (2009). Two-dimensional digital image correlation for in-plane displacement and strain measurement: a review. *Measurement Science and Technology*, 20, 062001. doi:[10.1088/0957-0233/20/6/062001](https://doi.org/10.1088/0957-0233/20/6/062001).
- Peach, C. (1991). *Influence of deformation on the fluid transport properties of salt rocks*. Ph.D. thesis Utrecht University.
- Peach, C. J., & Spiers, C. J. (1996). Influence of crystal plastic deformation on dilatancy and permeability development in synthetic salt rock. *Tectonophysics*, 256, 101–128. doi:[10.1016/0040-1951\(95\)00170-0](https://doi.org/10.1016/0040-1951(95)00170-0).
- Pellizzaro, C., Bérest, P., Brouard, B., & Karimi-Jafari, M. (2012). Nouvelles problématiques posées par le cyclage thermo-mécanique en cavités salines. In *Proceedings Journées Nationales de Géotechnique et de Géologie de l'Ingénieur*. Nancy, France.
- Peng, S. (1971). Stresses within elastic circular cylinders loaded uniaxially and triaxially. *International Journal of Rock Mechanics and Mining Sciences & Geomechanics Abstracts*, 8, 399–432. doi:[10.1016/1365-1609\(71\)90009-8](https://doi.org/10.1016/1365-1609(71)90009-8).
- Popp, T., & Kern, H. (1998). Ultrasonic wave velocities, gas permeability and porosity in natural and granular rock salt. *Physics and Chemistry of the Earth*, 23, 373 – 378.
- Popp, T., Kern, H., & Schulze, O. (2001). Evolution of dilatancy and permeability in rock salt during hydrostatic compaction and triaxial deformation. *Journal of Geophysical Research: Solid Earth*, 106, 4061–4078. doi:[10.1029/2000JB900381](https://doi.org/10.1029/2000JB900381).
- Popp, T., & Minkley, W. (2010). Salt barrier integrity during gas pressure build-up in a radioactive waste repository – Implications from lab and field investigations. In *44th US Rock Mechanics/Geomechanics Symposium* (ARMA 10-493). Salt Lake City, UT, United States.
- Popp, T., Minkley, W., Salzer, K., & Schulze, O. (2012). Gas transport properties of rock salt–synoptic view. In *7th Conference Mechanical Behavior of Salt (Saltmech VII)* (pp. 143–153). Paris, France.
- Popp, T., & Salzer, K. (2012). Microstructural deformation processes in granular salt during mechanical compaction. In *3rd US/German Workshop on Salt Repository Research, Design and Operation Meet. Abstr.* (p. 21). Albuquerque, NM, United States.
- Pouya, A. (2000). Micro–macro approach for the rock salt behaviour. *European Journal of Mechanics - A/Solids*, 19, 1015–1028. doi:[10.1016/S0997-7538\(00\)00204-7](https://doi.org/10.1016/S0997-7538(00)00204-7).
- Pruess, K., Oldenburg, C., & Moridis, G. (2012). *TOUGH2 User's Guide, v2*. Lawrence Berkeley National Laboratory University of California, Berkeley, United States.
- Pudewills, A., Müller-Hoeppe, N., & Papp, R. (1995). Thermal and thermomechanical analyses for disposal in drifts of a repository in rock salt. *Nuclear Technology*, 112, 79–88. doi:[10.13182/NT95-A15853](https://doi.org/10.13182/NT95-A15853).

- Raj, R. (1982). Creep in polycrystalline aggregates by matter transport through a liquid phase. *Journal of Geophysical Research: Solid Earth*, 87, 4731–4739. doi:10.1029/JB087iB06p04731.
- Reedlunn, B. (2022). A new rock salt constitutive model with back stress and drag stress hardening. In de Bresser, Drury, Fokker, Gazzani, Hanx, Niemeijer, & Spiers (Eds.), *10th Conference Mechanical Behavior of Salt (Saltmech X)*. Utrecht, The Netherlands.
- Roberts, L. A., Buchholz, S. A., Mellegard, K. D., & Düsterloh, U. (2015). Cyclic loading effects on the creep and dilation of salt rock. *Rock Mechanics and Rock Engineering*, 48, 2581–2590. doi:10.1007/s00603-015-0845-4.
- Rouabhi, A. (2019). *Problèmes de thermodynamique et de thermo-hydro-mécanique associés à l'exploitation du sous-sol*. Habilitation à diriger des recherches Sorbonne Université, France.
- Rouabhi, A., Labaune, P., Tijani, M., Gatelier, N., & Hévin, G. (2019). Phenomenological behavior of rock salt: On the influence of laboratory conditions on the dilatancy onset. *Journal of Rock Mechanics and Geotechnical Engineering*, 11, 723–738. doi:10.1016/j.jrmge.2018.12.011.
- Rutqvist, J., & Tsang, C.-F. (2003). TOUGH-FLAC: a numerical simulator for analysis of coupled thermal-hydrologic-mechanical processes in fractured and porous geological media under multi-phase flow conditions. In *TOUGH Symposium*. Berkeley, CA, United States.
- Rutter, E. H., & Elliott, D. (1976). The Kinetics of Rock Deformation by Pressure Solution [and Discussion]. *Philosophical Transactions of the Royal Society of London. Series A, Mathematical and Physical Sciences*, 283, 203–219. URL: <http://www.jstor.org/stable/74639>.
- Salzer, K., Günther, R.-G., Minkley, W., Naumann, D., Popp, T., Hampel, A., Lux, K.-H., Herchen, K., Düsterloh, U., Argüello, J., & Hansen, F. (2015). Joint Project III on the comparison of constitutive models for the mechanical behavior of rock salt III. Extensive laboratory test program with clean salt from WIPP. In Roberts, Mellegard, & Hansen (Eds.), *8th Conference Mechanical Behavior of Salt (Saltmech VIII)* (pp. 3–12). Rapid City, SD, United States.
- Schulze, O., Popp, T., & Kern, H. (2001). Development of damage and permeability in deforming rock salt. *Engineering Geology*, 61, 163 – 180. doi:10.1016/S0013-7952(01)00051-5.
- Senseny, P. (1981). Specimen size and history effects on creep of salt. In Reginald Hardy Jr., & Langer (Eds.), *1st Conference Mechanical Behavior of Salt (Saltmech I)* (pp. 369–379). University Park, PA, United States.
- Senseny, P., & Fossum, A. (1996). Testing to estimate the Munson-Dawson parameters. In Aubertin, & Reginald Hardy Jr. (Eds.), *4th Conference Mechanical Behavior of Salt (Saltmech IV)* (pp. 263–276). Montreal, Canada.
- Serbin, K., Ślizowski, J., Urbańczyk, K., & Nagy, S. (2015). The influence of thermodynamic effects on gas storage cavern convergence. *International Journal of Rock Mechanics and Mining Sciences*, 79, 166 – 171. doi:10.1016/j.ijrmms.2015.08.017.
- Sheng, D., Westerberg, B., Mattsson, H., & Axelsson, K. (1997). Effects of end restraint and strain rate in triaxial tests. *Computers and Geotechnics*, 21, 163–182. doi:10.1016/S0266-352X(97)00021-9.

- Shilko, S. (2002). The role of friction in mechanical tests of materials. *Journal of Friction and Wear*, 23, 98–102.
- Sicsic, P., & Bérest, P. (2014). Thermal cracking following a blowout in a gas-storage cavern. *International Journal of Rock Mechanics and Mining Sciences*, 71, 320 – 329. doi:[10.1016/j.ijrmms.2014.07.014](https://doi.org/10.1016/j.ijrmms.2014.07.014).
- Sjaardema, G., & Krieg, R. D. (1987). *A constitutive model for the consolidation of WIPP crushed salt and its use in analyses of backfilled shaft and drift configurations*. Report SAND-87-1977 Sandia National Laboratories Albuquerque, NM, United States.
- Sobolik, S., & Ehgartner, B. (2007). Effect of cavern shapes on cavern and well integrity for the strategic petroleum reserve. In Wallner, Lux, Minkley, & Hardy-Jr (Eds.), *6th Conference Mechanical Behavior of Salt (Saltmech VI)* (pp. 353–361). Hanover, Germany.
- Spiers, C., & Carter, N. (1996). Microphysics of rocksalt in nature. In *4th Conference Mechanical Behavior of Salt (Saltmech IV)* (pp. 115–128). Montreal, Canada.
- Spiers, C. J., Schutjens, P. M. T. M., Brzesowsky, R. H., Peach, C. J., Liezenberg, J. L., & Zwart, H. J. (1990). Experimental determination of constitutive parameters governing creep of rocksalt by pressure solution. *Geological Society, London, Special Publications*, 54, 215–227. doi:[10.1144/GSL.SP.1990.054.01.21](https://doi.org/10.1144/GSL.SP.1990.054.01.21).
- Staudtmeister, K., & Rokahr, R. (1997). Rock mechanical design of storage caverns for natural gas in rock salt mass. *International Journal of Rock Mechanics and Mining Sciences*, 34, 300.e1–300.e13. doi:[10.1016/S1365-1609\(97\)00199-8](https://doi.org/10.1016/S1365-1609(97)00199-8).
- Staudtmesiter, K., & Schmidt, T. (2000). Comparison of different methods for the estimation of primary stresses in rock salt mass with respect to cavern design. In Geertman (Ed.), *8th World Salt Symposium* (pp. 331–335). The Hague, The Netherlands.
- Stone, C., Holland, J., Bean, J., & Argüello, J. (2010). Coupled thermal-mechanical analyses of a generic salt repository for high level waste. In *44th US Rock Mechanics/Geomechanics Symposium* (ARMA 10-180). Salt Lake City, UT, United States.
- Stormont, J. (1997). In situ gas permeability measurements to delineate damage in rock salt. *International Journal of Rock Mechanics and Mining Sciences*, 34, 1055 – 1064. doi:[10.1016/S1365-1609\(97\)90199-4](https://doi.org/10.1016/S1365-1609(97)90199-4).
- Stormont, J., & Daemen, J. (1992). Laboratory study of gas permeability changes in rock salt during deformation. *International Journal of Rock Mechanics and Mining Sciences & Geomechanics Abstracts*, 29, 325–342. doi:[10.1016/0148-9062\(92\)90510-7](https://doi.org/10.1016/0148-9062(92)90510-7).
- Sutton, M. A., Matta, F., Rizos, D., Ghorbani, R., Rajan, S., Mollenhauer, D. H., Schreier, H. W., & Lasprilla, A. O. (2016). Recent Progress in Digital Image Correlation: Background and Developments since the 2013 W M Murray Lecture. *Experimental Mechanics*, 57, 1–30. doi:[10.1007/s11340-016-0233-3](https://doi.org/10.1007/s11340-016-0233-3).
- Thoms, R., & Gehle, R. (2000). A brief history of salt cavern use. In Geertman (Ed.), *8th World Salt Symposium* (pp. 207–214). The Hague, The Netherlands.

- Thorel, L., & Ghoreychi, M. (1996). Plasticity and damage of rocksalt (in French). *Revue Française de Géotechnique*, 77, 3–17. doi:[10.1051/geotech/2008124045](https://doi.org/10.1051/geotech/2008124045).
- Tijani, M. (2008). *Contribution à l'étude thermomécanique des cavités réalisées par lessivage dans des formations géologiques salines*. Habilitation à diriger des recherches Université Pierre et Marie Curie - Paris VI.
- Tijani, M., Hadj-Hassen, F., & Gatelier, N. (2009). Improvement of Lemaitre's creep law to assess the salt mechanical behavior for a large range of the deviatoric stress. In *9th International Symposium on Salt* (pp. 135–147). Beijing, China.
- Tijani, M., Vouille, G., & Hugout, B. (1983). Le sel gemme en tant que liquide visqueux. In *Congrès International de Mécanique des Roches* (pp. 241–246). Melbourne, Australia.
- Tijani, S.-M. (1996). Short description of VIPLEF code. *Developments in Geotechnical Engineering*, 79, 507–511. doi:[10.1016/S0165-1250\(96\)80039-3](https://doi.org/10.1016/S0165-1250(96)80039-3).
- Tounsi, H., Rutqvist, J., Hu, M., Wolters, R., & Blanco-Martín, L. (2022). Numerical Modeling of Coupled Thermal-Hydro-Mechanical Processes in Salt Formations for Geologic Disposal of Large Nuclear Waste Canisters. In *56th US Rock Mechanics/Geomechanics Symposium* (ARMA 22-794). Santa Fe, NM, United States.
- Tsang, C.-F., Stephansson, O., Jing, L., & Kautsky, F. (2009). DECOVALEX Project: from 1992 to 2007. *Environmental Geology*, 57, 1221–1237. doi:[10.1007/s00254-008-1625-1](https://doi.org/10.1007/s00254-008-1625-1).
- Urai, J. L., & Spiers, C. J. (2007). The effect of grain boundary water on deformation mechanisms and rheology of rocksalt during long-term deformation. In M. Wallner, K.-H. Lux, W. Minkley, & H. Hardy (Eds.), *6th Conference Mechanical Behavior of Salt (Saltmech VI)* (pp. 149–158). Hanover, Germany.
- van Keken, P., Spiers, C., van den Berg, A., & Muyzert, E. (1993). The effective viscosity of rocksalt: implementation of steady-state creep laws in numerical models of salt diapirism. *Tectonophysics*, 225, 457–476. doi:[10.1016/0040-1951\(93\)90310-G](https://doi.org/10.1016/0040-1951(93)90310-G).
- Van Sambeek, L. L., Ratigan, J. L., & Hansen, F. D. (1993). Dilatancy of rock salt in laboratory tests. *International Journal of Rock Mechanics and Mining Sciences & Geomechanics Abstracts*, 30, 735–738. doi:[10.1016/0148-9062\(93\)90015-6](https://doi.org/10.1016/0148-9062(93)90015-6).
- Wawersik, W., & Zeuch, D. (1986). Modeling and mechanistic interpretation of creep of rock salt below 200 °C. *Tectonophysics*, 121, 125–152. doi:[10.1016/0040-1951\(86\)90040-5](https://doi.org/10.1016/0040-1951(86)90040-5).
- Wieczorek, K., Czaikowski, O., Zhang, C.-L., & Stührenberg, D. (2012). Recent experimental and modeling results on crushed salt consolidation. In *3rd US/German Workshop on Salt Repository Research, Design and Operation Meet. Abstr.* (p. 22). Albuquerque, NM, United States.
- Wieczorek, K., & Schwarzianeck, P. (2001). *Untersuchungen zur hydraulisch wirksamen Auflockerungszone um Endlagerbereiche im Salinar in Abhängigkeit vom Hohlraumabstand und Spannungszustand (ALOHA 2)*. Final report BMBF Res. Proj. 02E9118 GRS.

- Wolters, R., Lux, K.-H., & Düsterloh, U. (2012). Evaluation of rock salt barriers with respect to tightness: Influence of thermomechanical damage, fluid infiltration and sealing/healing. In *7th Conference Mechanical Behavior of Salt (Saltmech VII)* (pp. 417–426). Paris, France.
- Xu, T., & Arson, C. (2022). Self-consistent approach for modeling coupled elastic and visco-plastic processes induced by dislocation and pressure solution. *International Journal of Solids and Structures*, *238*, 111376. doi:[10.1016/j.ijsolstr.2021.111376](https://doi.org/10.1016/j.ijsolstr.2021.111376).
- Zapf, D., Staudtmeister, K., & Rokahr, R. (2012). Analysis of thermal induced fractures in rock salt. In *SMRI Spring Technical Conference*. Regina, SK, Canada.
- Zhang, D. (2021). *Étude expérimentale des propriétés de transfert de gaz et des effets de couplage dans des roches salines*. Ph.D. thesis Centrale Lille.
- Zhu, C., Pouya, A., & Arson, C. (2015). Micro-macro analysis and phenomenological modelling of salt viscous damage and application to salt caverns. *Rock Mechanics and Rock Engineering*, *48*, 2567–2580. doi:[10.1007/s00603-015-0832-9](https://doi.org/10.1007/s00603-015-0832-9).

Appendix

Appendix A

Curriculum Vitæ

Laura Blanco Martín

Centre de Géosciences, Mines Paris, PSL University

35 rue Saint-Honoré, 77300 Fontainebleau (France)

laura.blanco_martin@minesparis.psl.eu

+33 1 64 69 49 21

Born 05/21/1985

Education

- 11/2008-03/2012** PhD, *Centre de Géosciences* Mines Paris (France)
Topic: Theoretical and experimental study of fully grouted rockbolts and cablebolts under axial loads
- 09/2006-06/2008** Civil engineering degree, Mines Paris (France)
Admission sur titres (AST), double degree exchange program with the University of Oviedo (Spain)
Minor: underground engineering and management
- 10/2003-06/2008** School of Mines, University of Oviedo (Spain)
Minors: energy, underground engineering

Professional Experience

- 01/2016-present** *Centre de Géosciences*, Mines Paris (France)
Researcher-lecturer, Geomechanics & Engineering Geology team
Experimental, theoretical and numerical work on rock salt rheology and salt cavern storage. Numerical work on CO₂ sequestration and induced seismicity
- 08/2012-12/2015** Lawrence Berkeley National Laboratory (USA)
Post-doctoral fellow, Energy Geosciences Division
Theoretical and numerical investigation into coupled THM processes (nuclear waste disposal in rock salt, unconventional reservoirs, CO₂ sequestration and induced seismicity)
- 11/2008-03/2012** EU Research Fund for Coal and Steel (RFCS), Mines Paris (France)
PhD student, Prosafercoal project (Increased PROductivity and SAFety of European COALmines by advanced techniques and planning tools enabling an improved strata control of the face-roadway junction)

Teaching

- MS GAZ** Advanced Master's Degree in Gas Engineering and Management (Mines Paris). Lecture on thermodynamical and geomechanical aspects of gas storage in salt caverns
- MIG** *Métiers de l'Ingénieur Généraliste* (Mines Paris). Modules on salt cavern storage (geomechanics, thermodynamics) to 1st year students
- Stage 2A, UE14** Modules on rock reinforcement, coupled THM processes and underground storage to 1st and 2nd year students (Mines Paris)

Invited Talks

- 2013** *Étude théorique et expérimentale du boulonnage à ancrage réparti sous sollicitations axiales* (Comité Français de Mécanique des Roches, Paris)
- 2014** Long-term THM modeling for nuclear waste disposal in salt with updated TOUGH-FLAC (Modeling Forum, LBNL, USA)
- 2014** *Sel gemme : modélisation THMC et développement d'un modèle d'écoulement pour la saumure* (Laboratoire de Mécanique des Solides, École Polytechnique, France)
- 2022** *Stockage de l'hydrogène en cavité saline, perspectives, risques* (Centre Energy4Climate, IP Paris)

Participation to PhD supervision

2014-2015	M. Miah, PhD candidate at the University of Mississippi on the topic “Development of a dynamic coupled hydro-geomechanical code and its application to induced seismicity”
2016-2017	P. Labaune, PhD candidate at Mines Paris on the topic “ <i>Comportement thermo-mécanique du sel gemme : Application au dimensionnement des cavités</i> ”
2017-2021	M. Azabou, PhD candidate at Mines Paris on the topic “ <i>Modélisation et prédiction du comportement macroscopique du sel gemme dans le contexte du stockage souterrain</i> ”

Main Research Projects

ROCKSTORHY	Multiscale investigation of ROCKsalt flow for underground STORage of HYdrogen (funded by ANR). Experimental, theoretical and experimental work to foster hydrogen storage in salt caverns and advance the understanding of rock salt rheology
MissCO₂	<i>Modélisation de la Sismicité induite pour le Stockage de CO₂</i> (funded by ANR through Géodénergies). Numerical investigations into coupled THM processes related to CO ₂ sequestration and induced seismicity and development of a sequential coupling scheme
Citeph-20-2018	Maîtriser le comportement géomécanique du sel pour optimiser le stockage de gaz en cavités salines (funded by Citeph innovation program). Large experimental campaign on several salts to improve measurement devices and investigate rock salt rheology under different thermo-mechanical load paths. Improvement of constitutive laws on the basis of the experimental results
SMILE	Multidisciplinary and Multiscale approach for coupled processes induced by geo-Energies (EU Doctoral Network, Marie Skłodowska-Curie action). Network of universities and companies across Europe to train 11 PhD students in the context of geo-energies and CCUS
FLUIDSTORY	Massive and reversible underground storage of FLUIDs (O ₂ , CO ₂ , CH ₄) for energy STORage and recoverY (funded by ANR). Theoretical and numerical work to investigate storage of pure fluids and mixtures in salt caverns

Miscellaneous Activities

Seminars	Organization of monthly scientific seminars at LBNL (Modeling Forum, 2014-2015). At Mines Paris, organization of 3 scientific international seminars and a one-day workshop involving two local research centers. Member of the organizing committee of a one-week seminar on underground storage and geoennergies (June 2023)
CFMR	<i>Comité Français de Mécanique des Roches</i> (French ISRM National Group). Member of the board and member of the <i>CFMR-Jeunes</i> group
Conferences	Member of the organizing committee of the TOUGH2015 Symposium and member of the organizing committee of the CouFrac conferences (2018, 2020, 2022). Member of the scientific advisory committee for DECOVALEX 2023
Editorial tasks	Member of the Editorial Board of the International Journal of Rock Mechanics and Mining Sciences since 2019. Coordination of two Special Issues (Computers & Geosciences in 2017 and Tunnelling and Underground Space Technology in 2020). Reviewer role for different journals since 2013
Examiner	Served in the thesis committee of Dongmei Zhang (Centrale Lille, France, 2021) and in a CNU committee to select a lecturer-researcher at Mines Nancy (France, 2022)

Journal Papers (*Underlined authors correspond to supervised PhD students*)

- [Art1] Ahamada, S., Valtz, A., Chabab, S., **Blanco-Martín, L.**, & Coquelet, C. (2020). Experimental Density Data of Three Carbon Dioxide and Oxygen Binary Mixtures at Temperatures from 276 to 416 K and at Pressures up to 20 MPa. *Journal of Chemical & Engineering Data*, 65, 5313–5327. doi:10.1021/acs.jced.0c00484.
- [Art2] Azabou, M., Rouabhi, A., & **Blanco-Martín, L.** (2021a). Effect of insoluble materials on the

volumetric behavior of rock salt. *Journal of Rock Mechanics and Geotechnical Engineering*, 13, 84–97. doi:[10.1016/j.jrmge.2020.06.007](https://doi.org/10.1016/j.jrmge.2020.06.007).

- [Art3] [Azabou, M., Rouabhi, A., & Blanco-Martín, L. \(2021b\)](#). On the Representativity of Rock Salt Specimens During Laboratory Tests. *Rock Mechanics and Rock Engineering*, 55, 2679–2692. doi:[10.1007/s00603-021-02590-0](https://doi.org/10.1007/s00603-021-02590-0).
- [Art4] [Azabou, M., Rouabhi, A., Blanco-Martín, L., Hadj-Hassen, F., Karimi-Jafari, M., & Hévin, G. \(2021c\)](#). Rock salt behavior: From laboratory experiments to pertinent long-term predictions. *International Journal of Rock Mechanics and Mining Sciences*, 142, 104588. doi:[10.1016/j.ijrmms.2020.104588](https://doi.org/10.1016/j.ijrmms.2020.104588).
- [Art5] [Bérest, P., Gharbi, H., Blanco-Martín, L., Brouard, B., Brückner, D., DeVries, K., Hévin, G., Hofer, G., Spiers, C. J., & Uraï, J. L. \(2022\)](#). Salt creep: transition between the low and high stress domains. *Rock Mechanics and Rock Engineering*, submitted (under review).
- [Art6] [Blanco-Martín, L., Azabou, M., Rouabhi, A., & Hadj-Hassen, F. \(2022a\)](#). Phenomenological behavior of rock salt: observations from laboratory work. *International Journal of Rock Mechanics and Mining Sciences*, submitted (minor revisions).
- [Art7] [Blanco-Martín, L., Hadj-Hassen, F., Tijani, M., & Armand, G. \(2011a\)](#). New numerical modelling of the mechanical long-term behaviour of the GMR gallery in ANDRA’s underground research laboratory. *Physics and Chemistry of the Earth, Parts A/B/C*, 36, 1872–1877. doi:[10.1016/j.pce.2011.07.027](https://doi.org/10.1016/j.pce.2011.07.027).
- [Art8] [Blanco-Martín, L., Jahangir, E., Rinaldi, A. P., & Rutqvist, J. \(2022b\)](#). Evaluation of possible reactivation of undetected faults during CO₂ injection. *International Journal of Greenhouse Gas Control*, 121, 103794. doi:[10.1016/j.ijggc.2022.103794](https://doi.org/10.1016/j.ijggc.2022.103794).
- [Art9] [Blanco-Martín, L., Rouabhi, A., Billiotte, J., Hadj-Hassen, F., Tessier, B., Hévin, G., Balland, C., & Hertz, E. \(2018a\)](#). Experimental and numerical investigation into rapid cooling of rock salt related to high frequency cycling of storage caverns. *International Journal of Rock Mechanics and Mining Sciences*, 102, 120–130. doi:[10.1016/j.ijrmms.2018.01.008](https://doi.org/10.1016/j.ijrmms.2018.01.008).
- [Art10] [Blanco-Martín, L., Rouabhi, A., & Hadj-Hassen, F. \(2021\)](#). Use of salt caverns in the energy transition: Application to power-to-gas–oxyfuel. *Journal of Energy Storage*, 44, 103333. doi:[10.1016/j.est.2021.103333](https://doi.org/10.1016/j.est.2021.103333).
- [Art11] [Blanco-Martín, L., Rutqvist, J., Battistelli, A., & Birkholzer, J. T. \(2018b\)](#). Coupled processes modeling in rock salt and crushed salt including halite solubility constraints: Application to disposal of heat-generating nuclear waste. *Transport in Porous Media*, 124, 159–182. doi:[10.1007/s11242-018-1057-7](https://doi.org/10.1007/s11242-018-1057-7).
- [Art12] [Blanco-Martín, L., Rutqvist, J., & Birkholzer, J. T. \(2015a\)](#). Long-term modeling of the thermal-hydraulic-mechanical response of a generic salt repository for heat-generating nuclear waste. *Engineering Geology*, 193, 198–211. doi:[10.1016/j.enggeo.2015.04.014](https://doi.org/10.1016/j.enggeo.2015.04.014).
- [Art13] [Blanco-Martín, L., Rutqvist, J., & Birkholzer, J. T. \(2017\)](#). Extension of TOUGH-FLAC to the finite strain framework. *Computers & Geosciences*, 108, 64–71. doi:[10.1016/j.cageo.2016.10.015](https://doi.org/10.1016/j.cageo.2016.10.015).
- [Art14] [Blanco-Martín, L., Rutqvist, J., Doughty, C., Zhang, Y., Finsterle, S., & Oldenburg, C. M. \(2016a\)](#). Coupled geomechanics and flow modeling of thermally induced compaction in heavy oil diatomite reservoirs under cyclic steaming. *Journal of Petroleum Science and Engineering*, 147, 474–484. doi:[10.1016/j.petrol.2016.09.002](https://doi.org/10.1016/j.petrol.2016.09.002).
- [Art15] [Blanco-Martín, L., Tijani, M., & Hadj-Hassen, F. \(2011b\)](#). A new analytical solution to the mechanical behaviour of fully grouted rockbolts subjected to pull-out tests. *Construction and Building Materials*, 25, 749–755. doi:[10.1016/j.conbuildmat.2010.07.011](https://doi.org/10.1016/j.conbuildmat.2010.07.011).

- [Art16] **Blanco-Martín, L.**, Tijani, M., Hadj-Hassen, F., & Noiret, A. (2013). Assessment of the bolt-grout interface behaviour of fully grouted rockbolts from laboratory experiments under axial loads. *International Journal of Rock Mechanics and Mining Sciences*, 63, 50–61. doi:[10.1016/j.ijrmms.2013.06.007](https://doi.org/10.1016/j.ijrmms.2013.06.007).
- [Art17] **Blanco-Martín, L.**, Tijani, M., Hadj-Hassen, F., & Noiret, A. (2016b). Boulonnage à ancrage réparti : étude de l'interface barre-scellement sous sollicitations axiales. *Revue Française de Géotechnique*, 146, 2. doi:[10.1051/geotech/2016002](https://doi.org/10.1051/geotech/2016002).
- [Art18] **Blanco-Martín, L.**, Wolters, R., Rutqvist, J., Lux, K.-H., & Birkholzer, J. T. (2015b). Comparison of two simulators to investigate thermal-hydraulic-mechanical processes related to nuclear waste isolation in saliferous formations. *Computers and Geotechnics*, 66, 219–229. doi:[10.1016/j.compgeo.2015.01.021](https://doi.org/10.1016/j.compgeo.2015.01.021).
- [Art19] **Blanco-Martín, L.**, Wolters, R., Rutqvist, J., Lux, K.-H., & Birkholzer, J. T. (2016c). Thermal-hydraulic-mechanical modeling of a large-scale heater test to investigate rock salt and crushed salt behavior under repository conditions for heat-generating nuclear waste. *Computers and Geotechnics*, 77, 120–133. doi:[10.1016/j.compgeo.2016.04.008](https://doi.org/10.1016/j.compgeo.2016.04.008).
- [Art20] Gharbi, H., Bérest, P., **Blanco-Martín, L.**, & Brouard, B. (2020). Determining upper and lower bounds for steady state strain rate during a creep test on a salt sample. *International Journal of Rock Mechanics and Mining Sciences*, 134, 104452. doi:[10.1016/j.ijrmms.2020.104452](https://doi.org/10.1016/j.ijrmms.2020.104452).
- [Art21] Jahangir, E., **Blanco-Martín, L.**, Hadj-Hassen, F., & Tijani, M. (2021). Development and application of an interface constitutive model for fully grouted rock-bolts and cable-bolts. *Journal of Rock Mechanics and Geotechnical Engineering*, 13, 811–819. doi:[10.1016/j.jrmge.2021.03.011](https://doi.org/10.1016/j.jrmge.2021.03.011).
- [Art22] Labaune, P., Rouabhi, A., Tijani, M., **Blanco-Martín, L.**, & You, T. (2018). Dilatancy criteria for salt cavern design: A comparison between stress- and strain-based approaches. *Rock Mechanics and Rock Engineering*, 51, 599–611. doi:[10.1007/s00603-017-1338-4](https://doi.org/10.1007/s00603-017-1338-4).
- [Art23] Rinaldi, A. P., Rutqvist, J., Luu, K., **Blanco-Martín, L.**, Hu, M., Sentís, M. L., Eberle, L., & Kästli, P. (2022). TOUGH3-FLAC3D: a modeling approach for parallel computing of fluid flow and geomechanics. *Computational Geosciences*, 26, 1563–1580. doi:[10.1007/s10596-022-10176-0](https://doi.org/10.1007/s10596-022-10176-0).
- [Art24] Thenevin, I., **Blanco-Martín, L.**, Hadj-Hassen, F., Schleifer, J., Lubosik, Z., & Wrana, A. (2017). Laboratory pull-out tests on fully grouted rock bolts and cable bolts: Results and lessons learned. *Journal of Rock Mechanics and Geotechnical Engineering*, 9, 843–855. doi:[10.1016/j.jrmge.2017.04.005](https://doi.org/10.1016/j.jrmge.2017.04.005).
- [Art25] Vilarrasa, V., Rutqvist, J., **Blanco-Martín, L.**, & Birkholzer, J. T. (2016). Use of a dual-structure constitutive model for predicting the long-term behavior of an expansive clay buffer in a nuclear waste repository. *International Journal of Geomechanics*, 16, D4015005. doi:[10.1061/\(ASCE\)GM.1943-5622.0000603](https://doi.org/10.1061/(ASCE)GM.1943-5622.0000603).

Peer Reviewed Conference Proceedings (*Underlined authors correspond to supervised PhD students*)

- [ConfPR1] Azabou, M., Rouabhi, A., **Blanco-Martín, L.**, & Hévin, G. (2022). Effect of impurities in rock salt samples on laboratory tests - consequences on rock mass representativity. In *SMRI Fall Technical Conference* (pp. 1–17). Chester, United Kingdom.
- [ConfPR2] Azabou, M., Rouabhi, A., **Blanco-Martín, L.**, Tijani, M., & Hadj-Hassen, F. (2020). On the effect of insoluble materials on rock salt dilatancy. In *54th US Rock Mechanics/Geomechanics Symposium* (ARMA 20-1429). Golden, CO, United States.

- [ConfPR3] Bérest, P., Gharbi, H., Gordeliy, E., Jehanno, D., Peach, C., Brouard, B., & **Blanco-Martín, L. (2022a)**. Creep tests on salt samples performed at very small stresses. In *SMRI Spring Technical Conference* (pp. 1–19). Rapid City, SD, United States.
- [ConfPR4] Bérest, P., Gharbi, H., Jehanno, D., Peach, C., Brouard, B., & **Blanco-Martín, L. (2022b)**. Creep tests on salt samples performed at very small stresses. In *56th US Rock Mechanics/Geomechanics Symposium* (ARMA 22-707). Santa Fe, NM, United States.
- [ConfPR5] **Blanco-Martín, L.**, Azabou, M., Rouabhi, A., Hadj-Hassen, F., & Hévin, G. (2022). Insights from an experimental campaign on rock salt and implications at the cavern scale. In *10th Conference Mechanical Behavior of Salt, Saltmech X* (pp. 1–12). Utrecht, The Netherlands.
- [ConfPR6] **Blanco-Martín, L.**, Hadj-Hassen, F., Tijani, M., & Armand, G. (2010). New Numerical Modelling of the Mechanical Long-term Behaviour of the GMR gallery in ANDRA’s Underground Research Laboratory. In *Clays in Natural & Engineered Barriers for Radioactive Waste Confinement, 4th International Meeting* (pp. 1–14). Nantes, France.
- [ConfPR7] **Blanco-Martín, L.**, Hadj-Hassen, F., Tijani, M., & Noiret, A. (2011). A new experimental and analytical study of fully grouted rockbolts. In *45th US Rock Mechanics/Geomechanics Symposium* (ARMA 11-242). San Francisco, CA, United States.
- [ConfPR8] **Blanco-Martín, L.**, Herchen, K., Rouabhi, A., Labaune, P., & Lux, K.-H. (2018). Use of laboratory tests in constitutive models for rock salt: a focus on volumetric strains. In S. Fahland, J. Hammer, F. D. Hansen, S. Heusermann, K.-H. Lux, & W. Minkley (Eds.), *Mechanical Behavior of Salt IX* (pp. 413–426). Hanover, Germany.
- [ConfPR9] **Blanco-Martín, L.**, Rutqvist, J., & Birkholzer, J. T. (2014a). Long-Term Analysis of Thermal-Hydraulic-Mechanical Processes in a Generic Salt Repository for High-Level Nuclear Waste. In *48th US Rock Mechanics/Geomechanics Symposium* (ARMA 14-7206). Minneapolis, MN, United States.
- [ConfPR10] **Blanco-Martín, L.**, Rutqvist, J., & Birkholzer, J. T. (2015a). Extension of the TOUGH-FLAC simulator to account for finite strains. In *TOUGH Symposium 2015*. Berkeley, CA, United States.
- [ConfPR11] **Blanco-Martín, L.**, Rutqvist, J., Birkholzer, J. T., & Battistelli, A. (2015b). Long-term modeling of coupled processes in a generic salt repository for heat-generating nuclear waste: preliminary analysis of the impacts of halite dissolution and precipitation. In *49th US Rock Mechanics/Geomechanics Symposium* (ARMA 15-440). San Francisco, CA, United States.
- [ConfPR12] **Blanco-Martín, L.**, Rutqvist, J., Birkholzer, J. T., & Houseworth, J. E. (2013a). Thermal-Hydraulic-Mechanical Processes Modeling to Evaluate Salt-based Repositories in the Long-Term. In *4th US Rock Mechanics/Geomechanics Symposium* (ARMA 13-621). San Francisco, CA, United States.
- [ConfPR13] **Blanco-Martín, L.**, Rutqvist, J., Birkholzer, J. T., Wolters, R., & Lux, K.-H. (2015c). Coupled modelling of the *Thermal Simulation for Drift Emplacement* underground test. In L. A. Roberts, K. D. Mellegard, & F. D. Hansen (Eds.), *Mechanical Behavior of Salt VIII*. Rapid City, SD, United States.
- [ConfPR14] **Blanco-Martín, L.**, Rutqvist, J., Birkholzer, J. T., Wolters, R., Lux, K.-H., Rutenberg, M., & Zhao, J. (2015d). Three-Dimensional Modeling of a Heater Test to Investigate Crushed Salt Reconsolidation and Rock Salt Creep for the Underground Disposal of High-Level Nuclear Waste. In *13th ISRM International Congress of Rock Mechanics*. Montreal, Canada.
- [ConfPR15] **Blanco-Martín, L.**, Rutqvist, J., Birkholzer, J. T., Wolters, R., Rutenberg, M., Zhao, J., & Lux, K.-H. (2014b). Comparison of two modeling procedures to evaluate thermal-hydraulic-mechanical processes in a generic salt repository for high-level nuclear waste. In *48th US Rock Mechanics/Geomechanics Symposium* (ARMA 14-7411). Minneapolis, MN, United States.

- [ConfPR16] **Blanco-Martín, L.**, Rutqvist, J., Doughty, C., Zhang, Y., Finsterle, S., & Oldenburg, C. M. (2015e). iTOUGH2-FLAC modeling of thermal-hydraulic-mechanical processes related to steam-assisted heavy oil recovery from diatomite. In *TOUGH Symposium 2015*. Berkeley, CA, United States.
- [ConfPR17] **Blanco-Martín, L.**, Rutqvist, J., Houseworth, J. E., & Birkholzer, J. T. (2013b). THM processes modeling to evaluate salt-based repositories in the long-term. In *14th International High-Level Radioactive Waste Management Conference, IHLRWMC 2013*. Albuquerque, NM, United States.
- [ConfPR18] Doughty, C., **Blanco-Martín, L.**, Zhang, Y., & Oldenburg, C. M. (2015). Modeling steam, water, and oil flow overlying a heavy oil reservoir undergoing cyclic steaming. In *TOUGH Symposium 2015*. Berkeley, CA, United States.
- [ConfPR19] Labaune, P., Rouabhi, A., Tijani, M., **Blanco-Martín, L.**, & You, T. (2017). Comparison between stress- and strain-based dilatancy criteria for salt cavern design. In *SMRI Fall Technical Conference* (pp. 1–12). Münster, Germany.
- [ConfPR20] Laigle, F. et al. (2011). Conception et justification du boulonnage, Réflexions et Avancées du Groupe de Travail N°30 de l’AFTES. In *AFTES Congrès International* (pp. 1–94). Lyon, France.
- [ConfPR21] Miah, M., **Blanco-Martín, L.**, Foxall, W., Rutqvist, J., Mullen, C., & Hutchings, L. (2015a). Dynamic Hydro-geomechanical Simulation of Earthquakes Induced by Fluid Injections in Geothermal Reservoirs. In *4th Workshop on Geothermal Reservoir Engineering*. Stanford, CA, United States.
- [ConfPR22] Miah, M., **Blanco-Martín, L.**, Foxall, W., Rutqvist, J., Rinaldi, A. P., & Mullen, C. (2015b). Development of a Hydro-geomechanical Model to Simulate Coupled Fluid Flow and Reservoir Geomechanics. In *TOUGH Symposium 2015*. Berkeley, CA, United States.
- [ConfPR23] Rinaldi, A. P., Rutqvist, J., **Blanco-Martín, L.**, Hu, M., & Sentís, M. L. (2018). Coupling TOUGH3 with FLAC3D for parallel computing of fluid flow and geomechanics. In *TOUGH Symposium 2018*. Berkeley, CA, United States.
- [ConfPR24] Tounsi, H., Rutqvist, J., Hu, M., Wolters, R., & **Blanco-Martín, L.** (2022). Numerical Modeling of Coupled Thermal-Hydro-Mechanical Processes in Salt Formations for Geologic Disposal of Large Nuclear Waste Canisters. In *56th US Rock Mechanics/Geomechanics Symposium* (ARMA 22-794). Santa Fe, NM, United States.
- [ConfPR25] Zhang, Y., **Blanco-Martín, L.**, Doughty, C., Finsterle, S., Zhou, Q., & Oldenburg, C. M. (2015). Determining optimal monitoring strategies for managing risks of cyclic steam injection using data-worth analysis. In *TOUGH Symposium 2015*. Berkeley, CA, United States.

Not Peer Reviewed Conference Proceedings

- [ConfNPR1] **Blanco-Martín, L.**, Rouabhi, A., & Hadj-Hassen, F. (2022). Underground storage in salt caverns related to Electrolysis-Methanation-Oxyfuel. In *CouFrac Conference*. Berkeley, CA, United States.
- [ConfNPR2] **Blanco-Martín, L.**, Rutqvist, J., Battistelli, A., & Birkholzer, J. T. (2015). Long-Term Modeling of Coupled Processes in a Generic Salt Repository for Heat-Generating Nuclear Waste: Analysis of the Impacts of Halite Solubility Constraints. In *AGU Fall Meeting*. San Francisco, CA, United States.
- [ConfNPR3] **Blanco-Martín, L.**, Rutqvist, J., & Birkholzer, J. T. (2013). On the importance of coupled THM processes to predict the long-term response of a generic salt repository for high-level nuclear waste. In *AGU Fall Meeting*. San Francisco, CA, United States.

- [ConfNPR4] **Blanco-Martín, L.**, Rutqvist, J., Birkholzer, J. T., Wolters, R., & Lux, K.-H. (2014). Modeling of the TSDE Heater Test to Investigate Crushed Salt Reconsolidation and Rock Salt Creep for the Underground Disposal of High-Level Nuclear Waste. In *AGU Fall Meeting*. San Francisco, CA, United States.
- [ConfNPR5] Rinaldi, A. P., Rutqvist, J., **Blanco-Martín, L.**, Hu, M., & Sentís, M. L. (2019). TOUGH3-FLAC3Dv6: a tool for parallel simulation of fluid flow and geomechanics. In *EGU General Assembly*. Vienna, Austria.
- [ConfNPR6] Rinaldi, A. P., Rutqvist, J., Luu, K., **Blanco-Martín, L.**, Hu, M., & Sentís, M. L. (2021). Parallel modeling of coupled processes: the recent development of TOUGH-FLAC. In *AGU Fall Meeting*. New Orleans, LA, United States.

Book chapters

- [Chap1] Hévin, G., Baland, C., Billiotte, J., Tessier, F., Hadj-Hassen, F., Rouabhi, A., **Blanco-Martín, L.**, Staudtmeister, K., Leuger, B., Zapf, D., Hertz, E., Tribout, D., & Thelier, N. (2017). Expérience de fissuration thermique dans une mine de sel. In M. Gasc-Barbier, V. Merrien-Soukatchoff, & P. Bérest (Eds.), *Manuel de mécanique des roches. Tome V : Thermomécanique des roches* (pp. 415–427). Presses des mines.

Appendix B

Selected Publications



Contents lists available at ScienceDirect

Computers & Geosciences

journal homepage: www.elsevier.com/locate/cageo

Research paper

Extension of TOUGH-FLAC to the finite strain framework



Laura Blanco-Martín*, Jonny Rutqvist, Jens T. Birkholzer

Energy Geosciences Division, Lawrence Berkeley National Laboratory, 1 Cyclotron Rd, MS 74R316C, Berkeley, CA 94720, USA

ARTICLE INFO

Keywords:

Finite strains
Coupled THM processes
TOUGH2
FLAC^{3D}
Sequential modeling
Voro++

ABSTRACT

The TOUGH-FLAC simulator for coupled thermal-hydraulic-mechanical processes modeling has been extended to the finite strain framework. In the approach selected, this extension has required modifications to the flow simulator (TOUGH2) and to the coupling scheme between the geomechanics and the flow sub-problems. In TOUGH2, the mass and energy balance equations have been extended to account for volume changes. Additionally, as large deformations are computed by FLAC^{3D}, the geometry is updated in the flow sub-problem. The Voronoi partition needed in TOUGH2 is computed using an external open source library (Voro++) that uses the centroids of the deformed geomechanics mesh as generators of the Voronoi diagram. TOUGH-FLAC in infinitesimal and finite strain frameworks is verified against analytical solutions and other approaches to couple flow and geomechanics. Within the finite strain framework, TOUGH-FLAC is also successfully applied to a large-scale case. The extension of TOUGH-FLAC to the finite strain framework has little impact to the user as only one additional executable is needed (for Voro++), and the input files and the workflow of a simulation are the same as in standard TOUGH-FLAC. With this new provision for finite strains, TOUGH-FLAC can be used in the analysis of a wider range of engineering problems, and the areas of application of this simulator are therefore broadened.

1. Introduction

Geoenergy and geoenvironmental applications in the subsurface often require that the coupling between different processes be considered. Typical examples of such applications are geological carbon sequestration, enhanced geothermal systems, oil/gas production, compressed air energy storage and underground disposal of nuclear waste. While in some cases coupling between hydraulic and mechanical processes may be sufficient to capture the main features of the coupled system (changes in effective stresses due to pore pressure changes and porosity changes due to volumetric deformation), in many cases the interactions need to be extended to thermal, chemical and possibly other (biological, etc.) processes.

In this study, we focus on coupled thermal-hydraulic-mechanical (THM) processes, for which two main solution approaches exist in the literature: fully coupled and sequentially coupled (Dean et al., 2006; Kim et al., 2009). In fully coupled methods, the governing equations of each sub-problem (i.e., mass and heat flows, and geomechanics) are solved simultaneously in a single system of equations. In sequential methods, the governing equations for flow and geomechanics are solved one-by-one within a time step, and relevant information (pore pressure, volumetric deformation, temperature, etc.) is passed from one sub-problem to the other using an intermediate solution informa-

tion technique (Settari and Mourits, 1998). The main advantage of fully coupled approaches is that they are unconditionally stable and converge if the coupled problem is well-posed; on the other hand, they require a unified flow-geomechanics simulator and are computationally expensive due to the size of the system of equations to be solved. In turn, sequentially coupled methods are less computationally intensive, provide more flexible code management, offer the possibility to use existing codes for flow and geomechanics, and can use different spatial domains for each sub-problem. Additionally, the converged solution is identical to that obtained using the fully coupled approach (Kim et al., 2009).

The sequential simulator TOUGH-FLAC was presented in the TOUGH Symposium 2003 as a new tool to solve coupled flow and geomechanics processes (Rutqvist et al., 2002; Rutqvist and Tsang, 2003). Since then, the capabilities of this simulator have been augmented considerably, and at present it can be successfully applied to a wide range of applications (Rutqvist, 2011, 2015). As the name suggests, in TOUGH-FLAC the multiphase, multicomponent and non-isothermal flow sub-problem is computed by TOUGH2 (Transport of Unsaturated Groundwater and Heat, v2, Pruess et al. (2012)), and the geomechanics sub-problem is computed by FLAC^{3D} (Fast Lagrangian Analysis of Continua in 3D, Itasca (2012)). TOUGH2 is an integral finite difference code and FLAC^{3D} is a finite difference code. In addition

* Corresponding author.

E-mail addresses: lblancomartin@lbl.gov (L. Blanco-Martín), jrutqvist@lbl.gov (J. Rutqvist), jbirkholzer@lbl.gov (J.T. Birkholzer).

to its flexibility to be used in a broad variety of applications, one main advantage of TOUGH-FLAC is that both TOUGH2 and FLAC^{3D} are used in both academia and industry, and are under constant development.

Recently, TOUGH-FLAC was extended to the finite strain framework (Blanco-Martín et al., 2015a, 2015b). This extension was motivated by the distortions and deformations observed in some applications, which exceed the limits of validity of the infinitesimal strain theory. For instance, the disposal of heat-generating nuclear waste in rock salt is expected to entail significant configuration changes: salt creeps and distorts under the effect of temperature and deviatoric stresses, and if damage and/or sealing occur(s), significant volume changes may take place (Hunsche and Hampel, 1999). Furthermore, compaction and dilation of geo-materials also involve large deformations. Still in the context of nuclear waste disposal in rock salt, the backfill material (crushed salt) is expected to undergo a reconsolidation process, in which its initial porosity (30–40%) reduces progressively to low residual values (< 10%), thereby triggering significant geometrical changes (Kröhn et al., 2015). Additionally, finite strains are common in oceanic gas hydrate reservoirs (Moridis et al., 2013).

In this paper, we summarize the architecture of TOUGH-FLAC and the modifications performed to extend this simulator to the finite strain framework. Then, we present some validation tests, first in infinitesimal mode, and later in large strain mode. Finally, we present a large-scale application in which TOUGH-FLAC in finite strains is successfully applied. The extension of TOUGH-FLAC to the finite strain framework widens the range of engineering problems that can be studied with this simulator and therefore broadens its areas of application.

2. Materials and methods

2.1. Architecture of TOUGH-FLAC

TOUGH-FLAC is based on the fixed-stress split sequential method to couple flow and geomechanics (Kim et al., 2009). In this method, the flow sub-problem is solved first within a time step. Once convergence has been reached in TOUGH2 (Newton-Raphson iteration process to solve mass and heat balances), relevant information (pore pressure, temperature and fluid mass) is sent to FLAC^{3D} to compute geomechanical equilibrium under drained conditions. Fluid mass is used to update the total mass of the system. The total stress tensor is updated using (direct coupling)

$$\sigma_{ij}^{corr} = \sigma_{ij} - \alpha \Delta P \delta_{ij} - 3\alpha_{th} K \Delta T \delta_{ij} \quad (1)$$

where σ_{ij}^{corr} [MPa] is the updated total stress tensor, σ_{ij} [MPa] is the total stress tensor at the end of the previous FLAC^{3D} run, α [-] is the Biot coefficient, ΔP [MPa] is the pore pressure change between two consecutive TOUGH2 runs, α_{th} [K⁻¹] is the linear thermal expansion coefficient, K [MPa] is the drained bulk modulus, ΔT [K] is the temperature change between two consecutive TOUGH2 runs, and δ_{ij} [-] is the Kronecker delta. Here, we consider that compressive stresses are negative. From Eq. (1), it can be inferred that the flow only affects the volumetric component of the stress tensor.

Pressure, temperature and fluid mass are transferred through text files handled by means of a THM interface, written both in Fortran (TOUGH2) and FISH (programming language embedded within FLAC^{3D}). Although less efficient, this approach has been selected because the source code of FLAC^{3D} is not available to users.

Within the framework of viscoelasticity or viscoplasticity, the time modeled in each FLAC^{3D} call is equal to the time step size of the last converged TOUGH2 time step (in elasticity, the physical time does not take part in the mechanical response). In this case, FLAC^{3D} splits the time to be modeled into smaller time steps, controlled internally to avoid exceedingly large out-of-balance forces. Once the system is in mechanical equilibrium, volumetric stresses of each zone are trans-

ferred to TOUGH2 by means of a text file; they will be used to compute a mechanically induced correction term in the porosity increment in the next flow time step (explicit evaluation). This increment reads

$$d\phi = A(\alpha, \phi, K)dP + B(\alpha_{th})dT + \Delta\phi \quad (2)$$

where $\Delta\phi$ [-] is the porosity correction from geomechanics (details can be found in Kim et al. [2012]). Additionally, other variables can be transferred to compute mechanically induced changes in permeability and capillary pressure (indirect coupling, see Rutqvist (2011) for details). A new flow time step is then taken, and the procedure described is repeated until the end of the simulation.

2.2. Extension of TOUGH-FLAC to the finite strain framework

Strain changes are computed within the geomechanics sub-problem, and, if they are large enough, it is necessary to ensure that the flow sub-problem is consistently updated. While FLAC^{3D} provides a capability for large strains, TOUGH2 does not. Therefore, in order to extend TOUGH-FLAC into the finite strain framework, it has been necessary to (i) adapt TOUGH2 to finite strains, and (ii) adapt the coupling between the two codes to the new framework.

Two main modifications have been necessary in TOUGH2. First, all geometrical data are updated as the geomechanics mesh deforms: volume of grid-blocks, interface area between two connected grid-blocks, distance from centers of two connected grid-blocks to common interface, and angle between the line linking two connected grid-blocks and the gravitational acceleration vector. Second, the heat and mass balance equations have been extended to include volume changes, and now read, for a grid-block n ,

$$\begin{aligned} \frac{d(M_n^\kappa V_n)}{dt} &= \sum_m A_{nm} F_{nm}^\kappa + q_n^\kappa \rightarrow \frac{dM_n^\kappa}{dt} + M_n^\kappa \frac{dV_n}{V_n dt} \\ &= \frac{1}{V_n} \left(\sum_m A_{nm} F_{nm}^\kappa + q_n^\kappa \right) \end{aligned} \quad (3)$$

for $\kappa=1, NK+1$ (NK is the total number of fluid components [air, water, etc.], and $NK+1$ represents the heat equation). In Eq. (3), M_n^κ is the accumulation term of component κ in grid-block n , V_n [m³] is the volume of the grid block (new volume after each FLAC^{3D} call), q_n^κ [kg/s or J/s] denotes sink/sources rates, and F_{nm}^κ is the flow of component κ across surface A_{nm} [m²] (new value after each FLAC^{3D} call). Eq. (3) reduces to the standard balance equations by setting $dV_n = 0$. The mass accumulation terms, M_n^κ [kg/m³], read

$$M_n^\kappa = \phi \sum_\beta S_\beta \rho_\beta \chi_\beta^\kappa \quad (4)$$

In Eq. (4), S_β [-] is the saturation of phase β , ρ_β [kg/m³] is the density of phase β , and χ_β^κ [-] is the mass fraction of component κ in phase β . The heat accumulation term, M_n^{NK+1} [J/m³], reads

$$M_n^{NK+1} = (1 - \phi) \rho_{gr} C_p T + \phi \sum_\beta S_\beta \rho_\beta u_\beta \quad (5)$$

where ρ_{gr} [kg/m³] is the rock grain density, C_p [J/kg/K] is the rock grain specific heat and u_β [J/kg] is the specific internal energy in phase β .

Mass transport occurs by advection and diffusion, so that the mass flux of component κ , F_{nm}^κ [kg/m²/s], reads

$$F_{nm}^\kappa = - \sum_\beta k \frac{k_{r\beta} \rho_\beta}{\mu_\beta} (\nabla P_\beta - \rho_\beta g) \chi_\beta^\kappa - \sum_\beta \rho_\beta D_\beta^\kappa \nabla \chi_\beta^\kappa \quad (6)$$

where k [m²] is the absolute permeability of the porous medium, $k_{r\beta}$ [-] is the relative permeability to phase β , μ_β [Pa·s] is viscosity of phase β , P_β [Pa] is phase pressure and g [m/s²] is the gravity acceleration vector. Regarding the diffusive term, D_β^κ [m²/s] is the hydrodynamic dispersion tensor of component κ in phase β , (see Pruess et al. (2012) for further details).

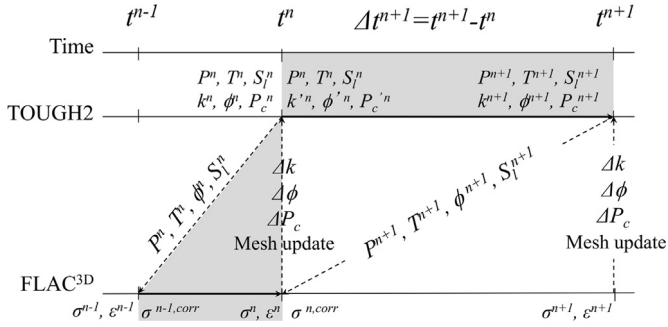


Fig. 1. TOUGH-FLAC numerical scheme in finite strains. The gray area corresponds to a time step between t^n and t^{n+1} .

Finally, heat transport occurs by conduction and convection, and the heat flux term, F_{nm}^{NK+1} [J/m²/s], reads

$$F_{nm}^{NK+1} = -\lambda \nabla T - \sum_{\beta} k_{r\beta} \frac{\rho_{\beta}}{\mu_{\beta}} (\nabla P_{\beta} - \rho_{\beta} g) h_{\beta} \quad (7)$$

where λ [W/m/K] is the thermal conductivity and h_{β} [J/kg] is the specific enthalpy in phase β .

Regarding the coupling between the two codes, the new geometrical data is transferred to TOUGH2 through a text file; this file is subsequently read by a new Fortran subroutine to update the corresponding geometrical arrays. We note that the main drawback of the approach selected to extend TOUGH-FLAC to the finite strain framework is an increase of computational time due to geometry update. An alternative approach would consist in keeping the geometry unchanged, and mapping relevant properties (such as permeability) onto the reference configuration; however, this approach requires full tensor (i.e., non-diagonal) permeability, and this is not supported in the current version of TOUGH2. For this reason, we selected an approach in which geometry is updated.

Fig. 1 shows the numerical scheme used in TOUGH-FLAC, including transfer of geometrical data. This scheme is also valid in creep mode (time-dependent geomechanical behavior). It should be noted that the general workflow of TOUGH-FLAC (Rutqvist, 2011) is not noticeably modified when finite strains are considered. Additionally, the impact for the user is minimal, as all modifications are taken care of internally. Only one additional executable is needed to properly update the flow mesh (see next sub-section).

2.3. Mesh update in the flow sub-problem

The resolution method used in TOUGH2 is based on the Voronoi partition (Pruess et al., 2012). As large deformations occur, the updated flow mesh should still be of Voronoi type for an accurate solution of the flow sub-problem. For this reason, we have linked the software library Voropp (Rycroft, 2009) to TOUGH-FLAC. Voropp is open source, and can compute 3D Voronoi partitions on a cell-based fashion. Moreover, customizing its output for a particular application is not time-consuming.

The new workflow to update the mesh in the flow sub-problem is as follows. First, the centroids of the deformed geomechanics mesh are transferred using a FISH routine to Voropp, which computes the corresponding Voronoi diagram. Then, data of the new partition relevant to TOUGH2 (volumes, distances, areas, etc.) are written into a text file. This file is finally read by TOUGH2, and the corresponding arrays are updated. In general, this operation is performed every time maximum volumetric strain changes are greater than 2–3%. We note however that this condition can be easily changed in the FISH routine written to transfer data to Voropp. For instance, in cases where the mesh distorts without significant volume changes, the flow mesh should be updated, as the interface areas, distances and angle between the line linking two connected grid-blocks and the gravity vector may

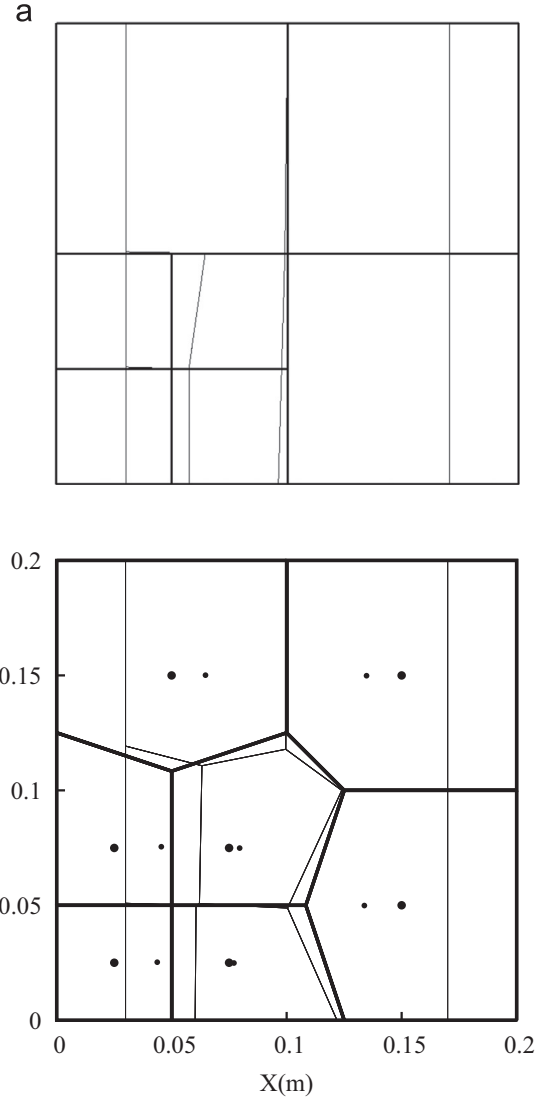


Fig. 2. Example of mesh used in the geomechanics sub-problem (a) and corresponding Voronoi partition for the flow sub-problem (b). Initial (thick lines) and deformed (thin lines) configurations are displayed.

change noticeably. Fig. 2 shows an example of a geomechanics mesh and the corresponding Voronoi partition, both in the non-deformed and deformed configurations.

3. Verification cases

In this section, TOUGH-FLAC is verified against classic analytical solutions of coupled problems, and it is also benchmarked against other simulators that can handle finite strains. The first three cases presented are related to well-known benchmark problems in small strains, which demonstrate the correct coupling between TOUGH2 and FLAC^{3D} prior to addressing finite strains.

3.1. Mandel's problem (small strains)

Mandel's problem is commonly used to test the validity of numerical codes of poroelasticity. The original problem is described in Mandel (1953). Later, this problem was extended to account for non-isotropic materials as well as compressible fluids (Abousleiman et al., 1996).

In Mandel's problem, a specimen with rectangular cross-section and infinite length along the out-of-plane direction is sandwiched at

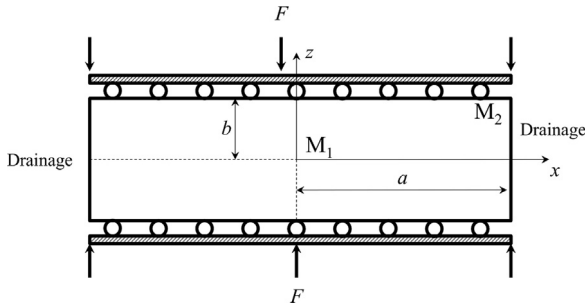


Fig. 3. Schematic representation of Mandel's problem. Monitoring points (M_1 and M_2) for Fig. 4 are displayed.

the top and the bottom by two stiff, frictionless plates. The pore space is in single-phase conditions. Laterally, the specimen is not mechanically constrained, and drainage is possible (no drainage at the top and bottom). The specimen is initially in equilibrium. At $t=0$, a compressive force is applied normal to the plates, and we seek to determine the evolution of pore pressure, as well as relevant displacements, strains and stresses within the sample. Fig. 3 shows a schematic representation of Mandel's problem.

Mandel's problem is a two-dimensional, plane strain problem. Because the plates are perfectly stiff, the vertical displacement is uniform along the top and bottom boundaries (but it changes with time). When the load is applied, an excess of pore pressure is generated (Skempton effect). Over time, drainage occurs at the open boundaries, which makes the laterals of the sample more compliant than its core. However, since the vertical displacement must be equal along the top and bottom boundaries, there is an increase of pore pressure in the central region. This yields a non-monotonic pore pressure evolution, known as the Mandel-Cryer effect (Schiffman et al., 1969). At a later

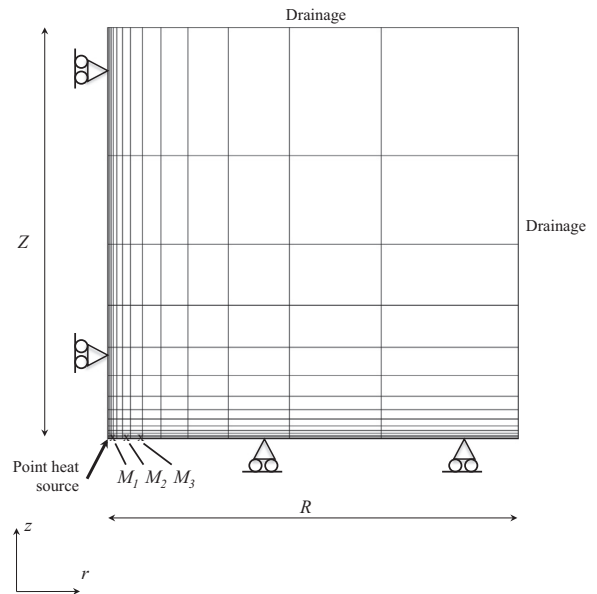


Fig. 5. Schematic representation of Booker and Savvidou's problem. Monitoring points (M_1 , M_2 and M_3) for Fig. 6 are indicated (they are all located along the radial axis).

time, the excess of pore pressure dissipates completely throughout the sample. We note that the Mandel-Cryer effect has been observed experimentally (Verruijt, 1969).

Mandel's problem has been modeled with TOUGH-FLAC. We have assumed a sample with $a=5$ m, $b=1.25$ m, $E=450$ MPa, and $\nu=0$. The initial stress field is 0.1 MPa (compressive), and we apply 10 MPa normal to the plates. The initial porosity is $\phi_0=42.5\%$ and the permeability of the sample is $k=6.51 \cdot 10^{-15}$ m². The sample is saturated

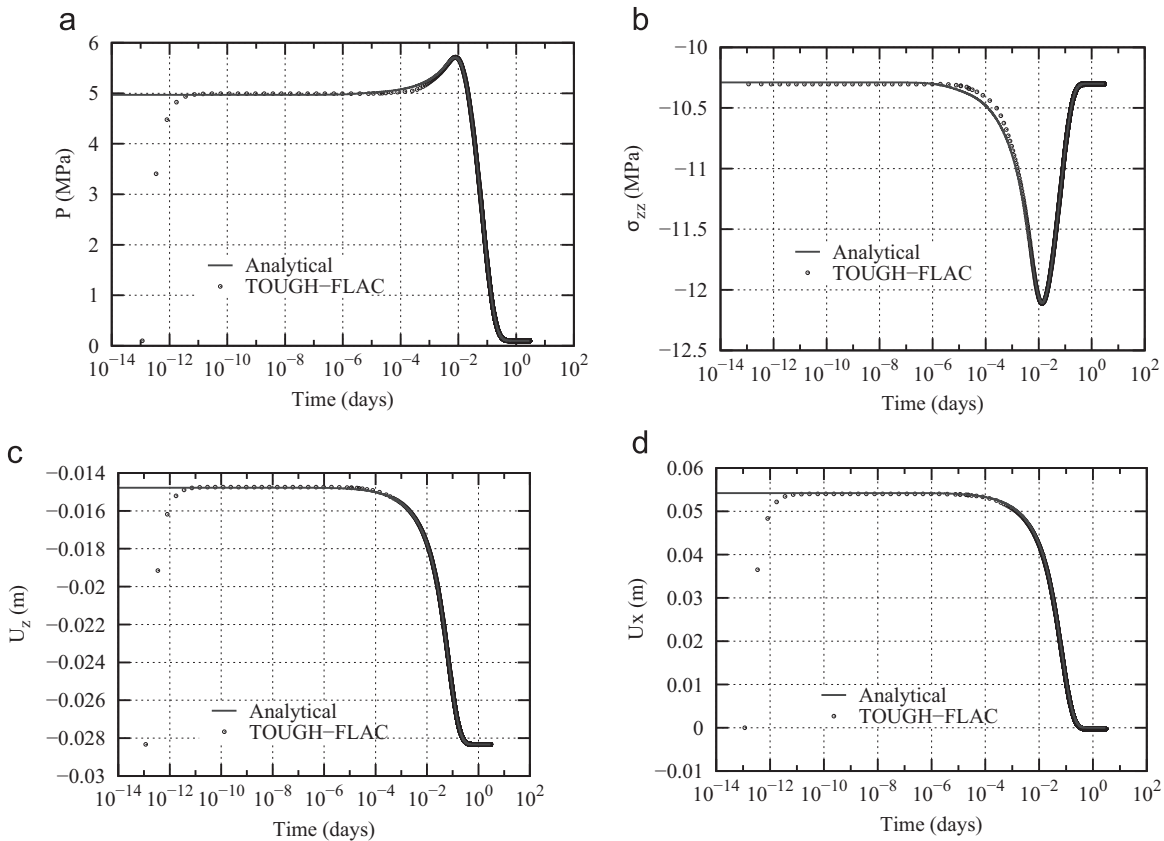


Fig. 4. Mandel's problem: comparison between analytical and modeling results for (a) pore pressure at M_1 ; (b) vertical stress at M_1 ; (c) vertical displacement at M_2 , and (d) horizontal displacement at M_2 .

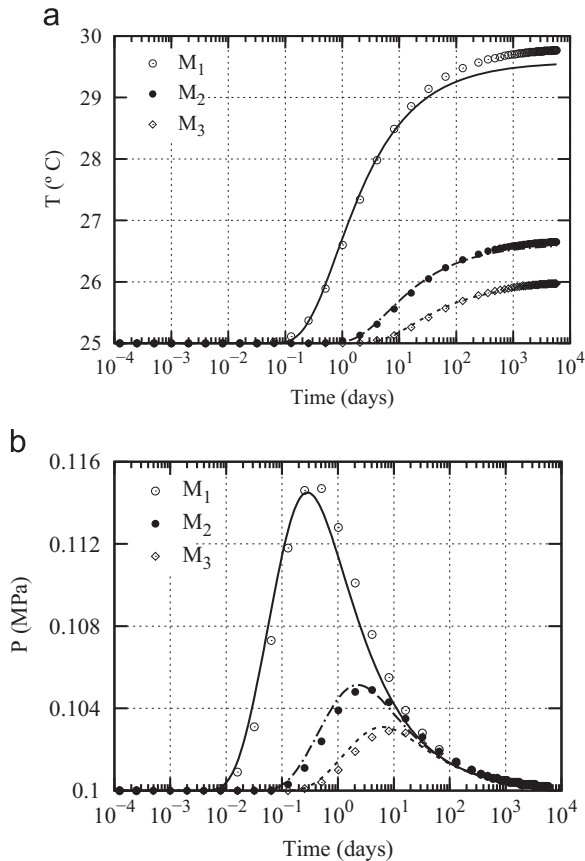


Fig. 6. Booker and Savvidou's problem: comparison between analytical (lines) and modeling (symbols) results for (a) temperature, and (b) pore pressure at locations $M_1 = 0.22$ m, $M_2 = 0.63$ m, and $M_3 = 1$ m.



Fig. 7. Schematic representation of Terzaghi's problem. The monitoring point (M) for Figs. 8, 9 and 11 is displayed.

with water, having $T=25$ °C (constant) and $p_o = 0.1$ MPa. Gravity is neglected. Given that TOUGH2 accounts for fluid compressibility changes, we have compared our modeling results with the analytical solution proposed by [Abousleiman et al. \(1996\)](#). Furthermore, in order to model frictionless plates, an interface is used between the sample and the plates.

The plots in [Fig. 4](#) compare analytical and modeling results at the locations displayed in [Fig. 3](#). As the figure shows, the comparisons are very satisfactory (note that the differences observed at the beginning are due to different initial states: in the analytical solution, the load is already applied and borne by the fluid, and the corresponding excess is calculated; on the other hand, in TOUGH-FLAC the initial state corresponds to a previous state of equilibrium, and at $t=0$ the load is applied to the sample). These results help verify the validity of TOUGH-FLAC to solve coupled flow and geomechanics problems.

3.2. Booker and Savvidou's problem (small strains)

[Booker and Savvidou \(1985\)](#) proposed an analytical solution for a problem involving a point heat source buried in a saturated medium. This configuration is characteristic of the underground disposal of heat-generating nuclear waste. The analytical solution was developed

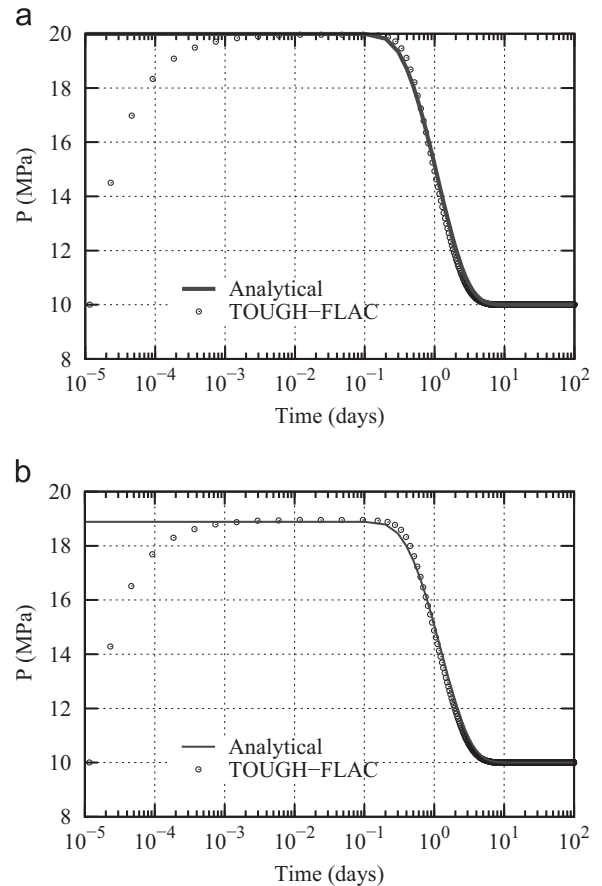


Fig. 8. Terzaghi's problem (infinitesimal strains): comparison between analytical and modeled pore pressure evolution at the monitoring point, for (a) incompressible water, and (b) real water compressibility.

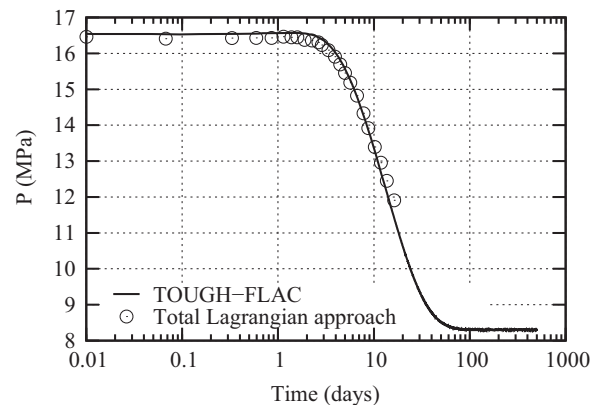


Fig. 9. Terzaghi's problem (finite strains): comparison between results from TOUGH-FLAC and those in [Kim \(2015\)](#) for the pore pressure evolution at the monitoring point.

assuming a poro-thermo elastic medium, and has been used to test the validity of THM codes ([Nguyen and Selvadurai, 1995](#)).

In Booker and Savvidou's problem, a saturated, infinite medium is initially in equilibrium. At $t=0$, a heat load is applied in the center of the medium. Over time, as temperature increases both the pore water and the solid skeleton expand. Since in general the thermal expansion of water is greater than that of the solid medium, the pore pressure increases, which leads to a reduction in effective stresses (THM coupling). The pore pressure increase gradually dissipates as the medium is allowed to consolidate. [Booker and Savvidou \(1985\)](#) proposed analytical solutions for pore pressure, temperature, stresses and displacements for a constant point heat source embedded in an

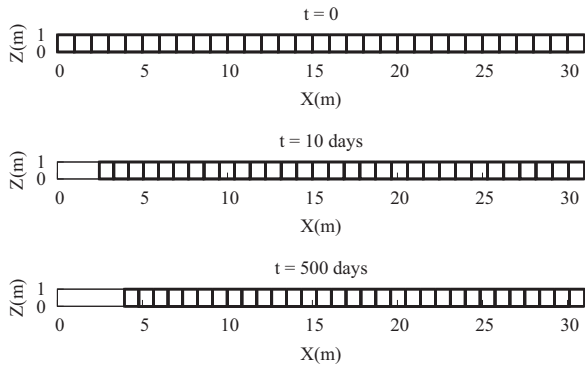


Fig. 10. Terzaghi's problem (finite strains): view of the mesh at $t=0$, $t=10$ days, and $t=500$ days (end of simulation).

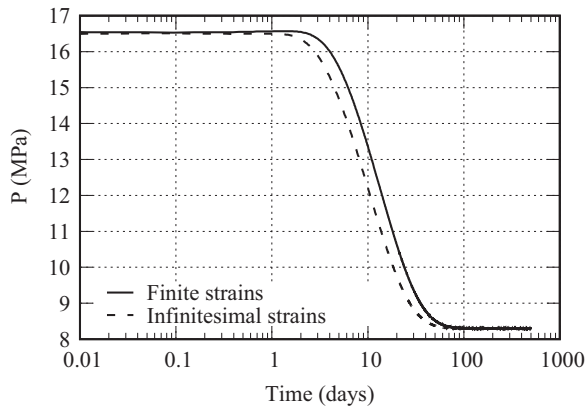


Fig. 11. Terzaghi's problem: pore pressure evolution at the monitoring point under the infinitesimal and the finite strain frameworks.

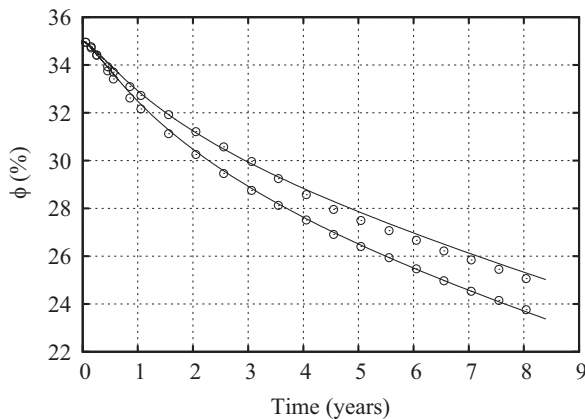


Fig. 12. Porosity evolution at two cross-sections in the heated part of a test drift during the TSDE experiment: comparison between measurements (symbols) and modeling results (lines).

infinite medium. An approximate solution for a cylindrical source was also given. It should be noted that this problem is three-dimensional, but can be reduced to axisymmetric conditions assuming an isotropic elastic material.

Fig. 5 shows the model prepared to benchmark TOUGH-FLAC against the analytical solutions in Booker and Savvidou (1985). We note that, in order to reproduce an infinite medium, Dirichlet boundary conditions (i.e., constant pore pressure and temperature) are imposed at the outer boundaries of the model ($R = Z = 200$ m in Fig. 5). The heat source is applied in a small element at $r = z = 0$. The medium is linear elastic with $E = 650$ MPa and $\nu = 0.24$. The initial stress field is 0.1 MPa (compressive), equal to the initial pore pressure. The sample is saturated with water. The initial temperature is $T_0 = 25$ °C, and we

apply a heat source of 15.6 W. The initial porosity of the sample is $\phi_0 = 45\%$, its permeability is $k = 6.51 \cdot 10^{-18}$ m², its thermal conductivity is $\lambda = 1.2$ W/m/K, and the coefficient of linear thermal expansion is $\alpha_{th} = 7 \cdot 10^{-6}$ K⁻¹. Solid density is $\rho = 2500$ kg/m³ and the specific heat of the solid skeleton is $C_p = 1000$ J/kg/K. Gravity is neglected.

Fig. 6a compares analytical and modeling results for temperature at three locations along the radial axis of the model. The pore pressure evolution at these locations is displayed in Fig. 6b. As the figures show, results from TOUGH-FLAC compare quite well with the analytical solutions, with biggest errors at shorter distances from the heat source (in TOUGH-FLAC, the heat load is applied to a small-volume element rather than to a point).

3.3. Terzaghi's problem (small strains)

Terzaghi's problem (Terzaghi, 1943) is a classic consolidation problem. It is a one-dimensional problem, in which a compressive load is applied on one side of a sample while the displacement normal to the other sides is blocked. The pore space is in single-phase conditions, and drainage is only allowed across the side where the load is applied. Fig. 7 shows schematically Terzaghi's problem.

Similarly to Mandel's problem, when the load is applied the pore pressure increases (Skempton effect) and then the excess of pore pressure dissipates as the fluid flows out of the sample. On the other hand, one main difference with Mandel's problem is that, in Terzaghi's problem, the load and the dissipation of pore pressure occur in the same direction. Moreover, the total stress is constant along the sample, and is equal to the applied load. Therefore, as the fluid flows out of the sample and the pore pressure decreases, there is a load transfer between the fluid and the solid, so that the effective stresses increase. We note that in Terzaghi's problem the pore pressure decreases monotonically after the initial rise, and therefore the Mandel-Cryer effect, distinctive feature of the coupled consolidation theory, is not observed.

Terzaghi's problem has been modeled with TOUGH-FLAC, using $L = 31$ m, $E = 600$ MPa, and $\nu = 0.15$. Initially, the sample is in equilibrium under a compressive stress of 10 MPa (the initial pore pressure is also 10 MPa). The initial porosity is $\phi_0 = 42.5\%$ and the permeability of the sample is $k = 6.5 \cdot 10^{-15}$ m². The sample is saturated with water, having $T = 25$ °C (constant). At $t = 0$, the applied load increases by 10 MPa. Gravity is neglected. The plots in Fig. 8 show a comparison between analytical and modeling results for the evolution of pore pressure at the monitoring point M (0.5 m from the right border). In Fig. 8a, the water is assumed incompressible and in Fig. 8b, real water compressibility is used. The latter corresponds to the standard procedure in TOUGH2; to obtain the modeling results in Fig. 8a, water compressibility in TOUGH2 is forced constant at a near-zero value. As Fig. 8a shows, if the water is assumed incompressible the initial pore pressure increase is equal to the applied load (i.e., the fluid bears the load initially), while it is about 1 MPa smaller if the real compressibility of water is used. In both cases, the pressure dissipation over time is very well captured by TOUGH-FLAC. We note that, similarly to Mandel's problem, the initial state is different between the analytical solution and TOUGH-FLAC.

3.4. Terzaghi's problem (large strains)

In order to test the validity of TOUGH-FLAC in finite strains, we compare results from this simulator with results issued from other approaches and codes that can handle large strains.

Kim (2015) presents an approach based on the total Lagrangian method to sequentially couple flow and geomechanics in finite strains. In this method, geometry is not updated, and instead pertinent properties are mapped onto a reference configuration (original). As explained in Section 2.2, the main advantage of this method is that the recalculation of geometry is not needed (therefore, the computational cost is reduced), and the main drawback is the need for full perme-

ability tensors, not implemented in standard versions of various flow simulators, including TOUGH2.

In Kim (2015), the total Lagrangian method is applied to Terzaghi's problem. The same scenario has been solved with TOUGH-FLAC. In this case, $L = 31$ m, $E = 60$ MPa, and $\nu = 0.15$. The initial compressive total stress and pore pressure are 8.3 MPa, and at $t=0$ the applied load increases by 8.3 MPa. The initial porosity is $\phi_0 = 42.5\%$ and the permeability of the sample is $k = 6.5 \cdot 10^{-15} \text{ m}^2$ ($T = 25^\circ\text{C}$). Gravity is neglected. In Fig. 9, results from TOUGH-FLAC and Kim (2015) are shown; as the figure shows, the comparison is very satisfactory. Three views of the mesh during the TOUGH-FLAC simulation are displayed in Fig. 10. As it can be seen, there has been a significant geometrical change, with volume evolution from 31 m^3 ($t=0$) to 27 m^3 ($t=500$ days).

Finally, in order to demonstrate the relevance of the large strain framework, the same case presented has been solved using small strains. The pore pressure evolution obtained in the two situations at location M is displayed in Fig. 11. It can be seen that when the problem is solved in small strains the pore pressure dissipates faster; however, this result is not general because it depends on the counteracting effects in finite strains of compressibility reduction (which reduces deformation) and diffusion length reduction (which facilitates consolidation). Moreover, it should be noted that, since the mesh is very small (31 grid-blocks), the computational times of the two simulations are approximately equal.

4. Field scale application: disposal of heat-generating nuclear waste in rock salt

TOUGH-FLAC in finite strains and creep modes has been used to model a large-scale underground heater test conducted in the Asse salt mine in Germany (Blanco-Martín et al., 2016). The goal of this test (Thermal Simulation for Drift Emplacement, or TSDE) was to investigate the feasibility of disposal of heat-generating nuclear waste in a rock salt formation, using crushed salt backfilling (Bechthold et al., 1999, 2004). The fundamentals of disposal of heat-generating nuclear waste in salt-based formations can be found in, e.g., Hansen and Leigh (2011), and Langer (1999). Details on the modeling of rock salt and salt excavations can be found in, e.g., Cristescu and Hunsche (1996), Hou and Lux (1999), Hunsche et al., (1994), Hunsche and Hampel (1999), and Munson (1997).

During the TSDE test, heating was provided by six electrical heaters placed in two 79 m-long parallel drifts. The heaters (three per drift) were placed in the central part of the drifts, spaced 3 m along the drift axis. The heating period lasted 8 years and 5 months, and an extensive measurement campaign was deployed to study the host rock, the backfill and also the corrosion of the heater casks.

Fig. 12 compares experimental and computed backfill porosity in two cross-sections in the heated area of one drift. Experimental porosity was derived from horizontal and vertical drift closure measurements (Bechthold et al., 1999). At emplacement, the porosity of the crushed salt was 35%, and it decreased to about 24–26% during the heating phase. Given the porosity reduction observed (about 10%), the finite strain framework was selected for the numerical analysis (details of this analysis can be found in Blanco-Martín et al., 2016). The figure displays a good agreement between experimental data and modeling results from TOUGH-FLAC. Although the experimental values are only approximate (they are average values within a cross-section), this comparison shows that TOUGH-FLAC can be successfully applied to a large-scale application involving finite strains and time-dependent rheology.

5. Conclusions

The simulator TOUGH-FLAC for coupled thermal-hydraulic-mechanical processes modeling has been extended to the finite strain

framework. Since FLAC^{3D} includes a capability for finite strains, the main modifications to TOUGH-FLAC have concerned the flow simulator (TOUGH2) and the coupling scheme between the two codes.

The approach selected consists in updating the geometry of the flow sub-problem as finite strains are computed in the geomechanics sub-problem. In TOUGH2, the mass and energy balance equations have been extended to account for volume changes. Moreover, all geometrical data (volumes, areas, distances, etc.) are updated during the simulation. Since the resolution method used in TOUGH2 is based on the Voronoi partition, a new Voronoi diagram is computed every time geometrical changes exceed a preset limit. The centroids of the deformed geomechanics mesh are sent to Voro++ (open source library that computes Voronoi diagrams given seed points), and geometrical data of the new partition is sent to TOUGH2 for the next time step. The update of geometrical data is carried out internally and the impact to the user is very limited, as only one additional executable (Voro++) is needed to perform a simulation.

TOUGH-FLAC has been verified against analytical solutions of Terzaghi, Booker and Savvidou, and Mandel's problems. In finite strains, this simulator has been successfully benchmarked against other approaches to perform large strain computations of coupled flow and geomechanics problems. A large-scale heater test designed to study the feasibility of disposal of heat-generating nuclear waste in rock salt formations using crushed salt backfilling has also been successfully modeled using this new version of TOUGH-FLAC.

The extension of TOUGH-FLAC to the large strain framework expands its use to the analysis of a variety of engineering problems, and therefore broadens its current areas of application.

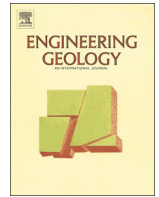
Acknowledgements

Funding for this work has been provided by the Used Fuel Disposition Campaign, Office of Nuclear Energy of the U.S. Department of Energy, under Contract Number DE-AC02-05CH11231 with Lawrence Berkeley National Laboratory.

References

- Abousleiman, Y., Cheng, A.H.-D., Cui, L., Detournay, E., Roegiers, J.-C., 1996. Mandel's problem revisited. *Géotechnique* 46 (2), 187–195. <http://dx.doi.org/10.1680/geot.1996.46.2.187>.
- Bechthold, W., Rothfuchs, T., Poley, A., Ghoreychi, M., Heusermann, S., Gens, A., Olivella, S., 1999. Backfilling and sealing of underground repositories for radioactive waste in salt (BAMBUS project). *Eur. At. Energy Community*, 283.
- Bechthold, W., Smailos, E., Heusermann, S., Bollingerfehr, W., Bazargan-Sabet, B., Rothfuchs, T., Kamlot, P., Grupa, J., Olivella, S., Hansen, F.D., 2004. Backfilling and sealing of underground repositories for radioactive waste in salt (BAMBUS II project). *Eur. At. Energy Community*, 305.
- Blanco-Martín, L., Rutqvist, J., Birkholzer, J.T., 2015a. Extension of the TOUGH-FLAC simulator to account for finite strains. In: *Proceedings of TOUGH Symposium*, Berkeley, CA, pp. 266–271.
- Blanco-Martín, L., Rutqvist, J., Birkholzer, J.T., 2015b. Long-term modelling of the thermal-hydraulic-mechanical response of a generic salt repository for heat generating nuclear waste. *Eng. Geol.* 193, 198–211. <http://dx.doi.org/10.1016/j.enggeo.2015.04.014>.
- Blanco-Martín, L., Wolters, R., Rutqvist, J., Lux, K.-H., Birkholzer, J.T., 2016. Thermal-hydraulic-mechanical modeling of a large-scale heater test to investigate rock salt and crushed salt behavior under repository conditions for heat-generating nuclear waste. *Comput. Geotech.* 77, 120–133. <http://dx.doi.org/10.1016/j.compgeo.2016.04.008>.
- Booker, J.R., Savvidou, C., 1985. Consolidation around a point heat source. *Int. J. Numer. Anal. Methods Geomech.* 9, 173–184. <http://dx.doi.org/10.1002/nag.1610090206>.
- Cristescu, N., Hunsche, U., 1996. A comprehensive equation for rock salt: determination and application. In: *Proceedings of the 3rd International Conference Mechanical Behavior of Rock Salt (SaltMech3)*, Palaiseau, pp. 191–205.
- Dean, R.H., Gai, X., Stone, C.M., Minkoff, S.E., 2006. A comparison of techniques for coupling porous flow and geomechanics. *SPE J.* 11 (1), 132–140. <http://dx.doi.org/10.2118/79709-PA>.
- Hansen, F.D., Leigh, C.D., 2011. *Salt Disposal of Heat-Generating Nuclear Waste*. Sandia National Laboratories, 110.
- Hunsche, U., Hampel, A., 1999. Rock salt – the mechanical properties of the host rock material for a radioactive waste repository. *Eng. Geol.* 52, 271–291. [http://dx.doi.org/10.1016/S0013-7952\(99\)00011-3](http://dx.doi.org/10.1016/S0013-7952(99)00011-3).

- Hunsche, U., Schulze, O., Langer, M., 1994. Creep and failure behavior of rock salt around underground cavities. In: Proceedings 16th World Mining Congress, vol. 5, Sofia, pp. 217–230.
- Itasca, 2012. *FLAC^{3D} (Fast Lagrangian Analysis of Continua in 3 Dimensions), Version 5.0*. Itasca Consulting Group, Minneapolis, MN.
- Kim, J., Tchelepi, H.A., Juanes, R., 2009. Stability, Accuracy and Efficiency of Sequential Methods for Coupled Flow and Geomechanics. In: SPE Reservoir Simulation Symposium, The Woodlands, TX, paper SPE 119084. <http://dx.doi.org/10.2118/119084-MS>
- Kim, J., Sonnenthal, E.L., Rutqvist, J., 2012. Formulation and sequential numerical algorithms of coupled fluid/heat flow and geomechanics for multiple porosity materials. *Int. J. Numer. Methods Eng.* 92 (5), 425–456. <http://dx.doi.org/10.1002/nme.4340>.
- Kim, J., 2015. A Numerically Stable Sequential Implicit Algorithm for Finite-strain Elastoplastic Geomechanics Coupled to Fluid Flow. In: SPE Reservoir Simulation Symposium, Houston, TX, paper SPE 173303. <http://dx.doi.org/10.2118/173303-MS>
- Kröhn, K.-P., Zhang, C.-L., Czaikowski, O., Stührenberg, D., Heemann, U., 2015. The compaction behaviour of salt backfill as a THM-process. In: Proceedings of the 8th International Conference Mechanical Behavior of Salt (SaltMech8), Rapid City, pp. 49–59. <http://dx.doi.org/10.1201/b18393-8>
- Hou, Z., Lux, K.-H., 1999. A constitutive model for rock salt including structural damages as well as practice-oriented applications. In: Proceedings of the 5th International Conference Mechanical Behavior of Rock Salt (SaltMech5), Bucharest, pp. 151–169.
- Langer, M., 1999. Principles of geomechanical safety assessment for radioactive waste disposal in salt structures. *Eng. Geol.* 52, 257–269. [http://dx.doi.org/10.1016/S0013-7952\(99\)00010-1](http://dx.doi.org/10.1016/S0013-7952(99)00010-1).
- Mandel, J., 1953. La consolidation des sols (étude mathématique). *Géotechnique* 3 (7), 287–299. <http://dx.doi.org/10.1680/geot.1953.3.7.287>.
- Moridis, G.J., Kim, J., Reagan, M.T., Kim, S.-J., 2013. Feasibility of gas production from a gas hydrate accumulation at the UBGH2-6 site of the Ullung basin in the Korean East Sea. *J. Pet. Sci. Eng.* 108, 180–210. <http://dx.doi.org/10.1016/j.petrol.2013.03.002>.
- Munson, D.E., 1997. Constitutive model of creep in rock salt applied to underground room closure. *Int. J. Rock. Mech. Min. Sci.* 34 (2), 233–247. [http://dx.doi.org/10.1016/S0148-9062\(96\)00047-2](http://dx.doi.org/10.1016/S0148-9062(96)00047-2).
- Nguyen, T.S., Selvadurai, A.P.S., 1995. Coupled thermal-mechanical-hydrological behaviour of sparsely fractured rock: implications for nuclear waste disposal. *Int. J. Rock. Mech. Min. Sci.* 32 (5), 465–479. [http://dx.doi.org/10.1016/0148-9062\(95\)00036-G](http://dx.doi.org/10.1016/0148-9062(95)00036-G).
- Pruess, K., Oldenburg, C., Moridis, G.J., 2012. *TOUGH2 User's Guide, Version 2.1*. Lawrence Berkeley National Laboratory, 210.
- Rutqvist, J., Wu, Y.-S., Tsang, C.-F., Bodvarsson, G., 2002. A modeling approach for analysis of coupled multiphase fluid flow, heat transfer, and deformation in fractured porous rock. *Int. J. Rock. Mech. Min. Sci.* 39 (4), 429–442. <http://dx.doi.org/10.1016/S1365-1609%2802%2900022-9>.
- Rutqvist, J., Tsang, C.-F., 2003. TOUGH-FLAC: a numerical simulator for analysis of coupled thermal-hydrologic-mechanical processes in fractured and porous geological media under multi-phase flow conditions. In: Proceedings TOUGH Symposium, Berkeley, CA, 9 pp.
- Rutqvist, J., 2011. Status of the TOUGH-FLAC simulator and recent applications related to coupled fluid flow and crustal deformations. *Comput. Geosci.* 37, 739–750. <http://dx.doi.org/10.1016/j.cageo.2010.08.006>.
- Rutqvist, J., 2015. An overview of TOUGH-based geomechanics models. In: Proceedings TOUGH Symposium, Berkeley, CA, pp. 301–313.
- Rycroft, C.H., 2009. *Voro++: a three-Dimens. Voronoi Cell Libr. C++* (<http://math.lbl.gov/voro++/>).
- Settari, A., Mourits, F., 1998. A coupled reservoir and geomechanical simulation system. *SPE J.* 3 (3), 219–226. <http://dx.doi.org/10.2118/50939-PA>.
- Schiffman, R.L., Chen, A.T.-F., Jordan, J.C., 1969. An analysis of consolidation theories. *J. Soil Mech. Found. Div.* 95 (1), 285–312.
- Terzaghi, K., 1943. *Theoretical Soil Mechanics*. John Wiley & Sons, New York, NY, 510. <http://dx.doi.org/10.1002/9780470172766>.
- Verruijt, A., 1969. Elastic storage of aquifers. In: De Wiest, R.J.M. (Ed.), *Flow through Porous Media*. Academic Press, New York, 331–376.



Long-term modeling of the thermal–hydraulic–mechanical response of a generic salt repository for heat-generating nuclear waste



Laura Blanco Martín^{*}, Jonny Rutqvist, Jens T. Birkholzer

Earth Sciences Division, Lawrence Berkeley National Laboratory, 1 Cyclotron Rd, MS 74R316C, Berkeley, CA 94720, USA

ARTICLE INFO

Article history:

Received 1 May 2014

Received in revised form 3 March 2015

Accepted 20 April 2015

Available online 24 April 2015

Keywords:

Nuclear waste disposal

Natural salt

Crushed salt

Large strains

Numerical modeling

Coupled processes

ABSTRACT

A modeling effort has been undertaken to investigate the long-term response of a generic salt repository for heat-generating nuclear waste, including processes that could affect the geological (natural salt host rock) and geotechnical (backfill) barriers. For this purpose, the TOUGH-FLAC sequential simulator for coupled thermal–hydraulic–mechanical processes modeling has recently been provided with a capability for large strains and creep. The responses of the saliferous host rock and the crushed salt backfill are modeled using dedicated constitutive relationships. Similarly, the coupling between the geomechanics and the flow sub-problems is performed on the basis of theoretical and experimental studies. The repository investigated in this work considers in-drift emplacement of the waste packages and subsequent backfill of the drifts with run-of-mine salt. Using the updated TOUGH-FLAC, the compaction of the backfill and the evolution of its properties as porosity decreases can be modeled. Additionally, different processes that may influence the initial tightness of the host rock can be investigated. On the basis of state-of-the-art phenomenological models, our simulation results show that, in order to evaluate the barriers integrity, it is necessary to consider full coupling between thermal, hydraulic and mechanical processes. A base case scenario that accounts for these coupled processes is presented and compared to a case in which the mechanical processes are disregarded. Also, we investigate the sensitivity of the coupled numerical predictions to two factors: the initial saturation within the host rock and the capillary forces. Although the outcome of these simulations is preliminary and will be improved as the understanding of relevant processes moves forward, the numerical tools required to perform the target predictions have been significantly improved.

© 2015 Elsevier B.V. All rights reserved.

1. Introduction

Rock salt is a potential medium for the underground disposal of nuclear waste because of several assets, in particular its near-zero primary permeability (i.e., undisturbed salt is water and gas tight), its very low porosity, its high ductility, its healing capacity and its relatively high thermal conductivity as compared to other shallow-crustal rock types (Bechthold et al., 1999; Carter et al., 2011a; Hardin and Voegele, 2013; Hou, 2003; Hunsche and Hampel, 1999). Moreover, rock salt is usually found underground in large volumes in stable geological areas and is easy to mine. Additionally, the run-of-mine salt may be used to backfill mined open emplacement areas (Carter et al., 2011a).

Because of these advantages, rock salt has been studied since the 1960s, and, since 1999, it is being used for disposal and isolation of defense-related transuranic nuclear waste (equivalent to long-lived, intermediate-level waste) at the WIPP site (Waste Isolation Pilot Plant) (DOE/WIPP, 2002). Furthermore, in Germany a complete safety assessment analysis has been recently performed for the Gorleben site,

describing all aspects which are of importance for a heat-generating nuclear waste repository in rock salt (Mönig et al., 2013).

In the current research, attention is being focused on heat-generating nuclear waste (such as used nuclear fuel or high-level waste). The work presented in this paper has been developed within the framework of the US Department of Energy Used Fuel Disposition Campaign (Nutt et al., 2011). One of the missions of this campaign is to conduct scientific research to enable underground disposal of used nuclear fuel and high-level waste generated by existing and future nuclear fuel cycles. Initially, the campaign focuses on generic research that will support future site-specific work. Accordingly, we have considered a generic salt repository (GSR) with in-drift emplacement of the waste packages and subsequent backfill of the drifts with crushed (run-of-mine) salt. In such a scenario, the crushed salt backfill gets progressively compacted as the natural salt creeps. Once the reconsolidation process is over, it is expected that the backfill will provide a geotechnical barrier (Bechthold et al., 2004; Wiczorek et al., 2012), thereby reinforcing the natural barrier function of the host rock. In this context, the ultimate goal of the present research is to evaluate the long-term integrity of the geological (host rock) barrier, as well as the development and long-term integrity of the geotechnical (backfill) barrier. Indeed, in the unfavorable event of a radionuclide release from the waste packages, these barriers are essential to prevent

^{*} Corresponding author.

E-mail addresses: lblancomartin@lbl.gov (L. Blanco Martín), jrutqvist@lbl.gov (J. Rutqvist), jtirkholzer@lbl.gov (J.T. Birkholzer).

the escape and the transport of undesired fluids into the biosphere. Key parameters of barrier integrity are permeability and porosity (Hansen, 2008; Schulze et al., 2001).

As for the natural salt, it is well known that its initial tightness could be affected by processes that take place at different stages during the lifetime of a repository (Hou, 2003; Hunsche and Hampel, 1999; Peach and Spiers, 1996; Schulze et al., 2001; Stormont and Daemen, 1992; Wolters et al., 2010). First, the development of an excavation damaged zone (EDZ) around the mined openings represents a potential risk because preferential flow pathways could be created. Thermo-mechanical damage occurs if the dilatancy boundary is exceeded (Minkley and Popp, 2010; Wolters et al., 2012). Second, a pore pressure-driven percolation process (fluid infiltration) can take place if the pore pressure locally exceeds the minimum compressive principal stress. Several factors can result in fluid permeation: thermal pressurization within the rock (due to thermal expansion of pore fluids that cannot escape in a very low-permeability medium – this is particularly true when the pore space is mostly occupied by low compressibility fluids, such as water or brine), convergence-induced pore pressure increase, and gas generation from the waste packages, among others. Should thermo-mechanical damage or fluid infiltration occur, the initial, near-zero permeability of the host rock would be superseded by an increased, secondary permeability (Wieczorek et al., 2012; Wolters et al., 2012). These perturbations, however, are generally not persistent in a plastic medium such as rock salt. Once the stress regime becomes favorable, healing takes place. Healing processes consist in the development of cohesion between former crack planes (in extension of pore space closure). They decrease damage by helping bond fracture surfaces and close micro-fractures (Hansen, 2008; Popp et al., 2012; Wolters et al., 2012), i.e., salt damage is reversible (Hansen, 2008). Additionally, local widening of grain boundaries caused by percolation of pore fluids ceases as the pore pressure decreases below the minimum compressive principal stress (Wolters et al., 2012). Damage, healing and percolation processes within natural salt have been thoroughly studied at the laboratory scale and have been included in advanced, validated constitutive relationships (Hampel et al., 2013; Wolters et al., 2012). They have also been observed in various field studies (Bechthold et al., 2004; GRS, 2001; Hou, 2003; Popp and Minkley, 2010).

The reconsolidation process of the crushed salt used for backfill has also been studied in the past years, and several time-dependent compaction models have been proposed (Callahan et al., 1998; Olivella and Gens, 2002; Sjaardema and Krieg, 1987). As compaction takes place, the mechanical and flow properties of the crushed salt evolve towards those of the natural salt. In particular, permeability decreases several orders of magnitude, the thermal conductivity increases and so do the elastic moduli (Bechthold et al., 2004; Bechthold et al., 1999; Callahan et al., 1998; Hurtado et al., 1997; Wieczorek et al., 2012). Experimental studies have shown that the compaction rate increases with the moisture content (Popp and Salzer, 2012). On the other hand, the reconsolidation process at the high temperatures associated with exothermic nuclear waste would benefit from further investigation (Carter et al., 2011a). Moreover, the compaction behavior at porosities lower than 5–10% is not currently well understood, and data in this range are scarce (Kröhn et al., 2012).

The safety assessment of a repository for nuclear waste requires the demonstration of the integrity of the geological and geotechnical barriers. For such demonstration, thermal, hydraulic, mechanical (and chemical) processes need to be considered. These processes interact and influence each other in a complex manner. In addition, they do not necessarily have the same spatial and temporal scales; therefore, numerical modeling using proper tools is needed (Tsang et al., 2009). Several modeling studies on the disposal of heat-generating nuclear waste in saliferous formations have been reported in the literature (Argüello and Rath, 2012, 2013; Bechthold et al., 1999, 2004; Clayton et al., 2012; Hampel et al., 2013; Javeri and Baltes, 2008; Kock et al., 2013; Lerch et al., 2012; Lowe and Knowles, 1989; Munson et al., 1990; Pudewills et al., 1995; Stone et al., 2010). Nevertheless, the

majority of these studies do not consider simultaneously important thermal, hydraulic and mechanical processes. In this research, we seek to improve the current understanding of the long-term integrity of the natural salt and the crushed salt by considering coupled thermal–hydraulic–mechanical (THM) processes. The TOUGH-FLAC sequential simulator for flow and geomechanics (Rutqvist and Tsang, 2003) has been adapted to predict the long-term response of a generic salt repository for heat-generating nuclear waste. In particular, the updated version of the simulator is able to deal with the large strains induced by the compaction of the backfill and the creep of the natural salt. State-of-the-art constitutive relationships and coupling functions between flow and geomechanical processes have been implemented.

This paper is organized as follows. First, the updated version of TOUGH-FLAC for coupled processes in saliferous media is described. Then, the constitutive relationships selected to model the long-term response of the natural salt and the crushed salt are presented, together with relevant flow and mechanical properties and their interrelated evolution. Such evolution is based on previous laboratory and field investigations. Next, the long-term response of the generic salt repository considered in this study is predicted using the new version of TOUGH-FLAC. After a description of the model and the simulation set-up, THM results of a base case scenario are presented and discussed. The predictions include the stages of excavation, waste emplacement, backfilling and post-closure (100000 years). Then, we compare results from THM and TH simulations to evaluate the relevance of the coupling to mechanical processes (in particular, fluid infiltration, damage and healing processes within the host rock, as well as backfill compaction). This comparison supports the need to develop a simulator able to deal with coupled THM processes, including large strains and creep. Finally, we investigate the sensitivity of the THM predictions to two factors: the initial saturation within the host rock and the strength of the capillary forces.

2. Materials and methods

2.1. The TOUGH-FLAC simulator for large strains and creep

The TOUGH-FLAC simulator has been developed at Lawrence Berkeley National Laboratory (Rutqvist and Tsang, 2003) and is based on an explicit sequential method to couple flow and geomechanics. The multiphase fluid and heat flows are computed by TOUGH2 (Pruess et al., 2011) and the geomechanical response of the system is calculated using FLAC^{3D} (Itasca, 2009). TOUGH-FLAC has been successfully used in different application fields, including nuclear waste disposal, geological carbon sequestration and geothermal reservoir engineering (Rutqvist, 2011; Rutqvist et al., 2002).

The coupling scheme between TOUGH2 and FLAC^{3D} is based on the fixed stress-split sequential method (Kim et al., 2011). In this method, the flow problem is solved first (with an explicit evaluation of the volumetric total stress) and the pore pressure and the temperature are prescribed during the geomechanical calculation, which therefore requires drained mechanical properties. The fundamentals of fully coupled and sequential approaches can be found in the literature (Jeannin et al., 2007; Jha and Juanes, 2007; Settari and Mourits, 1998; Settari and Walters, 2001), as well as discussions of the main advantages of sequential methods (Dean et al., 2006; Felippa and Park, 1980; Thomas et al., 2003; Vijalapura et al., 2005).

The applicability of TOUGH-FLAC to study coupled THM processes in saliferous media has required some modifications to the simulator. In particular, significant volume changes may result not only from the backfill reconsolidation, but also from the possible damage and healing processes within the natural salt. Also, the viscoplastic rheology of both materials may entail severe mesh distortions. While FLAC^{3D} is able to deal with large strains, TOUGH2 adaptation to large strains has required some modifications in the mass and heat balance equations.

Currently, the modeling sequence is as follows. TOUGH2 moves the simulation forward and FLAC^{3D} is executed once within a TOUGH2 time step, just before the Newton–Raphson iteration process to solve the residual nonlinear equations. A schematic view of the coupled THM modeling sequence is displayed in Fig. 1. The pressure, P^n , temperature, T^n , liquid saturation, S_l^n , and porosity, ϕ^n , of each grid block computed at the end of the previous time step (from t^{n-1} to t^n) are transferred to FLAC^{3D}. Note that the pressure transferred depends on the definition of pore pressure and effective stress in multiphase systems (Coussy, 2004; Kim et al., 2013).

From flow to geomechanics, the pore pressure change, $\Delta P = P^n - P^{n-1}$, and the temperature change, $\Delta T = T^n - T^{n-1}$, corresponding to two successive TOUGH2 time steps are accounted for as a correction to the total stress tensor, σ_{ij} (direct coupling). These changes are computed internally in FLAC^{3D} once the new values P^n and T^n are transferred from TOUGH2. The corrected total stress tensor, σ_{ij}^c , has the form

$$\sigma_{ij}^c = \sigma_{ij} - \alpha \Delta P \delta_{ij} - 3\alpha_T K \Delta T \delta_{ij} \quad (1)$$

where $\alpha [-]$ is the Biot coefficient of the material, $\alpha_T [K^{-1}]$ is its linear thermal expansion coefficient, $K [MPa]$ is its bulk modulus and $\delta_{ij} [-]$ is the Kronecker delta. Compressive stresses are defined negative here. From Eq. (1), it can be inferred that the coupling from flow to geomechanics only affects the volumetric component of the stress tensor. Porosity and liquid saturation are used to update the body forces in the quasi-static governing equations of the geomechanical analysis (see, e.g., Kim et al. (2012)). Note that these equations account for the thermal strains that result from the temperature change ΔT .

Once all the updates are made, FLAC^{3D} runs in creep and large-strain modes from time t^{n-1} to time t^n . A new equilibrium mechanical state is obtained at time t^n (stresses σ^n and strains ϵ^n in Fig. 1). Recall that during the mechanical calculation, the flow data (P^n , T^n , S_l^n and ϕ^n) remain constant.

From geomechanics to flow, geometrical changes are first accounted for. The geometrical data updated in TOUGH2 are: volume of the elements, distances of the centroids of two connected elements to their common interface, common interface area, and cosine of the angle between the gravitational acceleration vector and the line passing through the centroids of two connected elements. Moreover, we have extended the mass and heat balance equations to account for possible volume changes. Additionally, porosity variations during the current time step (i.e., from t^n to t^{n+1} in Fig. 1) are computed in TOUGH2 using a formulation of coupled geomechanics and multiphase fluid and heat flows, adapted from Kim et al. (2012). This analytical formulation is an extension of the classic thermodynamical approach implemented in TOUGH2 and includes a porosity correction term that accounts for geomechanical effects (via the volumetric component of the total stress tensor).

Additionally, the new mechanical state obtained at t^n is used through several coupling functions to compute mechanically induced changes in permeability and capillary pressure (Δk and ΔP_c in Fig. 1). The coupling

functions depend on each material (and the phenomena it goes through) and should be based on specific laboratory and theoretical results; they will be described in Sections 2.2 and 2.3 for the natural salt and the crushed salt respectively. The mechanically modified flow properties (k^n , ϕ^n and P_c^n in Fig. 1) are used to solve the residual equations of the flow problem. Within a time step, the Newton–Raphson iteration process is continued until the residuals are reduced below a preset convergence tolerance. At the end of the current time step (time t^{n+1} in Fig. 1), a new set of primary thermodynamic variables (P^{n+1} , T^{n+1} and S_l^{n+1} in Fig. 1) and new flow properties (k^{n+1} , ϕ^{n+1} and P_c^{n+1} in the figure) are obtained.

Finally, it should be noted that, while in this research it has been decided to update directly the geometrical data in the flow simulator (updated Lagrangian method), other approaches are possible (Bathe et al., 1975; Coussy, 1995). The main alternative consists in keeping the initial geometry as a reference and in mapping pertinent properties onto that initial configuration (total Lagrangian method). While both total and updated Lagrangian methods are mathematically equivalent, the total Lagrangian method is thought to reduce computational cost. Research is currently being undertaken on this topic (Rutqvist et al., 2013).

2.2. Thermal, hydraulic and mechanical characteristics of the natural salt

Rock salt is known to creep under the effect of temperature and deviatoric stresses, and also to experience thermo-mechanically induced damage and fluid permeation if certain stress thresholds are exceeded (Hou, 2003; Hunsche and Hampel, 1999; Minkley and Popp, 2010; Popp and Minkley, 2010; Schulze et al., 2001; Wolters et al., 2010). In order to predict the long-term response of a nuclear waste repository, a reliable extrapolation of the behavior observed in a shorter time scale is necessary. Such extrapolation should be performed on the basis of constitutive relationships with a physical foundation.

In this research, we use the Lux/Wolters constitutive model for rock salt (Hou, 2003; Hou and Lux, 1998, 1999, 2000; Hou et al., 1998; Lux, 1984; Wolters et al., 2012). This model is based on continuum damage mechanics and has been established using a series of laboratory investigations designed to study, from a macroscopic viewpoint, the mechanisms involved in the short- and long-term responses of rock salt. The Lux/Wolters model has been validated against field and laboratory scale data (Hou, 2003; Wolters et al., 2010) and has been implemented as a user-defined model in FLAC^{3D}.

In the Lux/Wolters model, the total strain rate tensor, $\dot{\epsilon}_{ij}$, is composed of the superposition of four strain rate tensors issued from different mechanisms: elastic, viscoplastic, damage-induced and healing processes. The total strain rate tensor reads

$$\dot{\epsilon}_{ij} = \dot{\epsilon}_{ij}^e + \dot{\epsilon}_{ij}^{vp} + \dot{\epsilon}_{ij}^d + \dot{\epsilon}_{ij}^h \quad (2)$$

where superscripts *e*, *vp*, *d* and *h* stand for elastic, viscoplastic, damage and healing, respectively. All the components of the strain rate tensor defined in Eq. (2) take a damage-induced reduction of the load-bearing cross-sectional area into account, in accordance with a previous study (Kachanov, 1986). Equations of the Lux/Wolters model can be found in Wolters et al. (2012). As compared to classical models developed to describe the mechanical behavior of rock salt (Chan et al., 1997; Cristescu, 1993; Munson, 1997, among others), one originality of the Lux/Wolters model is its capability to account for healing processes. Also, the Biot coefficient is damage-dependent. Other state-of-the-art constitutive models for rock salt are described in Hampel et al. (2012).

The damage-free viscoplastic strain rate tensor, $\dot{\epsilon}_{ij}^{vp}$, is purely deviatoric (i.e., there are no volumetric changes related to viscoplasticity). The viscoplastic response is modeled using the Lubby2 model (Lux, 1984). As compared to the nonlinear Burgers model – that accounts for transient and stationary creep (Kelvin and Maxwell elements, respectively) – in the

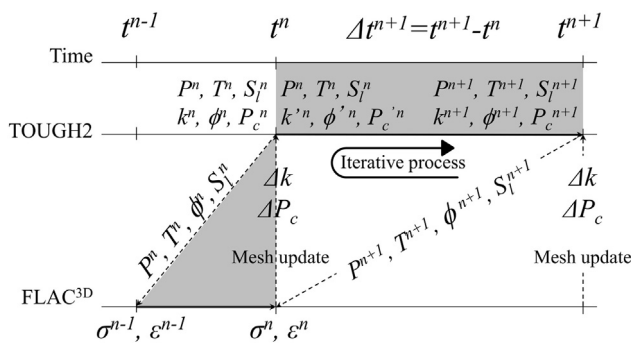


Fig. 1. TOUGH-FLAC explicit sequential scheme (adapted from Rutqvist et al., 2002). The highlighted zones correspond to the TOUGH2 time step between time t^n and t^{n+1} .

Lubby2 model the parameters are dependent on both stress and temperature.

The damage strain rate tensor, $\dot{\epsilon}_{ij}^d$, comes into play if there is an excess of either tensile or shear stresses beyond a failure (or dilatancy) boundary. The tensile strength of rock salt is small (typically <5 MPa). The shear strength is a function of the minimum principal stress and the Lode angle. The damage strain rate tensor has a non-zero volumetric component (i.e., damage causes a non-elastic volume change, also referred to as dilatancy). The analytical formulation of the damage-induced strain rate tensor conforms to the plasticity theory, with a non-associated flow rule.

The last component of the strain rate tensor, $\dot{\epsilon}_{ij}^h$, accounts for damage healing. Healing reduces dilatancy and damage, but cannot occur while damage (shear or tensile yielding) is taking place. Moreover, some damage is necessary before healing can actually start. According to laboratory observations, the recovery of damage in the *Lux/Wolters* model is faster at the beginning of the healing process (due to a rapid volume contraction), while in a second stage slower mechanisms such as recrystallization or diffusion dominate, cf. *Hou (2003)*. In the current version of the model, humidity effects are not accounted for.

The damage dependence of the Biot coefficient is also included in the model. In the undisturbed state, the Biot coefficient of rock salt is often considered to be very close to zero (*Hou, 2002*), but increases as damage takes place. On the other hand, healing can restore the initial Biot coefficient. From the interpretation of laboratory scale results, the evolution of the Biot coefficient is described by (*Hou, 2002; Kansy, 2007*)

$$\alpha_{\text{salt}} = \max\left(\frac{D}{D_\alpha}, 1 - \exp\left(\frac{\sigma_v m D}{D - D_\alpha}\right)\right) \quad (3)$$

where D [–] is a damage parameter (*Hou, 2002; Wolters et al., 2012*), $D_\alpha = 0.1$ [–] is a constant, $\sigma_v \geq 0$ [MPa] is von Mises equivalent stress and $m < 0$ [MPa^{–1}] is a parameter that enhances Maxwell viscosity (Maxwell viscosity is a parameter in rheological viscoplastic models and decreases if either temperature or equivalent stress increases. Following *Wolters et al. (2012)*, parameter m determines the influence of the equivalent stress on Maxwell viscosity).

In total, the *Lux/Wolters* constitutive model needs 34 parameters (*Lerche, 2012*). However, the number of parameters used in a simulation may be reduced depending on the phenomena under investigation.

From the perspective of heat flow, experimental results on salt rock mass suggest that the rock grain specific heat and the thermal conductivity are dependent on temperature. The evolution of the specific heat is described by

$$C = 855 + 0.177T \quad (4)$$

where T [°C] and C [J·kg^{–1}·K^{–1}] (*Bechthold et al., 1999*). On the other hand, the thermal conductivity of the natural salt has been found to decrease with temperature. From experimental evidence (*Bechthold et al., 1999*), the evolution may be described using

$$\lambda_{\text{salt}} = 5.734 - 1.838 \cdot 10^{-2}T + 2.86 \cdot 10^{-5}T^2 - 1.51 \cdot 10^{-8}T^3 \quad (5)$$

In Eq. (5), T [°C] and λ_{salt} [W·m^{–1}·K^{–1}].

Finally, laboratory and field investigations on rock salt have confirmed that there exist two independent mechanisms that could cause a loss of the natural barrier integrity (*Popp and Minkley, 2010; Wolters et al., 2012*). These mechanisms are likely to modify key parameters of fluid migration, such as permeability and porosity (*Cosenza and Ghoreychi, 1999; Wolters et al., 2010*). First, thermo-mechanically induced damage occurs if the dilatancy boundary is exceeded (this likely takes place in the EDZ). Several laboratory investigations show that the secondary permeability developed is a very nonlinear function of dilatancy (*Peach and Spiers, 1996; Popp and Kern, 1998; Stormont and*

Daemen, 1992; Wolters et al., 2010). From these investigations, a porosity–permeability relationship (or secondary permeability function) has been formulated (*Wolters et al., 2010*) as follows

$$k_{\text{salt}}^{\text{secondary}} = 10^{\log(k_{\text{min}}^{\text{secondary}}) + \left\langle \log(\epsilon_{\text{vol}}) - \log(\epsilon_{\text{vol},0}) + d \exp\left(\frac{f\sigma'_{\perp 2}}{\ln(10)}(Ei(e\epsilon_{\text{vol}}) - Ei(e\epsilon_{\text{vol},0}))\right) \right\rangle} k^* \quad (6)$$

with $\langle x \rangle = x$ if $x > 0$ and $\langle x \rangle = 0$ otherwise. Parameter $k_{\text{min}}^{\text{secondary}}$ [m²] is the minimum secondary permeability at the onset of thermo-mechanically induced damage, $\epsilon_{\text{vol}} \geq 0$ [–] is dilatancy ($\epsilon_{\text{vol},0}$ [–] is the initial dilatancy, i.e., the dilatancy limit at which $k_{\text{min}}^{\text{secondary}}$ starts to develop due to the connection of micro-fissures), $\sigma'_{\perp 2}$ [MPa] is the effective stress perpendicular to the orientation of the micro-fissures, $Ei(x)$ is the exponential integral function and $k^* = 1$ m². Parameters d , e and f are salt-specific. Note that the permeability recovery due to healing (dilatancy decrease) can be modeled using Eq. (6).

Secondly, natural salt may be subjected to a fluid infiltration (or percolation) process if the pore pressure locally exceeds the minimum compressive principal stress (*Popp and Minkley, 2010; Wolters et al., 2010*). Such a scenario is feasible in a repository for heat-generating nuclear waste in rock salt given the thermal pressurization of fluids within the very-low permeability host rock and the convergence-induced pore pressure increase. Gas generation from the waste packages may also trigger fluid permeation within the host rock. The study of fluid infiltration has led to the formulation of experimentally-determined relationships for the induced secondary permeability. In this study, we use

$$k_{\text{salt}}^{\text{secondary}} = 10^{i_1 + i_2 \arctan(i_3 \Delta P_{Fi}) + i_4 \exp(i_5 \Delta P_{Fi})} k^* \quad (7)$$

where $\Delta P_{Fi} = \sigma_3 + P$ [MPa] (σ_3 is the minimum compressive principal stress and P is the pore pressure), $k^* = 1$ m² and i_1 , i_2 , i_3 , i_4 and i_5 are salt-specific parameters (*Wolters et al., 2012*). Note that Eq. (7) is only used to compute a permeability increase if $\Delta P_{Fi} \geq 0$. Several studies (*Fokker, 1995; Kenter et al., 1990; Popp and Minkley, 2010*) show that for macro-fractures to develop (hydraulically induced damage), $\Delta P_{Fi} \approx 2$ –4 MPa (below this value, opening of grain boundaries and/or micro-fractures occur). Experimental results show that fluid infiltration occurs without necessarily exceeding the dilatancy boundary (*Popp et al., 2012; Wolters et al., 2012*).

An infiltration test conducted at Clausthal University of Technology (*Wolters et al., 2012*) has been modeled using TOUGH-FLAC and the simulation results have been compared with experimental data. The test was conducted on a cylindrical rock salt sample from a German salt mine. The sample was 350 mm long, had a diameter of 150 mm and was initially unsaturated. A 100 mm long and 50 mm diameter borehole was drilled along the core axis, see *Fig. 2a*. A fluid containing a fluorescent tracer was injected through the borehole, while the upper and lateral surfaces of the sample were no-flow boundaries (the downstream boundary was kept at atmospheric pressure). The test lasted 6 days and was held at room temperature (about 25 °C) in a tri-axial cell, with an axial stress of 20.5 MPa and a confining pressure of 20 MPa. The fluid was injected in the borehole at a constant pressure of 21 MPa. After the test, the rock salt sample was sliced axially and put under ultraviolet light; this caused the tracer in the injected fluid to fluoresce. The delimited area in *Fig. 2a* represents the extension of the fluorescent, infiltrated area within the rock salt sample. *Fig. 2b* displays the predicted infiltrated area at the end of the test (i.e., the area in which $\Delta P_{Fi} \geq 0$). In this area, the sample is saturated. It can be inferred from the two images in *Fig. 2* that the numerical prediction is similar to the experimental results. The TOUGH-FLAC run was carried out in axisymmetric conditions. The initial permeability of the salt sample was 10^{-22} m² and Eq. (7) was used in the grid blocks verifying the condition $\Delta P_{Fi} \geq 0$. Corey's relative permeability curves were used with zero residual liquid and gas saturations. The porosity of the sample was

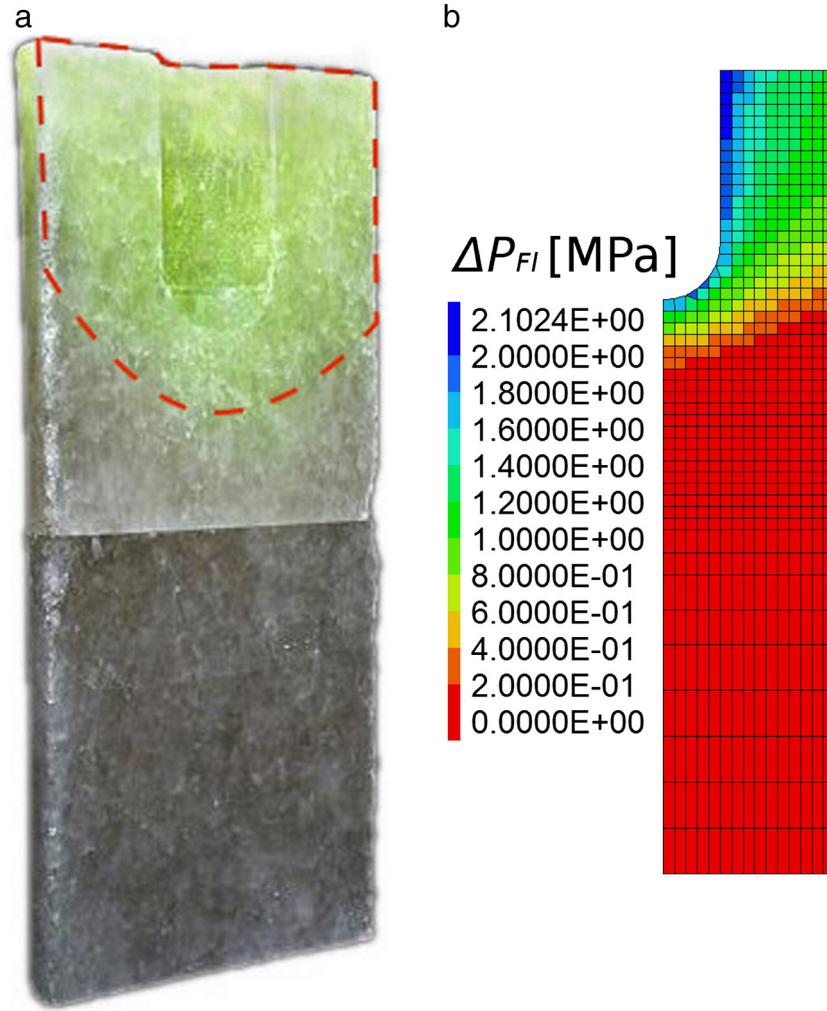


Fig. 2. Investigation on fluid infiltration in rock salt. (a): infiltrated area observed after a laboratory test performed by Wolters et al. (2012); (b): modeled infiltrated area using TOUGH-FLAC.

approximated to 0.5% based on the volume of fluid injected and the delimited area in Fig. 2a. Capillary effects were disregarded.

The solid line in Fig. 3 represents the modeled volume of fluid injected into the rock sample, while the points correspond to the volume of fluid injected during the experiment (these data are calculated subtracting the borehole volume from the raw values of injected volume). Note that the numerical prediction accounts for the borehole compressibility; this compressibility might explain the sharp increase in the volume injected at the beginning of the test. As the figure shows, the experimental and simulated injected volumes are in good agreement.

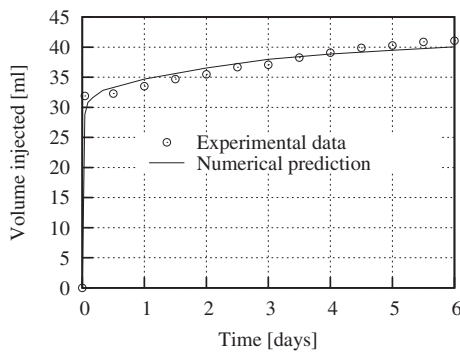


Fig. 3. Investigation on fluid infiltration in rock salt. Comparison between experimental and modeled volume of fluid injected into the sample.

2.3. Thermal, hydraulic and mechanical characteristics of the crushed salt

The reconsolidation process of the crushed salt is modeled using a modified version of the *cwipp* model available in FLAC^{3D}. The *cwipp* model is based on previous studies on crushed salt compaction (Callahan and DeVries, 1991; Sjaardema and Krieg, 1987) and on the *wipp* model for natural salt, also implemented in FLAC^{3D} (Itasca, 2009).

The main characteristic of the *cwipp* model is that it allows modeling time-dependent volumetric strain changes (classically, viscoplasticity occurs at constant volume). The total strain rate tensor, $\dot{\epsilon}_{ij}$, comprises a nonlinear elastic component, a viscous compaction component and a viscous shear contribution. The latter is adapted from the *wipp* model and is purely deviatoric. The total strain rate tensor reads

$$\dot{\epsilon}_{ij} = \dot{\epsilon}_{ij}^e + \dot{\epsilon}_{ij}^{vc} + \dot{\epsilon}_{ij}^{vs} \tag{8}$$

where superscripts *e*, *vc* and *vs* stand for elastic, viscous compaction and viscous shear, respectively. As reconsolidation occurs, density increases towards that of the natural salt. While density is not allowed to decrease in the *cwipp* model, it honors the volumetric strain evolution in our modified version. The nonlinear density rate is derived from experimental results. The viscous compaction term in the model accounts for the density evolution. This term is only active if the mean effective stress is compressive and if the monotonic density has not yet reached the intact salt density (i.e., there is no further compaction beyond the density

of intact salt). During compaction, the elastic parameters (shear, G , and bulk, K , moduli) increase as the monotonic density increases according to a nonlinear empirical expression of the form

$$a = a_{\text{salt}} \exp(a_1[\rho - \rho_{\text{salt}}]) \quad (9)$$

where $a = \{K, G\}$. Variables ρ and ρ_{salt} stand for the drained densities of the crushed salt and the natural salt, respectively (drained density is defined as rock mass divided by total volume). Parameter a_1 [$\text{kg}^{-1} \cdot \text{m}^3$] is obtained from the condition that the moduli take their initial values at the initial value of density. According to the model defined in Eq. (9), when $\rho = \rho_{\text{salt}}$ the elastic moduli are those of the natural salt. However, it is important to highlight that experimental data sets at realistic load conditions do not cover the porosity range below 5–10% (DBE, 2001; Kröhn et al., 2012). Therefore, some uncertainties exist about the accuracy of the *cwipp* model in that range.

In total, the *cwipp* model is characterized by 17 parameters. Note that as the bulk modulus increases towards that of the intact salt, the Biot coefficient decreases from almost 1 to the Biot coefficient of the host rock. In this study, we calculate the Biot coefficient using the classical definition (Coussy, 1995)

$$\alpha_{\text{crushed salt}} = 1 - \frac{K}{K_s} \quad (10)$$

where K is the drained bulk modulus and K_s is the bulk modulus of the solid material.

It should be noted that the long-term mechanical responses predicted by the *cwipp* and the *Lux/Wolters* models are similar: due to the creep over time, the stresses tend towards the isotropic state and therefore the deviatoric components of both models tend to zero; for the crushed salt, the compaction component vanishes after full reconsolidation, and for the natural salt, damage and healing counteract each other. Consequently, only the elastic components prevail, see Eqs. (2) and (8). Given that after reconsolidation the elastic moduli of the crushed salt are equal to those of the natural salt, the modeled long-term responses of the two materials are similar.

As for the flow properties of the crushed salt, experimental investigations suggest that not only the porosity, but also the permeability, the specific heat and the thermal conductivity evolve as reconsolidation occurs (Bechthold et al., 2004). After full reconsolidation, these properties reach the characteristic values of the natural salt; however, their evolution is uncertain because scarce data exist for low porosities (<5–10%). In this research, the permeability decrease is calculated using

$$k_{\text{crushed salt}} = 5.6810^{-11} \phi^{4.36} \quad (11)$$

where ϕ [–] is the current porosity and $k_{\text{crushed salt}}$ [m^2]. We note that we developed Eq. (11) as an approximation to available porosity data in the range 1.5–40%. The grain specific heat dependence on temperature is similar to that of the natural salt (Eq. (4)). The thermal conductivity increases nonlinearly as porosity decreases according to

$$\lambda_{\text{crushed salt}} = -270\phi^4 + 370\phi^3 - 136\phi^2 + 1.5\phi + 5 \quad (12)$$

where ϕ [–] is the current porosity and $\lambda_{\text{crushed salt}}$ [$\text{W} \cdot \text{m}^{-1} \cdot \text{K}^{-1}$] (Bechthold et al., 2004).

Finally, regarding the damage processes that could affect the flow properties of the crushed salt, fluid infiltration may take place after reconsolidation if $\Delta P_{fl} \geq 0$. In that case, we calculate the permeability increase using Eq. (7).

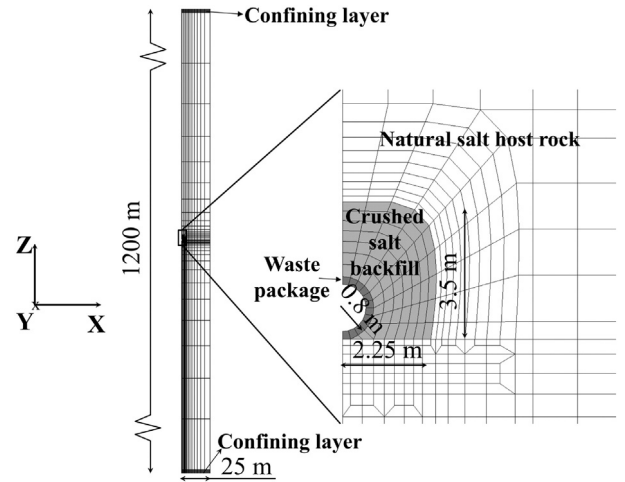


Fig. 4. Geometry of the generic salt repository studied in this work and enlarged view of the drift area.

3. Long-term prediction of a generic salt repository for heat-generating nuclear waste

3.1. Model description

We simulate a generic salt repository, i.e., without reference to a particular disposal program. We assume that the waste packages are emplaced parallel to the drift axis. Our model extends 1200 m in the vertical direction (Z axis) and starts at the ground surface ($Z = 0$). The repository is located in the middle of a 400 m thick salt layer, at a depth of 600 m. Two 400 m thick sandstone layers confine the salt seam. The drifts are 4.5 m wide and 3.5 m high. The cylindrical metallic waste packages are 5.5 m long, have a diameter of 1.6 m and are separated by 3 m along the drift axis.

At this initial stage of the research, we use a two-dimensional plane-strain assumption. Symmetry allows modeling just half of one drift. In the X direction, drifts are 50 m apart. The model geometry is presented in Fig. 4, with an enlarged view of the area near the drift. We acknowledge that more accurate predictions would be obtained in a three-dimensional configuration, including the space between waste packages (i.e., drift cross-sections containing only crushed salt). In a two-dimensional case, temperatures are slightly over-predicted, causing faster drift closure and consequently faster backfill reconsolidation. In the future, once further improvements are made into the simulator, in particular as regards computational efficiency, we intend to perform full 3D simulations.

Along with the mechanical response, two-phase flow of water and air (by advection and diffusion) and heat flow (by conduction and convection) are modeled. TOUGH2 Equation Of State (EOS) module 4

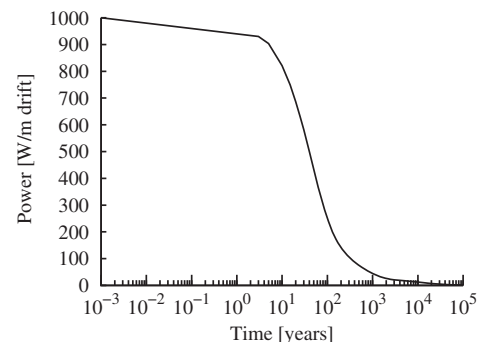


Fig. 5. Heat load per meter of drift for a waste package containing 10 PWR assemblies, assuming underground emplacement after 20 years of interim storage (after Carter et al., 2011b).

Table 1
Mechanical and flow properties of the crushed salt, natural salt and confining layers.

Property [unit]	Crushed salt	Rock salt	Confining rock
Grain density, ρ [$\text{kg}\cdot\text{m}^{-3}$]	2200	2200	2600
K [MPa]	150 ^a	16,650 ^b	37,900
G [MPa]	70 ^a	7690 ^b	19,500
α_f [K^{-1}]	$4 \cdot 10^{-5}$	$4 \cdot 10^{-5}$	10^{-5}
α [-]	1 ^a	0.003 ^b	1
Relative permeability functions	Corey	Corey	van Genuchten (liquid), Corey (gas)
Residual liquid saturation, S_{lr} [-]	0.1	0.1	0.02
Residual gas saturation, S_{gr} [-]	0	0	0.01
van Genuchten's λ [-]	0.6	0.6	0.6
van Genuchten's P_0 [MPa]	0.0004 ^c	5.7 ^c	3.6
van Genuchten's S_{lr} [-]	0.01	0.01	0.01

^a Non-constant value (see Section 2.3).

^b Values are damage- and healing-dependent (see Section 2.2).

^c Non-constant value (see Section 3.2).

is used (Pruess et al., 2011). This module provides a capability for vapor pressure lowering, which allows a liquid phase to exist when the vapor partial pressure and the gas phase pressure are lower than the saturation pressure (due to phase adsorption and capillary effects). Vapor pressure lowering is modeled via Kelvin's equation (Pruess et al., 2011).

The heat released by each waste package is consistent with the expected nuclear waste characteristics in the US Department of Energy Used Fuel Disposition Campaign (Carter et al., 2011b). It is assumed that each waste package comprises ten pressurized water reactor (PWR) assemblies and that the packages are emplaced underground after 20 years of interim storage. Under these conditions, and taking the size and distance between canisters into account, the average heat load per meter of drift is approximately 1000 W at the time of emplacement. The heat load evolution after emplacement is displayed in Fig. 5 (note that the time is reset to zero when the waste packages are emplaced underground).

3.2. THM properties, initial and boundary conditions

Table 1 lists parameters used for the crushed salt, the host rock and the confining layers. Some of these parameters have been adopted from previous research (Bechthold et al., 2004; Camphouse et al., 2012; Jové-Colón et al., 2012; Olivella et al., 2011). We highlight that, in the absence of sufficient experimental data on capillary effects in natural halite, we have used an extrapolation of capillary pressure data corresponding to granular salt (Olivella et al., 2011), using a Leverett factor (Cinar et al., 2006; Leverett, 1941). The van Genuchten function (van Genuchten, 1980) is used for all materials. Temperature and hysteresis effects on water retention are neglected.

From a mechanical viewpoint, the waste package and the confining layers are assumed to behave elastically. The *Lux/Wolters* model parameters used for the host rock have been obtained from the interpretation of experimental results (Lerche, 2012). Regarding the *cwipp* model for the crushed salt, the values used have been adapted from available experimental data (DBE, 2001; Itasca, 2009). We reiterate that experimental data for porosities smaller than 5–10% are scarce; therefore, some uncertainties exist about the validity of the parameters used.

Table 2
Initial flow parameters of the crushed salt, natural salt and confining layers.

Parameter [unit]	Crushed salt	Rock salt	Confining rock
S_r [-]	0.015	1	1
ϕ [-]	30%	0.2%	12%
k [m^2]	$3 \cdot 10^{-13}$	10^{-22}	10^{-17a}
C [$\text{J}\cdot\text{kg}^{-1}\cdot\text{K}^{-1}$]	860	860	900 ^a
λ [$\text{W}\cdot\text{m}^{-1}\cdot\text{K}^{-1}$]	0.9	4	1.8 ^a

^a Constant values.

For the waste package, we assume $\rho = 7800 \text{ kg}\cdot\text{m}^{-3}$, $\alpha = 1$, $k = 0 \text{ m}^2$ and $\phi = 0.01\%$. Its pores are saturated with gas, and capillary effects are disregarded because no phase changes are expected. Elastic properties correspond to standard steel.

The flow properties of the natural salt and the crushed salt evolve as described in Sections 2.2 and 2.3 respectively. We note that capillary forces are scaled during the simulations as porosity and permeability evolve (Leverett, 1941). On the other hand, properties of the waste package and the confining layers are kept constant during the simulations: the waste package is only modeled to account for the heat release into the repository, and the confining layers are far from the drift, so they are hardly influenced by the THM processes occurring in the drift area.

The molecular diffusion coefficients depend on pressure and temperature (Vargaftik, 1975; Walker et al., 1981). Tortuosity effects are accounted for using the Millington–Quirk model (Millington and Quirk, 1961).

Initial flow parameters are listed in Table 2. The absolute permeability k is assumed isotropic for every material.

A geothermal gradient of $0.025 \text{ K}\cdot\text{m}^{-1}$ is initially applied to the model. This corresponds to about $28 \text{ }^\circ\text{C}$ at the repository level assuming a ground surface temperature of $10 \text{ }^\circ\text{C}$. The initial mechanical condition is isotropic stress, equal to the lithostatic stress magnitude (overburden); this corresponds to about -14 MPa at $Z = -600 \text{ m}$. For the calculation of the pore pressure, we assume that the water table is at the ground surface. Regarding the fluid inclusions at the boundaries of natural salt crystals, we assume an initial liquid saturation of 100%. Prior to the THM run, the excavation, subsequent emplacement of the waste packages and drift backfilling are modeled in FLAC^{3D} to account for the induced stress redistribution and possible changes in the pore pressure. The pore pressure obtained after the excavation is exported to TOUGH2, so that the initial conditions of the THM run are the same in the two codes (the coupled THM simulation covers the post-closure phase of the repository, once the heat-generating waste packages are emplaced and the drifts backfilled). Note that the initial pore pressure within the backfill and the waste package is set to 0.1 MPa (atmospheric pressure). At this stage, and according to the fixed stress-split sequential method to couple flow and geomechanics (Kim et al., 2011), the FLAC^{3D} capability to calculate pore pressure is deactivated (i.e., the pore pressure computed by TOUGH2 is used in both codes, see Fig. 1).

In TOUGH2, Dirichlet boundary conditions are assigned to the top and bottom grid blocks, so that their thermodynamic state remains unchanged. Owing to symmetry, the lateral surfaces of the model are no-flow boundaries. In FLAC^{3D}, the horizontal displacement is blocked in planes $X = 0$ and $X = 25 \text{ m}$, as well as the vertical displacement in plane $Z = -1200 \text{ m}$. Gravitational effects are considered in both codes.

3.3. Base case THM simulation results

In the 2D simulations presented in this paper, our main goal is to analyze the numerical predictions obtained using the updated version of TOUGH-FLAC, in particular as regards the different processes occurring in the host rock and in the backfill material. We note that the discussions hereafter do not include a comprehensive validation based on measurement data of the physical processes.

3.3.1. Preliminary definitions

The base case scenario is characterized by the use of the equivalent pore pressure in the geomechanics sub-problem. The equivalent pore pressure is defined as

$$P_{\text{eq}} = \sum_{i=1}^{NPH} P_i S_i + U \quad (13)$$

where P_i is phase pressure, S_i is phase saturation, U is the interfacial energy per unit of pore volume and NPH is the number of phases present

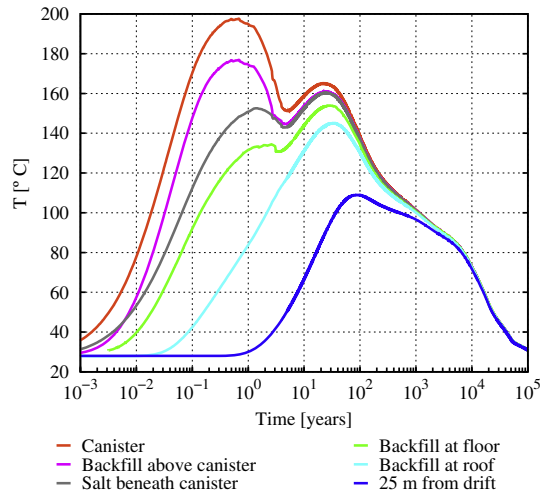


Fig. 6. THM base case scenario: evolution of temperature at several locations in the repository.

(Coussy, 2004). Neglecting the temperature dependence of capillary forces, the interfacial energy can be determined from the capillary curve according to

$$U(S_w) = \int_{S_w}^1 P_{\text{cap}}(S) dS \quad (14)$$

where $P_{\text{cap}} < 0$ is the capillary pressure. According to Coussy (2004), the equivalent pore pressure should be used when capillary forces are non-negligible, which is the case of the natural salt and the reconsolidated crushed salt due to their very low porosity ($\phi < 1\text{--}2\%$). In addition, this pressure is the proper definition of multiphase pore pressure because it renders a formulation that is dissipative (Kim et al., 2013).

We note that other common pore pressure concepts adopted in geomechanics when several fluid phases occupy the pores are the maximum phase pressure and the saturation-weighted average fluid pressure (Kim et al., 2013).

3.3.2. Results

Fig. 6 displays the temperature evolution at different positions in the repository over the simulated 100 000 years of post-closure phase. We stress that these results are dependent on the thermal loading applied (Fig. 5). The temperature at the waste package surface peaks slightly below 200 °C after about one year. Note that the nearby crushed salt and host rock also show an initial temperature peak. This local peak is due to the low thermal conductivity of the backfill before significant compaction takes place (cf. Eq. (12)). After 25 years, a temperature peak of about 160 °C is obtained in the drift area. The temperature 25 m away from the drift peaks at about 108 °C after 80 years, reflecting progressive heat propagation through the natural salt. As compared to other potential host rocks such as clay or granite, and for a given heat load, the peak temperature in a salt-based repository is lower owing to a higher thermal conductivity. A comparatively low peak temperature is a desirable performance indicator for a heat-generating nuclear waste repository.

During the excavation phase, a damaged zone develops in the host rock adjacent to the drift contour due to the high deviatoric stresses in this zone. The thickness of the EDZ is about 1.4 m at the drift floor and 1 m at the sidewalls and roof. Shear damage spreads all around the drift, but tensile damage mostly occurs in the corner area, due to the shape of the drift (see the enlarged view in Fig. 4). While after 4 years shear dilatancy peaks at about 1.2%, tensile dilatancy reaches 2.6% (but remains localized in the corner). As a consequence of damage, Eq. (6) predicts a permeability increase up to four–five orders of magnitude in

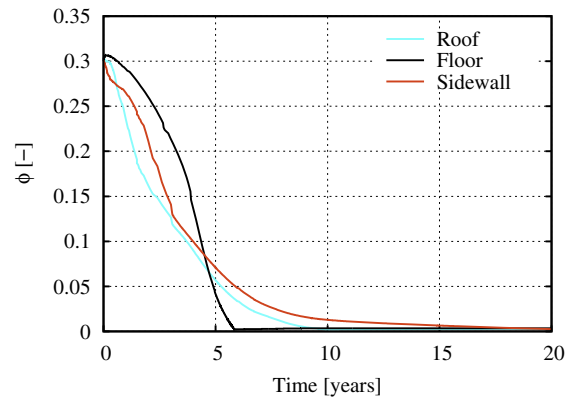


Fig. 7. THM base case scenario: evolution of backfill porosity at three locations during the first 20 years of the post-closure phase.

the EDZ; however, a permeability of $10^{-18}\text{--}10^{-17} \text{ m}^2$ is still characteristic of an impervious material (Bérest et al., 2005; Cosenza, 1996). Porosity also increases, but remains very low ($\phi_{\text{max}} < 1.3\%$). As permeability and porosity increase, capillary forces weaken. Moreover, the Biot coefficient increases according to Eq. (3) up to 0.8 in the most damaged areas, thereby intensifying the poromechanical effects.

As the salt creeps under the effect of temperature and deviatoric stresses, the reconsolidation of the crushed salt starts. Our results suggest that the reconsolidation process is not uniform in space, due mainly to the shape of the drift and the position of the heat source (the waste package acts as a rigid inclusion, resisting movement of the backfill above it, and increasing the local stress): greater compaction occurs in the roof and floor areas, and smaller in the sidewalls. These results agree with previous numerical investigations (Stone et al., 2010). Overall, in the scenario that we study, the backfill reconsolidation process takes between 6 and 20 years to complete. Fig. 7 displays the evolution of porosity at three crushed salt locations during the first 20 years after emplacement. When the crushed salt is reconsolidated, porosity has reached the characteristic value of the undisturbed salt. The predicted duration of the reconsolidation process may be too short and we highlight that it is uncertain for now. Therefore, these results are not conclusive. As more reconsolidation data at relevant loading conditions and temperatures become available, these predictions may change. In any case, we note that the new formulation implemented in TOUGH-FLAC to compute porosity changes successfully allows us to model mechanical compaction, and that the geomechanical component dominates over the pressure- and temperature-related components in the computation of porosity changes (this stresses the pertinence of the new version of TOUGH-FLAC). As the crushed salt reconsolidates, its permeability reduces by up to nine orders of magnitude according to Eq. (11), and its thermal conductivity increases following Eq. (12), from about 1 to $4\text{--}5 \text{ W}\cdot\text{m}^{-1}\cdot\text{K}^{-1}$. At the same time, the elastic moduli increase towards those of the natural salt (two-orders-of-magnitude increase, cf. Eq. (9)); as a result, the Biot coefficient decreases towards the characteristic value of the undisturbed natural salt (~ 0.003) according to Eq. (10). Note also that capillary forces become stronger as porosity and permeability decrease (Cinar et al., 2006; Leverett, 1941). A geotechnical barrier system is progressively created during the reconsolidation process.

As the crushed salt strengthens, an internal support is provided at the drift walls, which helps decrease the deviatoric stresses. The stress state in the drift area progressively evolves towards isotropic (thus, away from the dilatancy boundary). The occurrence of healing is closely related to the backfill compaction, which confirms the strong two-way interaction between the host rock and the backfill THM evolution. After about 6 years, healing has significantly reduced damage and dilatancy, and, after 7 years, dilatancy verifies $\varepsilon_{\text{vol}} \approx \varepsilon_{\text{vol},0}$. According to Eq. (6), in the current scenario the initial tightness of the host rock is re-stored after about 7 years. The three images in Fig. 8 compare the

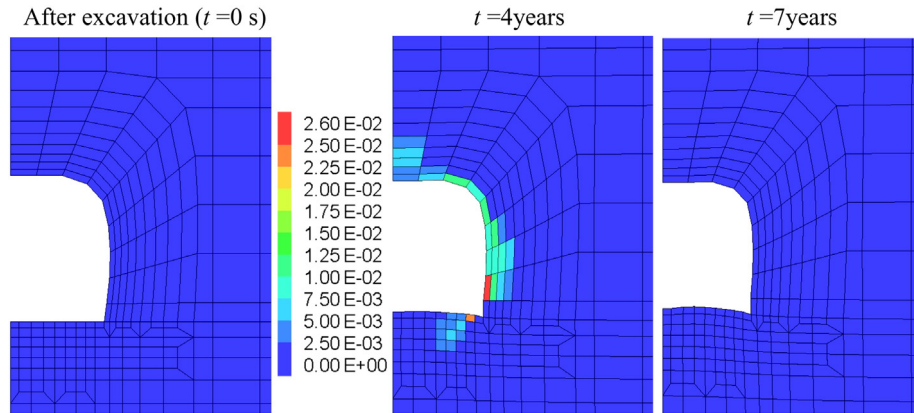


Fig. 8. THM base case scenario: extension of the EDZ (in terms of shear plus tensile dilatancy) at three different moments. Note that as the natural salt creeps, the drift span decreases.

extension of the EDZ at three moments: after excavation, after 4 years and after 7 years. While the damaged area increases during the first years, it decreases until vanishing once healing starts.

As temperature increases overall after about 5 years, the pore pressure increases too. In the natural salt, the very low permeability, saturated conditions and high thermal expansion coefficient of the pore fluid relative to the host rock are key factors for this thermal pressurization. Concerning the crushed salt backfill, the compaction-induced volume reduction facilitates resaturation and a significant pore pressure increase. Fig. 9a shows the evolution of pore pressure (equivalent pore pressure as defined in Eqs. (13)–(14)) and Fig. 9b displays the evolution of liquid saturation at five different positions in the repository: three locations in the host rock and two locations in the crushed salt. As the backfill liquid saturation increases steeply just before 10 years, the

pore pressure increases in a similar fashion. Additionally, as the backfill saturation increases the pore pressure is the same at the five locations monitored, see Fig. 9a. The equivalent pore pressure peaks below 16 MPa. According to Eq. (7), $\Delta P_{fl} \approx 1\text{--}2$ MPa; this results in fluid infiltration into the rock mass through the opening of grain boundaries and/or micro-fractures (Fokker, 1995; Kenter et al., 1990; Popp and Minkley, 2010). Indeed, pore pressure cannot increase much above the infiltration criterion because infiltration will work against further pore pressure increase, and it cannot decrease below the infiltration criterion because the infiltration-induced grain boundary openings and/or micro-fractures will close again, triggering a new pore pressure increase, which will result in infiltration. In the current scenario, the main cause to fluid permeation is the thermal pressurization of the liquid phase induced by the time-dependent release of decay heat from the waste packages. As the heat load and temperature decrease over time (see Figs. 5 and 6), pore pressure and infiltration reduce progressively (see Fig. 9a), and the initial permeability of the host rock is restored. As compared to a previous study (Blanco Martín et al., 2014), in this case the maximum pore pressure reached is lower because the secondary permeability increases beyond 10^{-20} m² during fluid infiltration.

The analysis of the results shows that fluid permeation into the rock starts after 6 years at a location 8 m away from the drift along the X axis. Permeation does not start in the drift area because the pore pressure is smaller in this zone due to the partial desaturation of the near-field host rock in the first years of the post-closure phase, see Fig. 9 (the first temperature peak and the porosity increase trigger this partial desaturation).

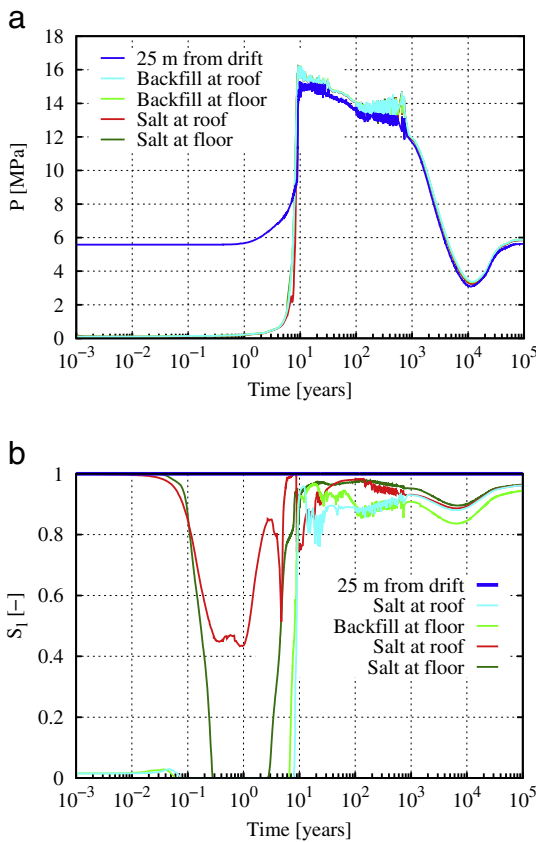


Fig. 9. THM base case scenario: evolution of (a) pore pressure and (b) liquid saturation at several locations in the repository.

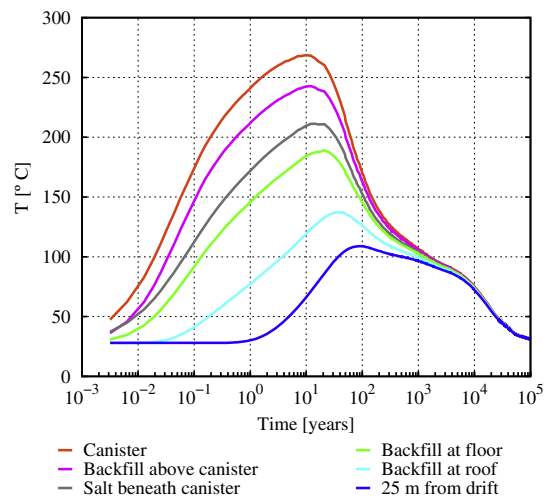


Fig. 10. TH results: evolution of temperature at the locations displayed in Fig. 6.

After 10–20 years, the pressure is uniform in the backfill and near-field host rock and pressure-driven fluid infiltration occurs. The area that undergoes infiltration is significantly larger than the area affected by thermo-mechanical damage (EDZ); it extends at the repository-level along the X and Z axes as pressure increases (thermal pressurization), but it does not reach the confining layers (the extension along the Z axis is about 100 m above and below the drift). The reconsolidated backfill also undergoes infiltration if $\Delta P_{fl} \geq 0$.

Finally, in Fig. 9, the pressure and saturation drop that occurs after 10000 years is due to a thermal depressurization at the repository-level (compare simultaneous temperature and pressure drops in Figs. 6 and 9). After 100000 years, once the heat load released by the waste packages tends to zero, the initial temperature and pore pressure are restored.

3.4. Comparison of TH and THM results

A thermal–hydraulic simulation (without the mechanical component) has been conducted to determine how relevant the coupling to mechanical processes is to evaluate the natural salt and crushed salt over time. Such a determination helps analyze the usefulness of the updated TOUGH-FLAC simulator to perform the target predictions.

Fig. 10 displays the temperature evolution at the same locations as in Fig. 6. The temperature at the waste package peaks at 267 °C after 10 years. As the figure shows, only one temperature peak is obtained. Indeed, if the mechanical effect is not accounted for, the backfill porosity hardly changes and therefore the thermal conductivity of this material remains low, cf. Table 2 and Eq. (12). The low thermal conductivity of the crushed salt explains the higher temperatures; the nearly constant value of this property explains that only one temperature peak is obtained. As in the THM case, the temperature 25 m away from the drift peaks at around 108 °C after 80 years.

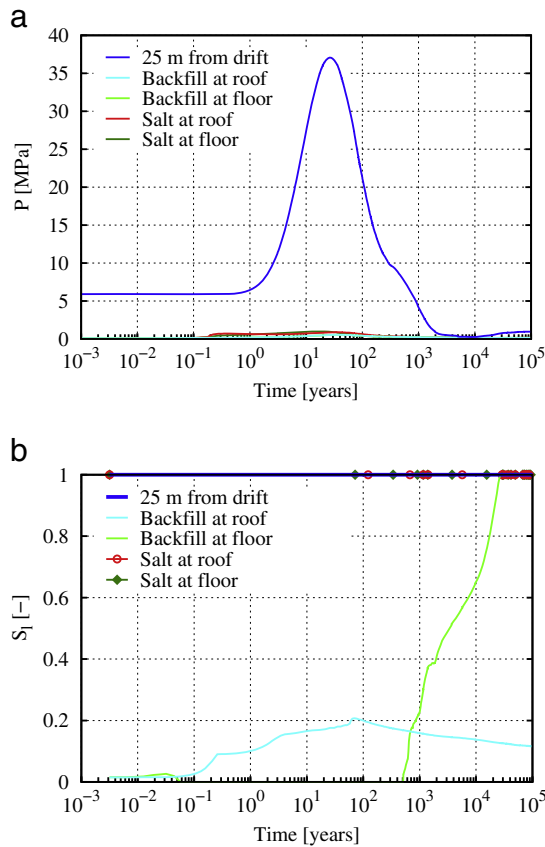


Fig. 11. TH results: evolution of (a) pore pressure and (b) liquid saturation at the locations displayed in Fig. 9.

In Fig. 11, the evolution of pore pressure and liquid saturation is given at the same locations as in Fig. 9. If the mechanical component is neglected, the far field pressure peaks above 37 MPa after 27 years. This pressure is significantly higher than the one obtained in the THM run, $P_{max} \approx 16$ MPa (see Fig. 9a). In the TH run, neither thermo-mechanical damage nor fluid infiltration is accounted for and as a result the permeability of the natural salt remains constant at its initial value, which explains the higher pressures reached. In the drift area, the pore pressure remains low: in the backfill, $P < 1$ MPa and in the host rock, $P < 1$ –2 MPa. Note that since the crushed salt porosity barely changes, $k = 3 \cdot 10^{-13}$ m², which is a very high value in the context of a nuclear waste repository. Also, the very low permeability of the host rock and its strong capillary forces delay the flow towards the drift in the long-term. The TH simulation captures the pressure decrease below the hydrostatic level after 10000 years. The initial pressure is not recovered in the area under investigation after 100000 years, see Fig. 11a.

As compared to Fig. 9b, the liquid saturation evolution displayed in Fig. 11b is also quite different: in the host rock around the drift, liquid saturation does not change noticeably because porosity and permeability remain very low. Because of the absence of compaction, the backfill saturation does not increase steeply as shown in Fig. 9b. In fact, the backfill resaturation is not complete after 100000 years (the initial saturation was very low, 1.5%, and the mass flow from the host rock is very small due to the near-zero permeability [maximum flow rates are about 10^{-9} kg · s⁻¹]). The liquid phase in the crushed salt progressively flows by gravity towards the drift floor, so that after 100000 years only the crushed salt in the floor area is saturated (note that capillary forces within the unconsolidated crushed salt are weak).

From these results, it can be concluded that TH simulations cannot capture key aspects such as backfill resaturation or temperature and pore pressure evolution. Furthermore, the backfill barrier development cannot be evaluated without accounting for the mechanical effects. Additionally, a realistic analysis of the natural salt barrier cannot be conducted if infiltration, damage and healing processes, which have been observed in the field and in the laboratory, are disregarded. Therefore, the coupling to mechanical processes is needed. This supports the development of the updated version of TOUGH-FLAC, which also allows HM and TM analyses.

3.5. Sensitivity of the THM predictions

In this section, we investigate the sensitivity of the THM simulation results to two factors: the initial saturation within the host rock and the capillary forces.

3.5.1. Initial saturation of the host rock

A THM simulation in which the host rock has an initial saturation of 50% has been performed. Intercrystalline brine has been observed in salt samples (Desbois et al., 2012; Jové-Colón et al., 2012) and justifies the assumption of initial fully saturated conditions in the host rock. However, it is considered important to analyze the effects of a possible lower initial saturation on the long-term predictions.

The temperature evolution obtained is similar to that of the base case scenario, displayed in Fig. 6. In the first years, damage and dilatancy develop as well, although after 4 years the values are slightly lower than in the base case, mainly because the equivalent pore pressure is lower in the current scenario (cf. Eqs. (13)–(14)). Dilatancy does not exceed 2.6% in this case. Its temporal evolution and spatial distribution are very similar to the base case scenario (Fig. 8). The crushed salt reconsolidation process and barrier development occur in a similar way. After 7 years, the EDZ is sealed and the initial tightness of the host rock restored.

The most important differences as compared to the reference case are related to the evolution of pore pressure and liquid saturation, which are displayed in Fig. 12, at the same locations as in Fig. 9. Regarding the pore pressure, a peak of about 15 MPa occurs after

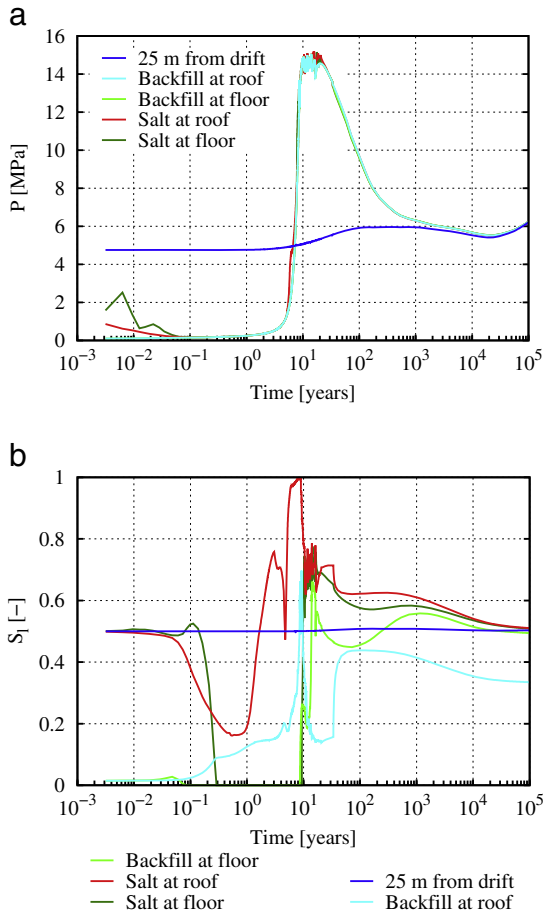


Fig. 12. THM predictions with 50% initial saturation in the host rock: evolution of (a) pore pressure and (b) liquid saturation at the locations shown in Fig. 9.

approximately 10 years. Therefore, the maximum pressure reached is similar to the maximum pressure in the base case (rock salt fully saturated); however, its temporal and spatial distributions are very different (compare Figs. 9a and 12a). In this case, fluid infiltration only occurs between 9 and 20 years due to the high compressibility of the gas phase (liquid saturation is 50%), which can accommodate the fluid thermal expansion. Because of this reduced thermal pressurization, the area affected by infiltration is very small, and does not spread farther than 1.5 m from the drift contour. After 20 years, the sealing capacity of the host rock is fully restored and the pressure decreases following the temperature decrease. Moreover, as Fig. 12a shows, the location 25 m away from the drift is not affected by the pressure increase. We also note that as the effect of the heat loading reduces, the pore pressure is the same in the five locations monitored.

The saturation curves shown in Fig. 9b are also quite different (recall that in the current case the initial saturation is 50%), although the processes involved are similar: in the first years, the temperature increase causes vaporization in the crushed salt and adjacent host rock, and the steam condenses subsequently following the temperature evolution. As the figure shows, backfill compaction also brings about a steep increase in liquid saturation after 10 years. The saturation at the location 25 m away from the drift remains unchanged.

From these results, it can be concluded that the most important effect of the initial saturation within the host rock is related to the temporal and spatial extent of fluid permeation: for a given heat loading, the higher the saturation, the higher the extent (compare Figs. 9a and 12a). This shows the importance of correctly assessing the initial conditions within the host rock.

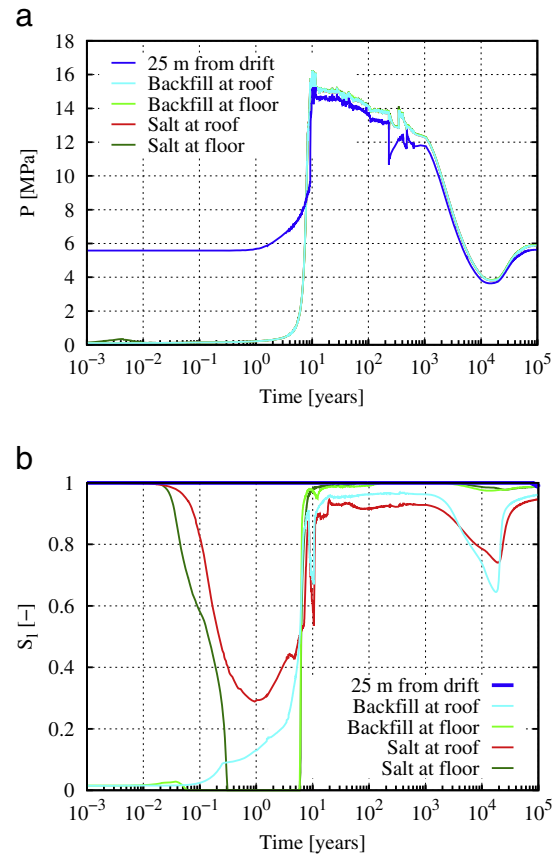


Fig. 13. THM predictions without capillary pressure: evolution of (a) pore pressure and (b) liquid saturation at the locations shown in Fig. 9.

3.5.2. Capillary forces

Capillary forces within natural salt are difficult to quantify and because of this, scarce experimental data are available (Kuhlman, 2014). In order to get a sense of how important capillarity effects are in the long-term predictions, we performed a coupled THM simulation in which we did not use water retention curves. When capillary forces are disregarded, the gas and liquid pressures are identical and equal to the equivalent pore pressure, defined in Eqs. (13)–(14).

As compared to the base case scenario, the most important differences when capillary effects are neglected are found in partially saturated areas. Given that for $S_l < 1$ the pore pressure is higher in the current case, damage and dilatancy in the EDZ are slightly higher (same extension and evolution as in Fig. 8, but maximum dilatancy gets to 2.67%). Like in the base case scenario, the EDZ is sealed after 7 years and the backfill is reconsolidated after 20 years.

Fig. 13 displays the pore pressure and liquid saturation evolution at the same locations as in Fig. 9. As the figure shows, pore pressure trends are very similar, with a maximum value of about 16 MPa and fluid infiltration occurring while $\Delta P_{fl} \geq 0$. Regarding liquid saturation, it reduces to lower values at the drift contour when temperature peaks initially (compare corresponding locations in Figs. 9b and 13b).

On the other hand, in the long-term the saturation profile in the host rock around the drift is quite different: the lack of capillary forces promotes gravity-dictated mass flow in the long-term (although very small); as a result, some desaturation occurs above the drift. Fig. 14 compares the liquid saturation profile after 100000 years in two situations: when capillary forces are considered (base case scenario) or neglected (current case). As the figure shows, when capillary forces are neglected the host rock above the drift is not completely saturated owing to the downwards flow.

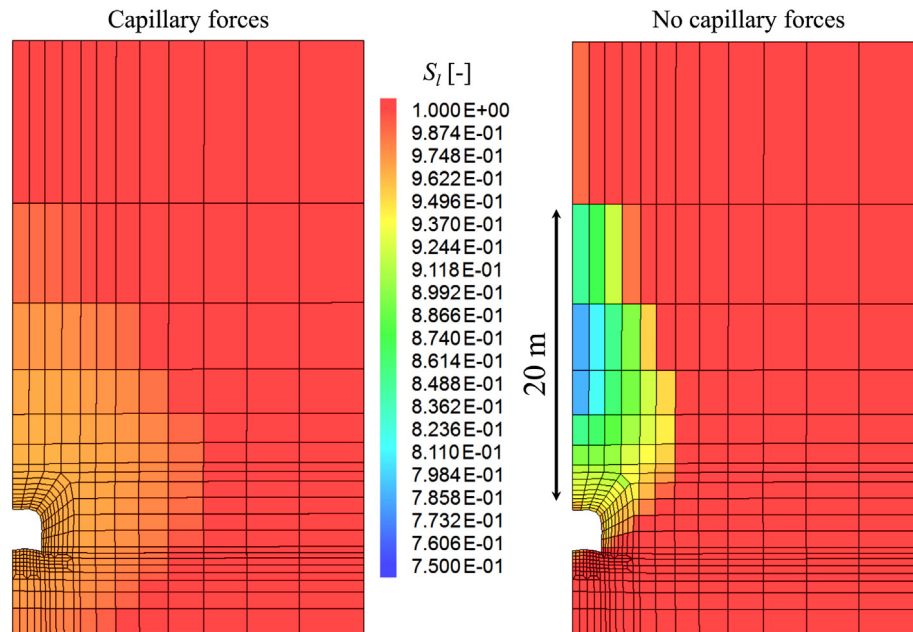


Fig. 14. Liquid saturation within the host rock close to the drift after 100000 years, when capillary forces are considered (left) and disregarded (right).

To conclude, if capillary forces are disregarded, the most important effect is found in the natural salt above the drift, where some desaturation occurs over the long-term as water flows slowly by gravity. In terms of thermo-mechanically induced damage and fluid infiltration within the formation, no significant differences have been observed.

4. Conclusions

The sequential TOUGH-FLAC simulator for coupled THM processes in porous media has recently been provided with a capability for large strains and creep behavior. This update has been required in order to investigate the long-term response of a generic salt repository for heat-generating nuclear waste with crushed salt backfill.

The updated TOUGH-FLAC includes state-of-the-art constitutive relationships that provide a phenomenological description of relevant processes within the natural salt and the crushed salt backfill. Theoretical and material-specific experimental studies have been accounted for in the coupling of the geomechanics and flow simulators. Using the updated version of TOUGH-FLAC, current knowledge about the compaction of the backfill and subsequent evolution of its properties towards those of the natural salt can be modeled. Several processes that are known to influence the initial tightness of the host rock can also be investigated.

The simulations presented in this paper comprise the stages of excavation, waste emplacement, backfilling and a post-closure period of 100000 years. Important performance indicators of a nuclear waste repository are examined, such as peak temperature and fluid pressure, EDZ evolution and time for backfill reconsolidation. Overall, the simulation results suggest that the EDZ is healed within the first few years. On the other hand, uncertainties remain regarding the backfill compaction, as available data at relevant loading and temperature conditions are scarce, and therefore current models cannot be fully validated against experimental data and may overestimate the time required for full reconsolidation, which is unknown so far. Depending on the magnitude of the pore pressure relative to the minimum compressive principal stress, fluid infiltration and secondary permeability may occur at a larger temporal and spatial scales. Once damage processes are over, our predictions show that the initial tightness of the host rock is restored.

The comparison of coupled THM simulation results with those obtained when the mechanical processes are disregarded reflects the importance of accounting for the latter and supports the development of

the updated TOUGH-FLAC simulator (for TM, HM and THM analyses). Indeed, if the mechanical component is omitted, the temperature and the pore pressure evolution cannot be correctly captured. Most importantly, the backfill reconsolidation and the barrier development cannot be investigated if the coupling to mechanical processes is neglected. We have also investigated the sensitivity of the predictions to features that are more difficult to assess. Our results show that the initial saturation within the natural salt has a significant impact on the simulation results, in particular as regards fluid infiltration, and that capillary effects should be properly included for more realistic long-term predictions.

Although the simulation results presented are preliminary, the numerical tools needed to investigate coupled processes in saliferous media have been considerably improved. In future work, we intend to account for gas generation from the waste packages (due to corrosion), and we will include the effects of brine dissolution and precipitation in the coupling scheme (halite solubility constraints). Moreover, a three-dimensional simulation of an emplacement drift will allow us to analyze the evolution of the displacement field, including thermally-induced uplift.

Acknowledgments

The authors gratefully acknowledge Stefan Finsterle and Víctor Vilarrasa for their careful review of a draft manuscript. The cooperation with Prof. Lux's team at the Department of Waste Disposal and Geomechanics, Clausthal University of Technology, is kindly appreciated. The constructive comments issued from the anonymous review process have significantly improved the quality of this paper. Funding for this work has been provided by the Used Fuel Disposition Campaign, Office of Nuclear Energy of the U.S. Department of Energy, under Contract Number DE-AC02-05CH11231 with Lawrence Berkeley National Laboratory.

References

- Argüello, J.G., Rath, J.S., 2012. SIERRA mechanics for coupled multi-physics modeling of salt repositories. In: Bérest, P., Ghoreychi, M., Hadj-Hassen, F., Tijani, M. (Eds.), Proc. 7th Int. Conf. Mech. Behav. Salt (SaltMech7), Paris, France, pp. 405–415.
- Argüello, J.G., Rath, J.S., 2013. Revisiting the 1980's WIPP Room D and B in-situ experiments: performing thermo-mechanical simulations of rock salt using a state-of-the-art code suite. Proc. 47th US Rock Mech./Geomech. Symp., San Francisco, CA, USA (pap. ARMA 13-370, (on CD-ROM)).

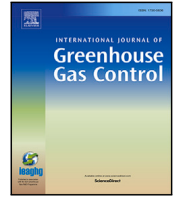
- Bathe, K.-J., Ramm, E., Wilson, E.L., 1975. Finite element formulations for large deformation dynamic analysis. *Int. J. Numer. Methods Eng.* 9 (2), 353–386. <http://dx.doi.org/10.1002/nme.1620090207>.
- Bechtold, W., Rothfuchs, T., Poley, A., Ghoreychi, M., Heusermann, S., Gens, A., Olivella, S., 1999. Backfilling and sealing of underground repositories for radioactive waste in salt (BAMBUS Proj.). *Eur. Atomic Energy Community. Rep. EUR19124 EN* (283 pp.).
- Bechtold, W., Smalios, E., Heusermann, S., Bollingerfehr, W., Bazargan Sabet, B., Rothfuchs, T., Kamlot, P., Grupa, J., Olivella, S., Hansen, F.D., 2004. Backfilling and Sealing of Underground Repositories for Radioactive Waste in Salt (BAMBUS II Proj.). *Eur. Atomic Energy Community (Rep. EUR20621 EN, 305 pp.)*.
- Bérest, P., Brouard, B., Karimi-Jafari, M., 2005. Deep salt caverns abandonment. *Proc. Post-Min. Symp., Nancy, France* (12 pp.).
- Blanco Martín, L., Rutqvist, J., Birkholzer, J.T., 2014. Long-term analysis of thermal-hydraulic-mechanical processes in a generic salt repository for high-level nuclear waste. *Proc. 48th US Rock Mech./Geomech. Symp., Minneapolis, MN, USA* (pap. ARMA 14-7206 (on CD-ROM)).
- Callahan, G.D., DeVries, K.L., 1991. Analyses of Backfilled Transuranic Waste Disposal Rooms. RE/SPEC Inc. (Prep. for Sandia Natl. Labs.), Rapid City, SD, USA (Rep. SAND-91-7052, 128 pp.).
- Callahan, G.D., Mellegard, K.D., Hansen, F.D., 1998. Constitutive Behavior of Reconsolidating Crushed Salt. RE/SPEC Inc. (Prep. for US DOE), Rapid City, SD, USA (Rep. SAND-98-0179C, 15 pp.).
- Camphouse, R.C., Gross, M., Herrick, C.G., Kicker, D.C., Thompson, B., 2012. Recommendations and justifications of parameter values for the run-of-mine salt panel closure system design modeled in the PCS-2012 PA. Final Memo 5412. Sandia Natl. Labs, Albuquerque, NM, USA (28 pp.).
- Carter, J.T., Hansen, F.D., Kehrman, R., Hayes, T., 2011a. A generic salt repository for disposal of waste from a spent nuclear fuel recycle facility. Savannah River Natl. Lab. (Prep. for US DOE), Aiken, SC, USA (Rep. SRNL-RP-2011-00149 Rev. 0, 123 pp.).
- Carter, J.T., Luptak, A.J., Gastelum, J., Stockman, C., Miller, A., 2011b. Fuel cycle potential waste inventory for disposition. *Prep. for US DOE Used Nucl. Fuel. Rep. FCR&D-USED-2010-000031 Rev. 5* (328 pp.).
- Chan, K.S., Bodner, S.R., Fossum, A.F., Munson, D.E., 1997. A damage mechanics treatment of creep failure in rock salt. *Int. J. Damage Mech.* 6 (2), 121–152. <http://dx.doi.org/10.1177/105678959700600201>.
- Cinar, Y., Pusch, G., Reitenbach, V., 2006. Petrophysical and capillary properties of compacted salt. *Trans. Porous Media* 64, 199–228. <http://dx.doi.org/10.1007/s11242-005-2848-1>.
- Clayton, D.J., Argüello Jr., J.G., Hardin, E.L., Hansen, F.D., Bean, J.E., 2012. Thermal-mechanical modeling of a generic high-level waste salt repository. In: Bérest, P., Ghoreychi, M., Hadj-Hassen, F., Tijani, M. (Eds.), *Proc. 7th Int. Conf. Mech. Behav. Salt (SaltMech7)*, Paris, France, pp. 427–432.
- Cosenza, Ph., 1996. Sur les couplages entre comportement mécanique et processus de transfert de masse dans le sel gemme. Université Paris 6, Paris, France (Ph.D. dissertation, 184 pp.).
- Cosenza, Ph., Ghoreychi, M., 1999. Effects of very low permeability on the long-term evolution of a storage cavern in rock salt. *Int. J. Rock Mech. Min. Sci.* 36 (4), 527–533. [http://dx.doi.org/10.1016/S0148-9062\(99\)00018-2](http://dx.doi.org/10.1016/S0148-9062(99)00018-2).
- Coussy, O., 1995. *Mechanics of Porous Continua*. 2nd edn. John Wiley and Sons, Chichester, UK (472 pp.).
- Coussy, O., 2004. *Poromechanics*. 1st edn. John Wiley and Sons, Chichester, UK (312 pp.).
- Cristescu, N.D., 1993. A general constitutive equation for transient and stationary creep of rock salt. *Int. J. Rock Mech. Min. Sci.* 30 (2), 125–140. [http://dx.doi.org/10.1016/0148-9062\(93\)90705-1](http://dx.doi.org/10.1016/0148-9062(93)90705-1).
- DBE, 2001. Numerische Untersuchungen zum Konvergenzverhalten eines Einzelhohraumes. DBE Technology GmbH, Peine, Germany (Rep. 22341011, 80 pp.).
- Dean, R.H., Gai, X., Stone, C.M., Minkoff, S.E., 2006. A comparison of techniques for coupling porous flow and geomechanics. *SPE J.* 11 (1), 132–140. <http://dx.doi.org/10.2118/79709-PA>.
- Department of Energy (DOE)/WIPP, 2002. Waste isolation pilot plant initial report for PCB disposal authorization. Carlsbad, NM, USA. Rep. DOE/WIPP 02-3196 (45 pp.).
- Desbois, G., Urai, J.L., Schmatz, J., Zavada, P., de Bresser, H., 2012. The distribution of fluids in natural rock salt to understand deformation mechanisms. In: Bérest, P., Ghoreychi, M., Hadj-Hassen, F., Tijani, M. (Eds.), *Proc. 7th Int. Conf. Mech. Behav. Salt (SaltMech7)*, Paris, France, pp. 3–12.
- Felippa, C.A., Park, K.C., 1980. Staggered transient analysis procedures for coupled mechanical systems: formulation. *Comput. Methods Appl. Mech. Eng.* 24 (1), 61–111. [http://dx.doi.org/10.1016/0045-7825\(80\)90040-7](http://dx.doi.org/10.1016/0045-7825(80)90040-7).
- Fokker, P.A., 1995. *The Behaviour of Salt and Salt Caverns*. Delft University of Technology, Delft, The Netherlands (Ph.D. Dissertation, 142 pp.).
- GRS, 2001. Untersuchungen zur hydraulisch wirksamen Auflockerungszone um Endlagerbereiche im Salinar in Abhängigkeit vom Hohlraumabstand und Spannungszustand (ALOHA 2). GRS, Köln, Germany. Final Rep. BMBF Res. Proj. 02 E 9118.
- Hampel, A., Salzer, K., Günther, R.-M., Minkley, W., Pudewills, A., Leuger, B., Zapf, D., Staudmeister, K., Rokahr, R., Herchen, K., Wolters, R., Lux, K.-H., 2012. Joint projects on the comparison of constitutive models for the mechanical behavior of rock salt II. Overview of the models and results of 3-D benchmark simulations. In: Bérest, P., Ghoreychi, M., Hadj-Hassen, F., Tijani, M. (Eds.), *Proc. 7th Int. Conf. Mech. Behav. Salt (SaltMech7)*, Paris, France, pp. 227–236.
- Hampel, A., Argüello, J.G., Hansen, F.D., Günther, R.M., Salzer, K., Minkley, W., Lux, K.-H., Herchen, K., Düsterloh, U., Pudewills, A., Yildirim, S., Staudmeister, K., Rokahr, R., Zapf, D., Gährken, A., Missal, C., Stahlmann, J., 2013. Benchmark calculations of the thermo-mechanical behavior of rock salt – results from a US–German Joint Project. *Proc. 47th US Rock Mech./Geomech. Symp., San Francisco, CA, USA* (pap. ARMA 13-456 (on CD-ROM)).
- Hansen, F.D., 2008. Disturbed rock zone geomechanics at the waste isolation pilot plant. *Int. J. Geomech.* 8 (1), 30–38. [http://dx.doi.org/10.1061/\(ASCE\)1532-3641\(2008\)8:1\(30\)](http://dx.doi.org/10.1061/(ASCE)1532-3641(2008)8:1(30)).
- Hardin, E., Voegelé, M., 2013. Alternative concepts for direct disposal of dual-purpose canisters. *Prep. for US DOE Used Fuel Disposition Campaign Rep. FCRD-UF-2013-000102 Rev. 0* (53 pp.).
- Hou, Z., 2002. Geomechanische Planungskonzepte für Untertägige Tragwerke mit Besonderer Berücksichtigung von Gefügeschädigung, Verheilung und Hydromechanischer Kopplung. 1st edn. Papierflieger, Clausthal-Zellerfeld, Germany (366 pp.).
- Hou, Z., 2003. Mechanical and hydraulic behaviour of rock salt in the excavation disturbed zone around underground facilities. *Int. J. Rock Mech. Min. Sci.* 40, 725–738. [http://dx.doi.org/10.1016/S1365-1609\(03\)00064-9](http://dx.doi.org/10.1016/S1365-1609(03)00064-9).
- Hou, Z., Lux, K.-H., 1998. Ein neues Stoffmodell für duktile Salzgesteine mit Einbeziehung von Gefügeschädigung und tertiärem Kriechen auf der Grundlage der Continuum-Damage-Mechanik. *Geotechnik* 21 (3), 259–263.
- Hou, Z., Lux, K.-H., 1999. A constitutive model for rock salt including structural damages as well as practice-oriented applications. *Proc. 5th Conf. Mech. Behav. Salt, Bucharest, Romania*, pp. 151–169.
- Hou, Z., Lux, K.-H., 2000. Ein Schädigungsmodell mit Kriechbruchkriterium für duktile Salzgesteine auf der Grundlage der Continuum-Damage-Mechanik. *Bauing* 75 (13), 300–307.
- Hou, Z., Lux, K.-H., Düsterloh, U., 1998. Bruchkriterium und Fließmodell für duktile Salzgesteine bei kurzzeitiger Beanspruchung. *Glueckauf-Forschungshäfte* 59 (2), 59–67.
- Hunsche, U., Hampel, A., 1999. Rock salt – the mechanical properties of the host rock material for a radioactive waste repository. *Eng. Geol.* 52, 271–291. [http://dx.doi.org/10.1016/S0013-7952\(99\)00011-3](http://dx.doi.org/10.1016/S0013-7952(99)00011-3).
- Hurtado, L.D., Knowles, M.K., Kelley, V.A., Jones, T.L., Ogintz, J.B., Pfeifle, T.W., 1997. WIPP Shaft Seal System Parameters Recommended to Support Compliance Calculations. Sandia Natl. Labs, Albuquerque, NM, USA <http://dx.doi.org/10.2172/563218> (Rep. SAND-97-1287, 136 pp.).
- Itasca, 2009. *FLAC^{3D} (Fast Lagrangian Analysis of Continua in 3 Dimensions)*, Version 4.0. Itasca Consulting Group, Minneapolis, MN, USA (438 pp.).
- Javeri, V., Baltes, B., 2008. Three dimensional analyses of combined gas, heat and nuclide transport in a repository considering thermo-hydro-geo-mechanical processes. *Proc. 12th Int. Conf. Int. Assoc. Comput. Methods Advances Geomech. IACMAG, Goa, India*, pp. 1264–1268.
- Jeannin, L., Maingué, M., Masson, R., Vidal-Gilbert, S., 2007. Accelerating the convergence of coupled geomechanical-reservoir simulations. *Int. J. Numer. Anal. Methods Geomech.* 31 (10), 1163–1181. <http://dx.doi.org/10.1002/nag.576>.
- Jha, B., Juanes, R., 2007. A locally conservative finite element framework for the simulation of coupled flow and reservoir geomechanics. *Acta Geotech.* 2 (3), 139–153. <http://dx.doi.org/10.1007/s11440-007-0033-0>.
- Jové-Colón, C., Greathouse, J.A., Teich-McGoldrick, S., Cygan, R.T., Hadgu, T., Bean, J.E., Martínez, M.J., Hopkins, P.L., Argüello, J.G., Hansen, F.D., 2012. Evaluation of Generic EBS Design Concepts and Process Models: Implications to EBS Design Optimization. Sandia Natl. Labs, Albuquerque, NM, USA (Rep. FCRD-USED-2012-000140, 250 pp.).
- Kachanov, L.M., 1986. *Introduction to Continuum Damage Mechanics*. 1st edn. Martinus Nijhoff Publishers, Dordrecht, The Netherlands (135 pp.).
- Kansy, A., 2007. Einfluss des Biot-Parameters auf das hydraulische Verhalten von Steinsalz unter Berücksichtigung des Porendruckes. Technische Universität Clausthal, Clausthal-Zellerfeld, Germany (Ph.D. Dissertation).
- Kenter, C.J., Doig, S.J., Rogaar, H.P., Fokker, P.A., Davies, D.R., 1990. Diffusion of brine through rock salt of roof caverns. *Proc. SMRI Fall Meet., Paris, France* (19 pp.).
- Kim, J., Tchelepi, H.A., Juanes, R., 2011. Stability and convergence of sequential methods for coupled flow and geomechanics: fixed-stress and fixed-strain splits. *Comput. Methods Appl. Mech. Eng.* 200 (13–16), 1591–1606. <http://dx.doi.org/10.1016/j.cma.2010.12.022>.
- Kim, J., Sonnenthal, E.L., Rutqvist, J., 2012. Formulation and sequential numerical algorithms of coupled fluid/heat flow and geomechanics for multiple porosity materials. *Int. J. Numer. Methods Eng.* 92 (5), 425–456. <http://dx.doi.org/10.1002/nme.4340>.
- Kim, J., Tchelepi, H.A., Juanes, R., 2013. Rigorous coupling of geomechanics and multiphase flow with strong capillarity. *SPE J.* 18 (6), 1123–1139. <http://dx.doi.org/10.2118/141268-PA>.
- Kock, I., Larue, J., Fischer, H., Frieling, G., Navarro, M., Seher, H., 2013. Results from one- and two-phase fluid flow calculations within the preliminary safety analysis of the Gorleben site-13310. *Proc. WM2013 Conf., Phoenix, AZ, USA* (15 pp.).
- Kröhn, K.P., Zhang, C.L., Wolf, J., Stührenberg, D., Jobmann, M., von Borstel, L., Lerch, C., 2012. The compaction behaviour of salt backfill at low porosities. In: Bérest, P., Ghoreychi, M., Hadj-Hassen, F., Tijani, M. (Eds.), *Proc. 7th Int. Conf. Mech. Behav. Salt (SaltMech7)*, Paris, France, pp. 155–162.
- Kuhlman, K.L., 2014. Summary Results for Brine Migration Modeling Performed by LANL, LBNL and SNL for the UFD Program. Sandia Natl. Labs, Albuquerque, NM, USA (Rep. FCRD-UF-2014-000071, 250 pp.).
- Lerch, C., Bollingerfehr, W., Filbert, W., Zhang, Q., 2012. Thermo-mechanical analyses for evaluating a HLW-repository concept. In: Bérest, P., Ghoreychi, M., Hadj-Hassen, F., Tijani, M. (Eds.), *Proc. 7th Int. Conf. Mech. Behav. Salt (SaltMech7)*, Paris, France, pp. 433–442.
- Lerche, S., 2012. Kriech- und Schädigungsprozesse im Salinargebirge bei mono- und multizyklischer Belastung. Technische Universität Clausthal, Clausthal-Zellerfeld, Germany (Ph.D. Dissertation, 319 pp.).
- Leverett, M.C., 1941. Capillary behaviour in porous solids. *Petrol. Trans. AIME* (192), 152–169.
- Lowe, M.J.S., Knowles, N.C., 1989. Further benchmark exercises to compare geomechanical computer codes for salt (COSA II Proj.). *Comm. Eur. Communities. Rep. EUR12135 EN* (418 pp.).

- Lux, K.-H., 1984. *Gebirgsmechanischer Entwurf und Felderfahrung im Salzkavernenbau: Ein Beitrag zur Entwicklung von Prognosemodellen für den Hohlraumbau im duktilen Salzgebirge*. 1st edn. Ferdinand Enke Verlag, Stuttgart, Germany (360 pp.).
- Millington, R.J., Quirk, J.P., 1961. Permeability of porous solids. *Trans. Faraday Soc.* 57, 1200–1207. <http://dx.doi.org/10.1039/TF9615701200>.
- Minkley, W., Popp, T., 2010. Final disposal in rock salt – geomechanical assessment of the barrier integrity. *Proc. 44th US Rock Mech./Geomech. Symp., Salt Lake City, UT, USA* (pap. ARMA 10-492 (on CD-ROM)).
- Mönig, J., Beuth, T., Wolf, J., Lommerzhelm, A., Mrugalla, S., 2013. Preliminary safety analysis of the Gorleben site: safety concept and application to scenario development based on a site-specific features, events and processes (FEP) database-13304. *Proc. WM2013 Conf., Phoenix, AZ, USA* (10 pp.).
- Munson, D.E., 1997. Constitutive model of creep in rock salt applied to underground room closure. *Int. J. Rock Mech. Min. Sci.* 34 (2), 233–247. [http://dx.doi.org/10.1016/S0148-9062\(96\)00047-2](http://dx.doi.org/10.1016/S0148-9062(96)00047-2).
- Munson, D.E., DeVries, K.L., Callahan, G.D., 1990. Comparison of calculations and in situ results for a large, heated test room at the Waste Isolation Pilot Plant (WIPP). In: Hustrulid, Johnson (Ed.), *Proc. 31st US Symp. Rock Mech., Golden, CO, USA*, pp. 389–396.
- Nutt, M., Voegelé, M., Jové-Colón, C., Wang, Y., Howard, R., Blink, J., Liu, H.-H., Hardin, E., Jenni, K., 2011. Used fuel disposition campaign disposal research and development roadmap. *Prep. for US DOE Used Fuel Disposition Campaign Rep. FCR&D-USED-2011-000065 Rev. 0* (121 pp.).
- Olivella, S., Gens, A., 2002. A constitutive model for crushed salt. *Int. J. Numer. Anal. Methods Geomech.* 26, 719–746. <http://dx.doi.org/10.1002/nag.220>.
- Olivella, S., Castagna, S., Alonso, E.E., Lloret, A., 2011. Porosity variations in saline media induced by temperature gradients: experimental evidences and modelling. *Transp. Porous Media* 90, 763–777. <http://dx.doi.org/10.1007/s11242-011-9814-x>.
- Peach, C.J., Spiers, C.J., 1996. Influence of crystal plastic deformation on dilatancy and permeability development in synthetic salt rock. *Tectonophysics* 256 (1), 101–128. [http://dx.doi.org/10.1016/0040-1951\(95\)00170-0](http://dx.doi.org/10.1016/0040-1951(95)00170-0).
- Popp, T., Kern, H., 1998. Ultrasonic wave velocities, gas permeability and porosity in natural and granular rock salt. *Phys. Chem. Earth* 23 (3), 373–378. [http://dx.doi.org/10.1016/S0079-1946\(98\)00040-8](http://dx.doi.org/10.1016/S0079-1946(98)00040-8).
- Popp, T., Minkley, W., 2010. Salt barrier integrity during gas pressure build-up in a radioactive waste repository – implications from lab and field investigations. *Proc. 44th US Rock Mech./Geomech. Symp., Salt Lake City, UT, USA* (pap. ARMA 10-493 (on CD-ROM)).
- Popp, T., Salzer, K., 2012. Microstructural deformation processes in granular salt during mechanical compaction. *Proc. 3rd US/German Workshop on Salt Repository Research, Design and Operation Meet. Abstr., Albuquerque, NM, USA*, p. 21.
- Popp, T., Minkley, W., Salzer, K., Schulze, O., 2012. Gas transport properties of rock salt – synoptic review. In: Bérest, P., Ghoreychi, M., Hadj-Hassen, F., Tijani, M. (Eds.), *Proc. 7th Int. Conf. Mech. Behav. Salt (SaltMech7)*, Paris, France, pp. 139–148.
- Pruess, K., Oldenburg, C., Moridis, G., 2011. *TOUGH2 User's Guide, Version 2*. Lawrence Berkeley National Laboratory, Berkeley, CA, USA (Rep. LBNL-43134 (revised), 197 pp.).
- Pudewills, A., Müller-Hoeppe, N., Papp, R., 1995. Thermal and thermomechanical analyses for disposal in drifts of a repository in rock salt. *Nucl. Technol.* 112 (1), 79–88.
- Rutqvist, J., 2011. Status of the TOUGH-FLAC simulator and recent applications related to coupled fluid flow and crustal deformations. *Comput. Geosci.* 37 (6), 739–750. <http://dx.doi.org/10.1016/j.cageo.2010.08.006>.
- Rutqvist, J., Tsang, C.-F., 2003. TOUGH-FLAC: a numerical simulator for analysis of coupled thermal–hydrologic–mechanical processes in fractured and porous geological media under multi-phase flow conditions. *Proc. TOUGH Symp. 2003, Berkeley, CA, USA* (12 pp.).
- Rutqvist, J., Wu, Y.-S., Tsang, C.-F., Bodvarsson, G., 2002. A modeling approach for analysis of coupled multiphase fluid flow, heat transfer, and deformation in fractured porous rock. *Int. J. Rock Mech. Min. Sci.* 39 (4), 429–442. [http://dx.doi.org/10.1016/S1365-1609\(02\)00022-9](http://dx.doi.org/10.1016/S1365-1609(02)00022-9).
- Rutqvist, J., Blanco Martín, L., Kim, J., Birkholzer, J.T., 2013. Modeling coupled THMC processes and brine migration in salt at high temperatures. Lawrence Berkeley National Laboratory (Prep. for US DOE Used Fuel Disposition Campaign), Berkeley, CA, USA (Rep. FCRD-UFD-2013-000262, 46 pp.).
- Schulze, O., Popp, T., Kern, H., 2001. Development of damage and permeability in deforming rock salt. *Eng. Geol.* 61, 163–180. [http://dx.doi.org/10.1016/S0013-7952\(01\)00051-5](http://dx.doi.org/10.1016/S0013-7952(01)00051-5).
- Settari, A., Mourits, F., 1998. A coupled reservoir and geomechanical simulation system. *SPE J.* 3 (3), 219–226. <http://dx.doi.org/10.2118/50939-PA>.
- Settari, A., Walters, D.A., 2001. Advances in coupled geomechanical and reservoir modeling with applications to reservoir compaction. *SPE J.* 6 (3), 334–342. <http://dx.doi.org/10.2118/74142-PA>.
- Sjaardema, G.D., Krieg, R.D., 1987. *A Constitutive Model for the Consolidation of WIPP Crushed Salt and Its Use in Analyses of Backfilled Shaft and Drift Configurations*. Sandia Natl. Labs, Albuquerque, NM, USA (Rep. SAND-87-1977, 72 pp.).
- Stone, C.M., Holland, J.F., Bean, J.E., Argüello, J.G., 2010. Coupled thermal–mechanical analyses of a generic salt repository for high-level waste. *Proc. 44th US Rock Mech./Geomech. Symp., Salt Lake City, UT, USA* (pap. ARMA 10-180 (on CD-ROM)).
- Stormont, J.C., Daemen, J.J.K., 1992. Laboratory study of gas permeability changes in rock salt during deformation. *Int. J. Rock Mech. Min. Sci.* 29 (4), 325–342. [http://dx.doi.org/10.1016/0148-9062\(92\)90510-7](http://dx.doi.org/10.1016/0148-9062(92)90510-7).
- Thomas, L.K., Chin, L.Y., Pierson, R.G., Sylte, J.E., 2003. Coupled geomechanics and reservoir simulation. *SPE J.* 8 (4), 350–358. <http://dx.doi.org/10.2118/87339-PA>.
- Tsang, C.-F., Stephansson, O., Jing, L., Kautsky, F., 2009. DECOVALEX project: from 1992 to 2007. *Environ. Geol.* 57, 1221–1237. <http://dx.doi.org/10.1007/s00254-008-1625-1>.
- van Genuchten, M.T., 1980. A closed-form equation for predicting the hydraulic conductivity of unsaturated soils. *Soil Sci. Soc. Am. J.* 44 (5), 892–898. <http://dx.doi.org/10.2136/sssaj1980.03615995004400050002x>.
- Vargaftik, N.B., 1975. *Tables on the Thermophysical Properties of Liquids and Gases*. 2nd edn. Hemisphere Publishing, New York, USA <http://dx.doi.org/10.1002/aic.690210636> 758 pp.
- Vijalapura, P.K., Strain, J., Govindjee, S., 2005. Fractional step methods for index-1 differential-algebraic equations. *J. Comput. Phys.* 203, 305–320. <http://dx.doi.org/10.1016/j.jcp.2004.08.015>.
- Walker, W.R., Sabey, J.D., Hampton, D.R., 1981. *Studies of Heat Transfer and Water Migration in Soils*. Department Agric. Chem. Eng., Colorado State University, Fort Collins, CO, USA (Final Rep., 140 pp.).
- Wieczorek, K., Czaikowski, O., Zhang, C.-L., Stührenberg, D., 2012. Recent experimental and modeling results on crushed salt consolidation. *Proc. 3rd US/German Workshop on Salt Repository Research, Design and Operation Meet. Abstr., Albuquerque, NM, USA*, p. 22.
- Wolters, R., Lux, K.-H., Düsterloh, U., 2010. Evaluation of rock salt barriers with respect to tightness: influence of thermomechanical damage, fluid infiltration and sealing/healing. *Proc. 44th US Rock Mech./Geomech. Symp., Salt Lake City, UT, USA* (pap. ARMA 10-215 (on CD-ROM)).
- Wolters, R., Lux, K.-H., Düsterloh, U., 2012. Evaluation of rock salt barriers with respect to tightness: influence of thermomechanical damage, fluid infiltration and sealing/healing. In: Bérest, P., Ghoreychi, M., Hadj-Hassen, F., Tijani, M. (Eds.), *Proc. 7th Int. Conf. Mech. Behav. Salt (SaltMech7)*, Paris, France, pp. 417–426.



Contents lists available at ScienceDirect

International Journal of Greenhouse Gas Control

journal homepage: www.elsevier.com/locate/ijggcEvaluation of possible reactivation of undetected faults during CO₂ injectionLaura Blanco-Martín^{a,b,*}, Emad Jahangir^a, Antonio P. Rinaldi^{b,c}, Jonny Rutqvist^b^a Mines Paris, Université PSL, Centre de Géosciences, 77300, Fontainebleau, France^b Lawrence Berkeley National Laboratory, Energy Geosciences Division, 94720, Berkeley, USA^c Swiss Seismological Service, Swiss Federal Institute of Technology, ETH Zürich, 8092, Zürich, Switzerland

ARTICLE INFO

Keywords:

CO₂ geologic storage
 THM modeling
 TOUGH-Pylith
 Undetected faults
 Fluid-induced seismicity
 Leakage

ABSTRACT

Geologic storage of carbon dioxide can efficiently contribute to reduce greenhouse gas emissions to the atmosphere. Two major hazards of this technology are leakage towards the ground surface and fluid-induced seismicity. While major faults may be detected and avoided during site characterization, undetected subseismic faults could be encountered once injection has started. This paper investigates leakage and reactivation of undetected faults through coupled thermal-hydraulic-mechanical modeling. The simulations are performed using a recently developed sequential simulator, TOUGH-Pylith, that allows to accurately account for the thermodynamics of brine-CO₂ mixtures, and to model faults as surfaces of discontinuity using state-of-the-art fault friction laws. The simulator is benchmarked against well-known analytical solutions and subsequently applied to investigate two cases of CO₂ injection close to undetected faults under normal and strike-slip faulting regimes. Although the scenarios are generic and represent unfavorable conditions, they suggest that leakage could occur and that undetected faults could trigger minor seismic events. Therefore, careful site characterization and continuous monitoring during operations should be always performed.

1. Introduction

Carbon dioxide (CO₂) emissions to the atmosphere are the main contributors to anthropogenic global warming (Collins et al., 2013). Important strategies to reduce greenhouse gas emissions include enhancing the efficiency of energy use, transitioning from fossil to low-carbon energy, and implementing carbon capture, utilization and storage (CCUS) (IEA, 2022). In CCUS, CO₂ is captured from fuel combustion and industrial processes, transported by ships or pipelines, and either used as a resource or permanently stored in deep underground formations. Here, we focus on CO₂ underground storage, for which extensive experimental, theoretical and numerical investigations have been undertaken, see e.g. (Chu, 2009; Sarkus et al., 2016; Raza et al., 2019; Cooper, 2009; IEA, 2008; Iglauer, 2011; Ennis-King and Paterson, 2001; Leung et al., 2014; Rutqvist, 2012; Herzog, 2016).

Potential risks associated with CO₂ sequestration must be evaluated prior to any site implementation. In addition to possible leakage (Meguerdijian and Jha, 2021), one aspect of concern is induced seismicity through the activation of faults (Pawar et al., 2015; Vilarrasa and Carrera, 2015; Zoback and Gorelick, 2012). Faults are conceptually zones of discontinuity within underground formations, and as such they often have markedly different properties compared to the surrounding layers (e.g., reduced stiffness, orders-of-magnitude different permeability). In the Earth's upper crust, fault zone architecture typically consists

of a low-permeability core surrounded by a damaged zone having higher permeability (Caine et al., 1996; Sibson, 1977; Wibberley and Shimamoto, 2003). As the injection proceeds, the *in situ* stress state is modified in the storage formation and surrounding layers. If a fault is present, slip along the weakest surface could be triggered, with possible aseismic or seismic response. It should be noted however that to date, measured seismicity associated with CO₂ sequestration is limited to microseismicity and some minor felt events (White and Foxall, 2016): exploration and high resolution geophysical reflection surveys are conducted prior to any injection operation and help characterizing the target formations and detecting major faults. On the other hand, minor faults (often referred to as the subseismic region, e.g. (Lohr et al., 2008)), having negligible initial offset across geological layers, could be unnoticed during site selection and characterization. Reactivation of undetected faults has been discussed in the literature. Mazzoldi et al. (2012) and Rinaldi et al. (2014) performed 2D hydro-mechanical (HM) modeling in a reservoir system intersected by a subseismic fault having no vertical offset with the aim of studying the integrity of the reservoir, possible seismicity and CO₂ leakage as a result of fault reactivation. Later, Rinaldi et al. (2015) extended the model to 3D and investigated the influence of well orientation. Using the same conceptual model, Mortezaei and Vahedifard (2015) performed

* Corresponding author at: Mines Paris, Université PSL, Centre de Géosciences, 77300, Fontainebleau, France.

E-mail address: laura.blanco_martin@minesparis.psl.eu (L. Blanco-Martín).

<https://doi.org/10.1016/j.ijggc.2022.103794>

Received 5 April 2022; Received in revised form 10 October 2022; Accepted 22 October 2022

Available online 19 November 2022

1750-5836/© 2022 Elsevier Ltd. All rights reserved.

2D thermal–hydraulic–mechanical (THM) modeling to investigate the seismic potential. In this case, the thermal effect was considered by means of a heat flux, without considering the full thermodynamics of CO₂–brine mixtures. Rohmer (2014) performed 2D HM modeling to investigate the influence of dissimilar properties and thicknesses across a subseismic fault. Le Gallo (2016) performed 3D HM modeling of a potential injection site in the Paris basin to investigate CO₂ leakage and to evaluate the effect of the overpressure in the stress field. A subseismic fault extending up to a control aquifer was present not far from the injection well. In these works, the fault zone was implemented in a continuum framework, without including a surface of discontinuity. In the current work, we take a step forward and include an interface within the fault zone. Two scenarios of undetected faults, in normal and strike-slip regimes, are investigated through numerical modeling.

The underground injection of CO₂ is a multi-physics problem and involves, at least, thermal, hydraulic and mechanical coupled processes. Coupled numerical modeling of CO₂ sequestration and fault reactivation is extensive in the literature, with conceptual models, numerical approaches and material behavior covering a wide range of complexity, e.g. (Rutqvist et al., 2002; White and Borja, 2008; McClure and Horne, 2011; Cappa and Rutqvist, 2011; Meng, 2017; Jin and Zoback, 2018; Torberntsson et al., 2018; Yang and Dunham, 2021; Jha and Juanes, 2014; Dieterich et al., 2015; Vilarrasa et al., 2010). The fault zone can be modeled either as a continuum having different (often reduced) mechanical properties as compared to the adjacent formations (Rinaldi et al., 2014), or as a region including one or several surfaces of discontinuity that allow to model slip using advanced laws more representative of fault frictional strength (Jha and Juanes, 2014). The main advantage of the latter is that it allows for a more accurate estimation of the induced events; however, it often requires the use of specialized codes. In this work, we use two existing codes to perform sequential two-way THM coupling, TOUGH2 (Pruess et al., 2012) and Pylith (Aagaard et al., 2017, 2013), and take advantage of their strengths: TOUGH2 includes several Equation-Of-State (EOS) modules to model non-isothermal subsurface multiphase and multicomponent flow, and Pylith allows for the modeling of continua and fault surfaces, the latter being implemented as zero-thickness cohesive cells. The codes are successfully coupled for the first time in a THM framework, allowing to conduct coupled simulations accounting for the thermodynamics of the relevant fluids, and for faults in a more realistic manner.

In this paper, we first present the TOUGH-Pylith simulator and briefly describe the coupling approach and fault interface implementation. Then, the coupling is verified against analytical solutions of coupled processes. In Section 4, we apply the simulator to investigate CO₂ injection into deep saline aquifers intersected by subseismic faults, with a focus on possible fault reactivation and leakage. Some conclusions and perspectives are given in the last section.

2. Material and methods

2.1. Numerical simulator

TOUGH-Pylith is a sequential simulator for coupled THM processes modeling based on the sequential coupling of TOUGH2 (Pruess et al., 2012) and Pylith (Aagaard et al., 2017, 2013). A rich discussion of different approaches to perform coupled THM simulations (fully coupled, sequential, one-way, two-way) is available in the literature (see e.g. (Dean et al., 2006; Kim et al., 2009)) and is out of the scope of this work. TOUGH2 allows for the modeling of multiphase, multicomponent and non-isothermal flow in porous and fractured media, and is based on the integral finite difference method. One main advantage of TOUGH2 is that it includes a wide range of EOS modules that permit to account for the thermodynamic behavior of pure fluids and mixtures encountered in natural and anthropogenic processes in the subsurface (water, air, oil, CO₂, NaCl, hydrogen, water–NaCl–CO₂, ...). In turn, Pylith allows for the computation of geomechanical equilibrium

under static, quasi-static and dynamic conditions, in domains including discontinuities at different scales. This open-source, finite-element code embeds several constitutive laws for faults, and provides templates to implement additional bulk and fault models. While TOUGH2 is written in Fortran77, Pylith is written in C++ and Python. Pylith allows for parallel computing and TOUGH2 runs in serial; however, a recent version, TOUGH3, can be run in parallel (Jung et al., 2017).

Similarly to TOUGH-FLAC (Rutqvist, 2011; Blanco-Martín et al., 2017), TOUGH-Pylith is based on the fixed-stress split sequential method to couple flow and geomechanics (Kim et al., 2009). After an initial version of the simulator (Miah et al., 2015; Miah, 2016), its full development has been achieved recently. The governing equations of the flow and geomechanics sub-problems are solved one at a time within a time step, and relevant information (pore pressure, temperature, volumetric deformation, etc.) is passed between sub-problems using the intermediate solution information technique (Settari and Mourits, 1998). Fig. 1 shows a schematic representation of the coupling sequence. In each time step, the flow sub-problem is solved first, and after convergence (circle in the Figure), relevant information is passed to the geomechanics sub-problem via a THM interface (arrow “1” in the Figure) to compute geomechanical equilibrium under drained conditions. Every time the coupling is made (square in the Figure), the total stress tensor is updated using

$$\underline{\underline{\sigma}}^{new} = \underline{\underline{\sigma}} - \alpha \Delta P \underline{\underline{1}} - 3\alpha_{th} K \Delta T \underline{\underline{1}} \quad (1)$$

where $\underline{\underline{\sigma}}^{new}$ is the updated total stress tensor, $\underline{\underline{\sigma}}$ is the total stress tensor at the end of the previous Pylith run, $\underline{\underline{1}}$ is the unit tensor, $K = \frac{E}{3(1-2\nu)}$ is the bulk modulus (E is the Young’s modulus and ν is the Poisson’s ratio), α is the Biot coefficient, α_{th} is the linear thermal expansion coefficient, and ΔP and ΔT are respectively the changes in pore pressure and temperature between two consecutive TOUGH2 time steps. Pressure, temperature and fluid mass are transferred to Pylith by means of the THM interface. Pylith then runs until mechanical equilibrium is reached (arrow “2” in the Figure). At equilibrium (triangle in the Figure), volumetric stresses (or strains) are transferred to TOUGH2 by means of the THM interface (arrow “3” in the Figure) and used to compute a mechanically-induced porosity correction in the next time step:

$$\Delta\phi = A(\alpha, \phi, K) \Delta P + B(\alpha_{th}) \Delta T + \Delta\phi^{corr} \quad (2)$$

where $\Delta\phi^{corr}$ is the porosity correction from geomechanics, a function of the total mean stress (Kim et al., 2012). Note that in order to compute mechanically-induced changes in other flow variables, such as permeability k or capillary pressure P_c , additional variables may be transferred through the THM interface (Rutqvist, 2011). A new time step of the flow sub-problem begins with the updated flow variables (arrow “4” in the Figure), and the described procedure is repeated until the end of the simulation.

2.2. Fault interface implementation and constitutive models

Pylith specializes in the modeling of earthquake faulting (prescribed and spontaneous ruptures) and embeds several constitutive laws for fault surfaces. However, in agreement with the classic Andersonian theory (Anderson, 1951), no distinction is made between total and effective stresses. Fault surfaces, which are not necessarily planar, are modeled using cohesive elements having no thickness and allowing in-plane and normal relative displacements (details can be found in Aagaard et al. (2017)). The fault slip vector is defined as the relative displacement between the two sides of the fault,

$$\vec{d} = \vec{u}_+ - \vec{u}_- \quad (3)$$

where \vec{u}_+ and \vec{u}_- are the displacements on the positive and negative sides of the fault surface, respectively. Vector \vec{d} has a tangent component on the fault surface, and a normal component to the fault surface.

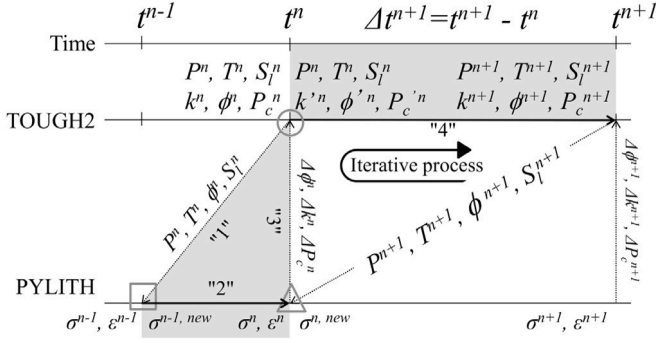


Fig. 1. TOUGH-Pylith coupling sequence (adapted from Blanco-Martín et al. (2015)). The gray zones correspond to the time step marching from t^n to t^{n+1} (the symbols and labels are explained in the text).

Penetration is not allowed. Likewise, the stress state in the fault is represented as a normal component, σ_n , and a shear component, τ ,

$$\sigma_n = (\underline{\underline{\sigma}} \cdot \vec{n}) \cdot \vec{n} \quad (4)$$

$$\tau = \sqrt{\|\underline{\underline{\sigma}}\| - \sigma_n^2} \quad (5)$$

where \vec{n} is the fault normal vector, pointing from the negative to the positive side of the fault surface. In the context of TOUGH-Pylith, new fault constitutive models have been implemented in Pylith, in which the effective stress is used, $\underline{\underline{\sigma}}' = \underline{\underline{\sigma}} + \alpha P \mathbf{1}$ (note that compression is assumed to be negative here). For such purpose, the pore pressure is passed from TOUGH2 to the fault constitutive models every time the coupling is made. In agreement with (Jha and Juanes, 2014), a fault pressure P_f is defined, which is a function of the pore pressure on both sides of the fault surface. Since the side on which the failure criterion is first met determines fault stability, we take $P_f = \max(P_+, P_-)$ (maximum pore pressure of all adjacent cells on both sides of the fault surface). This allows to uniquely define the effective normal stress on the fault, $\sigma_n' = (\underline{\underline{\sigma}}' \cdot \vec{n}) \cdot \vec{n}$.

In order to evaluate fault stability, the shear stress on the fault is compared against a Coulomb-type criterion that provides the shear strength, τ_c ,

$$\tau_c = C - \mu \cdot \sigma_n' \quad (6)$$

where C is the cohesion and μ is the friction coefficient. Note that in Pylith, if $\sigma_n' > 0$ (tensile regime), $\tau_c = C$. As long as $\tau < \tau_c$, there is no relative movement between the two sides of the fault, i.e., the fault is locked. On the other hand, if the failure criterion is exceeded, slip occurs until the criterion is met again. In this case, a Lagrange multipliers approach is used. Note that when the fault surface does not reach the boundaries of the model (i.e., it has buried edges), the Pylith algorithm adjusts the topology automatically, so that cohesive cells are inserted up to the buried edge, and no additional degrees of freedom are added along that edge (Aagaard et al., 2017). For this purpose, the user defines an additional group of nodes including only those that form the buried edge.

The evolution of the friction coefficient μ is described differently among the constitutive models. In this work, we focus on two models widely used to evaluate fault frictional strength: slip weakening and rate-and-state. In the slip weakening model, the coefficient of friction evolves from a peak value, μ_p , to a residual value, μ_r , as the slip $d = \|\vec{d}\|$ increases from 0 to the critical slip distance, d_c :

$$\mu = \mu_p - (\mu_p - \mu_r) \frac{d}{d_c} \quad (7)$$

In the rate-and-state model, the friction coefficient evolves as a function of the slip rate, $v = \|d\vec{d}/dt\|$, and also as a function of a state

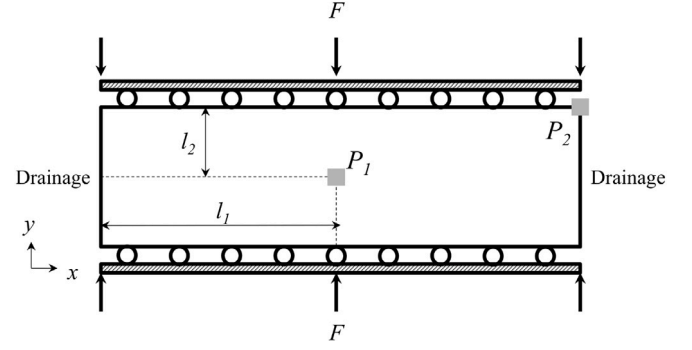


Fig. 2. Schematic representation of Mandel's problem, including monitoring points P_1 and P_2 for Fig. 3.

variable, θ :

$$\mu = \mu^* + a \ln\left(\frac{v}{v^*}\right) + b \ln\left(\frac{\theta v^*}{L}\right) \quad (8)$$

where μ^* is the friction coefficient at the reference slip rate v^* , L is the characteristic length and a , b are empirical parameters. Note that in Pylith, a linearization is applied to the friction coefficient when the slip rate falls below a threshold (Aagaard et al., 2017). The evolution of the state variable θ is given by the aging law described in Ruina (1983),

$$\frac{d\theta}{dt} = 1 - \frac{v\theta}{L} \quad (9)$$

The state variable, homogeneous to time, represents the maturity of the asperities in the fault interface (Rice, 1993). Depending on the parameter set, this model can account both for friction increase (strengthening) and decrease (weakening). At steady-state, the state variable tends towards L/v and therefore $\mu = \mu^* + (a - b)\ln(v/v^*)$. Rate-and-state allows to simulate repetitive stick-slip behavior and the seismic cycle (Dieterich, 1981). Also, as state evolution occurs over time scales in the order of L/v , adaptive time stepping is more efficient when using this law.

3. Verification cases

In this section, we benchmark TOUGH-Pylith against well-known analytical solutions of HM and THM coupling. Indeed, TOUGH2 and Pylith have been tested and verified previously (Aagaard et al., 2017; White et al., 2016; Pruess, 2005; Okada, 1992), but the validity of the coupling scheme between the two codes has to be demonstrated before it is applied to subsurface scenarios.

3.1. Mandel's problem (HM coupling)

Mandel's problem of poroelasticity (Mandel, 1953) is illustrated in Fig. 2. A saturated porous material with rectangular cross-section and infinite length in the out-of-plane direction is sandwiched by two stiff, frictionless plates. Drainage is possible along the lateral boundaries. The sample is initially in equilibrium, and at $t = 0^+$ a compressive force is applied normal to the plates. The original resolution of this 2D plane strain problem was extended by Abousleiman et al. (1996) to account for compressible fluids and non-isotropic materials.

Initially, the load applied to the plates induces an excess of pore pressure (Skempton effect). Over time, drainage occurs at the open boundaries, which makes the laterals of the sample more compliant than its core. However, since the vertical displacement must be equal along the stiff top and bottom boundaries, there is an increase of pore pressure in the central region, yielding a non-monotonic pore pressure evolution, known as the Mandel-Cryer effect (Schiffman et al., 1969). At a later time, the excess of pore pressure dissipates completely.

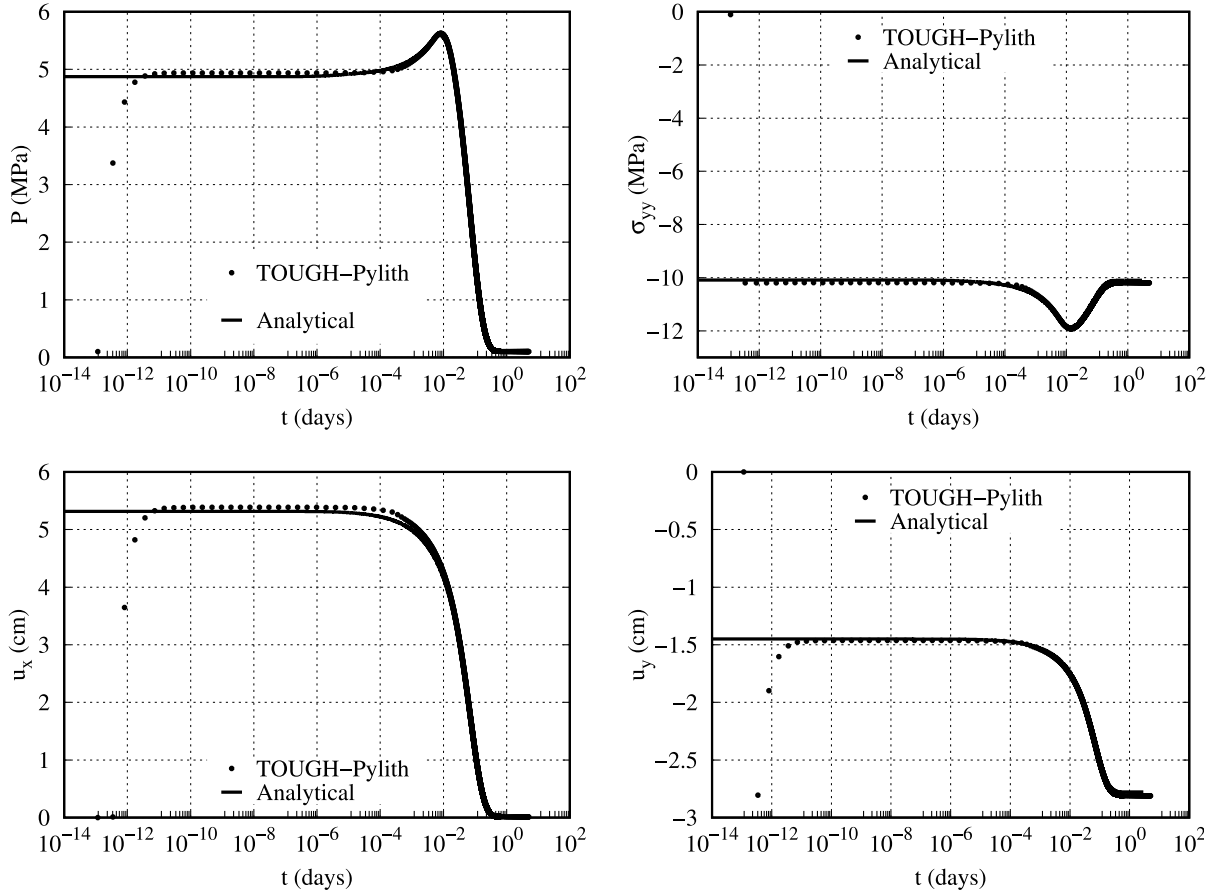


Fig. 3. Mandel's problem: comparison of TOUGH-Pylith with the analytical solution in [Abousleiman et al. \(1996\)](#): pore pressure (upper left) and total vertical stress (upper right) at P_1 , horizontal (lower left) and vertical (lower right) displacements at P_2 .

Table 1
Mandel's problem: parameters used in the simulation.

Parameter (unit)	Value
k (m ²)	$6.51 \cdot 10^{-15}$
ϕ_0 (-)	0.425
E (MPa)	450
ν (-)	0
α (-)	1
μ_f (Pa · s)	10^{-3}
C_f (Pa ⁻¹)	$4.5 \cdot 10^{-10}$

For the comparison with TOUGH-Pylith, we have assumed a sample with dimensions $l_1 = 5$ m and $l_2 = 1.25$ m. Gravity is neglected and cohesive elements are inserted above and below the sample to model frictionless plates. The initial stress field is -0.1 MPa (isotropic) and at $t^+ = 0$ we apply -10 MPa normal to the plates. The initial pore pressure is 0.1 MPa. [Table 1](#) lists the parameters used. Module EOS1 of TOUGH2 (only one component, water) is used in isothermal conditions, and we force constant viscosity, μ_f , and compressibility, C_f , for compliance with the analytical solution detailed in [Abousleiman et al. \(1996\)](#).

[Fig. 3](#) compares the evolution of the pore pressure, relevant stresses and displacements at the monitoring points shown in [Fig. 2](#). As the plots show, the comparison is very satisfactory. Note that the differences observed initially are due to different initial states: while in the analytical solution the load is already applied and borne by the fluid, in the simulation the load is applied at $t = 0^+$.

3.2. McTigue's problem (THM coupling)

[McTigue \(1986\)](#) proposed a theory for linear thermoporoelasticity in a saturated medium. Compressibility and thermal expansion of the fluid are taken into account. Analytical solutions for the one-dimensional heating of a half space are also provided, considering different boundary conditions for the temperature and the pressure fields. As demonstrated in the original paper, solutions for the temperature and pressure depend on the ratio of the fluid and thermal diffusivities, $R = (D_f/D_h)^{1/2}$.

Here, we investigate the case with a constant temperature boundary. Two cases are studied for the pressure field: drained and undrained boundary conditions at $x = 0$. A constant stress condition is applied normal to this boundary. A 1D model is built with sufficient extent for compliance with the analytical solution. At the boundary $x \rightarrow \infty$, the temperature, pressure and stress are kept at their initial values. Module EOS1 of TOUGH2 is used. To comply with the assumptions of the analytical solution, water viscosity (μ_f), compressibility (C_f) and expansivity (α_f) are taken as constant values. Moreover, convective heat transport is disabled, so that only conductive heat transport is active with thermal conductivity λ , and, in the heat accumulation term, grain density ρ_{gr} and specific heat C . [Table 2](#) lists the parameters used in the simulation. The initial stress field is -0.1 MPa (isotropic), the initial pore pressure is 0.1 MPa and the initial temperature is 50 °C. At $t = 0^+$, we apply a temperature of 55 °C at $x = 0$. [Fig. 4](#) shows a schematic representation of the problem being solved and compares the simulation results with the analytical solution for different ratios of fluid and thermal diffusivities (in practice, the permeability listed in

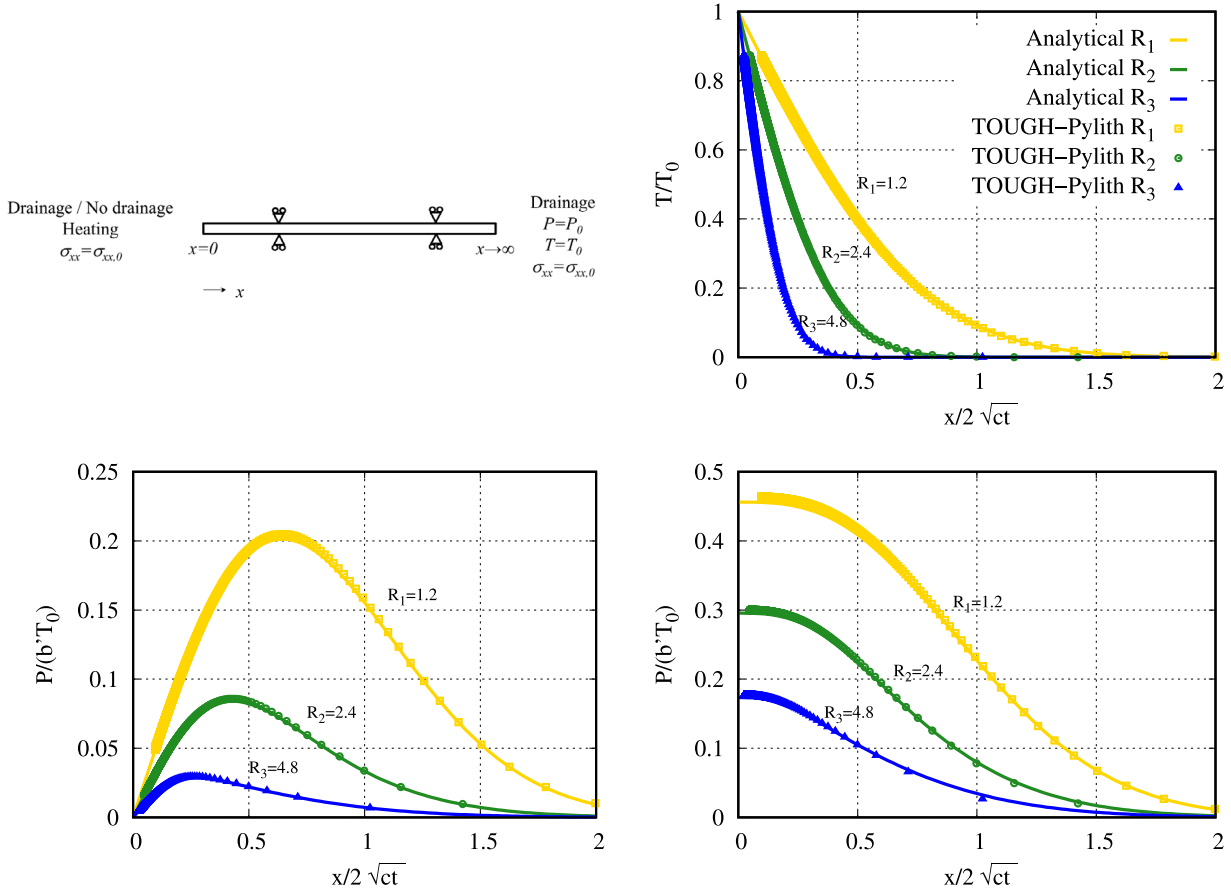


Fig. 4. McTigue’s problem: schematic representation (upper left) and comparison of TOUGH-Pylith with the analytical solution in McTigue (1986). Pore pressure is shown for the drained (lower left) and undrained (lower right) cases (the temperature field is the same for both, displayed in the upper right). The pore pressure coefficient b' is defined in McTigue (1986), Eq. (27).

Table 2
McTigue’s problem: parameters used in the simulations.

Parameter (unit)	Value
k (m ²)	$1.27 \cdot 10^{-19}$
ϕ_0 (-)	0.01
ρ_{gr} (kg/m ³)	2500
C (J/kg/K)	800
λ (W/m/K)	4
E (GPa)	21
ν (-)	0.25
α (-)	1
α_{th} (K ⁻¹)	$4 \cdot 10^{-5}$
μ_f (Pa · s)	10^{-3}
C_f (Pa ⁻¹)	$4.5 \cdot 10^{-10}$
α_f (K ⁻¹)	$1.6 \cdot 10^{-4}$

Table 2 corresponds to R_1 and a factor is applied for the cases R_2 and R_3). Overall, considering the simplifications of the analytical solution and the different definition of the pore pressure coefficient in TOUGH2 and McTigue (1986), the comparison is very satisfactory.

4. CO₂ injection cases

4.1. Subseismic fault in strike-slip regime

In this section, we investigate a scenario inspired from the foreseen storage project NER300 ULCOS, which aimed to reduce CO₂ emissions related to the steel industry (Lupion and Herzog, 2013). Based on (Le Gallo, 2016), CO₂ injection targets lower Triassic sandstone formations,

and we investigate possible leakage and induced seismicity associated with a subseismic fault, assumed to be vertical and with negligible offset. Fig. 5 displays the conceptual model investigated, which considers seven material layers from the underburden (Permian basement) to the ground surface. The size of the model is $22 \times 17.5 \times 3$ km³. The fault, which extends about 800 m along the z axis (limited vertical extent), intercepts the storage aquifer, the overlying caprock and the control aquifer. The thickness of these layers are 200, 500 and 90 m, respectively.

In the model proposed in Le Gallo (2016), the fault was oriented N155E, which is parallel to the maximum horizontal stress (y direction in Fig. 5); in these conditions, the initial shear stress on the fault is negligible and fault reactivation is highly unlikely (note that in Le Gallo (2016), the target was to investigate fault leakage rather than induced seismicity). In our scenario, the fault is oriented N145E, which corresponds to an angle of 80° between the maximum horizontal stress and the fault normal vector, or equivalently, 10° between the maximum horizontal stress and the fault direction. The thickness of the fault zone is about 100 m (x direction), and the fault core is about 20 m thick. Since field data suggest that the core-damaged zone contact may slip at an early stage during earthquakes (Cappa and Rutqvist, 2011), a fault interface is added between the fault core and the damaged zone closest to the injection well. CO₂ is injected at a depth of about 1900 m, with a rate of 0.8 Mt/y through a vertical well located about 1 km down-dip from the fault; this rate is typical of a mid-size onshore scenario. The salinity of the storage aquifer is 50 g/l. Injection conditions are $P = 25$ MPa and $T = 45$ °C (supercritical state). Table 3 lists relevant properties of the different layers and the fault; these properties are average values for each formation and are taken from the literature

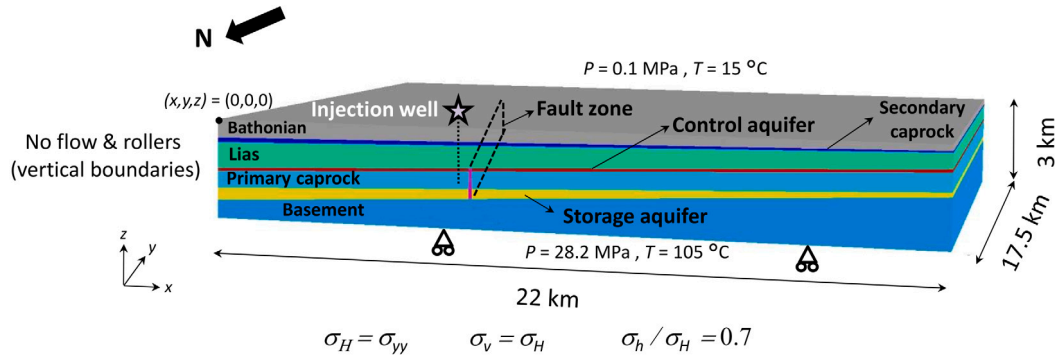


Fig. 5. Subseismic fault in strike-slip regime: conceptual model.

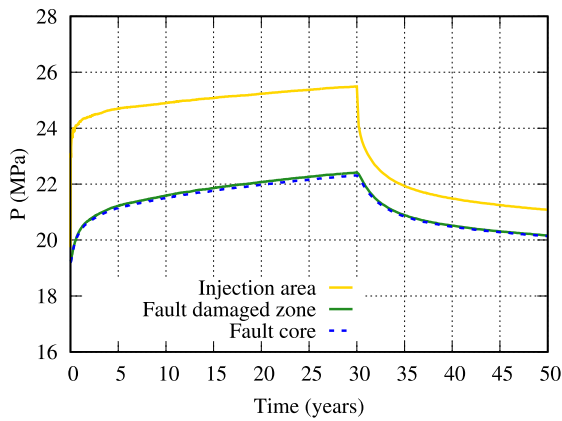


Fig. 6. Subseismic fault in strike-slip regime: evolution of pore pressure in the injection and fault zones.

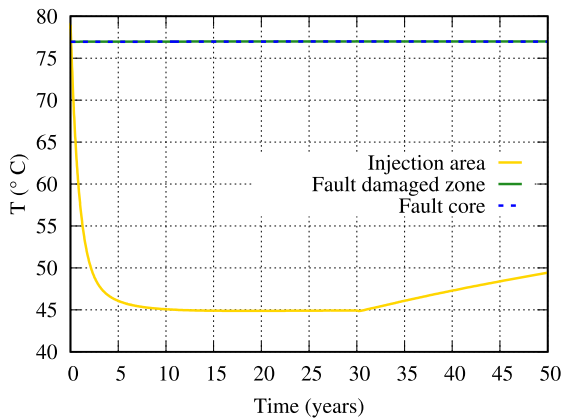


Fig. 7. Subseismic fault in strike-slip regime: evolution of temperature in the injection and fault zones.

when available (Millien, 1993; Bésuelle et al., 2000; Vidal-Gilbert et al., 2009; Rohmer, 2014). Except for the fault interface, it is assumed that the materials behave elastically. The fault interface responds to the criterion described in Eq. (6), and the evolution of the friction coefficient follows the slip-weakening law with $C = 0$, $\mu_p = 0.2$, $\mu_r = 0.1$ and $d_c = 0.1$ m; μ_p and μ_r are purposely low to force reactivation, but could be representative of clay-rich materials that are sometimes found in the fault gouge (Ikari et al., 2011; Le Gallo, 2016). Note that the permeability of the fault core is ten times smaller than that of the damaged zone. Also, in the fault zone, the vertical permeability (k_v , along the z direction) is 40 times smaller than the horizontal permeability (k_h); this reduces possible up-dip leakage along

the fault, but it is a conservative assumption for fault reactivation. Corey's relative permeability model (Pruess et al., 2012) is used for all layers with $S_{lr} = 0.1$ and $S_{gr} = 0.05$. For capillary pressure, we use van Genuchten's model (van Genuchten, 1980) with $\lambda_{VG} = 0.457$, $P_0 = 600$ kPa, $P_{cap}^{max} = 10$ MPa and $S_{lr} = 0.01$.

Regarding initial and boundary conditions, the top and bottom boundaries are kept at $P = 0.1$ MPa, $T = 15$ °C and $P = 28.2$ MPa, $T = 105$ °C, respectively. All lateral boundaries are closed to fluid flow. For the geomechanics sub-problem, displacement is fixed to zero normal to the bottom and the lateral boundaries. Initial stress conditions are those of the Bure site (Wileveau et al., 2007). The major horizontal stress σ_H is oriented N155E, and $\sigma_H = \sigma_v$ (lithostatic). The ratio between horizontal stresses is $\sigma_h/\sigma_H = 0.7$ (Vidal-Gilbert et al., 2009). The geothermal gradient is 30 °C/km.

We use module ECO2N of TOUGH2, which accounts for the thermodynamics and thermophysical properties of H_2O -NaCl- CO_2 mixtures (Pruess, 2005). Three phases are possible: an aqueous phase, a CO_2 -rich phase (liquid or gas) and solid phase (precipitated NaCl, which may reduce the effective porosity and the permeability). Phase partitioning of H_2O and CO_2 is modeled as a function of pressure, temperature and salinity using the correlations in Spycher et al. (2003), Spycher and Pruess (2005). Salting out effects (CO_2 solubility reduction with increasing salinity) are accounted for. Note that this EOS does not account for CO_2 phase changes nor mixtures of liquid and gaseous CO_2 ; in fact, in the scenarios that we investigate CO_2 remains in supercritical state, and phase changes do not occur. In cases where phase changes are likely, module ECO2M should be used (Pruess, 2013), with minimal impact in the coupling procedure.

Prior to the start of the injection, a simulation is run to obtain equilibrium (hydrostatic, geothermal and lithostatic gradients). Subsequently, we model 30 years of CO_2 injection, followed by a period of 20 years of post-injection phase. In the injection horizon, the initial pore pressure and temperature are about 19 MPa and 78 °C, respectively. Fig. 6 shows the evolution of pore pressure in the injection area as well as in the fault. After 30 years of injection, the overpressure is about 6.5 MPa in the injection area and about 3.2 MPa in the fault area. Note that this is an unfavorable scenario, as permeability is assumed to remain constant (another assumption will be investigated in Section 4.2). As the injection stops, the pore pressure decreases towards the initial value. The temperature evolution is displayed in Fig. 7. As CO_2 is injected at $T = 45$ °C, the temperature decreases in the injection area, but the extent of the cooled zone does not exceed 500 m around the well. Similarly to the pressure evolution, the temperature evolves towards the initial gradient once the injection stops.

As the injection proceeds, a fraction of CO_2 is dissolved in the aqueous phase to ensure thermodynamic equilibrium (the CO_2 concentration in the aqueous phase is about 4.5% at the given conditions). A CO_2 plume is created rapidly, and after 30 years of injection, the saturation of the CO_2 -rich phase is about 65% around the well, see Fig. 8. Owing to the reservoir properties and the injection rate, the

Table 3

Subseismic fault in strike-slip regime: parameters used in the simulation. Each layer is represented by a different color in Fig. 5. For all layers, $\lambda = 2 \text{ W/m/K}$, $C = 880 \text{ J/kg/K}$, $\alpha_{th} = 10^{-6} \text{ K}^{-1}$, $\nu = 0.25$ and $\alpha = 1$.

Layer	ρ_{gr} (kg/m^3)	ϕ (-)	k_h (m^2)	k_v (m^2)	E (GPa)
Bathonian	2400	0.15	$5 \cdot 10^{-13}$	$5 \cdot 10^{-13}$	10
Secondary caprock	2500	0.05	10^{-15}	10^{-15}	15
Lias	2500	0.10	10^{-14}	10^{-14}	15
Control aquifer	2400	0.15	10^{-13}	10^{-13}	20
Primary caprock	2600	0.05	10^{-18}	10^{-18}	20
Storage aquifer	2400	0.15	10^{-14}	10^{-14}	20
Permian basement	2700	0.07	10^{-17}	10^{-17}	25
Fault (damaged zone)	2400	0.10	10^{-16}	$2.5 \cdot 10^{-18}$	10
Fault core	2400	0.10	10^{-17}	$2.5 \cdot 10^{-19}$	5

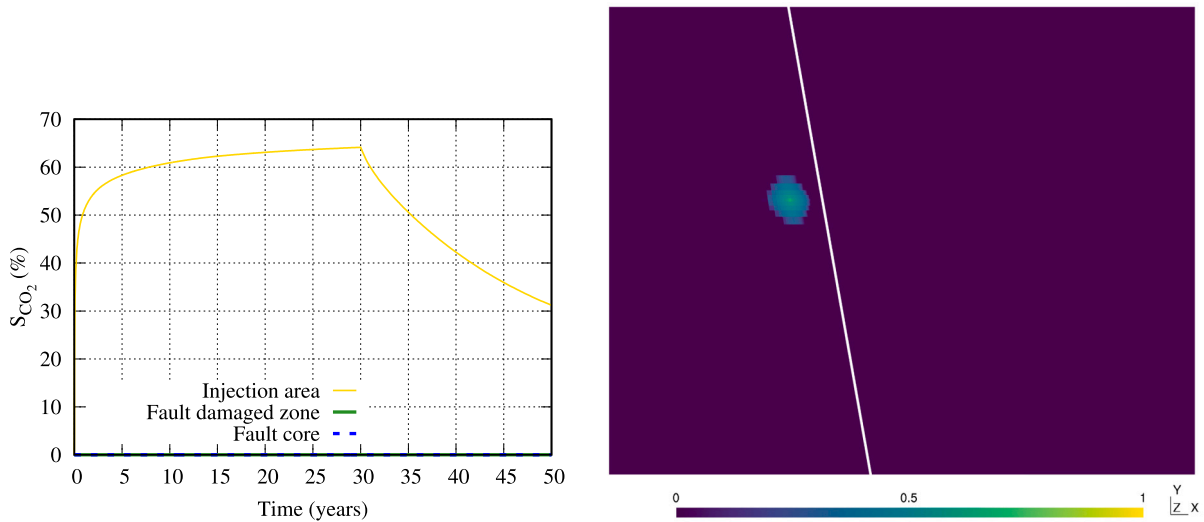


Fig. 8. Subseismic fault in strike-slip regime: evolution of CO₂ plume in the injection and fault zones (left), and CO₂ plume in the storage aquifer at $t = 30$ years (the white line indicates the position of the fault) (right).

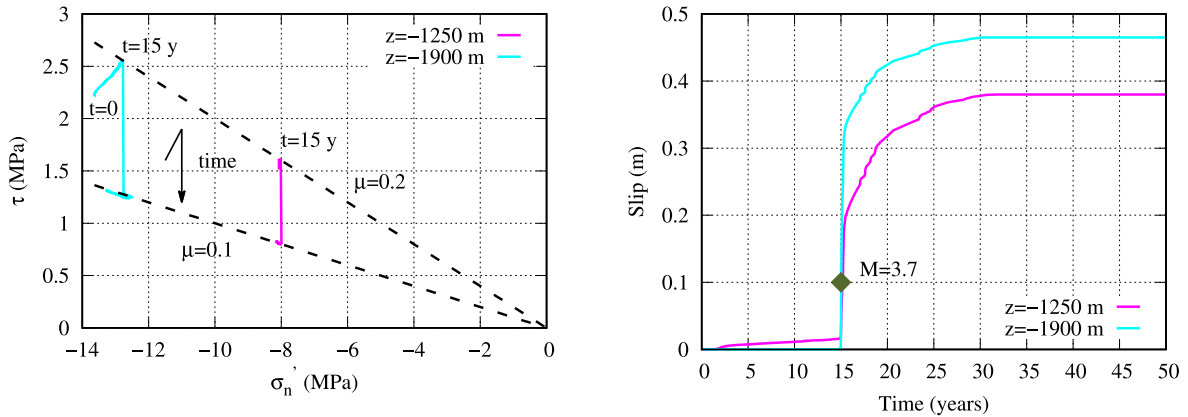


Fig. 9. Subseismic fault in strike-slip regime: stress path in the storage aquifer ($z = -1900 \text{ m}$) and the control aquifer ($z = -1250 \text{ m}$) (left), and cumulative slip at the same locations (right). The maximum instantaneous slip at 15 years is 16 cm.

CO₂ plume does not reach the fault area; therefore, in this particular scenario there is no risk of CO₂ leakage along the fault.

From a mechanical viewpoint, both the shear and the effective normal stresses on the fault plane increase, and eventually the failure criterion is reached, see Fig. 9. After about 0.8 years of injection, the fault plane shows very small amounts of slip (right plot) in the upper part, which is more critically stressed as the left plot shows. After 15 years of injection, a slip event of maximum instantaneous magnitude 16 cm occurs over an area of about 2.03 km², affecting all the vertical extent of the fault. During this event, the friction coefficient decreases

from μ_p to μ_r . Later on, there is continuous slip until the end of the injection because the failure criterion is reached due to the low value of the friction coefficient (very unfavorable conditions). Note that in this simulation we have neglected possible fault healing, so that the slip in Eq. (7) is not reset to zero every time step (accounting for fault healing may also affect the permeability evolution as discussed in Aochi et al. (2013)). Although the simulation is quasi-static, we can estimate the magnitude of the associated event at 15 years. The seismic magnitude M is calculated from the seismic moment M_0 using the following equations (Kanamori and Brodsky, 2004; Kanamori and

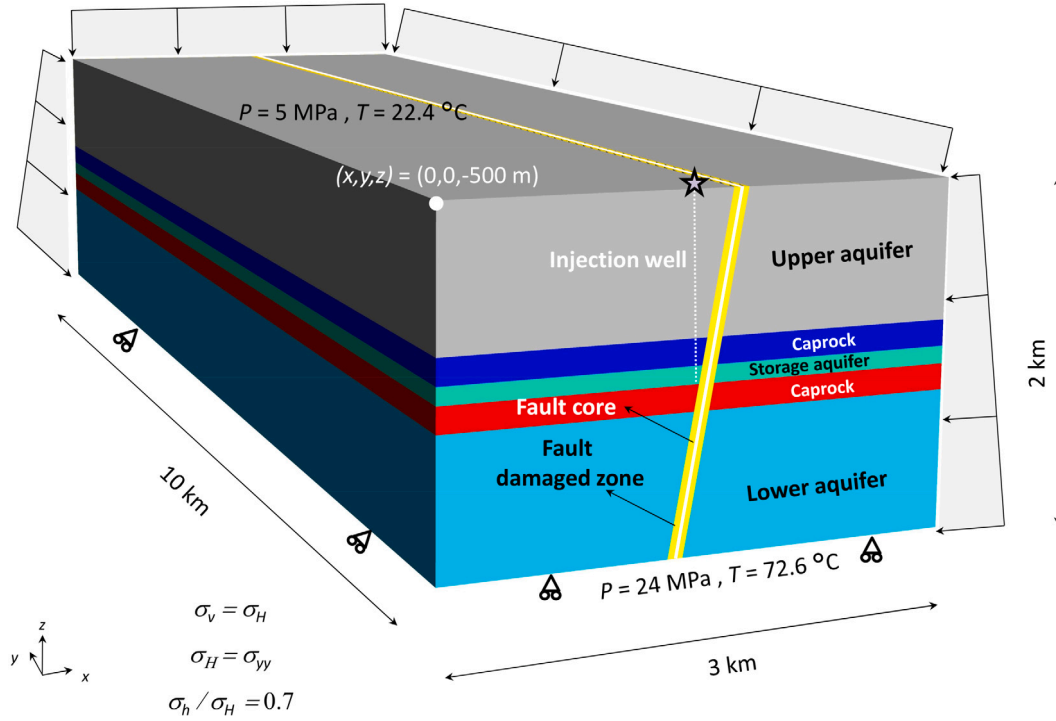


Fig. 10. Subseismic fault in normal faulting regime: conceptual model.

Anderson, 1975):

$$M_0 = GAd \quad (10)$$

$$M = \frac{2}{3} \log_{10} M_0 - 6.1 \quad (11)$$

where $G = \frac{E}{2(1+\nu)}$ is the shear modulus, A is the ruptured area and d is the current slip magnitude on A (the area associated to each node is computed, and multiplied by the current slip on that node). Note that in Eq. (11), the seismic moment is expressed in N·m. Applying these equations, we get a magnitude of 3.7 at 15 years.

4.2. Subseismic fault in normal faulting regime

In this section, we investigate a scenario inspired from Rinaldi et al. (2015), in which CO_2 is injected in the vicinity of a subseismic fault. Fig. 10 shows the conceptual model, with dimensions $3 \times 10 \times 2 \text{ km}^3$. Owing to symmetry, the geometry shown in Fig. 10 corresponds to one quarter of the total domain being modeled, which features two faults about 3 km apart. The storage aquifer is 100 m thick and lies between two 150 m thick caprocks. The thickness of the upper and lower aquifers is 800 m. A quasi-vertical fault (dip 80°) with negligible offset intersects the five layers shown. As in the previous case, the fault comprises a low-permeability core surrounded by a damaged zone with higher permeability. A fault interface is added between the fault core and the damage zone closest to the injection well. The thickness of the fault zone along the x axis is 90 m. CO_2 injection occurs through a vertical well located at $x \approx 1440 \text{ m}$ and $y = 0$, and open along the lowest 50 m of the storage aquifer layer. In this case, CO_2 is injected at a rate of 120 kg/s (3.78 Mt/y). The minimum distance between the injection well and the fault plane is 75 m; note that the high injection rate used and the well location are intended to represent an unfavorable scenario of an undetected fault that happens to be very close to the injection well, thereby increasing the likelihood of fault reactivation and leakage. Injection conditions are 15 MPa and 37°C (supercritical state), and the salinity of the storage aquifer is 50 g/l. Table 4 lists relevant properties of the five layers and the fault. Except for the

Table 4

Subseismic fault in normal faulting regime: parameters used in the simulation. Each layer is represented by a different color in Fig. 10. For all layers, $\rho_{gr} = 2260 \text{ kg/m}^3$, $\phi = 0.1$, $\lambda = 1.8 \text{ W/m/K}$, $C = 900 \text{ J/kg/K}$, $\alpha_{th} = 10^{-5} \text{ K}^{-1}$, $\nu = 0.25$ and $\alpha = 1$.

Layer	k (m^2)	E (GPa)	P_0 (kPa)
Upper aquifer	10^{-14}	10	20
Upper caprock	10^{-19}	10	620
Storage aquifer	10^{-13}	10	20
Lower caprock	10^{-19}	10	620
Lower aquifer	10^{-18}	10	620
Fault damaged zone	10^{-15a}	10	20
Fault core	10^{-17a}	5	20

^aNon-constant value (see text).

fault interface, all materials are assumed to behave elastically. Corey's relative permeability model is used for all layers with $S_{lr} = 0.3$ and $S_{gr} = 0.05$. For capillary pressure, we use van Genuchten's model with $\lambda_{VG} = 0.457$, $P_{cap}^{max} = 50 \text{ MPa}$ and $S_{lr} = 0$. Permeability is assumed isotropic in all layers.

In this case, the evolution of the friction coefficient follows the rate-and-state law (Eqs. (8)–(9)) with parameters $C = 0$, $\mu_0 = 0.6$, $\nu_0 = 2 \cdot 10^{-9} \text{ m/s}$, $L = 0.01 \text{ m}$, $a = 0.002$ and $b = 0.08$ (note that these values favor unstable sliding). It is assumed that the fault is initially in a steady state, with $\theta = 5 \cdot 10^6 \text{ s}$. To ensure stability, the maximum grid size Δx is smaller than the critical length scale, $L_c = \frac{\pi GL}{\sigma_n^{(b-a)}}$ (Rice, 1993). Additionally, we use adaptive time stepping.

As in Rinaldi et al. (2015), we account for mechanically-induced permeability changes along the fault. For the damaged zone, having randomly oriented fractures, we use a formulation based on experimental data on sandstone initially proposed by Davies and Davies (2001). It relates permeability changes to changes in porosity and mean effective stress, $\Delta\sigma'_M$,

$$k_{hm} = k_0 \exp \left[22.2 \left(\frac{(\phi_0 - \phi_r) \exp(5 \cdot 10^{-8} \Delta\sigma'_M) + \phi_r}{\phi_0} - 1 \right) \right] \quad (12)$$

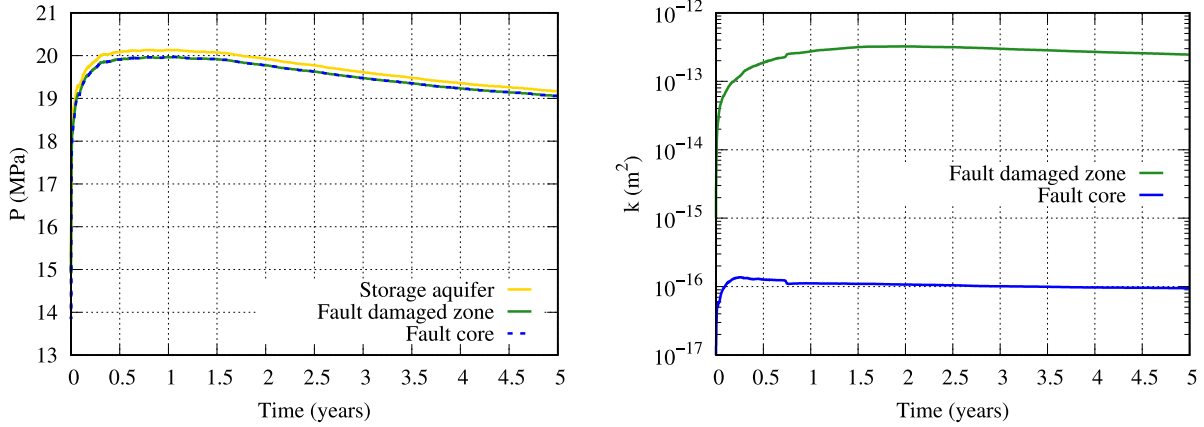


Fig. 11. Subseismic fault in normal faulting regime: evolution of pore pressure in the injection horizon (left), and permeability changes in the fault core and damaged zone (right).

where ϕ_0 and k_0 are the initial porosity and permeability, respectively, and ϕ_r is the residual porosity, taken to be 5% (Rutqvist and Tsang, 2002). This formulation allows for up to 3 orders of magnitude change in permeability (Rinaldi et al., 2014). The fault core permeability evolves following a model inspired from Hsiung et al. (2005):

$$k_{hm} = k_0 \left[\frac{a}{1 - c(c\sigma'_n)} \sqrt{\frac{\phi_0}{12k_0} + \frac{\phi - \phi_0}{\phi_0}} \right]^3 \quad (13)$$

where

$$c = \frac{1 - \sqrt{1 + 4\sigma'_n a \sqrt{\frac{\phi_0}{12k_0}}}}{2\sigma'_{n0}} \quad (14)$$

and $a = K^{-1}$ is an empirical constant.

As for the boundary conditions, no flow is allowed across planes $x = 0$ and $y = 0$, and the displacement normal to those planes is fixed to zero. The vertical displacement is zero at $z = -2500$ m, and at $z = -500$ m, the overburden weight is applied. Pressure and temperature are fixed at the top (5 MPa, 22.4 °C) and the bottom (24 MPa, 72.6 °C) boundaries. Hydrostatic, geothermal and lithostatic gradients are applied on the lateral boundaries at $x = 3$ km and $y = 10$ km. The geothermal gradient is 25 °C/km. The minor horizontal stress is parallel to the x direction, and $\sigma_H = \sigma_v$ (lithostatic). The ratio between horizontal stresses is $\sigma_h/\sigma_H = 0.7$. Note that fault orientation relative to the stress field is intended to represent an unfavorable scenario.

Similarly to Section 4.1, a first simulation is run to obtain equilibrium (hydrostatic, geothermal and lithostatic gradients). The initial pore pressure and temperature at the injection horizon are about 15 MPa and 48 °C, respectively. Subsequently, we model 5 years of CO₂ injection. Fig. 11 shows the evolution of pore pressure and permeability in the injection horizon. The pressure increases rapidly with injection, and peaks at about 20 MPa after 180 days. Later on, it decreases due to the permeability increase in the fault, see right plot. This is in contrast with the pore pressure evolution in the previous scenario discussed in Section 4.1, where permeability remained constant. Here, in the damaged zone permeability increases by a factor up to 300, while in the fault core, it increases up to a factor of 10. As compared to the results in Rinaldi et al. (2015), here the pressure peaks at a lower value due to the different porosity evolution model, which induces different permeability variations according to Eqs. (12)–(14).

The temperature evolution in the injection horizon is displayed in Fig. 12. Injection of cold CO₂ reduces the temperature around the well, in an area correlated with the extent of the CO₂ plume, displayed in Fig. 13. Given the high injection rate used, the proximity of the fault to the well and the fault permeability increase, leakage occurs along the fault, primarily along the damaged zone as shows the vertical profile

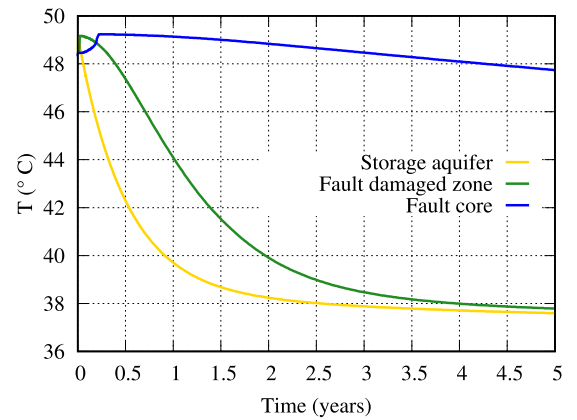


Fig. 12. Subseismic fault in normal faulting regime: evolution of temperature in the injection horizon.

at 5 years, and reaches the upper aquifer. Despite the permeability increase, the fault core still acts as a flow barrier, and as Fig. 13 shows, no CO₂ is observed across the fault.

The stress path at different locations is displayed in Fig. 14. After about 2 weeks of injection, a slip event of maximum instantaneous amplitude 6 cm occurs over an area of 94000 m². Using Eqs. (10)–(11), the associated magnitude is $M = 2.4$. Slip starts at the injection depth (bottom of storage aquifer) and propagates particularly into the underlying layers, see right plot. This evolution is consistent with previous investigations, e.g., (Jha and Juanes, 2014; Meguerdijian and Jha, 2021; Rinaldi et al., 2014). The friction coefficient decreases to 0.23 as a consequence of the reduction in the state variable during the event. Later on, it increases as the state variable increases due to slip rate reduction (Eqs. (8)–(9)). Some minor, sudden slip events ($M \approx 1$) occur until a second $M = 2.1$ event takes place after about 270 days of injection, with an associated maximum slip of 2 cm, rupture area of 132000 m² and a friction coefficient reduction to 0.34. Again, after the event the friction coefficient increases as the slip rate decreases and the state variable increases. At 5 years, $\mu = 0.85$.

5. Discussion and conclusions

Geologic storage of anthropogenic CO₂ has the potential to reduce greenhouse gas emissions to the atmosphere. From the geomechanical perspective, two major hazards associated with this technology that need to be addressed before any site implementation are fault reactivation (injection-induced seismicity) and leakage along the fault. Proper site characterization conducted before injection may help detect and

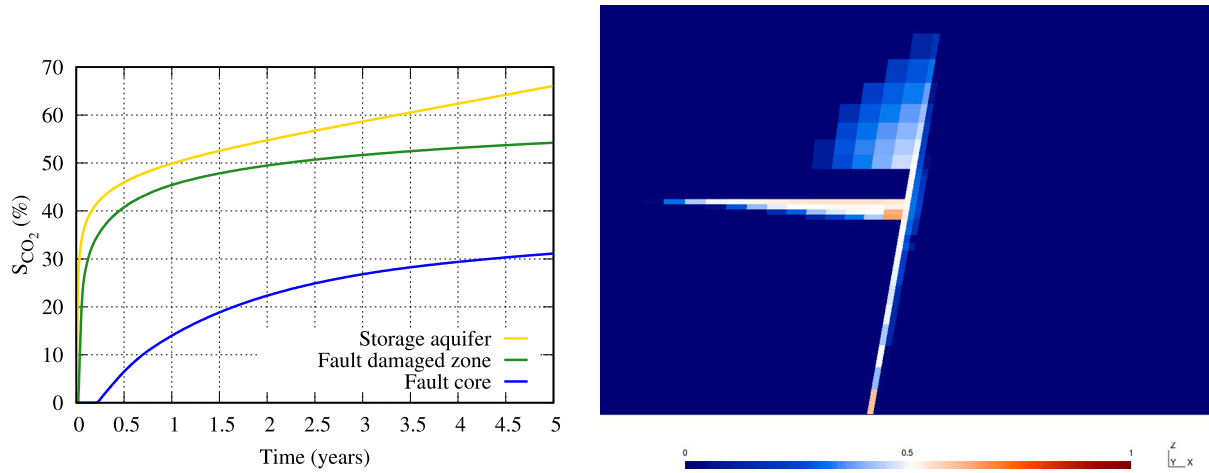


Fig. 13. Subseismic fault in normal faulting regime: evolution of CO₂ plume in the injection horizon (left), and CO₂ plume at $t = 5$ years in plane $y=0$ (right).

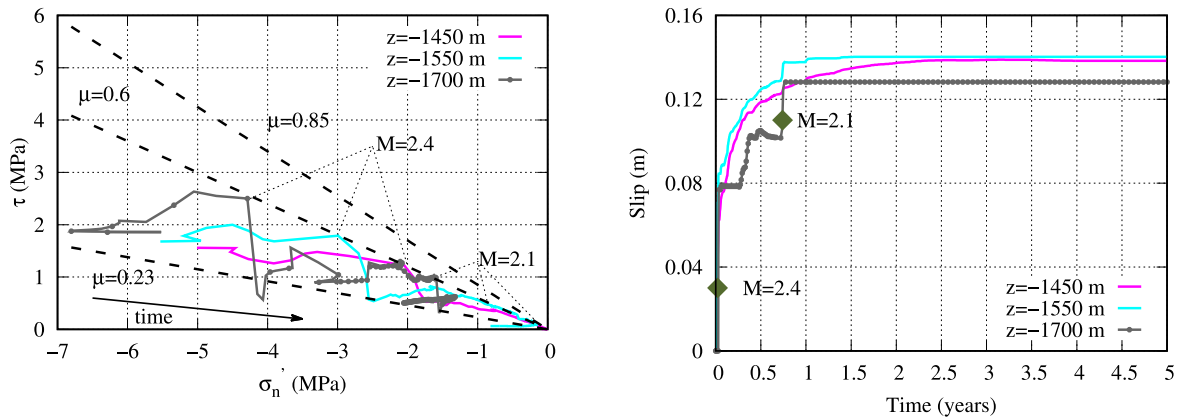


Fig. 14. Subseismic fault in normal faulting regime: stress path in the storage aquifer ($z = -1450$ m, $z = -1550$ m) and the lower caprock ($z = -1700$ m) (left), and cumulative slip at the same locations (right). The maximum instantaneous slip at 14 and 270 days is 6 and 2 cm, respectively.

avoid major faults, and in fact, to date seismicity associated with CO₂ sequestration is scarce. In this paper, we focus on subseismic faults having negligible offset that could be undetected during site selection and characterization.

We perform coupled THM modeling of CO₂ injection into deep saline aquifers intersected by undetected faults under two different tectonic regimes, strike-slip and normal faulting. To study fault failure more accurately, the fault zone includes a surface of discontinuity. We perform sequential, two-way THM coupling using TOUGH-Pylith, a simulator based on the non-isothermal, multiphase and multicomponent flow simulator TOUGH2, and the geomechanics, open-source code Pylith. The two simulators are successfully coupled for the first time in a THM framework, and TOUGH-Pylith takes advantage of the strengths of the two codes, namely, a wide range of equations-of-state to account for the thermodynamic behavior of pure fluids and mixtures, and the implementation of fault surfaces as discontinuities whose behavior is more representative of observed fault frictional strength, with quasi-static and dynamic ruptures. 2D and 3D simulations can be performed with TOUGH-Pylith. The coupling of the two codes is verified by means of comparison of numerical results with available analytical solutions. Then, we investigate two 3D cases of CO₂ injection in the vicinity of subseismic faults. The scenarios are taken from the literature and do not intend to reproduce real conditions; instead, to a certain extent they represent unfavorable situations for fault reactivation and leakage (high injection rates, moderate to high overpressures, proximity of the fault to the injection well, favorable *in situ* stress field relative to fault orientation, choice of friction parameters and permeability evolution).

They suggest that minor events could be triggered, and highlight the need of thorough site characterization and careful monitoring during operations. Although not discussed here, the grid resolution used should be fine enough to accurately predict the CO₂ plume (Youssef et al., 2021) and allow for numerical stability (Rice, 1993).

In a broader sense, TOUGH-Pylith allows to investigate many situations beyond subseismic faults. For instance, it could be used to estimate leakage rates over long periods of time (Mioic et al., 2019), or to model different fault architectures (e.g., homogeneous vs. fault system comprising a core and a damaged zone) and evaluate their impact on fault stability and possible leakage paths. In this context, the permeability evolution within the fault zone is not fully understood, and different evolution laws could be tested with the simulator, and the uncertainties could be quantified. Additionally, it could be used as a numerical support to many field studies, such as those at the decameter scale and under controlled conditions, that seek to better understand the link between induced seismicity and leakage in reservoir and caprock analogs (Guglielmi et al., 2021; Zappone et al., 2021), or the monitorability and the impacts of a fault zone on CO₂ migration (Michael et al., 2020). The applications are not solely related to CO₂ storage, but rather extend to scenarios comprising one or several faults in different natural or anthropogenic settings, such as geothermal (Amann et al., 2018) or nuclear waste disposal (Orellana et al., 2018).

Finally, it should be noted that in the cases investigated here, the fluid-induced slip rates are slow, much smaller than 0.1 mm/s, so the use of a quasi-static approach with appropriate parameters (in

particular, large values of the characteristic length) is justified (Torberntsson et al., 2018). While the current methodology enables the simulation of a sudden slip, the quasi-static approach does not allow for a complete separation of aseismic and seismic slips. The resulting magnitudes could then be overestimated, as the final co-seismic deformation accounts for more than the true seismic slip. As a next stage, adapting the coupling scheme to quasi-dynamic (through the introduction of a radiation damping term in the shear stress, such as in Torberntsson et al. (2018), Yang and Dunham (2021) or (Rice, 1993)) and fully dynamic approaches (through the introduction of the inertial term in the momentum equation, such as in Jin and Zoback (2018) or (Yang and Dunham, 2021)) would extend the use of TOUGH-Pylith to investigate dynamic fault seismic slip. Additionally, the use of TOUGH3 would allow for parallelized simulations of both the flow and the geomechanics sub-problems, thereby reducing the computational time (Rinaldi et al., 2022).

CRedit authorship contribution statement

Laura Blanco-Martín: conceptualization, Methodology, Software, Analysis, Writing. **Emad Jahangir:** conceptualization, Analysis, Writing. **Antonio P. Rinaldi:** Methodology, Writing, Validation. **Jonny Rutqvist:** Methodology, Writing, Validation.

Declaration of competing interest

The authors declare that they have no known competing financial interests or personal relationships that could have appeared to influence the work reported in this paper.

Data availability

Data can be made available upon reasonable request

Acknowledgments

Funding for this work has been provided by the French National Research Agency (ANR) through Geodnergies under contract No. 10-IEED-0810-04 (MissCO₂ project). Additional funding was provided by the U.S. Department of Energy under contract No. DE-AC0205CH11231 to the Lawrence Berkeley National Laboratory.

References

- Aagaard, B.T., Knepley, M.G., Williams, C.A., 2013. A domain decomposition approach to implementing fault slip in finite-element models of quasi-static and dynamic crustal deformation. *J. Geophys. Res.: Solid Earth* 118, 3059–3079. <http://dx.doi.org/10.1002/jgrb.50217>.
- Aagaard, B.T., Knepley, M., Williams, C., 2017. PyLith User Manual, Version 2.2.1. Computational Infrastructure for Geodynamics (CIG), University of California, Davis, https://geodynamics.org/resources/1673/download/pylith-2.2.1_manual.pdf.
- Abousleiman, Y., Cheng, A.H.-D., Cui, L., Detournay, E., Roegiers, J.-C., 1996. Mandel's problem revisited. *Géotechnique* 46 (2), 187–195. <http://dx.doi.org/10.1680/geot.1996.46.2.187>.
- Amann, F., Gischig, V., Evans, K., Doetsch, J., Jalali, R., Valley, B., Krietsch, H., Dutler, N., Villiger, L., Brixel, B., Klepikova, M., Kittilä, A., Madonna, C., Wiemer, S., Saar, M.O., Loew, S., Driesner, T., Maurer, H., Giardini, D., 2018. The seismo-hydronechanical behavior during deep geothermal reservoir stimulations: open questions tackled in a decimeter-scale in situ stimulation experiment. *Solid Earth* 9, 115–137. <http://dx.doi.org/10.5194/se-9-115-2018>.
- Anderson, E., 1951. *The Dynamics of Faulting and Dyke Formation with Applications to Britain*. Oliver and Boyd, New York.
- Aochi, H., Poisson, B., Toussaint, R., Rachez, X., Schmittbuhl, J., 2013. Self-induced seismicity due to fluid circulation along faults. *Geophys. J. Int.* 196 (3), 1544–1563. <http://dx.doi.org/10.1093/gji/ggt356>.
- Bésuelle, P., Desrues, J., Raynaud, S., 2000. Experimental characterisation of the localisation phenomenon inside a vosges sandstone in a triaxial cell. *Int. J. Rock Mech. Min. Sci.* 37 (8), 1223–1237. [http://dx.doi.org/10.1016/S1365-1609\(00\)00057-5](http://dx.doi.org/10.1016/S1365-1609(00)00057-5).
- Blanco-Martín, L., Rutqvist, J., Birkholzer, J.T., 2015. Long-term modeling of the thermal-hydraulic-mechanical response of a generic salt repository for heat-generating nuclear waste. *Eng. Geol.* 193, 198–211. <http://dx.doi.org/10.1016/j.enggeo.2015.04.014>.
- Blanco-Martín, L., Rutqvist, J., Birkholzer, J.T., 2017. Extension of TOUGH-FLAC to the finite strain framework. *Comput. Geosci.* 108, 64–71. <http://dx.doi.org/10.1016/j.cageo.2016.10.015>.
- Caine, J.S., Evans, J.P., Forster, C.B., 1996. Fault zone architecture and permeability structure. *Geology* 24 (11), 1025–1028. [http://dx.doi.org/10.1130/0091-7613\(1996\)024<1025:FZAAPS>2.3.CO;2](http://dx.doi.org/10.1130/0091-7613(1996)024<1025:FZAAPS>2.3.CO;2).
- Cappa, F., Rutqvist, J., 2011. Modeling of coupled deformation and permeability evolution during fault reactivation induced by deep underground injection of CO₂. *Int. J. Greenhouse Gas Control* 5 (2), 336–346. <http://dx.doi.org/10.1016/j.ijggc.2010.08.005>.
- Chu, S., 2009. Carbon capture and sequestration. *Science* 325 (5948), <http://dx.doi.org/10.1126/science.1181637>.
- Collins, M., Knutti, R., Arblaster, J., Dufresne, J.-L., Fichet, T., Friedlingstein, P., Gao, X., Gutowski, W., Johns, T., Krinner, G., Shongwe, M., Tebaldi, C., Weaver, A., Wehner, M., 2013. Long-term climate change: Projections, commitments and irreversibility. In: *Climate Change 2013: The Physical Science Basis. Contribution of Working Group I to the Fifth Assessment Report of the Intergovernmental Panel on Climate Change*. Cambridge University Press, Cambridge, United Kingdom and New York, NY, USA, pp. 1029–1136.
- Cooper, C., 2009. A technical basis for carbon dioxide storage. *Energy Procedia* 1 (1), 1727–1733. <http://dx.doi.org/10.1016/j.egypro.2009.01.226>.
- Davies, J., Davies, D., 2001. Stress-dependent permeability: Characterization and modeling. *SPE J.* 6 (2), 224–235. <http://dx.doi.org/10.2118/71750-PA>.
- Dean, R.H., Gai, X., Stone, C.M., Minkoff, S.E., 2006. A comparison of techniques for coupling porous flow and geomechanics. *SPE J.* 11 (01), 132–140. <http://dx.doi.org/10.2118/79709-pa>.
- Dieterich, J.H., 1981. Constitutive properties of faults with simulated gouge. In: *Mechanical Behavior of Crustal Rocks*. American Geophysical Union (AGU), pp. 103–120. <http://dx.doi.org/10.1029/GM024p0103>.
- Dieterich, J.H., Richards-Dinger, K.B., Kroll, K.A., 2015. Modeling injection-induced seismicity with the physics-based earthquake simulator RSQSim. *Seismol. Res. Lett.* 86 (4), 1102–1109. <http://dx.doi.org/10.1785/0220150057>.
- Ennis-King, J., Paterson, L., 2001. Reservoir engineering issues in the geological disposal of carbon dioxide. In: *Fifth International Conference on Greenhouse Gas Control Technologies*, Cairns, vol. 1. pp. 290–295.
- Guglielmi, Y., Nussbaum, C., Cappa, F., De Barros, L., Rutqvist, J., Birkholzer, J., 2021. Field-scale fault reactivation experiments by fluid injection highlight aseismic leakage in caprock analogs: Implications for CO₂ sequestration. *Int. J. Greenhouse Gas Control* 111, 103471. <http://dx.doi.org/10.1016/j.ijggc.2021.103471>.
- Herzog, H., 2016. Lessons learned from CCS demonstration and large pilot projects. In: *An MIT Energy Initiative Working Paper*. MIT Energy Initiative, Massachusetts Institute of Technology.
- Hsiung, S., Chowdhury, A., Nataraja, M., 2005. Numerical simulation of thermal-mechanical processes observed at the Drift-Scale Heater Test at Yucca Mountain, Nevada, USA. *Int. J. Rock Mech. Min. Sci.* 42 (5), 652–666. <http://dx.doi.org/10.1016/j.ijrmms.2005.03.006>.
- IEA, 2008. CO₂ Capture and Storage: A Key Carbon Abatement Option. p. 264. <http://dx.doi.org/10.1787/9789264041417-en>.
- IEA, 2022. <https://www.iea.org/fuels-and-technologies/carbon-capture-utilisation-and-storage>. Last accessed 25 January 2022.
- Iglauer, S., 2011. *Dissolution Trapping of Carbon Dioxide in Reservoir Formation Brine - A Carbon Storage Mechanism*. INTECH Open Access Publisher.
- Ikari, M.J., Marone, C., Saffer, D.M., 2011. On the relation between fault strength and frictional stability. *Geology* 39 (1), 83–86. <http://dx.doi.org/10.1130/G31416.1>.
- Jha, B., Juanes, R., 2014. Coupled multiphase flow and poromechanics: A computational model of pore pressure effects on fault slip and earthquake triggering. *Water Resour. Res.* 50 (5), 3776–3808. <http://dx.doi.org/10.1002/2013WR015175>.
- Jin, L., Zoback, M.D., 2018. Fully dynamic spontaneous rupture due to quasi-static pore pressure and poroelastic effects: An implicit nonlinear computational model of fluid-induced seismic events. *J. Geophys. Res.: Solid Earth* 123 (11), 9430–9468. <http://dx.doi.org/10.1029/2018JB015669>.
- Jung, Y., Pau, G.S.H., Finsterle, S., Pollyea, R.M., 2017. TOUGH3: A new efficient version of the TOUGH suite of multiphase flow and transport simulators. *Comput. Geosci.* 108, 2–7. <http://dx.doi.org/10.1016/j.cageo.2016.09.009>.
- Kanamori, H., Anderson, D.L., 1975. Theoretical basis of some empirical relations in seismology. *Bull. Seismol. Soc. Am.* 65 (5), 1073–1095.
- Kanamori, H., Brodsky, E.E., 2004. The physics of earthquakes. *Rep. Progr. Phys.* 67 (8), 1429–1496. <http://dx.doi.org/10.1088/0034-4885/67/8/r03>.
- Kim, J., Sonnenthal, E.L., Rutqvist, J., 2012. Formulation and sequential numerical algorithms of coupled fluid/heat flow and geomechanics for multiple porosity materials. *Internat. J. Numer. Methods Engrg.* 92 (5), 425–456. <http://dx.doi.org/10.1002/nme.4340>.
- Kim, J., Tchelepi, H.A., Juanes, R., 2009. Stability, accuracy and efficiency of sequential methods for coupled flow and geomechanics. In: *SPE Reservoir Simulation Conference*. SPE-119084-MS <http://dx.doi.org/10.2118/119084-MS>.

- Le Gallo, Y., 2016. Hydro-mechanical influence of sub-seismic blind faults on integrity of CO₂ geological storage in deep saline aquifer. *Int. J. Greenhouse Gas Control* 51, 148–164. <http://dx.doi.org/10.1016/j.ijggc.2016.05.018>.
- Leung, D.Y., Caramanna, G., Maroto-Valer, M.M., 2014. An overview of current status of carbon dioxide capture and storage technologies. *Renew. Sustain. Energy Rev.* 39, 426–443. <http://dx.doi.org/10.1016/j.rser.2014.07.093>.
- Lohr, T., Krawczyk, C.M., Tanner, D.C., Samiee, R., Endres, H., Thierer, P.O., Oncken, O., Trappe, H., Bachmann, R., Kukla, P.A., 2008. Prediction of sub-seismic faults and fractures: Integration of three-dimensional seismic data, three-dimensional retrodeformation, and well data on an example of deformation around an inverted fault. *AAPG Bull.* 92 (4), 473–485. <http://dx.doi.org/10.1306/11260707046>.
- Lupion, M., Herzog, H.J., 2013. NER300: Lessons learnt in attempting to secure CCS projects in Europe. *Int. J. Greenhouse Gas Control* 19, 19–25. <http://dx.doi.org/10.1016/j.ijggc.2013.08.009>.
- Mandel, J., 1953. Consolidation des sols (étude mathématique). *Géotechnique* 3 (7), 287–299. <http://dx.doi.org/10.1680/geot.1953.3.7.287>.
- Mazzoldi, A., Rinaldi, A.P., Borgia, A., Rutqvist, J., 2012. Induced seismicity within geological carbon sequestration projects: Maximum earthquake magnitude and leakage potential from undetected faults. *Int. J. Greenhouse Gas Control* 10, 434–442. <http://dx.doi.org/10.1016/j.ijggc.2012.07.012>.
- McClure, M.W., Horne, R.N., 2011. Investigation of injection-induced seismicity using a coupled fluid flow and rate/state friction model. *Geophysics* 76 (6), WC181–WC198. <http://dx.doi.org/10.1190/geo2011-0064.1>.
- McTigue, D.F., 1986. Thermoelastic response of fluid-saturated porous rock. *J. Geophys. Res.: Solid Earth* 91 (B9), 9533–9542. <http://dx.doi.org/10.1029/JB091iB09p09533>.
- Meguerdijian, S., Jha, B., 2021. Quantification of fault leakage dynamics based on leakage magnitude and dip angle. *Int. J. Numer. Anal. Methods Geomech.* 45 (16), 2303–2320. <http://dx.doi.org/10.1002/nag.3267>.
- Meng, C., 2017. Benchmarking Defmod, an open source FEM code for modeling episodic fault rupture. *Comput. Geosci.* 100, 10–26.
- Miah, M., 2016. Development of a Dynamic Coupled Hydro-Geomechanical Code and Its Application to Induced Seismicity (Ph.D. thesis). University of Mississippi, p. 164.
- Miah, M., Blanco-Martín, L., Foxall, W., Rutqvist, J., Rinaldi, A.P., Mullen, C., 2015. Development of a hydro-geomechanical model to simulate coupled fluid flow and reservoir geomechanics. In: *TOUGH Symposium 2015*.
- Michael, K., Avijegon, A., Ricard, L., Myers, M., Tertyshnikov, K., Pevzner, R., Strand, J., Horte, A., Stalker, L., Pervukhina, M., Harris, B., Feitz, A., Pejčić, B., Larcher, A., Rachakonda, P., Freifeld, B., Woitt, M., Langhi, L., Dance, T., Myers, J., Roberts, J., Saygin, E., White, C., Seyyedi, M., 2020. A controlled CO₂ release experiment in a fault zone at the In-Situ Laboratory in Western Australia. *Int. J. Greenhouse Gas Control* 99, 103100. <http://dx.doi.org/10.1016/j.ijggc.2020.103100>.
- Millien, A., 1993. Comportement anisotrope du grès des Vosges: élasto-plasticité, localisation, rupture (Ph.D. thesis). University of Grenoble I, p. 220.
- Miocic, J.M., Gilfillan, S.M.V., Frank, N., Schroeder-Ritzrau, A., Burnside, N.M., Haszeldine, R.S., 2019. 420,000 Year assessment of fault leakage rates shows geological carbon storage is secure. *Sci. Rep.* 9 (1), 769. <http://dx.doi.org/10.1038/s41598-018-36974-0>.
- Mortezaei, K., Vahedifard, F., 2015. Numerical simulation of induced seismicity in carbon capture and storage projects. *Geotech. Geol. Eng.* 33 (2), 411–424.
- Okada, Y., 1992. Internal deformation due to shear and tensile faults in a half-space. *Bull. Seismol. Soc. Am.* 82, 1018–1040.
- Orellana, L.F., Scuderi, M.M., Collettini, C., Violay, M., 2018. Do scaly clays control seismicity on faulted shale rocks? *Earth Planet. Sci. Lett.* 488, 59–67. <http://dx.doi.org/10.1016/j.epsl.2018.01.027>.
- Pawar, R.J., Bromhal, G.S., Carey, J.W., Foxall, W., Korre, A., Ringrose, P.S., Tucker, O., Watson, M.N., White, J.A., 2015. Recent advances in risk assessment and risk management of geologic CO₂ storage. *Int. J. Greenhouse Gas Control* 40, 292–311. <http://dx.doi.org/10.1016/j.ijggc.2015.06.014>.
- Pruess, K., 2005. *ECO2N: A TOUGH2 Fluid Property Module for Mixtures of Water, NaCl and CO₂*. Lawrence Berkeley National Laboratory, University of California, Berkeley.
- Pruess, K., 2013. *ECO2M: A TOUGH2 Fluid Property Module for Mixtures of Water, NaCl, and CO₂, Including Super- and Sub-Critical Conditions, and Phase Change Between Liquid and Gaseous CO₂*. Lawrence Berkeley National Laboratory, University of California, Berkeley.
- Pruess, K., Oldenburg, C., Moridis, G., 2012. *TOUGH2 User's Guide, v2*. Lawrence Berkeley National Laboratory, University of California, Berkeley.
- Raza, A., Gholami, R., Rezaee, R., Rasouli, V., Rabiei, M., 2019. Significant aspects of carbon capture and storage - A review. *Petroleum* 5 (4), 335–340. <http://dx.doi.org/10.1016/j.petlm.2018.12.007>.
- Rice, J.R., 1993. Spatio-temporal complexity of slip on a fault. *J. Geophys. Res.: Solid Earth* 98 (B6), 9885–9907. <http://dx.doi.org/10.1029/93JB00191>.
- Rinaldi, A.P., Rutqvist, J., Cappa, F., 2014. Geomechanical effects on CO₂ leakage through fault zones during large-scale underground injection. *Int. J. Greenhouse Gas Control* 20, 117–131. <http://dx.doi.org/10.1016/j.ijggc.2013.11.001>.
- Rinaldi, A.P., Rutqvist, J., Luu, K., Blanco-Martín, L., Hu, M., Sentis, M.L., Eberle, L., Kästli, P., 2022. TOUGH3-FLAC3D: a modeling approach for parallel computing of fluid flow and geomechanics (Preprint). *Earth Space Sci. Open Arch.* 36. <http://dx.doi.org/10.1002/essoar.10505967.3>.
- Rinaldi, A.P., Vilarrasa, V., Rutqvist, J., Cappa, F., 2015. Fault reactivation during CO₂ sequestration: Effects of well orientation on seismicity and leakage. *Greenhouse Gases: Sci. Technol.* 5 (5), 645–656. <http://dx.doi.org/10.1002/ghg.1511>.
- Rohmer, J., 2014. Induced seismicity of a normal blind undetected reservoir-bounding fault influenced by dissymmetric fractured damage zones. *Geophys. J. Int.* 197 (1), 636–641. <http://dx.doi.org/10.1093/gji/ggu018>.
- Ruina, A., 1983. Slip instability and state variable friction laws. *J. Geophys. Res.: Solid Earth* 88 (B12), 10359–10370. <http://dx.doi.org/10.1029/JB088iB12p10359>.
- Rutqvist, J., 2011. Status of the TOUGH-FLAC simulator and recent applications related to coupled fluid flow and crustal deformations. *Comput. Geosci.* 37 (6), 739–750. <http://dx.doi.org/10.1016/j.cageo.2010.08.006>.
- Rutqvist, J., 2012. The geomechanics of CO₂ storage in deep sedimentary formations. *Geotech. Geol. Eng.* 30 (3), 525–551. <http://dx.doi.org/10.1007/s10706-011-9491-0>.
- Rutqvist, J., Tsang, C.-F., 2002. A study of caprock hydromechanical changes associated with CO₂-injection into a brine formation. *Environ. Geol.* 42 (2), 296–305. <http://dx.doi.org/10.1007/s00254-001-0499-2>.
- Rutqvist, J., Wu, Y.-S., Tsang, C.-F., Bodvarsson, G., 2002. A modeling approach for analysis of coupled multiphase fluid flow, heat transfer, and deformation in fractured porous rock. *Int. J. Rock Mech. Min. Sci.* 39 (4), 429–442. [http://dx.doi.org/10.1016/S1365-1609\(02\)00022-9](http://dx.doi.org/10.1016/S1365-1609(02)00022-9).
- Sarkus, T., Tennyson, M., Vikara, D., 2016. Geologic carbon storage. In: *Fossil Fuels*. pp. 49–80, (Chapter 3). http://dx.doi.org/10.1142/9789814699983_0003.
- Schiffman, R.L., Chen, A.T.-F., Jordan, J.C., 1969. An analysis of consolidation theories. *J. Soil Mech. Found. Div.* 95 (1), 285–312. <http://dx.doi.org/10.1061/JSEFAQ.0001222>.
- Settari, A., Mourits, F., 1998. A coupled reservoir and geomechanical simulation system. *SPE J.* 3, 219–226. <http://dx.doi.org/10.2118/50939-PA>.
- Sibson, R.H., 1977. Fault rocks and fault mechanisms. *J. Geol. Soc.* 133 (3), 191–213. <http://dx.doi.org/10.1144/gsjgs.133.3.0191>.
- Spycher, N., Pruess, K., 2005. CO₂-H₂O mixtures in the geological sequestration of CO₂. II. Partitioning in chloride brines at 12–100 C and up to 600 bar. *Geochim. Cosmochim. Acta* 69 (13), 3309–3320. <http://dx.doi.org/10.1016/j.gca.2005.01.015>.
- Spycher, N., Pruess, K., Ennis-King, J., 2003. CO₂-H₂O mixtures in the geological sequestration of CO₂. I. Assessment and calculation of mutual solubilities from 12 to 100 C and up to 600 bar. *Geochim. Cosmochim. Acta* 67 (16), 3015–3031. [http://dx.doi.org/10.1016/S0016-7037\(03\)00273-4](http://dx.doi.org/10.1016/S0016-7037(03)00273-4).
- Torberntsson, K., Stiernström, V., Mattsson, K., Dunham, E.M., 2018. A finite difference method for earthquake sequences in poroelastic solids. *Comput. Geosci.* 22 (5), 1351–1370. <http://dx.doi.org/10.1007/s10596-018-9757-1>.
- van Genuchten, M., 1980. A Closed form Equation for Predicting the Hydraulic Conductivity of Unsaturated Soils. *Soil Sci. Am. J.* 44 (5), 892–898. <http://dx.doi.org/10.2136/sssaj1980.03615995004400050002x>.
- Vidal-Gilbert, S., Nauroy, J.-F., Brosse, E., 2009. 3D geomechanical modelling for CO₂ geologic storage in the Dogger carbonates of the Paris Basin. *Int. J. Greenhouse Gas Control* 3 (3), 288–299. <http://dx.doi.org/10.1016/j.ijggc.2008.10.004>.
- Vilarrasa, V., Bolster, D., Olivella, S., Carrera, J., 2010. Coupled hydromechanical modeling of CO₂ sequestration in deep saline aquifers. *Int. J. Greenhouse Gas Control* 4 (6), 910–919. <http://dx.doi.org/10.1016/j.ijggc.2010.06.006>.
- Vilarrasa, V., Carrera, J., 2015. Geologic carbon storage is unlikely to trigger large earthquakes and reactivate faults through which CO₂ could leak. *Proc. Natl. Acad. Sci.* 112 (19), 5938–5943. <http://dx.doi.org/10.1073/pnas.1413284112>.
- White, J.A., Borja, R.I., 2008. Stabilized low-order finite elements for coupled solid-deformation/fluid-diffusion and their application to fault zone transients. *Comput. Methods Appl. Mech. Engrg.* 197 (49), 4353–4366. <http://dx.doi.org/10.1016/j.cma.2008.05.015>.
- White, J.A., Foxall, W., 2016. Assessing induced seismicity risk at CO₂ storage projects: Recent progress and remaining challenges. *Int. J. Greenhouse Gas Control* 49, 413–424. <http://dx.doi.org/10.1016/j.ijggc.2016.03.021>.
- White, M.D., Podgorney, R., Kelkar, S.M., McClure, M.W., Danko, G., Ghassemi, A., Fu, P., Bahrami, D., Barbier, C., Cheng, Q., Chiu, K.-K., Detournay, C., Elsworth, D., Fang, Y., Furtney, J.K., Gan, Q., Gao, Q., Guo, B., Hao, Y., Horne, R.N., Huang, K., Im, K., Norbeck, J., Rutqvist, J., Safari, M.R., Sesetty, V., Sonnenthal, E., Tao, Q., White, S.K., Wong, Y., Xia, Y., 2016. Benchmark Problems of the Geothermal Technologies Office Code Comparison Study. Technical Report PNNL-26016, Pacific Northwest National Laboratory, USA.
- Wibberley, C., Shimamoto, T., 2003. Internal structure and permeability of major strike-slip fault zones: the Median Tectonic Line in Mie Prefecture, Southwest Japan. *J. Struct. Geol.* 25 (1), 59–78. [http://dx.doi.org/10.1016/S0191-8141\(02\)00014-7](http://dx.doi.org/10.1016/S0191-8141(02)00014-7).
- Wileveau, Y., Cornet, F., Desroches, J., Blumling, P., 2007. Complete in situ stress determination in an argillite sedimentary formation. *Phys. Chem. Earth Parts A/B/C* 32 (8), 866–878. <http://dx.doi.org/10.1016/j.pce.2006.03.018>.

- Yang, Y., Dunham, E.M., 2021. Effect of porosity and permeability evolution on injection-induced aseismic slip. *J. Geophys. Res.: Solid Earth* 126 (7), p. e2020JB021258. <http://dx.doi.org/10.1029/2020JB021258>.
- Youssef, A.A., Tran, L., Matthäi, S., 2021. Impact of the vertical resolution of corner-point grids on CO₂ plume migration predictions for layered aquifers. *Int. J. Greenhouse Gas Control* 106, 103249. <http://dx.doi.org/10.1016/j.ijggc.2021.103249>.
- Zappone, A., Rinaldi, A.P., Grab, M., Wenning, Q.C., Roques, C., Madonna, C., Obermann, A.C., Bernasconi, S.M., Brennwald, M.S., Kipfer, R., Soom, F., Cook, P., Guglielmi, Y., Nussbaum, C., Giardini, D., Mazzotti, M., Wiemer, S., 2021. Fault sealing and caprock integrity for CO₂ storage: an in situ injection experiment. *Solid Earth* 12, 319–343. <http://dx.doi.org/10.5194/se-12-319-2021>.
- Zoback, M.D., Gorelick, S.M., 2012. Earthquake triggering and large-scale geologic storage of carbon dioxide. *Proc. Natl. Acad. Sci.* 109 (26), 10164–10168. <http://dx.doi.org/10.1073/pnas.1202473109>.



Contents lists available at ScienceDirect

International Journal of Rock Mechanics and Mining Sciences

journal homepage: <http://www.elsevier.com/locate/ijrmms>

Rock salt behavior: From laboratory experiments to pertinent long-term predictions

M. Azabou^{a,*}, A. Rouabhi^a, L. Blanco-Martín^a, F. Hadj-Hassen^a, M. Karimi-Jafari^b, G. Hévin^c

^a MINES ParisTech, PSL Research University, Centre de Géosciences, 35 Rue St Honoré, Fontainebleau, 77300, France

^b Geostock Entrepose, 2 Rue des Martinets, RUEIL-MALMAISON, 92500, France

^c Storengy, 12 Rue Raoul Nordling, Bois-Colombes, 92274, France

ARTICLE INFO

Keywords:

Rock salt
Constitutive modeling
Long-term creep
Laboratory tests
Time extrapolation

ABSTRACT

In the energy transition context, salt caverns are probably the most promising storage solution that promotes the development of intermittent renewable energies, due to their flexible and high deliverability. However, their design is still challenging since it should account for their entire lifetime, from rapid cycling exploitation to centuries of abandonment. The key to an optimal design is a constitutive model for rock salt that ensures pertinent short and long-term predictions. In this paper, we confront the results of five experimental campaigns conducted on different salts with existing rheological models. This confrontation proved that the studied models are capable of describing laboratory tests, however their predictions for the long term are either too conservative or overly optimistic. In practice, conservative or optimistic approaches do not ensure the optimal design of the facility. For this reason, we propose a new constitutive model that provides pertinent long-term predictions while interpreting satisfactorily short-term and long-term laboratory tests.

1. Introduction

Solution mined caverns in salt formations have proven to be among the most efficient techniques for storage of different energy vectors since the 1960s.^{1–10} Today these facilities have an important role in the energy transition context. Their flexible and high deliverability makes them the most promising solution to respond to peak demand for intermittent clean energies. The feasibility studies and the design of these caverns should account for the exploitation phase and for the decades and sometimes centuries of the abandonment phase. The optimal design of these structures rests upon the use of a constitutive model with pertinent short and long-term predictions.

There cannot be a unique rheological model able to describe the behavior of a geological material such as rock salt, under all kinds and within all ranges of thermo-mechanical loadings. What is sought instead, are approximate laws that can provide a close enough description to the real behavior of the rock within a given range of loading conditions. This explains the abundance of rock salt constitutive models in the literature. All the existing models, despite the differences in the phenomena they account for (dilatancy, healing, inverse creep, transient, steady state and tertiary creep, damage, extension, strain under tensile loading ...), agree on two facts: first, rock salt has a

strongly time dependent behavior and second, laboratory tests are essential for their parameters calibration. The multitude of models proves their limitations and justifies the need for the research on rock salt rheology to continue.

Long-term behavior is one of the main challenges for the rheological modeling of rock salt. In fact, it is technically possible to conduct tests under all desired loading conditions (different strain rates, temperatures, mechanical and thermal cycling ...). However, contrary to the thermo-mechanical variables, we do not have control over the time of laboratory experiments, which is negligible compared to the lifetime of the underground facilities (a few months or years in the best case scenario, compared to few decades or even centuries in the field). When performing a time-extrapolation of the existing models, three kinds of responses are obtained: (i) a transient response where the strain rate continuously decreases,^{11–13} (ii) a purely steady-state response where the strain rate remains constant and the strain increases linearly over time¹⁴ and (iii) a transient response that stabilizes into a steady-state regime where the strain starts increasing linearly over time.^{15–25}

Fig. 1 illustrates this point where we show a qualitative comparison of the three responses based on the simulation of a uniaxial creep test over 30 years. As shown, the transient model gives an overly optimistic prediction while the two other models are rather conservative.²⁶ studied

* Corresponding author.

E-mail address: mejda.azabou@mines-paristech.fr (M. Azabou).

<https://doi.org/10.1016/j.ijrmms.2020.104588>

Received 13 November 2020; Accepted 23 December 2020

Available online 2 May 2021

1365-1609/© 2021 Elsevier Ltd. All rights reserved.

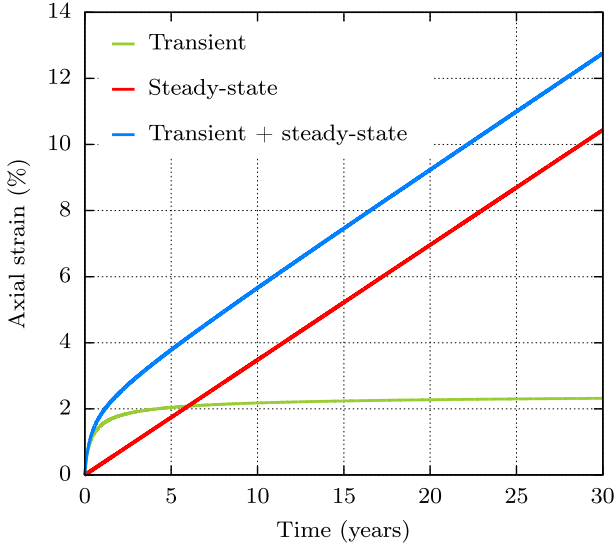


Fig. 1. Time-extrapolation of three models with different creep responses on a uniaxial creep test.

the differences in the long-term behavior predicted by these types of models. The study confirmed that the transient models and the steady state ones predict significantly different behaviors on the long term, and suggested that, since in terms of laboratory tests both models give satisfactory interpretations, the most conservative predictions should be selected. However in practice, the optimal design of salt caverns cannot be based on overly conservative approaches.

The purpose of this paper is to propose a model with pertinent predictions for long-term creep behavior. We propose an enrichment to the distortion part of a model that has been detailed in Ref. 13. The modification consists in adding to the transient component, a second transient mechanism inspired by the Munson-Dawson¹⁵ transient creep. This allows to have a compromise between the steady state models and the transient ones in terms of the strain rate and the characteristic time. The added mechanism allows also to describe inverse creep^{17,22,27-30} and links it to hysteresis loops of the unloading-loading cycles of triaxial compression tests. The authors are aware that in-situ data that covers years of exploitation activity, is needed to fully validate the model and truly assess the pertinence of its time extrapolation. However, acquiring such data and using it for research work is difficult, since -even if they exist-these measurements are destined for exploitation purposes.

This paper is structured as follows. In the first section two existing models and the new proposed one are presented. In section 3, we compare these constitutive laws on the basis of five experimental campaigns conducted at Mines ParisTech on rock salts from different geographic locations. The comparison concerns the capability of the three models to fit long-term (creep) and short-term (conventional triaxial compression) tests with the same parameter set, and the pertinence of their long-term predictions. In section 4 the new model is used to analyze a comprehensive test campaign and the inverse creep phenomenon is discussed in section 5.

2. Constitutive models

All these constitutive laws agree on the partition of the total strain rate tensor $\dot{\underline{\underline{\epsilon}}}$ into elastic $\dot{\underline{\underline{\epsilon}}}_{el}$, thermal $\dot{\underline{\underline{\epsilon}}}_{th}$ and viscoplastic parts $\dot{\underline{\underline{\epsilon}}}_{vp}$:

$$\dot{\underline{\underline{\epsilon}}} = \dot{\underline{\underline{\epsilon}}}_{el} + \dot{\underline{\underline{\epsilon}}}_{th} + \dot{\underline{\underline{\epsilon}}}_{vp}; \quad \dot{\underline{\underline{\epsilon}}}_{el} = \frac{1+\nu}{E} \underline{\underline{\sigma}} - \frac{\nu}{E} tr(\underline{\underline{\sigma}}) \underline{\underline{1}}; \quad \dot{\underline{\underline{\epsilon}}}_{th} = \alpha_{th} T \underline{\underline{1}} \quad (1)$$

where E, ν are the elastic constants, $\underline{\underline{\sigma}}$ is the Cauchy stress tensor, $\underline{\underline{1}}$ is the unit tensor, α_{th} is the linear thermal expansion coefficient and T is the

temperature. The viscoplastic strain tensor is generally given as a function of the thermodynamic state $(\underline{\underline{\sigma}}, T)$ and internal variables ξ with a rate that depends on $\underline{\underline{\sigma}}, T$ and the internal variables:

$$\dot{\underline{\underline{\epsilon}}}_{vp} = \underline{\underline{\mathcal{F}}}(\underline{\underline{\sigma}}, T, \xi); \quad \dot{\xi} = \underline{\underline{\mathcal{G}}}(\underline{\underline{\sigma}}, T, \xi) \quad (2)$$

it is on the definitions of $\xi, \underline{\underline{\mathcal{F}}}$ and $\underline{\underline{\mathcal{G}}}$ that those models differ. In this section we present the following models: Munson-Dawson, Lemaitre and the model developed in this work that we shall call RTL2020.

2.1. The Munson-Dawson constitutive model

This model has been detailed in Ref. 15 and it states the following

$$\dot{\underline{\underline{\epsilon}}}_{vp} = F \dot{\underline{\underline{\epsilon}}}_{ss}; \quad \dot{\underline{\underline{\epsilon}}}_{ss} = \dot{\underline{\underline{\epsilon}}}_{ss} J = \dot{\underline{\underline{\epsilon}}}_{ss}(\underline{\underline{\sigma}}, T) J; \quad J = \underline{\underline{\sigma}}' / \|\underline{\underline{\sigma}}'\| \quad (3)$$

where $\underline{\underline{\sigma}}'$ is the deviatoric part of the Cauchy stress tensor ($\underline{\underline{\sigma}}' = \underline{\underline{\sigma}} - \frac{1}{3} tr(\underline{\underline{\sigma}}) \underline{\underline{1}}$), $\dot{\underline{\underline{\epsilon}}}_{ss}$ denotes the steady state strain rate tensor and F is defined as follows

$$F = \begin{cases} \exp(\Delta(1 - \zeta/\epsilon_t^*)^2) & \text{if } \zeta \leq \epsilon_t^* \\ \exp(-\delta(1 - \zeta/\epsilon_t^*)^2) & \text{if } \zeta \geq \epsilon_t^* \end{cases} \quad (4)$$

$$\dot{\zeta} = (F - 1)\dot{\underline{\underline{\epsilon}}}_{ss} \quad (5)$$

In this work we assume the following

$$\dot{\underline{\underline{\epsilon}}}_{ss}(\underline{\underline{\sigma}}, T) = A \exp\left(A_M \left(\frac{1}{T_r} - \frac{1}{T}\right)\right) \langle G \rangle^n; \quad \epsilon_t^* = K_0 e^{cT} q^m \quad (6)$$

where G is a loading function chosen as $G = q$, with q the von mises equivalent stress, $\langle \cdot \rangle$ are the Macaulay brackets, i.e., $\langle x \rangle = (x + |x|)/2$, T_r is the reference temperature, $A, A_M, n, c, K_0, m, \Delta$ and δ are material constants. We note that this model accounts for transient creep (via the function F) that saturates at ϵ_t^* and the steady state flow $\dot{\underline{\underline{\epsilon}}}_{ss}$ takes over.

2.2. The lemaître constitutive model

This model assumes that rock salt creep is a purely transient flow, the viscoplastic strain rate decreases asymptotically to zero. It states the following

$$\dot{\underline{\underline{\epsilon}}}_{vp} = \sqrt{3/2} \dot{\gamma}_{vp} J \quad (7)$$

where γ_{vp} is the viscoplastic distortion defined as

$$\dot{\gamma}_{vp} = \gamma_{vp}(\underline{\underline{\sigma}}, T, \gamma_{vp}) = \alpha \exp\left(A_L \left(\frac{1}{T} - \frac{1}{T_r}\right)\right) \left\langle \frac{G}{K} \right\rangle^{\beta/\alpha} \gamma_{vp}^{1-\frac{1}{\alpha}} \quad (8)$$

α, β, A_L and K and positive rheological constants and T_r the reference temperature. Similarly to the previous model, G is a loading function $G = G(\underline{\underline{\sigma}}, T, \gamma_{vp})$ and is chosen as $G = q$.

2.3. The RTL2020 constitutive model

Similar to the model detailed in Ref. 13; for the viscoplastic strain rate tensor, RTL2020 assumes the following

$$\dot{\underline{\underline{\epsilon}}}_{vp} = \sqrt{\frac{3}{2}} \dot{\gamma}_{vp} \underline{\underline{N}} - \frac{1}{\sqrt{3}} \dot{\zeta}_{vp} J \quad (9)$$

where $\dot{\zeta}_{vp} = -tr(\dot{\underline{\underline{\epsilon}}}_{vp})$ and $\dot{\gamma}_{vp} = \sqrt{2/3} \|\dot{\underline{\underline{\epsilon}}}_{vp}\|$ are the rates of the volu-

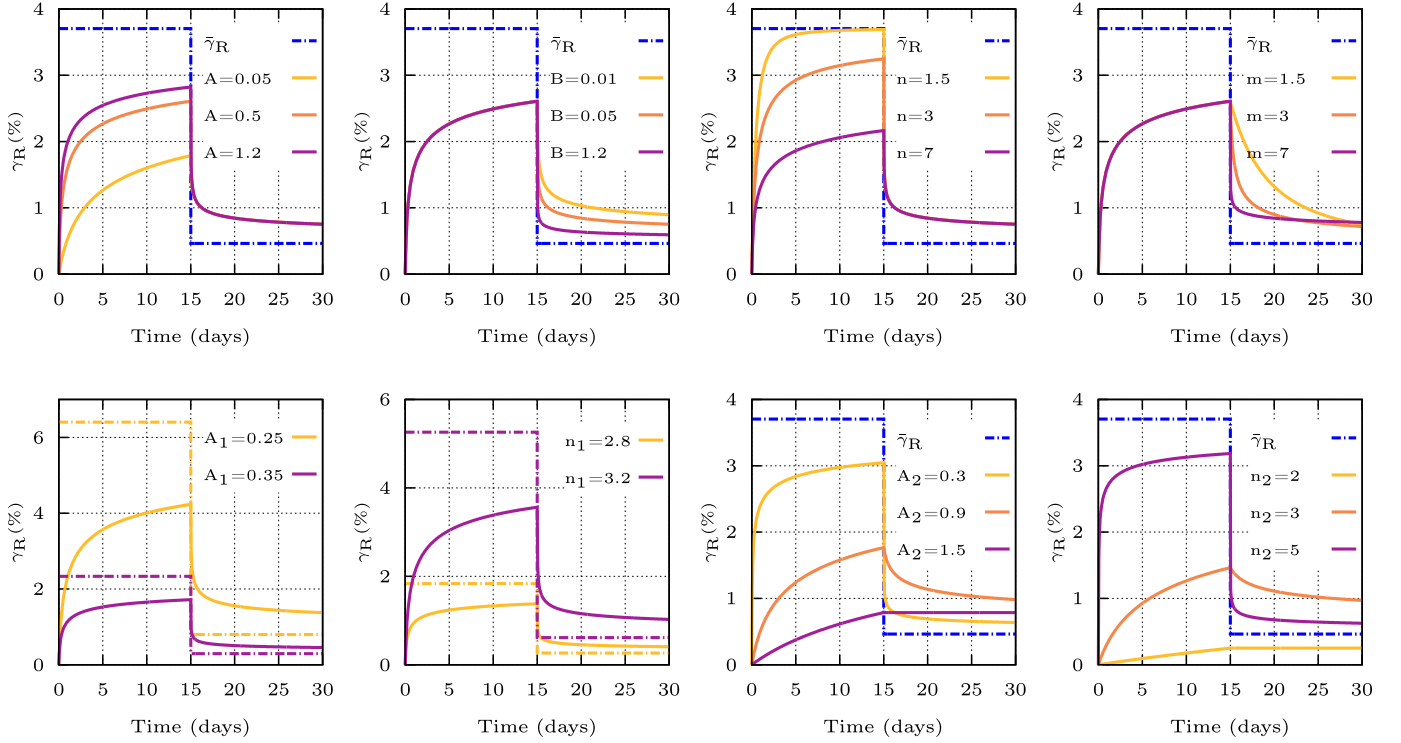


Fig. 2. Effect of the parameters of the distortion mechanism γ_R in RTL2020 model, predictions of a multistage creep test, note that in the sub-figures describing the effects of parameters A_1 and n_1 , the value of $\bar{\gamma}_R$ corresponding to each parameter is plotted in the same color in dashed line. (For interpretation of the references to color in this figure legend, the reader is referred to the Web version of this article.)

metric strain and the viscoplastic distortion, respectively, \underline{N} is a unit tensor defining the deviatoric flow direction and $\underline{I} = \underline{1}/\sqrt{3}$. The general formalism of the viscoplastic distortion is defined as

$$\dot{\gamma}_{vp} = \dot{\gamma}_L + \dot{\gamma}_R ; \text{with } \begin{cases} \dot{\gamma}_L = \psi_L(\underline{\sigma}, T, \gamma_L) \\ \dot{\gamma}_R = \psi_R(\underline{\sigma}, T, \gamma_R) \end{cases} \quad (10)$$

here $\dot{\gamma}_L$ describes a transient creep mechanism of Lemaitre's type, and $\dot{\gamma}_R$ is an added transient mechanism inspired by the Munson-Dawson model. The first transient mechanism is defined by

$$\psi_L(\underline{\sigma}, T, \gamma_L) = \alpha \exp\left(A_R \left(\frac{1}{T_r} - \frac{1}{T}\right)\right) \left(\frac{G}{A_2}\right)^{n_2} \gamma_L^{1-\frac{1}{n_1}} \quad (11)$$

where α , A_R , A_2 and n_2 are material parameters, G is a loading function. The added distortion mechanism γ_R is defined as

$$\psi_R(\underline{\sigma}, T, \gamma_R) = \begin{cases} A \left(1 - \gamma_R / \bar{\gamma}_R\right)^n R(\underline{\sigma}, T) & \text{if } \gamma_R \leq \bar{\gamma}_R \\ \dot{\gamma}_R = \bar{\gamma}_R(\underline{\sigma}, T) & \\ -B \left(\gamma_R / \bar{\gamma}_R - 1\right)^m R(\underline{\sigma}, T) & \text{if } \gamma_R \geq \bar{\gamma}_R \end{cases} \quad (12)$$

here A , B , m and n are material parameters such that $A > 0$, $B > 0$ and $m > 1$, $n > 1$.

The model offers enough flexibility in the choice of the functions ψ_L , $\bar{\gamma}_R$ and R . In this work we have made the following considerations:

- $\dot{\gamma}_L$ corresponds to the viscoplastic distortion of Lemaitre model $\dot{\gamma}_{vp}$;
- $\bar{\gamma}_R$ is considered to be analogue to the saturation value ϵ_t^* in Munson-Dawson model, it is given by

$$\bar{\gamma}_R = \left(\frac{G}{A_1}\right)^{n_1} \quad (13)$$

where A_1 and n_1 are material parameters.

- As for the definition of the function R , it is considered to be the same as ψ_L in order to link the two mechanisms and ensure that their contributions have the same order of magnitude

$$R(\underline{\sigma}, T) = \exp\left(A_R \left(\frac{1}{T_r} - \frac{1}{T}\right)\right) \left(\frac{G}{A_2}\right)^{n_2} \quad (14)$$

- We chose the loading function G such that $G = q$.

As for the volumetric viscoplastic strain, it remains unchanged from the definition given in RTL¹³ as

$$\dot{\zeta}_{vp} = \varphi(\underline{\sigma}, T, \gamma_{vp}) \dot{\gamma}_{vp} = z \frac{\langle p/N_z \rangle^{n_z} - \gamma_{vp}}{\langle p/M_z \rangle^{m_z} + \gamma_{vp}} \dot{\gamma}_{vp} \quad (15)$$

where z , N_z , n_z , M_z and m_z are material parameters and p is the mean pressure ($p = -tr(\underline{\sigma})/3$).

We note that the RTL2020 model is equivalent to the Munson Dawson model when the following considerations are made:

- the parameter α from equation (11) is set to 1;
- the parameter A from equation (12) is taken as $A = \exp(\Delta)$;
- the parameter n from equation (12) is linked to the parameter Δ via the following equation

$$n = \begin{cases} -0.0098\Delta^3 + 0.2040\Delta^2 + 0.5622\Delta + 2.0252 & \text{when } \Delta \leq 6 \\ 1.9987\Delta - 1.4567 & \text{when } \Delta > 6 \end{cases} \quad (16)$$

- $B = \delta = 0$ (equations (4) and (12)).

The advantage of the mechanism γ_R in this model is that it can be

Table 1

Initial parameter set used to study the role of the parameters of the distortion mechanism γ_R (the unit system is such that strain is in $\mu\text{m}/\text{m}$, stress is in MPa and time in days).

A	B	n	m	A ₁	n ₁	A ₂	n ₂
0.5	0.05	5	5	0.3	3	0.5	4

easily integrated compared to the exponential formulation used in Munson-Dawson. Under constant stress and temperature, the analytical solution for equation (12) can be written as

$$\gamma_R(t) = \gamma_{R0} + (\bar{\gamma}_R - \gamma_{R0})\xi \quad (17)$$

where ξ is given by

$$\xi(t) = 1 - \left(\frac{1}{1 + V(t - t_0)} \right)^{\frac{1}{k-1}} \quad (18)$$

with

$$V = (k - 1)U \frac{A_1^{n_1}}{A_2^{n_2}} q^{n_2 - n_1} \quad (19)$$

When $\gamma_R \leq \bar{\gamma}_R$ we have: $k = n$, $U = A \left(1 - \gamma_{R0}/\bar{\gamma}_R \right)^{n-1}$ and if $\gamma_R \geq \bar{\gamma}_R$ then $k = m$, $U = B \left(\gamma_{R0}/\bar{\gamma}_R - 1 \right)^{m-1}$.

In Fig. 2 we illustrate the role of each of the parameters A , B , n , m , A_1 , n_1 , A_2 and n_2 . We start from the parameter set given in Table 1 and in each case one parameter is varied, the simulated scenario is one of a uniaxial creep test where the axial stress (q in this case) is held constant at 10 MPa during 15 days and then dropped to 5 MPa for another 15 days.

In the plots we present the evolution of the distortion γ_R in time and the value of $\bar{\gamma}_R$ in each deviatoric stage (recall that $\bar{\gamma}_R = \left(\frac{q}{A_1} \right)^{n_1}$).

The parameters A , B , n and m affect the rate at which γ_R tends to $\bar{\gamma}_R$ as shown in the four top sub-figures of Fig. 2. Particularly after a load drop, the parameters B and m affect the duration of the observed transient flow. The four sub-figures in the bottom of Fig. 2 show that the mechanism is more sensitive to the parameters defining $\bar{\gamma}_R$ (A_1 and n_1) and to A_2 and n_2 . As shown in Fig. 2, the parameters of the γ_R distortion mechanism give the model a great flexibility to fit different experimental responses.

3. Models comparison on the basis of laboratory tests

3.1. Laboratory tests

We analyzed 5 experimental campaigns conducted at Mines ParisTech between 2012 and 2020 on salts from different locations (USA, Europe, Middle East), to which we will refer as salt 1, salt 2, salt 3, salt 4 and salt 5. From each of the campaigns we chose a multistage creep test (considered as a long-term test) and a conventional triaxial compression test (short-term test). The tests of the first four campaigns were all conducted following the same procedure (preconditioning, measurement techniques -strain gauges-, experimental set up and the axial strain rate $\dot{\epsilon}_{ax}$ for the short-term tests). In addition, in these four series of tests the confining pressure (P) is maintained constant during the creep tests and the changes in the deviatoric stages are applied by modifying the axial stress (Q). However, for salt 5 the procedure for the short-term tests was slightly different (duration and confining pressure for specimen preconditioning, measurement techniques -radial extensometer and global axial displacement-, axial strain rate). Also the creep test on this salt lasted significantly longer compared to the creep tests from the first four campaigns and it differs from them in the testing procedure: the

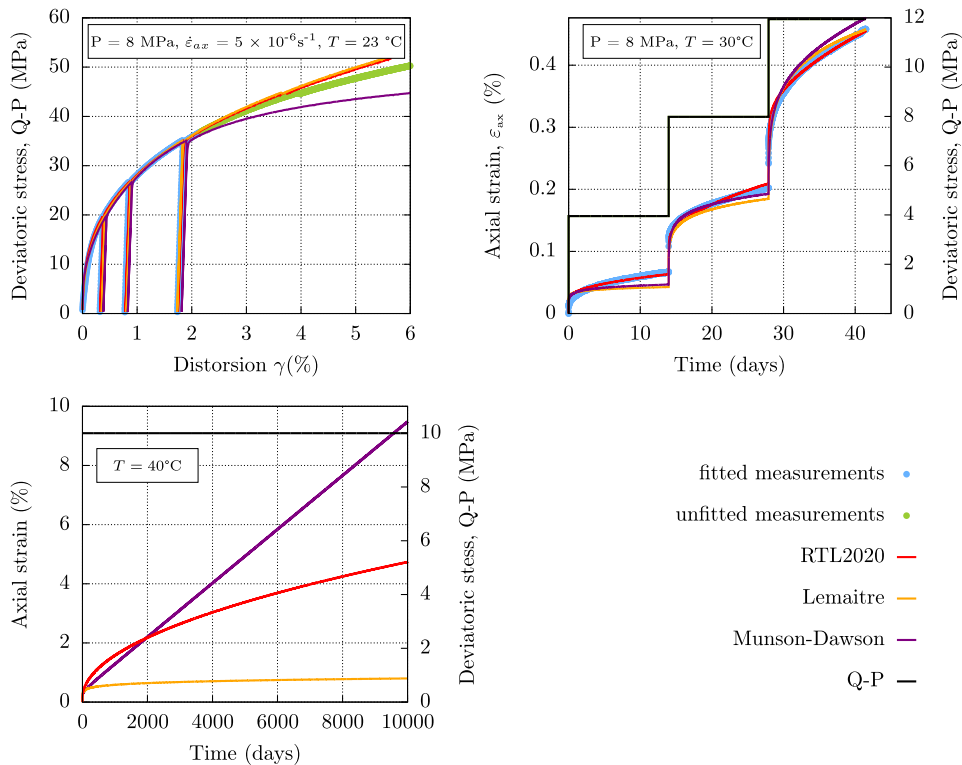


Fig. 3. Fittings of tests on salt 1 and time extrapolation of the three fitted models.

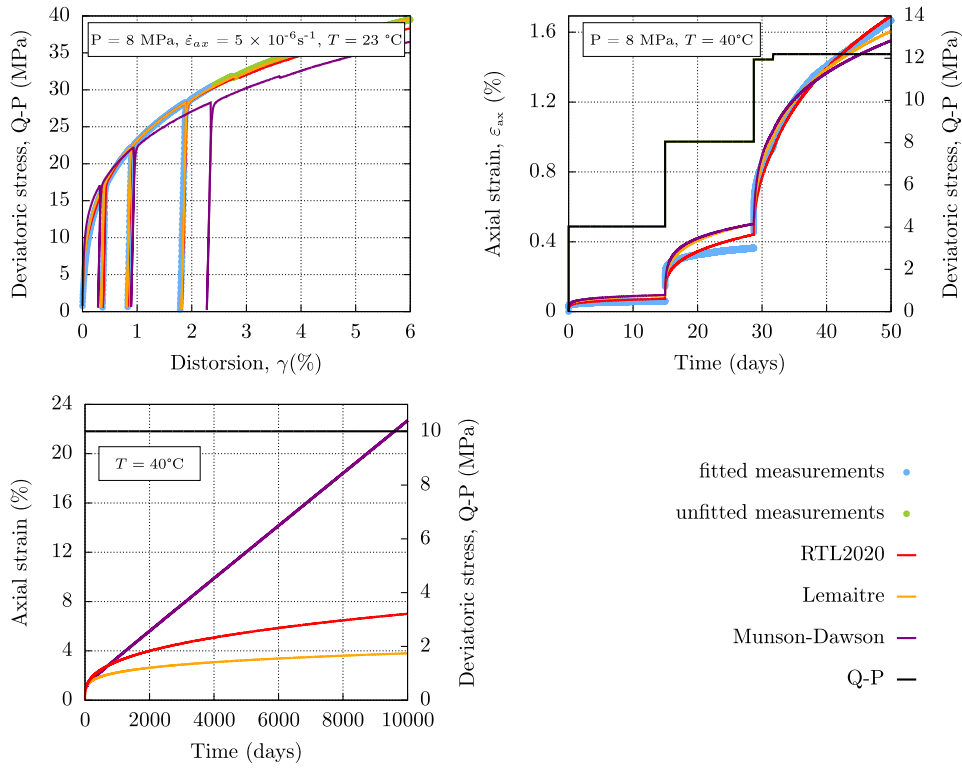


Fig. 4. Fittings of tests on salt 2 and time extrapolation of the three fitted models.

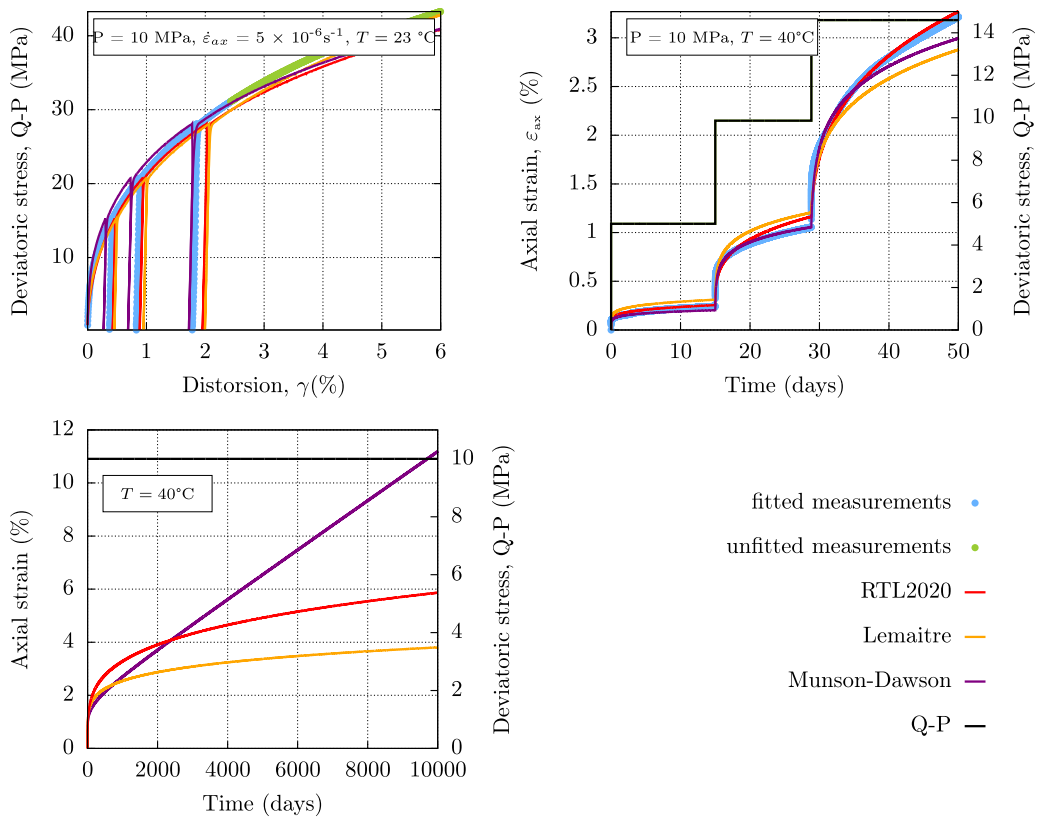


Fig. 5. Fittings of tests on salt 3 and time extrapolation of the three fitted models.

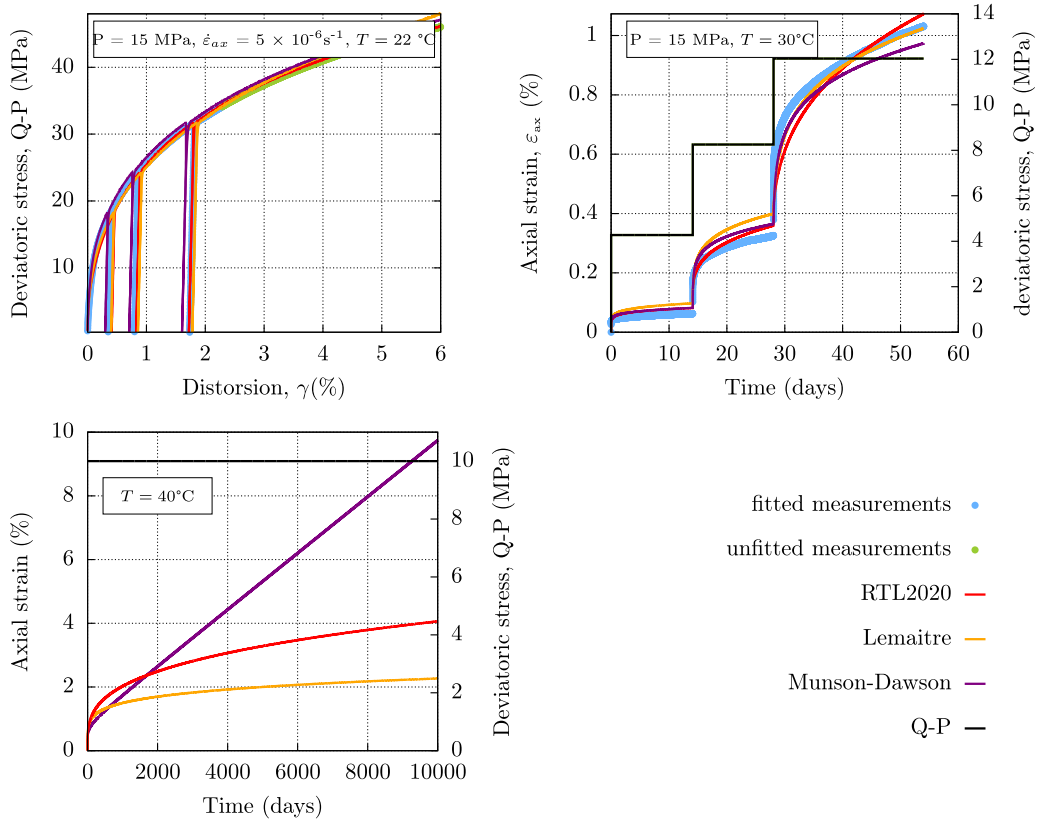


Fig. 6. Fittings of tests on salt 4 and time extrapolation of the three fitted models.

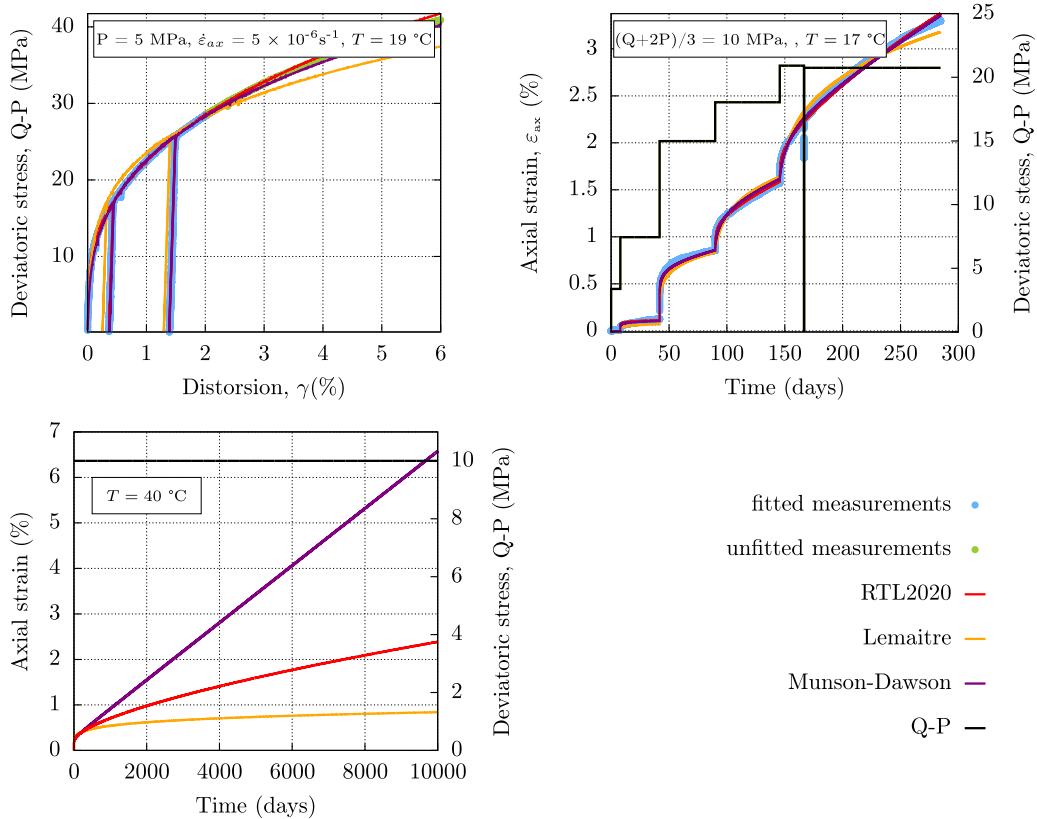


Fig. 7. Fittings of tests on salt 5 and time extrapolation of the three fitted models.

Table 2

Parameters used to fit the experimental data in Figs. 3–7. The unit system is such that strain is in $\mu\text{m}/\text{m}$, stress is in MPa and time in days.

Parameters	Salt 1	Salt 2	Salt 3	Salt 4	Salt 5
Elasticity					
E	29518	27499	28567	32172	22126
ν	0.32	0.32	0.30	0.31	0.2
Munson-Dawson					
A	4.636×10^{-8}	2.713×10^{-3}	0.5882	0.5513	4.46×10^{-4}
n	8.0975	3.7	1.	1.01	3.936
m	1.387	2.3	2.8075	2.6922	2.7062
K_0	159.5602	69.6769	31.2385	18.5017	5.8505
Δ	14.0464	9.3	11.1551	11.6182	15.3698
Lemaitre					
α	0.1363	0.2288	0.1746	0.1801	0.1904
β	2.4189	2.6356	2.0518	2.265	3.4854
K	0.4938	0.4832	0.16	0.3034	1.4091
RTL2020					
α	0.5072	0.3601	0.2601	0.3201	0.6709
A_1	0.4896	0.061	0.0181	0.04107	0.2937
n_1	2.5093	1.473	1.162	1.3711	2.2839
A_2	0.1916	1.0945	0.3986	0.868	4.5478
n_2	2.7967	9.2482	9.6768	9.1676	6.3023
A	36.055	6.81×10^{-3}	0.01	2.94×10^{-2}	684
n	11.5263	9.2644	13.5	12.11	8.8926

deviatoric stages are obtained by varying both the axial and lateral stresses such that the mean pressure $(Q+2P)/3$ is held constant at 10 MPa throughout the test.

3.2. Parameters fitting and time extrapolation

For each salt, the results are analyzed with the three models (Munson-Dawson, Lemaitre and RTL2020) and the best fitting obtained (with the same parameter set for each model) is provided. Afterwards, these parameters are used to perform a time extrapolation of the models on a virtual scenario of a uniaxial creep test of 10000 days.

In the three models we are studying, the temperature effect is given by the Arrhenius law, and all the creep tests we are analyzing in this section are carried out at constant temperature. For this reason, we have set the parameters $A_M = A_L = A_R = 1725$ K, also the reference temperature T_r was set to 289 K. In addition, since the stages of deviatoric stress in all the creep tests are ascending, the parameter B from equations 12 was set to 0 and therefore the parameter m was not adjusted. Figs. 3–7 show the fittings of the three models on the tests from the five campaigns and the results of the time extrapolation. In each of these figures, the top graph represents the analysis of a triaxial compression test (at a constant confining pressure and a constant strain rate that are specified on the graph), the middle graph corresponds to a multistage creep test (the test temperature and conditions are indicated on the graph) and the bottom figure is a time extrapolation of the three models for a uniaxial creep test at $T = 40^\circ\text{C}$. The fitting parameters are provided in Table 2.

We can see that the three models give satisfactory interpretations to both the short-term and the long-term tests, they are all able to describe the behavior of rock salt at the laboratory scale for this specific type of tests (time and loading ranges). As for the long-term predictions, the transient creep phase described by Munson-Dawson model is practically inexistent compared to the steady state flow and it has the same time span of laboratory tests durations (a few days), the time extrapolation of this model is rather conservative since the steady state flow is dominant and the strain increases linearly over time. However, the Lemaitre model is overly optimistic as it assumes that the strain rate keeps on decreasing infinitely and the strain almost tends to stabilize. On the other hand, in all the studied cases RTL2020 gives predictions that are between these two extremes, the strain increases in time but neither linearly nor with

an almost-zero rate. Besides, in RTL2020 time extrapolation we distinguish a characteristic time (for the mechanism γ_R) that is comparable to the duration of the prediction.

4. Analysis of a comprehensive testing campaign with RTL2020

In order to show the capabilities of RTL2020 to fit simultaneously short and long-term tests, with different and relatively complicated loading paths, we use this constitutive model to analyze a comprehensive testing campaign performed on specimens from salt 5 at Mines ParisTech.

4.1. Laboratory tests

In addition to the triaxial compression and the creep tests shown in Fig. 7, we conducted the following tests on specimens from salt 5:

- a typical triaxial compression test under a confining pressure $P = 5$ MPa and an constant axial strain rate of $\dot{\epsilon}_{ax} = 10^{-5} \text{ s}^{-1}$, performed at room temperature;
- a constant mean stress triaxial compression test, where the confining and the axial pressures (respectively P and Q) vary with the respective rates of $\dot{P} = -1\text{MPa/d}$ and $\dot{Q} = 2\text{MPa/d}$ in order to maintain a constant mean stress of $(Q+2P)/3 = 17$ MPa (at room temperature);
- a multistage creep test at room temperature, where the effect of the mean pressure is investigated: during some of the stages the axial and lateral stresses are changed in order to maintain a constant deviatoric stress and change the mean pressure;
- a multistage creep test similar to the last one, but performed at $T = 70^\circ\text{C}$.

This testing campaign is comprehensive as it includes tests with different and non-classic loading paths, also all the creep tests last over 200 days.

4.2. Parameters fitting

Since some of the tests have different temperature stages, the parameters A_R and α_{th} were fitted. The elastic parameters E and ν were fitted using the unloading/reloading cycles of the triaxial compression tests. The remaining parameters were fitted in two independent steps: those related to the deviatoric part and those related to the volumetric part. The experimental measurements of the distortion were used to fit the volumetric strain part; this ensures the independence of the two fittings. The fittings of the analyzed tests are given in Fig. 8 and the corresponding single parameter set in Table 3. As can be seen, RTL2020 allows a satisfactory matching to the experimental measurements and it describes correctly the deviatoric and the volumetric behavior. The quality of the fittings shown in Fig. 8 proves the robustness of RTL2020 as a rock salt constitutive law.

5. Inverse creep

When the deviatoric stress level decreases during a classic creep test, the specimen's length increases for a brief duration before it starts decreasing again. This phenomenon assumes that the viscoplastic strain rate can be negative following a loading drop (inverse creep). Observing this during classic creep tests is delicate due to its small magnitude and brief duration. However this phenomenon is exhibited during the unloading-loading cycles of classic triaxial compression tests, in fact we observed that during these tests the decrease of the deviatoric stress comes with an irreversible strain and the creation of a hysteresis loop. We select the first triaxial compression test and the third creep test presented in Fig. 8, we fit the two data sets with RTL2020 and a single parameter set twice: the first fitting does not allow a change in the

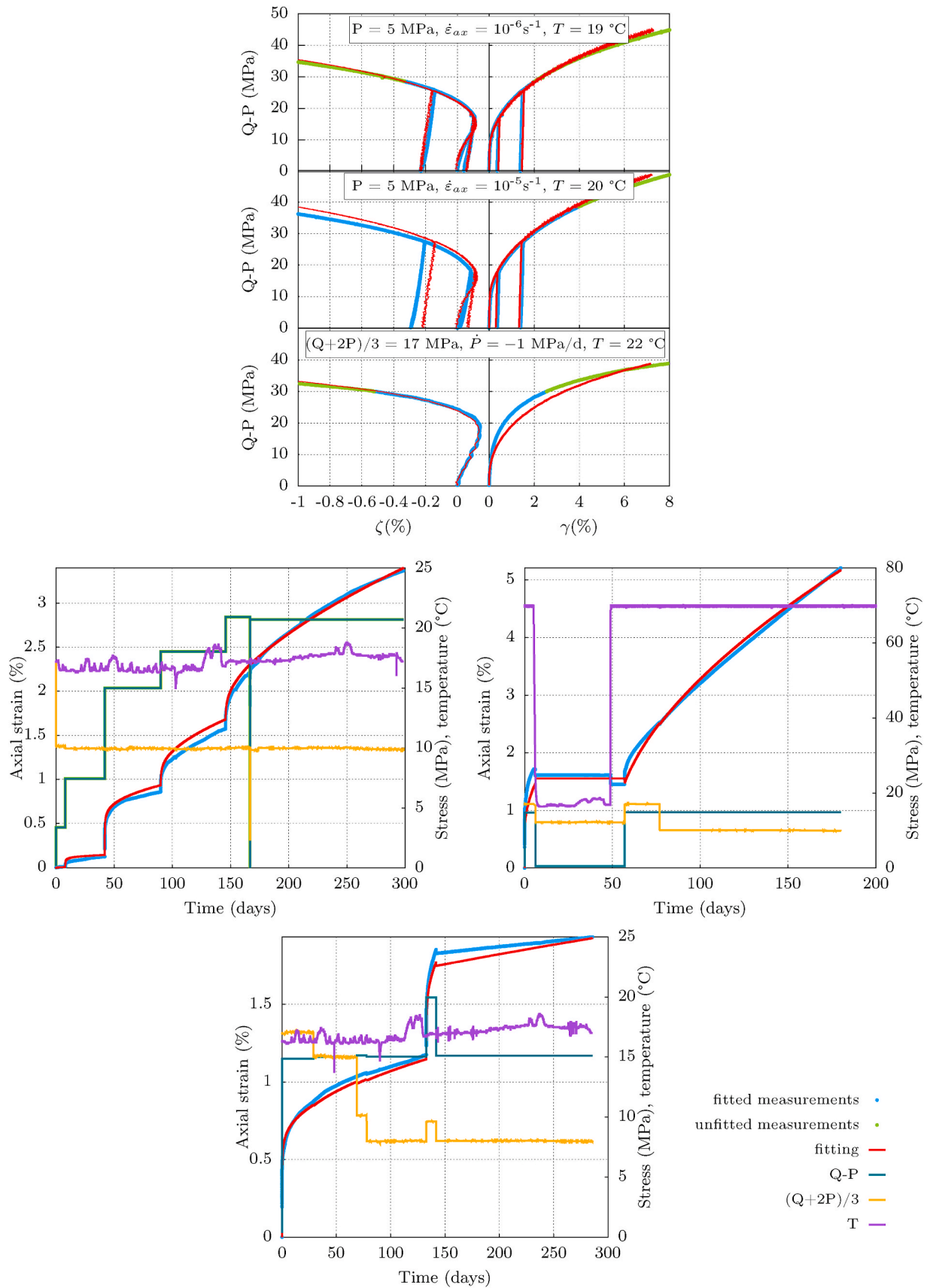


Fig. 8. Fitting of three short-term tests (top) and three creep tests (bottom) with a single parameter set. Note that for the second creep test, an isothermal (room temperature), isotropic phase (at $(Q+2P)/3 = 12 \text{ MPa}$) was applied.

Table 3

Parameters used to fit both short-term and creep tests on salt 5 (the unit system is such that strain is in $\mu\text{m}/\text{m}$, stress is in MPa and time in days).

Elasticity and Temperature effect								
E	ν	A_R	α_{th}					
22126	0.2	4457	3.27×10^{-5}					
Distorsion								
a	A_1	n_1	A_2	n_2	A	n	B	m
0.5812	0.1854	2.1012	3.7009	6.7562	155.6582	11.989	0.01918	2.2195
Dilatancy								
z	n_z	N_z	m_z	M_z				
0.4523	1.2644	0.0241	1.028	0.024				

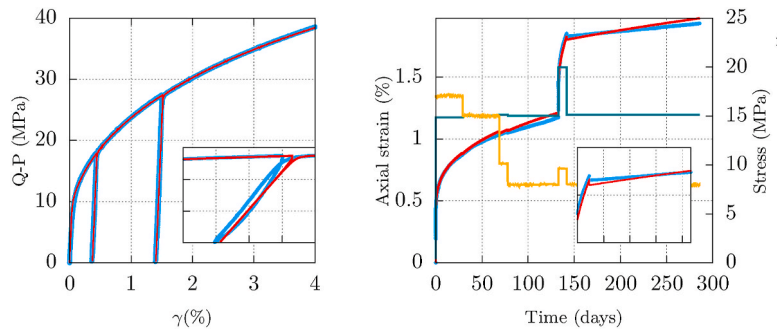


Fig. 9. Fitting of a conventional triaxial test (left) and a multistage creep test (right) with a single parameter set without accounting for inverse creep.

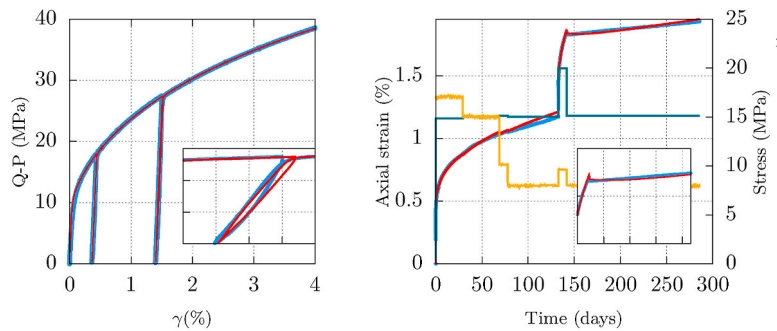


Fig. 10. Fitting of a conventional triaxial test (left) and a multistage creep test (right) with a single parameter set accounting for inverse creep.

direction of the viscoplastic strain (i.e., the parameter B is set to 0) and the second fitting is performed with $B \neq 0$. The results are respectively shown in Figs. 9 and 10 and the corresponding parameters are listed in Table 4.

Both fittings qualities are satisfactory, in Fig. 9 the loading drop during the two analyzed tests is purely elastic as it can be seen in the zoomed plots. However, activating the inverse creep mechanism ($B \neq 0$) allows to describe the hysteresis loop observed during the short-term test; it characterizes correctly the viscoplastic flow that comes with this unloading-loading cycle. Also, following the load drop in the creep

test, the model describes a very small and hardly distinguishable inverse creep: the strain rate decreases and then starts increasing again. We would like to highlight the fact that in the experimental measurements inverse creep was not observed, which is almost always the case during creep tests. This phenomenon has a very small order of magnitude (as predicted by the model in Fig. 10), yet this fitting proves that it is directly linked to the loops of the unloading-loading cycles of triaxial compression tests. In Fig. 11 we detail the fitting of the creep test in Fig. 10 and we explicit the contributions of the distorsion mechanisms of RTL2020. We can see that following the load drop γ_R decreases and

Table 4

Parameters used for the fittings shown in Figs. 9–11 (the unit system is such that strain is in $\mu\text{m}/\text{m}$, stress is in MPa and time in days).

Elasticity and Temperature effect								
E	ν	A_R	α_{th}					
22126	0.2	4457	3.27×10^{-5}					
Distorsion without accounting for inverse creep								
a	A_1	n_1	A_2	n_2	A	n	B	m
0.5812	0.1854	2.1012	3.7009	6.7562	155.6582	12.11	0	–
Distorsion accounting for inverse creep								
a	A_1	n_1	A_2	n_2	A	n	B	m
0.3840	0.2136	2.0581	2.4199	9.9698	0.2223	12.11	3.72×10^{-5}	4.5795

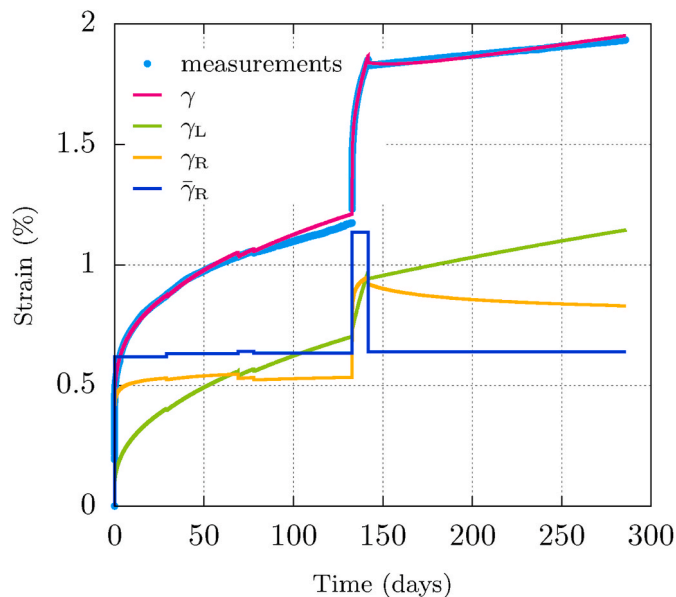


Fig 11. Fitting of a the multistage creep test shown in Fig. 10 and detailing of the contributions of the distortion mechanisms in RTL2020.

tends to the new $\bar{\gamma}_R$ but with a very small rate, which is why γ_L (steadily increasing) prevails and this results in a very discreet inverse creep phenomenon.

6. Conclusion

In this paper we discussed the aptitude of rock salt constitutive models to provide pertinent short and long-term predictions, since they are crucial for the optimal design of salt caverns. Our discussion was based on the confrontation of existing models with five experimental campaigns conducted on salts from different geographic locations. We found that the studied models gave satisfactory interpretations to laboratory tests. However, their long-term predictions were either too conservative or very optimistic. A new model was developed and included in this confrontation. It also allowed correct interpretations for laboratory tests but unlike the existing models, it gave pertinent predictions for the long term. This new model was also tested against a comprehensive testing campaign that comprises short-term, long-term and non-classic creep tests. It provided a valid fitting for the campaign with a single parameters set.

We note that an absolute validation of the model and the pertinence of its long-term predictions, requires confrontation with in-situ data over years of the cavern's lifetime. This can be done when a continuous monitoring of the underground facilities is performed and in-situ measurements are used to re-calibrate the model parameters and update the predictions.

Declaration of competing interest

The authors declare that they have no known competing financial interests or personal relationships that could have appeared to influence the work reported in this paper.

Acknowledgments

This work has been performed in the framework of the projects CITEPH-20-2018 and STOPIL-H2, the authors thank the sponsors and partners of the projects. The authors would also like to acknowledge Michel Tijani from Mines ParisTech and Nicolas Gatelier from Geostock, for their constructive discussions.

References

- Bays CA. Use of salt cavities for underground storage. In: *Symposium on Salt*. Cleveland, Ohio: Northern Ohio Geological Society; 1963:564–578.
- Ozarslan A. Large-scale hydrogen energy storage in salt caverns. *Int J Hydrogen Energy*. 2012;37(19):14265–14277. <http://www.sciencedirect.com/science/article/pii/S0360319912017417>.
- Bai M, Song K, Sun Y, He M, Li Y, Sun J. An overview of hydrogen underground storage technology and prospects in China. *J Petrol Sci Eng*. 2014;124:132–136. <http://www.sciencedirect.com/science/article/pii/S0920410514003374>.
- Iordache I, Schitea D, Gheorghe AV, Iordache M. Hydrogen underground storage in Romania, potential directions of development, stakeholders and general aspects. *Int J Hydrogen Energy*. 2014;39(21):11071–11081. <http://www.sciencedirect.com/science/article/pii/S0360319914014153>.
- Lord AS, Kobos PH, Borns DJ. Geologic storage of hydrogen: scaling up to meet city transportation demands. *Int J Hydrogen Energy*. 2014;39(28):15570–15582. <http://www.sciencedirect.com/science/article/pii/S0360319914021223>.
- Michalski J, Bünger U, Crot, Heide D. Hydrogen generation by electrolysis and storage in salt caverns: potentials, economics and systems aspects with regard to the German energy transition. *Int J Hydrogen Energy*. 2017;42(19):13427–13443. Special Issue on The 21st World Hydrogen Energy Conference (WHEC 2016), 13-16 June 2016, Zaragoza, Spain <http://www.sciencedirect.com/science/article/pii/S0360319917306109>.
- Tarkowski R, Czapowski G. Salt domes in Poland - potential sites for hydrogen storage in caverns. *Int J Hydrogen Energy*. 2018;43(46):21414–21427. <http://www.sciencedirect.com/science/article/pii/S0360319918331410>.
- Firme PA, Roehl D, Romanel C. Salt caverns history and geomechanics towards future natural gas strategic storage in Brazil. *J Nat Gas Sci Eng*. 2019;72:103006. <http://www.sciencedirect.com/science/article/pii/S1875510019302586>.
- Soubeyran A, Rouabhi A, Coquelet C. Thermodynamic analysis of carbon dioxide storage in salt caverns to improve the power-to-gas process. *Appl Energy*. 2019;242:1090–1107. <http://www.sciencedirect.com/science/article/pii/S0306261919305112>.
- Lankof L, Tarkowski R. Assessment of the potential for underground hydrogen storage in bedded salt formation. *Int J Hydrogen Energy*. 2020;45(38):19479–19492. <http://www.sciencedirect.com/science/article/pii/S0360319920317523>.
- Tijani M, Vouille G, Hugot B. Le sel gemme en tant que liquide visqueux. In: *International Congress on Rock Mechanics, Melbourne, Australia*. 1983:241–246.
- Labaune P, Rouabhi A, Tijani M, Blanco-Martín L, You T, Feb. Dilatancy criteria for salt cavern design: a comparison between stress- and strain-based approaches. *Rock Mech Rock Eng*. 2018;51(2):599–611.
- Rouabhi A, Labaune P, Tijani M, Gatelier N, Hévin G. Phenomenological behavior of rock salt: on the influence of laboratory conditions on the dilatancy onset. *Journal of Rock Mechanics and Geotechnical Engineering*. 2019;11(4):723–738. <http://www.sciencedirect.com/science/article/pii/S1674775518304323>.
- Odqvist FKG. *Mathematical Theory of Creep and Rupture*. Oxford University Press; 1966.
- Munson D, Dawson P. Salt constitutive modeling using mechanism maps. In: *First Conference on the Mechanical Behavior of Salt*. 1981:717–737.
- DeVries KL, Mellegard KD, Callahan GD. *Salt Damage Criterion Proof-Of-Concept Research. Technical Report Rsi-1675 De-fc-26-00nt41026*. South Dakota: RESPEC, Rapid city; 2002, 11.
- Heusermann S, Rolfs O, Schmidt U. Nonlinear finite-element analysis of solution mined storage caverns in rock salt using the Lubby2 constitutive model. *Comput Struct*. 2003;81(8):629–638. k.J Bathe 60th Anniversary Issue <http://www.sciencedirect.com/science/article/pii/S0045794902004157>.
- Bérest P, Brouard B, Karimi M, Van Sambeek L. Transient behaviour of salt caverns. Interpretation of mechanical integrity tests. *Int J Rock Mech Min Sci*. 2007;44:767–786, 07 <http://www.sciencedirect.com/science/article/pii/S1365160906001894>.
- Hampel A. The CDM constitutive model for the mechanical behavior of rock salt: recent developments and extensions. In: *Mechanical Behavior of Salt VII - Proceedings of the 7th Conference on the Mechanical Behavior of Salt*. 2012:45–55, 01.
- Nazary Moghadam S, Mirzabozorg H, Noorzad A. Modeling time-dependent behavior of gas caverns in rock salt considering creep, dilatancy and failure. *Tunn Undergr Space Technol*. 2013;33:171–185. <http://www.sciencedirect.com/science/article/pii/S0886779812001605>.
- Wolters R, Lux K, Düsterloh U, April. Evaluation of rock salt barriers with respect to tightness: influence of thermomechanical damage, fluid infiltration and sealing/healing. In: *Proceedings of the 7th International Conference on the Mechanical Behavior of Salt, Paris*. 2012:425–434.
- Günther R-M, Salzer K, Popp T, Lüdeling C. Steady-state creep of rock salt: improved approaches for lab determination and modelling. *Rock Mech Rock Eng*. 2015;48, 09.
- Khaledi K, Mahmoudi E, Datcheva M, Schanz T. Stability and serviceability of underground energy storage caverns in rock salt subjected to mechanical cyclic loading. *Int J Rock Mech Min Sci*. 2016;86:115–131. <http://www.sciencedirect.com/science/article/pii/S1365160916300612>.
- Deng J, Liu Y, et al Li B. A viscoelastic, viscoplastic, and viscodamage constitutive model of salt rock for underground energy storage cavern. *Comput Geotech*. 2020;119:103288. <http://www.sciencedirect.com/science/article/pii/S0266352X19303520>.
- Wu F, Zhang H, Zou Q, Li C, Chen J, Gao R. Viscoelastic-plastic damage creep model for salt rock based on fractional derivative theory. *Mech Mater*. 2020;150:103600. <http://www.sciencedirect.com/science/article/pii/S0167663620306426>.

- 26 Bérest P, Karimi M, Brouard B. Comportement mécanique à très long terme des mines et cavernes dans le sel gemme : loi de Norton-Hoff ou loi de Lemaitre ? *Revue française de Géotechnique*. 2008;124, 01.
- 27 Julien M. *Une modélisation constitutive et numérique du comportement rhéologique du sel gemme*, 10. Ecole Polytechnique de Montréal; 1999. Ph.D. thesis.
- 28 Karimi-Jafari M. *Comportement transitoire des cavités salines profondes*. Ecole Polytechnique X; Nov. 2007. Ph.d. thesis.
- 29 Labaune P. *Comportement thermomécanique du sel gemme : Application au dimensionnement des cavités*, 10. Mines ParisTech; 2018. Ph.D. thesis.
- 30 Gharbi H, Bérest P, Blanco-Martín L, Brouard B. Determining upper and lower bounds for steady state strain rate during a creep test on a salt sample. *Int J Rock Mech Min Sci*. 2020;134:104452. <http://www.sciencedirect.com/science/article/pii/S1365160920308212>.



On the Representativity of Rock Salt Specimens During Laboratory Tests

Mejda Azabou¹ · Ahmed Rouabhi¹ · Laura Blanco-Martín¹

Received: 21 December 2020 / Accepted: 6 July 2021

© The Author(s), under exclusive licence to Springer-Verlag GmbH Austria, part of Springer Nature 2021

Abstract

Experimental measurements during laboratory tests on salt specimens are important for the design of underground facilities in salt formations. These measurements, especially of the volumetric strain, can be influenced not only by the errors inherent to the experimental work, but also by the material heterogeneity. The natural variability due to the presence of impurities can lead to a non-negligible data scattering in the volumetric strain measurements and therefore raises questions concerning the specimens representativity. In this work, we study the effect of the presence of insoluble materials on the representativity of salt specimens during laboratory tests. An experimental investigation of this matter is delicate due to the shortcomings of laboratory work, thus we suggest a numerical method where salt specimens are modeled as pure halite matrices with insoluble inclusions. The insolubles distribution is described via a leveled Gaussian random field. Instead of using three different constitutive models, we use one law that is flexible enough to be adapted for each material involved (pure halite, inclusions and rock salt) with the adequate choice of parameter set. The modeling approach is presented, compared to the morphological modeling approach, and validated. It is employed to study the natural variability effect on strain measurements and to specify the size requirements to achieve representativity. The study proves that using non-representative specimens can misguide the rock characterization process and might even lead to optimistic design criteria. We propose a methodology that combines numerical and experimental work to overcome representativity issues.

Keywords Rock salt · Dilatancy · Material heterogeneity · Gaussian random fields · Representativity · Natural variability

List of Symbols

Main Symbols

$\underline{\underline{\dot{\epsilon}}}$	Strain rate tensor
$\underline{\underline{\gamma}}$	Viscoplastic distortion
$\sigma_1, \sigma_2, \sigma_3$	Eigenvalues of the stress tensor
$\underline{\underline{\sigma}}$	Stress tensor
$\underline{\underline{I}}, \underline{\underline{J}}, \underline{\underline{K}}$	Orthonormal basis of the stress space
$\underline{\underline{N}}$	Deviatoric flow direction
$\underline{\underline{\zeta}}$	Viscoplastic volumetric strain
p, q, ℓ	Invariants of the stress tensor

Subscripts

vp	Viscoplastic
----	--------------

Superscripts

c	Compressive loading
t	Tensile loading

1 Introduction

Rock salt has been used for decades as a storage and disposal medium (hydrocarbons, nuclear and chemical waste...) because of several assets, such as its very low permeability and porosity (Bays 1963; Wernt and Tilmann 2007; Ozarslan 2012; Gallo et al. 2016; Soubeyran et al. 2019). Designing storage facilities in salt formations requires a constitutive model that is able to describe the rock behavior on the short and long terms. The parameters of such models are calibrated on experimental measurements during laboratory tests on salt specimens that are supposed to be representative volume elements (RVE) of the concerned rock, and the model itself should be irrespective of the size of the tested specimens. Rock salt is a geological material and the presence of heterogeneities in different aspects and sizes is

✉ Mejda Azabou
mejda.azabou@mines-paristech.fr

¹ Centre de Géosciences, MINES ParisTech, PSL Research University, 35 Rue St Honoré, 77300 Fontainebleau, France

inevitable (Chemin 1990; Van-Hasselt 1991; Speranza et al. 2016; Thiemeyer et al. 2015, 2016; Li et al. 2019; Mansouri et al. 2019; Liu et al. 2020; Song et al. 2020). This means that theoretically, the RVE for each tested salt rock, should be determined based on the characteristics of its material heterogeneity. However, in practice, it is neither pragmatic nor convenient to adapt the experimental equipment to the tested specimens and usually, all the tested specimens, regardless of the rock they were cored from, have the same dimensions. This raises questions concerning the effect of heterogeneities on experimental measurements during laboratory tests and the representativity of the tested specimens. Azabou et al. (2020a) studied the effect of insolubles on the macroscopic behavior of rock salt, and highlighted the fact that the natural variability of the tested specimens can lead to a representativity issue, especially in terms of the volumetric response due to its small magnitude. Under compressive loading, rock salt volume decreases and then increases irreversibly due to the opening of micro-fractures, this is known as dilatancy and the volumetric strain measurements are particularly important since they are used to establish dilatancy criteria to design underground facilities (Spiers et al. 1989; Staudtmeister and Rokahr 1997; Heusermann et al. 2003; DeVries et al. 2005; Sobolik and Ehgartner 2011; Khaledi et al. 2016; Wang et al. 2016; Yang et al. 2016; Popp et al. 2017; Labaune et al. 2018; Wang et al. 2018). Various other studies, proved that material heterogeneity has a significant impact on the properties and the behavior of rock salt (Erickson et al. 2015; Fan et al. 2019, ...). For instance, Speranza et al. (2013) studied the effect of impurities on the mechanical properties of rock salt, such as wave velocity and Young's modulus and Xu et al. (2016) studied their effect on the permeability. Such studies are based on specific rock salt specimens, i.e. given insolubles content, distribution and nature which makes them rather particular case studies. Rock salt specimens are in general naturally different due to the presence of impurities, for this reason, the conclusions reached by such studies can sometimes be variable from different researchers. For example, Wu et al. (2012) found that the impurities could reduce the permeability of rock salt but the work of Liu et al. (2016) proved the contrary. This leads us to seek quantitative analyses on the effect of insolubles on the behavior of rock salt rather than a specific qualitative study on their effect on measurable rock salt properties. This paper aims to understand and to quantify the impacts of heterogeneities on salt specimens during laboratory tests. It seeks as well to propose the size requirements for achieving representative behavior from both deviatoric and volumetric perspectives in the laboratory, and to suggest a methodology to overcome representativity issues during the experimental work.

An experimental investigation of this matter is challenging and problematic; first because the measured volumetric

strains are small (Alkan et al. 2007; Roberts et al. 2015; Labaune 2018; Rouabhi et al. 2019) which means that the uncertainties inherent to the laboratory work can be non-negligible and can affect the results. Second, we do not have control over the material heterogeneity; as it was mentioned before, various aspects of heterogeneity exist within a salt sample so we would not be able to attribute an observed behavior to one particular aspect. Finally, in order to further investigate the representativity of the specimens, we need to perform tests on samples of different sizes. This is often complicated due to the limitations of the experimental facilities. For these reasons, we chose to carry our investigation within a virtual laboratory built on numerical modeling and simulation tools. We focus on macroscopic heterogeneities that are visible on specimens, an example of a rock salt specimen presenting such heterogeneity is shown in Fig. 1.

Morphological modeling of the heterogeneities is cumbersome and demands high computational times due to the meshing requirements (Azabou et al. 2020b), it is even impossible to use this explicit approach to conduct simulations when the inclusions size is significantly small compared to the modeled specimen. We propose an alternative method based on the assumption that rock salt is as a two-phase medium (pure halite and insolubles) that has a random microstructure. A random distribution is chosen in this study because our main goal is to generally understand the effect of the presence of heterogeneity on specimens representativity rather than to numerically reproduce the complex microstructure of a given salt specimen. This assumption is also motivated by the fact that the tested specimens do not show any particular anisotropy. A robust method of modeling such materials is based on leveled Gaussian random fields (Torquato and Haslach 2002; Lantuéjoul 2002; Bargmann et al. 2018; Soyarslan et al. 2018). It requires two steps: (i) generating a Gaussian random field over a studied domain, and (ii) performing a level cut on the generated field. Such approaches, which were initially proposed for bicontinuous

Fig. 1 An example of a rock salt specimen tested at Mines Paris-Tech, with visible inclusions of insoluble materials



material morphologies formed due to phase-separation (Cahn 1965), have found attention in several fields (Teubner 1991; Berk 1991; Roberts and Garboczi 2002; Field and Grigoriu 2012; Roubin 2013). Our method consists in considering one material and then applying the leveled random field distribution to a specific material property. With the proper choice for the material property to vary, this method allows us to significantly reduce the computational time and implicitly model rock salt as a two-phase medium.

This paper is structured as follows. In Sect. 2, we briefly present the constitutive model used for the numerical work in Sects. 3 and 4. In Sect. 3, the modeling approach is detailed, compared to the morphological modeling approach and validated. In Sect. 4, the impact of heterogeneity on specimens representativity is investigated, the size requirements to reach representative behavior are specified and a methodology to overcome representativity issues is suggested. This study is purely mechanical, neither the thermal nor the hydraulic aspects were taken into account.

2 Constitutive Model

In this work, three constitutive models are required: the first one is for the pure salt phase, the second is for the insolubles phase and the third is to describe the macroscopic behavior of rock salt. We chose to use a rheological law that has been developed by Rouabhi et al. (2019) since it includes the relevant phenomena for each of the three materials (distortion, dilatancy, tension) and these mechanisms can be activated/deactivated depending on the intent of the simulation. With the adequate parameters choice, this model can be adapted to describe the behavior of these different materials. Thus, the three models used to describe the behavior of the pure salt phase, the heterogeneities and the rock salt have the same mathematical formalism but different parameters set. In this paper, we use a simplified version of this constitutive law that we detail in the present section.

The model assumes that the total strain rate tensor is composed of an elastic, a thermal and a viscoplastic part. The viscoplastic strain rate tensor $\dot{\underline{\underline{\epsilon}}}_{vp}$ is decomposed into compressive $\dot{\underline{\underline{\epsilon}}}_{vp}^c$ and tensile $\dot{\underline{\underline{\epsilon}}}_{vp}^t$ components and is given by:

$$\dot{\underline{\underline{\epsilon}}}_{vp} = \underbrace{\left(-\sqrt{1/3}\dot{\underline{\underline{\zeta}}}_{vp}^c \underline{\underline{I}} + \sqrt{3/2}\dot{\underline{\underline{\gamma}}}_{vp}^c \underline{\underline{N}}^c \right)}_{\dot{\underline{\underline{\epsilon}}}_{vp}^c} + \underbrace{\left(-\sqrt{1/3}\dot{\underline{\underline{\zeta}}}_{vp}^t \underline{\underline{I}} + \sqrt{3/2}\dot{\underline{\underline{\gamma}}}_{vp}^t \underline{\underline{N}}^t \right)}_{\dot{\underline{\underline{\epsilon}}}_{vp}^t} \tag{1}$$

Both compressive and tensile parts are decomposed into the basis $(\underline{\underline{I}}, \underline{\underline{J}}, \underline{\underline{K}})$ defined as:

$$\underline{\underline{I}} = \underline{\underline{1}}/\sqrt{3}, \quad \underline{\underline{J}} = \underline{\underline{\sigma}}'/\|\underline{\underline{\sigma}}'\|, \quad \underline{\underline{K}} = (\sqrt{2}\underline{\underline{I}} + \ell\underline{\underline{J}} - \sqrt{6}\underline{\underline{J}}^2)/\sqrt{1-\ell^2} \tag{2}$$

where $\underline{\underline{\sigma}}'$ is the deviatoric part of the stress tensor $\underline{\underline{\sigma}}$ and $\ell = \sqrt{6tr(\underline{\underline{J}}^3)}$ is the third invariant of $\underline{\underline{\sigma}}'$.

Concerning the compressive part of the viscoplastic strain rate tensor, the deviatoric flow direction tensor under compressive loading $\underline{\underline{N}}^c$, is assumed to be equal to $\underline{\underline{J}}$. $\dot{\underline{\underline{\zeta}}}_{vp}^c = -tr(\dot{\underline{\underline{\epsilon}}}_{vp}^c)$ and $\dot{\underline{\underline{\gamma}}}_{vp}^c = \sqrt{2/3}\|\dot{\underline{\underline{\epsilon}}}_{vp}^c\|$ are the rates of the viscoplastic volumetric strain and distortion, respectively, and are given by:

$$\dot{\underline{\underline{\zeta}}}_{vp}^c = \psi(\underline{\underline{\sigma}}, \gamma_{vp}^c) \dot{\underline{\underline{\gamma}}}_{vp}^c \tag{3}$$

with

$$\psi(\underline{\underline{\sigma}}, \gamma_{vp}^c) = z \frac{\langle p/N \rangle^n - \gamma_{vp}^c}{\langle p/M \rangle^m + \gamma_{vp}^c} \tag{4}$$

where $p = -tr(\underline{\underline{\sigma}})/3$ is the mean stress, z, N, n, M and m are material constants. In this equation, the sign of $\langle p/N \rangle^n - \gamma_{vp}^c$ indicates whether the behavior is contracting or dilating. As for γ_{vp}^c , it is defined by:

$$\frac{d(\gamma_{vp}^c)^{1/\alpha}}{dt} = \left\langle \frac{q-C}{K} \right\rangle^{\beta} \tag{5}$$

where $q = \sqrt{3/2}\|\underline{\underline{\sigma}}'\|$ is the deviatoric stress, C, K, β and α are material parameters. As for the tensile part of the total viscoplastic strain rate tensor, the deviatoric flow direction tensor is defined as:

$$\underline{\underline{N}}^t = \left[(Y \cos \theta + Z \sin \theta) \underline{\underline{J}} + (Z \cos \theta - Y \sin \theta) \underline{\underline{K}} \right] / \sqrt{Y^2 + Z^2} \tag{6}$$

where $\theta = \cos^{-1}(\ell)/3$ is the Lode angle, and the quantities X, Y and Z are such that:

$$\begin{cases} X = G'_1 + G'_2 + G'_3 \\ Y = (2G'_1 - G'_2 - G'_3)/3 \\ Z = (G'_2 - G'_3)/\sqrt{3} \end{cases} \tag{7}$$

with $G'_i = \langle \sigma_i/G \rangle^{d-1}$ the eigenvalues of $\partial G/\partial \underline{\underline{\sigma}}$ and G has the following expression:

$$G = (\langle \sigma_1 \rangle^d + \langle \sigma_2 \rangle^d + \langle \sigma_3 \rangle^d)^{1/d} \tag{8}$$

where $\langle . \rangle$ are the Macaulay brackets, i.e. $\langle x \rangle = (x + |x|)/2$; $\sigma_1 \geq \sigma_2 \geq \sigma_3$ are the principal stresses of $\underline{\underline{\sigma}}$ and $d \geq 1$ is a material parameter.

As for $\dot{\underline{\underline{\zeta}}}_{vp}^t$ and $\dot{\underline{\underline{\gamma}}}_{vp}^t$, they are given by:

$$\dot{\underline{\underline{\zeta}}}_{vp}^t = -\lambda X, \quad \dot{\underline{\underline{\gamma}}}_{vp}^t = \lambda \sqrt{Y^2 + Z^2} \tag{9}$$

where the multiplier λ has the following expression:

$$\lambda = \Lambda \langle (G - R_t) / S \rangle^s \tag{10}$$

with R_t , S and s are material parameters.

This constitutive law is used to describe the pure salt phase and the insolubles phase in Sects. 3 to 4.2, as well as the macroscopic behavior of rock salt in Sect. 4.3. Obviously, a different parameter set is used for each case.

3 Numerical Approach

In this section we detail the proposed numerical modeling approach, we validate it by simulating typical laboratory tests. We also demonstrate its equivalence to the morphological modeling approach in which the insolubles are modeled explicitly as spherical inclusions.

3.1 An Implicit Modeling Approach

The real micro-structure of natural rock is very complex to be accurately described numerically. In this work, we aim at obtaining a global understanding of the effect of heterogeneities on the macroscopic behavior of salt specimens during laboratory tests. For this reason, it is accepted to make the simplifying assumption that rock salt is a two-phase medium composed of a pure halite matrix and insolubles that are randomly shaped and distributed.

An efficient way to generate such materials is leveled Gaussian random fields. This method has two steps:

- (i) Generating a Gaussian random field over a given domain:

The domain is meshed such that the maximum element size is smaller than the characteristic size of the heterogeneities. A scalar Gaussian random field, f , is then generated in the nodes of the mesh. It is obtained by superposition of sinusoidal waves of fixed wave length and amplitude but random in direction and phase (Cahn 1965; Lantuéjoul 2002; Soyarslan et al. 2018; Liu et al. 2019):

$$f(\vec{X}) = \sqrt{\frac{2}{N}} \sum_{i=1}^N \cos(\vec{\Omega}_i \cdot \vec{X} + \phi_i) \tag{11}$$

here, \vec{X} is the spatial position vector of a given node, N represents the number of waves, and $\vec{\Omega}_i$ and ϕ_i denote, respectively, wave direction and phase of the i th wave, and are given as follows:

$$\vec{\Omega}_i = \frac{\sqrt{2}}{a} N_i(0, 1) \begin{pmatrix} 1 \\ 1 \\ 1 \end{pmatrix}; \quad \phi_i = 2\pi U_i(0, 1) \tag{12}$$

where a is the characteristic size of the heterogeneities, $N_i(0, 1)$ is the standard normal distribution for the i th wave and $U_i(0, 1)$ is the uniform random distribution in the interval 0 to 1, for the i th wave. The obtained field is that of a stationary, isotropic Gaussian random field with mean zero and unit variance. For \vec{X} and \vec{Y} two spatial position vectors of two nodes, the covariance function $\rho(\vec{X}, \vec{Y})$ of this field is Gaussian and isotropic, it is given by:

$$\rho(\vec{X}, \vec{Y}) = \exp\left(-\frac{||\vec{X} - \vec{Y}||}{a^2}\right) \tag{13}$$

- (ii) Applying a level cut ξ such as:

$$\begin{aligned} \vec{X} \in S & \text{ if } f(\vec{X}) \leq \xi \\ \vec{X} \in I & \text{ if } f(\vec{X}) > \xi \end{aligned}$$

Here, S and I denote the salt and the insolubles domains, respectively. The threshold value ξ is related to the volume fraction of the insolubles, φ , by the following equation:

$$\xi = \sqrt{2} \operatorname{erf}^{-1}(1 - 2\varphi) \tag{14}$$

where erf is the error function.

The parameters we used for our simulations are the following:

- The block of salt is a cube of 1 m long edge: a significantly larger volume than what is usually available for laboratory tests;
- The characteristic size of the heterogeneities is $a = 20$ mm: visible inclusions on typical laboratory specimens;
- The size of the mesh was fixed to 7 mm: smaller than the characteristic size of the heterogeneities and it assures a fine mesh to all the chosen sizes of the specimens to sample;
- The number of waves is $N = 10,000$ as recommended in Soyarslan et al. (2018);
- The level cut was performed at $\xi = 1.5$: this value gives an insolubles distribution and content similar to typical laboratory specimens.

The resulting distribution is shown in Fig. 2.

The level cut can be applied to the mesh nodes or to the elements (the value affected to a finite element corresponds to the average of the values of its nodes). For our

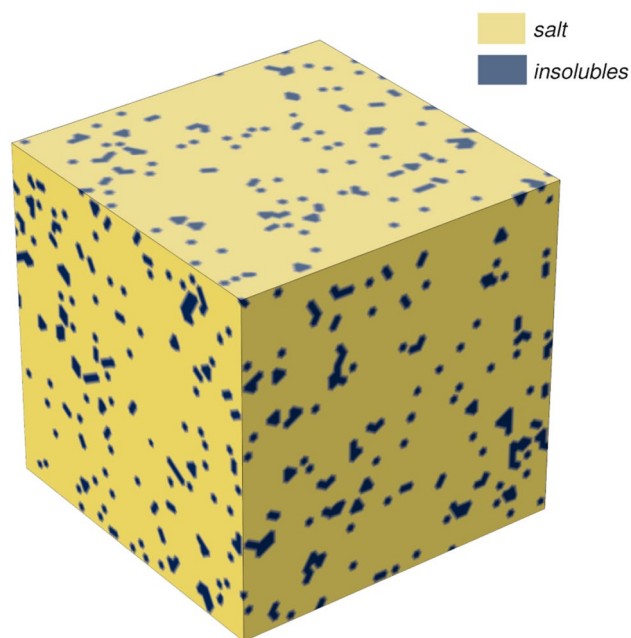


Fig. 2 Simulated block of rock salt as a cube of 1 m long edge, with insolubles distributed via a leveled Gaussian random field

calculations, the leveling is performed on the elements, so we have elements that are tagged as salt and elements that are tagged as insolubles. In order to differentiate these two phases, we make the following considerations:

- If an integration point is inside an element that is tagged as pure salt then it has elasto-viscoplastic behavior, only the distortion and the tensile mechanisms of the constitutive model in Sect. 2 are activated;
- If an integration point is inside an element that is tagged as insoluble then it has a purely elastic behavior.

Note that Azabou et al. (2020a, b) proved that when the insolubles are modeled morphologically as a different material from the halite matrix, tensile zones appear on the interface between the two materials. These are areas where the least compressive principle stress is positive and their propagation translates into a microcracking activity (Pouya 1991, 2000; Pouya et al. 2016). For this reason we chose to activate the tensile mechanism for the salt phase. The viscoplastic dilatancy mechanism was deactivated since, as will be proven in Sect. 3.2, the initiation and propagation of the tensile zones translate into a microcracking activity which in turn leads to a global dilatancy of the structure. Also, with a view to simplification, the elastic constants for the insolubles phase were chosen to be the same as the pure salt phase.

The approach explained in the present section as well as the constitutive model from Sect. 2, was implemented in an

Fig. 3 Virtually sampled cylindrical specimen of diameter 10 cm and height 20 cm, from the rock salt block shown in Fig. 2



in-house finite element code called PHIMEF that we used to perform the simulations presented in this paper.

3.2 Validation of the Modeling Approach

From the modeled block of salt shown in Fig. 2, we numerically sample the cylindrical specimen of diameter $D = 10$ cm and height $H = 20$ cm shown in Fig. 3. We conduct a simulation of a typical triaxial compression test following the specifications in Sect. 3.1 and using the parameters in Table 1: the distortion and the tensile mechanisms are activated and the dilatancy is deactivated. These parameters were adopted from Labaune et al. (2018) and were obtained by fitting short and long-term laboratory tests performed at MINES ParisTech. The results of this simulation are shown in Fig. 4, both the deviatoric and volumetric responses are very similar in terms of patterns and order of magnitude to what is typically observed during laboratory tests. We note that the observed global dilatancy results from the microcracking activity that occurred when tensile zones developed due to the difference in ductility between the salt and the insolubles phases. In order to confirm the aptitude of this modeling approach to correctly describe the behavior of salt specimens during laboratory tests, we use the same specimen from Fig. 3 with the parameters from Table 1 and we perform a series of simulations of typical laboratory tests:

- 6 typical triaxial compression tests under the same confining pressure but with different axial strain rates;
- 6 typical triaxial compression tests under the same axial strain rate but with different confining pressures, and a uniaxial compression test with the same axial strain rate;
- 1 multistage creep test.

The results of these simulations are shown in Figs. 5, 6 and 7 and they confirm that this modeling approach is

Fig. 4 Simulation results of a typical triaxial compression test under a confining pressure of 5 MPa and a constant axial strain rate of 10^{-6} s^{-1} , on the specimen in Fig. 3

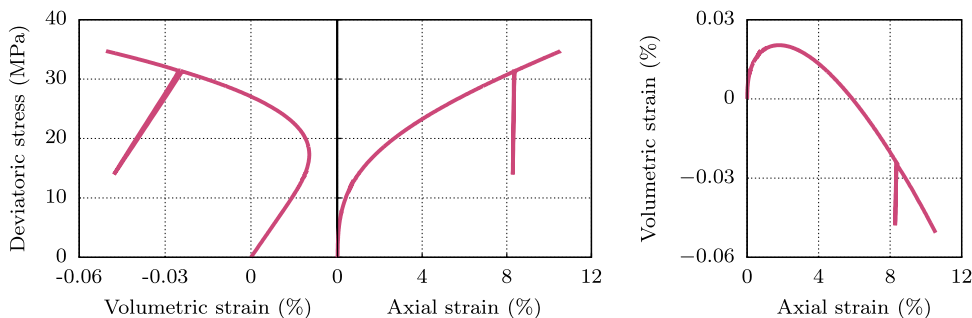


Fig. 5 Simulations results of typical triaxial compression tests under a constant confining pressure of 5 MPa and different axial strain rates, on the specimen in Fig. 3

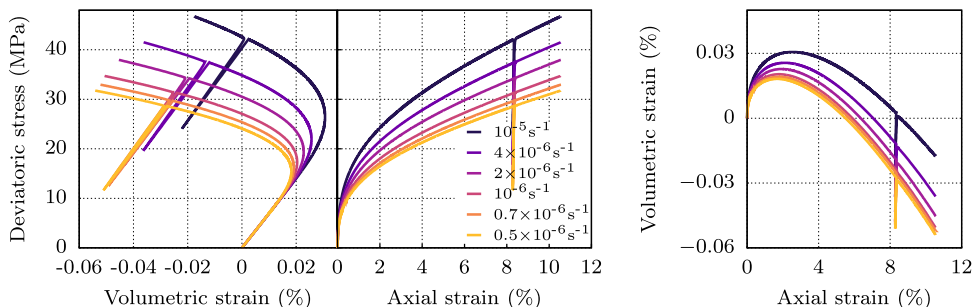


Fig. 6 Simulations results of typical triaxial compression tests under a constant strain rate of 10^{-6} s^{-1} and different confining pressures, on the specimen in Fig. 3

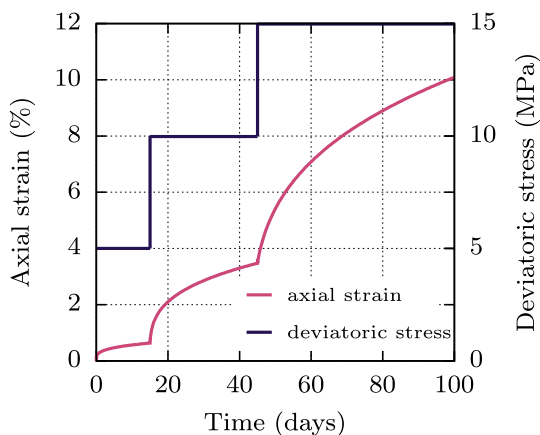
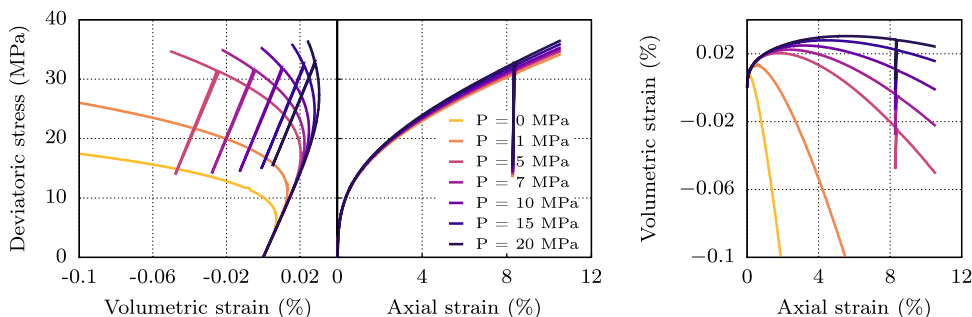


Fig. 7 Simulation results of a typical multistage creep test under a constant confining pressure of 5 MPa, on the specimen in Fig. 3

capable of describing the behavior of salt specimens during laboratory tests. In fact, the strain rate effect and the confining pressure influence are correctly predicted: the dilatancy onset increases with the strain rate and with the confining pressure (Labaune et al. 2018; Rouabhi et al. 2019). Also, Fig. 7 shows a very similar pattern to what is typically observed in the laboratory during multistage creep tests.

3.3 Comparison with the Morphological Modeling Approach

The results shown in Figs. 5 and 7, allow us to validate the proposed modeling approach, and in order to further demonstrate its capabilities, we perform a comparison with the morphological modeling approach proposed in Azabou et al. (2020a, b). We model the specimen in Fig. 8, the gray matrix represents the pure halite and the cyan inclusions are the impurities. We try to reproduce this specimen with the implicit method proposed in this paper: on a uniformly meshed cylinder, the inclusions are replaced with finite

Table 1 Parameters used to simulate the behavior of the salt matrix

Elasticity					
E	ν				
20,000	0.32				
Distortion					
α	β	K	C		
0.29	2.2	0.13	0		
Dilatancy					
z	n	N	m	M	
0	–	–	–	–	
Tension					
d	Λ	R_t	S	s	
10	5×10^4	0	1	1	

The unit system is such that strain is in $\mu\text{m/m}$, stress is in MPa and time in days

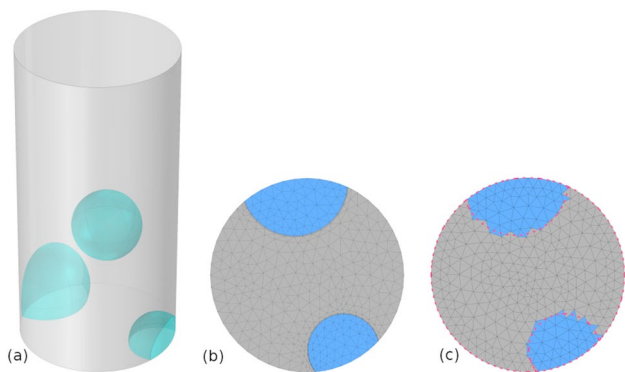


Fig. 8 **a** Modeled salt specimen as a pure halite matrix (gray) and nodules of insoluble materials (cyan), **b** 2D view of the lower surface when the inclusions are modeled explicitly and **c** 2D view of the lower surface when the inclusions are modeled implicitly

elements tagged as insolubles (see Sect. 3.1), this is illustrated in Fig. 8 on a 2D view of the lower surface of the cylinders.

On the specimen with the spherical inclusions (the morphological or explicit modeling approach), we conduct a simulation of a typical triaxial compression test using the

parameters in Table 1 for the salt matrix. Concerning the inclusions, they are modeled as a second material that is elastic, and they have the same elastic properties given to the salt matrix in Table 1. Similarly for the implicit modeling, we use the parameters in Table 1 for the salt phase, the same elastic constants for the insolubles phase and we conduct the same simulation on the cylinder where the insolubles are modeled implicitly.

The results of this comparison are shown in Figs. 9 and 10 and they demonstrate the equivalence between the explicit and the implicit approaches, and all else being equal, the computing time for the second simulation (implicit approach) was approximately 3 times lower than that of the simulation based on the explicit approach. We note the slight difference in the volumetric behavior between the two simulations, in fact in the implicit calculation the angular points of the elements tagged as insolubles, favor the development of tensile zones. This can be seen clearly in Fig. 10, which explains the fact that dilatancy is seen earlier in the simulation with this approach.

The results from Figs. 4, 5, 6, 7, 8, 9 and 10, prove the validity and efficiency of the proposed modeling approach

Fig. 9 Simulations results of a typical triaxial compression test under a confining pressure of 5 MPa and a constant axial strain rate of 10^{-6} s^{-1} , on the specimen in Fig. 8 modeled with both the implicit and the explicit approaches

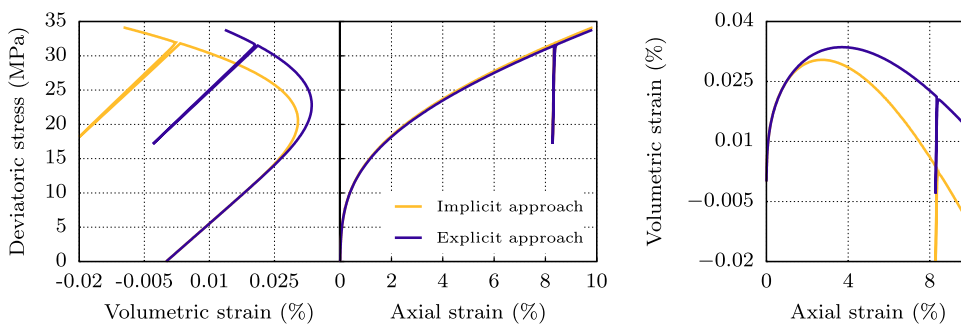


Fig. 10 Distribution of the tensile mechanism internal variable at the end of the simulations of Fig. 9: explicit approach on the left and implicit approach on the right

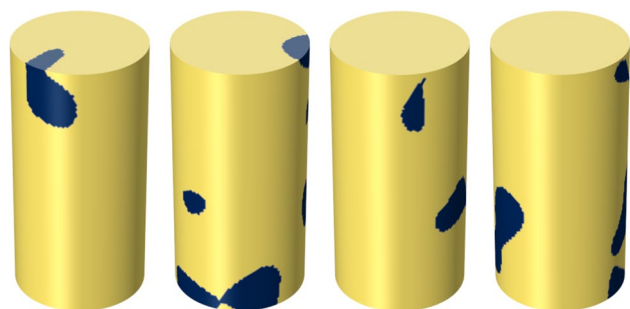
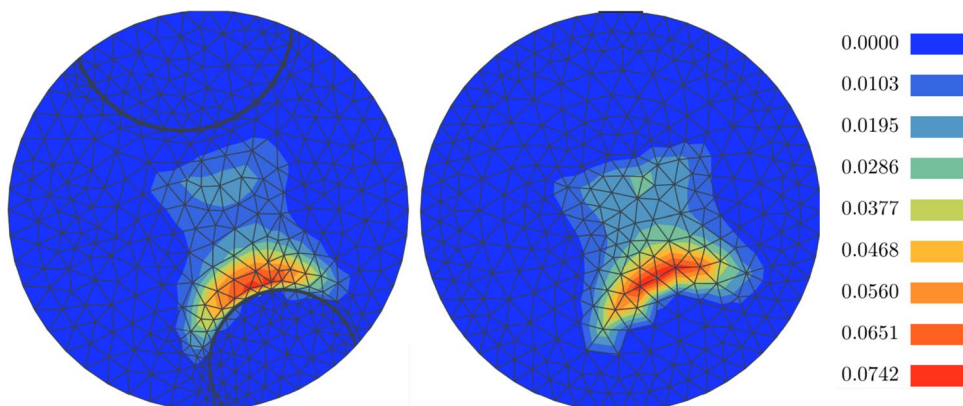


Fig. 11 Four cylindrical samples of diameter 6.5 cm and a slenderness ratio of 2 virtually cored from the block in Fig. 2. The specimens are labeled C1 to C4 from left to right

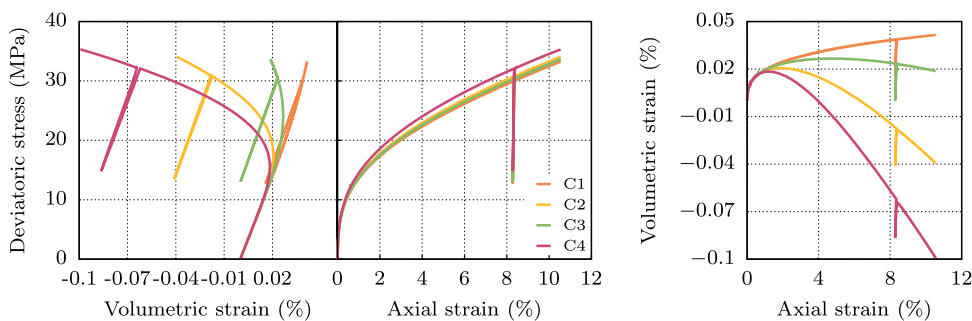
and its capability to describe correctly the phenomenological behavior of rock salt specimens during laboratory tests.

4 Numerical Investigation

4.1 Natural Variability and Specimens Representativity

We use the modeled salt block from Fig. 2 and we virtually sample 4 specimens of diameter $D = 6.5$ cm (approximately $3a$, where a is the size of the heterogeneities, see Eq. 12) and height $H = 13$ cm and on each, we conduct

Fig. 12 Simulations results of the same typical triaxial compression test (confining pressure of 5 MPa and axial strain rate of 10^{-6} s^{-1}) on the specimens in Fig. 11



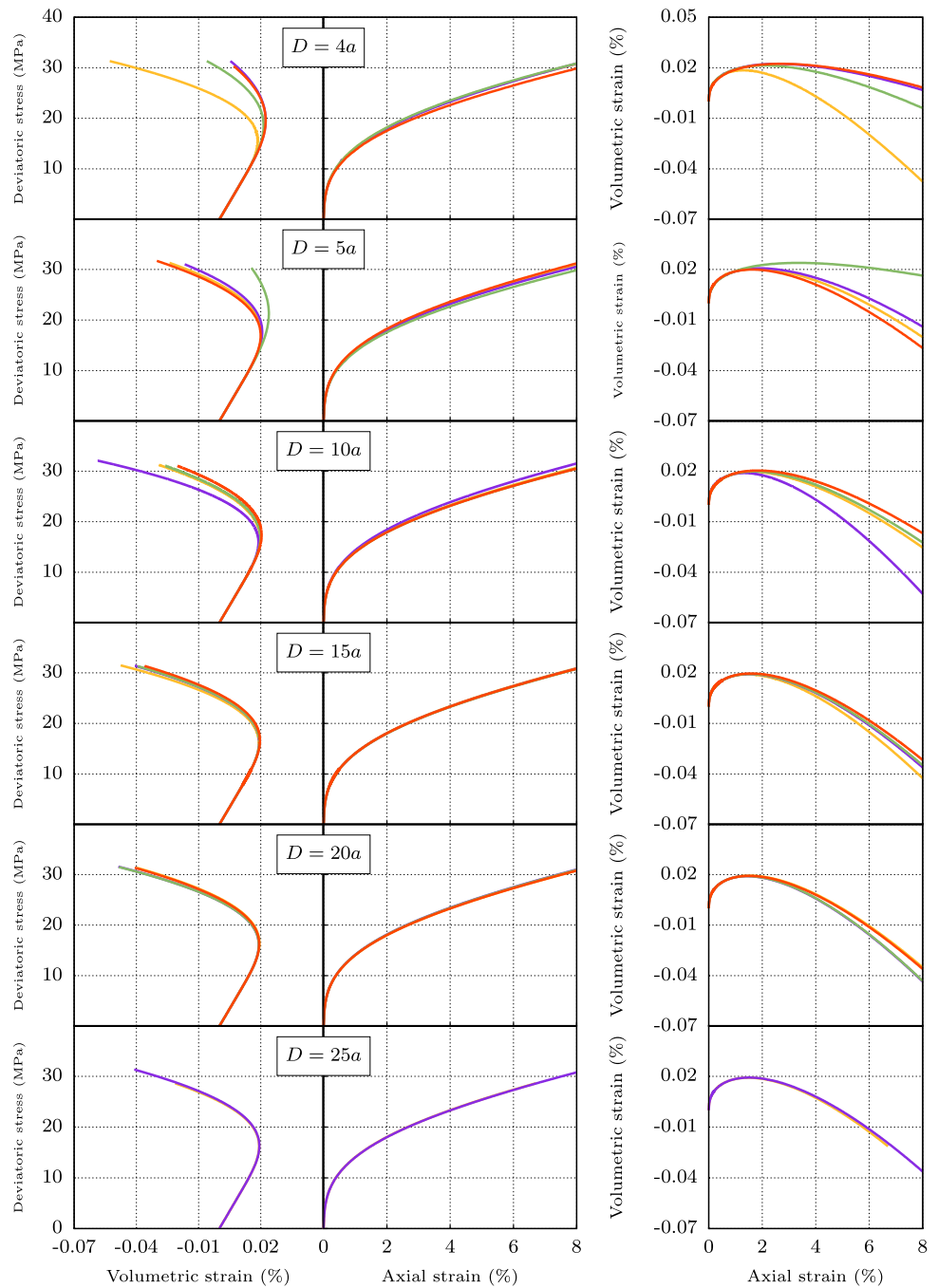
the same simulation of a typical triaxial compression test. The specimens are shown in Fig. 11 and the results of the simulations in Fig. 12.

We note that the specimen-to-specimen variation slightly affects the deviatoric response but it has a significant impact on the volumetric strain measurements. This is often observed during laboratory tests and it means that the used specimens are smaller than the required RVE for the studied rock. We also note that when the heterogeneities size is comparable to the cored specimens dimensions, we risk sampling specimens with very low insolubles content (see specimen C1 in Fig. 11) or specimens with rather high insolubles content (specimen C4 in Fig. 11). In terms of volumetric behavior, the specimen C1 indicates a very high dilatancy onset (see Fig. 12): relying only on this test results would misguide the design process by providing an overly optimistic dilatancy criterion. However, relying solely on information from test on specimen C4 would give a rather conservative criterion. This is problematic since conservative criteria ensure a safe but far from optimal functioning of the underground facility, whereas optimistic criteria do not guarantee the safety of the site which can lead to dangerous consequences.



Fig. 13 Virtual sampling of cylindrical specimens with a slenderness ratio of 2 from the block in Fig. 2. From left to right, four specimens are cored having the diameters of $4a$, $5a$, $10a$, $15a$, $20a$ and two specimens of diameter $25a$, with a the characteristic size of the heterogeneities

Fig. 14 Simulation results of a typical triaxial compression test (confining pressure of 5 MPa and axial strain rate of 10^{-6} s^{-1}) on the specimens in Fig. 13



4.2 Determination of the RVE Size for Volumetric Behavior

In order to reach the required RVE and further understand the effect of the impurities on the specimens representativity, we repeat the process explained in Sect. 4.1 (virtual sampling of specimens from the block in Fig. 2 from random positions, and conducting the same simulation on all the samples), but each time we increase the size of the specimens. This process is repeated on cylindrical specimens of slenderness ratio of 2 and diameters 4, 5, 10, 15, 20 and 25 times bigger than a , the characteristic size of the heterogeneities. The specimens are shown in Fig. 13 and the results of the simulations in Fig. 14.

Figure 14 shows that the dispersion of the results decreases with the size of the specimens, especially in terms of the volumetric strain and therefore the dilatancy onset. When the chosen diameter is $\geq 15a$, there is almost no data scattering which implies that the representative size is reached. This leads us to recommend the size of the RVE in our case: a cylindrical specimen of a slenderness ratio of 2 and a diameter of $15a$ where a is the characteristic size of the visible heterogeneities. In our case, we considered $a = 2\text{cm}$ so our REV is a cylinder of diameter $D = 30\text{cm}$ and height $H = 60\text{cm}$.

In practice, it may not be possible to test specimens of such size or bigger. For this reason, in the following section, we propose a methodology that combines experimental and numerical work to overcome this issue.

4.3 Equivalent Homogeneous Material

When laboratory tests are performed on non-representative specimens, and when it is not possible to use bigger specimens we propose the following methodology:

1. After the experimental measurements are taken on a non-representative specimen, the distribution of the insolubles should be numerically modeled. This could be achieved by considering a two-phase medium similarly to what has been presented in this work.
2. Perform a history matching of the parameters of the model detailed in Sect. 2, in order to obtain the parameters for the viscoplastic phase and the elastic one.
3. Once each phase is correctly described, numerically model a representative and bigger specimen.
4. Simulate the test conducted in the laboratory on the modeled representative specimen with the specifications in Sect. 3.1.
5. The obtained results could be considered as experimental measurements and therefore could be fitted using a macroscopic model that accounts for dilatancy at a con-

stitutive level. This model could be the one presented in Sect. 2 when the distortion and dilatancy mechanisms are activated and the tensile one is not: different considerations that allow the model to be adequate to describe the macroscopic behavior of rock salt as it was mentioned in Sect. 2.

We illustrate this methodology based on the results of the simulations shown in Fig. 14. Consider the results obtained in Fig. 14 on the specimens of diameter $15a$, experimental measurements. We choose one of the four presented curves randomly (since all the specimens meet the RVE size requirement), on these measurements we fit the parameters of the model presented in Sect. 2 with the following considerations when assuming the homogeneity of the stress and strain fields:

- Only the distortion and the viscoplastic dilatancy mechanisms are activated: $C = 0$ (Eq. 5) and $z \neq 0$ (Eq. 4). The observed dilatancy was originally the result of a microscopic tensile phenomenon, at this stage, we do not consider neither the structure of the specimen nor any microscopic phenomena. We use the model of Sect. 2 to describe the observed behavior (distorsion and dilatancy) regardless of the internal structure of the specimen;
- The tensile mechanism is not taken into account ($\lambda = 0$ Eq. 10) since the simulation is that of a compressive triaxial test and the assumption of homogeneity of the stress and strain fields is made.

We present the obtained fitting in Fig. 15 and the corresponding parameter set in Table 2. If the fitted measurements were real experimental data on rock salt specimens, the resulting parameter set would be valid to study an underground facility in the corresponding salt formation.

In order to demonstrate the importance of fitting the model parameters on a RVE, we compare the fitting in Fig. 15 to a global fitting of the tests in Fig. 12. The results are shown in Fig. 16 and the corresponding parameter sets in Tables 2 and 3. We note the difference between the two fittings and the corresponding parameter sets. In our case, fitting on non-RVE led to an optimistic dilatancy design criterion: the dilatancy onset indicated by the representative behavior is lower than that measured on volumes smaller than the required RVE. This fitting accounts for the results of specimen C1 (see Figs. 11 and 12), which were extremely optimistic due to the low insolubles content in this cored specimen (see Sect. 4.1), thus the resulting global behavior was optimistic as well. However the results of specimen C4 (see Figs. 11 and 12) are conservative compared to the representative behavior. In fact, as explained in Sect. 4.1,

Table 2 Parameters used to fit the measurements in Fig. 16 (measurements on the RVE)

Elasticity					
E	ν				
29,117	0.30				
Distortion					
a	β	K	C		
0.232	2.041	0.1	0		
Dilatancy					
z	n	N	m	M	
1.93	1.07	0.07	1.736	0.0015	
Tension					
d	Λ	R_t	S	s	
10	0	0	1	1	

The unit system is such that strain is in $\mu\text{m}/\text{m}$, stress is in MPa and time in days

Fig. 15 Fitting of the results of the simulations on specimens of diameter $15a$ presented in Fig. 14, with the constitutive model presented in Sect. 2 following the specifications of Sect. 4.3

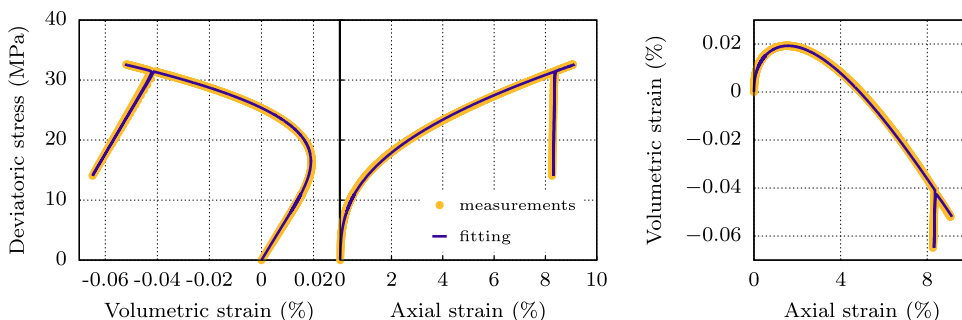
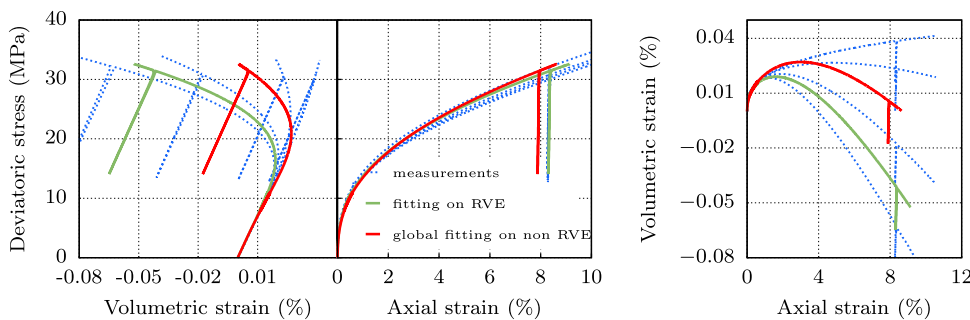


Fig. 16 Comparison of a global fitting on the measurements from Fig. 12 (non-RVE) and the fitting on the RVE from Fig. 15



when the cored specimens have dimensions comparable to the heterogeneities, the cored specimens can randomly have higher or lower insolubles content than the REV. The first case leads to overly conservative design criteria, which compromises the optimal functioning of the underground facility, and the second case leads to optimistic design criteria that can endanger the facility. Thus, using tests conducted on non-RVE can induce critical errors when determining dilatancy criteria.

5 Conclusions and Perspectives

In this work, the effect of the material heterogeneity of rock salt on the representativity of the tested specimens was investigated. Due to the small magnitude of the measured volumetric strains and the shortcomings of experimental works, this investigation was carried out numerically. We made the assumption that rock salt is a two-phase medium composed of pure halite and insoluble materials. We proposed an implicit modeling approach based on leveled Gaussian random fields to describe the heterogeneities

Table 3 Parameters used to perform the global measurements in Fig. 16 (measurements on non-RVE specimens)

Elasticity					
E	ν				
29,061	0.30				
Distortion					
a	β	K	C		
0.219	1.968	0.08	0		
Dilatancy					
z	n	N	m	M	
0.05	2.04	0.001	1.296	0.001	
Tension					
d	Λ	R_t	S	s	
10	0	0	1	1	

The unit system is such that strain is in $\mu\text{m}/\text{m}$, stress is in MPa and time in days

within the pure halite matrix. Three different constitutive laws were needed to describe the pure salt, the insolubles and rock salt. We used a single model that is flexible enough and that can be adapted to describe the behavior of each material with the proper choice of parameters (Table 3).

The approach was validated and it proved that the global dilatancy of specimens can be a result of a micro-fracturing activity due to the tensile zones created between pure halite and insoluble materials. The study proved also that the presence of heterogeneities can lead to representativity issues which in their turn can misguide the design of underground facilities. A virtual sampling of specimens of different sizes from a salt block was performed. Simulations of typical triaxial compression tests were conducted on these virtual specimens and the size requirements to reach representativity were specified. Since it is not always possible to test representative specimens, we proposed a methodology that uses the experimental results on non-RVE and the numerical approach proposed in this paper, to construct an RVE and numerically build a data base that could be fitted with a macroscopic model for rock salt. This model and the resulting parameter set could be used to study underground facilities in salt formations.

The authors are aware that considering rock salt as a two-phase medium is a simplifying assumption. In the future, the proposed approach can be applied to consider a multi-phase material with more adequate rheological laws for the heterogeneities rather than the simple elastic one.

Acknowledgements The authors would like to thank their colleagues Michel Tijani and Christian Lantuéjoul from Mines ParisTech, for their constructive discussions.

References

- Alkan H, Cinar Y, Pusch G (2007) Rock salt dilatancy boundary from combined acoustic emission and triaxial compression tests. *Int J Rock Mech Mining Sci* 44(1):108–119. <https://doi.org/10.1016/j.ijrmms.2006.05.003>
- Azabou M, Rouabhi A, Blanco-Martín L (2020a) Effect of insoluble materials on the volumetric behavior of rock salt. *J Rock Mech Geotech Eng*. <https://doi.org/10.1016/j.jrmge.2020.06.007>
- Azabou M, Rouabhi A, Blanco-Martín L, Hadj-Hassen F, Tijani M (2020b) On the effect of insoluble materials on rock salt dilatancy. In: 54th US rock mechanics/geomechanics symposium. American Rock Mechanics association
- Bargmann S, Klusemann B, Markmann J, Schnabel JE, Schneider K, Soyarslan C, Wilmers J (2018) Generation of 3d representative volume elements for heterogeneous materials: a review. *Prog Mater Sci* 96:322–384. <https://doi.org/10.1016/j.pmatsci.2018.02.003>
- Bays CA (1963) Use of salt cavities for underground storage. Symposium on salt. Northern Ohio Geological Society, Cleveland, Ohio, pp 564–578
- Berk NF (1991) Scattering properties of the leveled-wave model of random morphologies. *Phys Rev A* 44:5069–5079. <https://doi.org/10.1103/PhysRevA.44.5069>
- Cahn JW (1965) Phase separation by spinodal decomposition in isotropic systems. *J Chem Phys* 42(1):93–99. <https://doi.org/10.1063/1.1695731>
- Chemin P (1990) Etude du rôle des inclusions fluides dans les mécanismes de déformation des roches halitiques. Application aux formations salifères du bassin bressan. PhD thesis, Ecole Nationale des Ponts et Chaussées
- DeVries K, Mellegard K, Callahan G, Goodman W (2005) Cavern roof stability for natural gas storage in bedded salt. Technical report de-fg26-02nt41651, RESPEC, Rapid City, South Dakota
- Erickson KP, Lempp C, Pöllmann H (2015) Geochemical and geomechanical effects of scCO_2 and associated impurities on physical and petrophysical properties of permotriassic sandstones (Germany): an experimental approach. *Environ Earth Sci*. <https://doi.org/10.1007/s12665-015-4437-0>
- Fan J, Jiang D, Liu W, Wu F, Chen J, Daemen J (2019) Discontinuous fatigue of salt rock with low-stress intervals. *Int J Rock*

- Mech Mining Sci 115:77–86. <https://doi.org/10.1016/j.ijrmms.2019.01.013>
- Field R, Grigoriu M (2012) Level cut gaussian random field models for transitions from laminar to turbulent flow. *Probab Eng Mech* 28:91–102. <https://doi.org/10.1016/j.probengmech.2011.08.023>
- Gallo A, Simões-Moreira J, Costa H, Santos M, Moutinho dos Santos E (2016) Energy storage in the energy transition context: a technology review. *Renew Sustain Energy Rev* 65:800–822. <https://doi.org/10.1016/j.rser.2016.07.028>
- Heusermann S, Rolfs O, Schmidt U (2003) Nonlinear finite-element analysis of solution mined storage caverns in rock salt using the lubby2 constitutive model. *Comput Struct* 81(8):629–638. [https://doi.org/10.1016/S0045-7949\(02\)00415-7](https://doi.org/10.1016/S0045-7949(02)00415-7)
- Khaledi K, Mahmoudi E, Datcheva M, Schanz T (2016) Stability and serviceability of underground energy storage caverns in rock salt subjected to mechanical cyclic loading. *Int J Rock Mech Mining Sci* 86:115–131. <https://doi.org/10.1016/j.ijrmms.2016.04.010>
- Labaune P (2018) Comportement thermomécanique du sel gemme: application au dimensionnement des cavités. PhD thesis, École Nationale Supérieure des Mines de Paris
- Labaune P, Rouabhi A, Tijani M, Blanco-Martín L, You T (2018) Dilatancy criteria for salt cavern design: a comparison between stress- and strain-based approaches. *Rock Mech Rock Eng* 51(2):599–611. <https://doi.org/10.1007/s00603-017-1338-4>
- Lantuéjoul C (2002) Geostatistical simulation. *Models Algorithms*. <https://doi.org/10.1007/978-3-662-04808-5>
- Li H, Yang J, Han Y, Yang C, Daemen J, Li P (2019) Weibull grain-based model (W-GBM) for simulating heterogeneous mechanical characteristics of salt rock. *Eng Anal Bound Elem* 108:227–243. <https://doi.org/10.1016/j.enganabound.2019.09.001>
- Liu W, Muhammad N, Chen J, Spiers C, Peach C, Deyi J, Li Y (2016) Investigation on the permeability characteristics of bedded salt rocks and the tightness of natural gas caverns in such formations. *J Nat Gas Sci Eng* 35:468–482. <https://doi.org/10.1016/j.jngse.2016.07.072>
- Liu Y, Li J, Sun S, Yu B (2019) Advances in gaussian random field generation: a review. *Comput Geosci*. <https://doi.org/10.1007/s10596-019-09867-y>
- Liu W, Zhang X, Fan J, Zuo J, Zhang Z, Chen J (2020) Study on the mechanical properties of man-made salt rock samples with impurities. *J Nat Gas Sci Eng* 84:103683. <https://doi.org/10.1016/j.jngse.2020.103683>
- Mansouri H, Prior DJ, Ajalloeian R, Elyaszadeh R (2019) Deformation and recrystallization mechanisms inferred from microstructures of naturally deformed rock salt from the diapiric stem and surface glaciers of a salt diapir in southern iran. *J Struct Geol* 121:10–24. <https://doi.org/10.1016/j.jsg.2019.01.005>
- Ozarslan A (2012) Large-scale hydrogen energy storage in salt caverns. *Int J Hydrog Energy* 37(19):14265–14277. <https://doi.org/10.1016/j.ijhydene.2012.07.111>
- Popp T, Wiedemann M, Kansy A, Pusch G (2017) Gas transport in dry rock salt - implications from laboratory investigations and field studies. In: *The mechanical behavior of salt—understanding of THMC processes in salt*
- Pouya A (1991) Comportement rhéologique du sel gemme. application a l'étude des excavations souterraines. PhD thesis, thèse de doctorat dirigée par Nguyen-Minh, Duc Terre, océan, espace Marne-la-vallée, ENPC 1991
- Pouya A (2000) Micro-macro approach for the rock salt behaviour. *Eur J Mech A/Solids* 19(6):1015–1028. [https://doi.org/10.1016/S0997-7538\(00\)00204-7](https://doi.org/10.1016/S0997-7538(00)00204-7)
- Pouya A, Zhu C, Arson C (2016) Micro-macro approach of salt viscous fatigue under cyclic loading. *Mech Mater* 93:13–31. <https://doi.org/10.1016/j.mechmat.2015.10.009>
- Roberts AP, Garboczi EJ (2002) Computation of the linear elastic properties of random porous materials with a wide variety of microstructure. *Proc R Soc Lond Ser A Math Phys Eng Sci* 458(2021):1033–1054. <https://doi.org/10.1098/rspa.2001.0900>
- Roberts LA, Buchholz SA, Mellegard KD, Düsterloh U (2015) Cyclic loading effects on the creep and dilation of salt rock. *Rock Mech Rock Eng* 48(6):2581–2590. <https://doi.org/10.1007/s00603-015-0845-4>
- Rouabhi A, Labaune P, Tijani M, Gatelier N, Hévin G (2019) Phenomenological behavior of rock salt: on the influence of laboratory conditions on the dilatancy onset. *J Rock Mech Geotech Eng* 11(4):723–738. <https://doi.org/10.1016/j.jrmge.2018.12.011>
- Roubin E (2013) Meso-scale fe and morphological modeling of heterogeneous media: applications to cementitious materials. PhD thesis
- Sobolik S, Ehgartner B (2011) Analysis of the stability of large-diameter caverns for the strategic petroleum reserve. In: *SMRI spring 2011 technical conference*
- Song X, Xu F, Shi Y, Zhang Y, Pan Z, Song G (2020) Numerical simulation of the rotating water jet flushing the insoluble particles in the salt cavern underground gas storage. *J Energy Storage*. <https://doi.org/10.1016/j.est.2020.101869>
- Soubeyran A, Rouabhi A, Coquelet C (2019) Thermodynamic analysis of carbon dioxide storage in salt caverns to improve the power-to-gas process. *Appl Energy* 242:1090–1107. <https://doi.org/10.1016/j.apenergy.2019.03.102>
- Soyarslan C, Bargmann S, Pradas M, Weissmüller J (2018) 3d stochastic bicontinuous microstructures: generation, topology and elasticity. *Acta Mater* 149:326–340. <https://doi.org/10.1016/j.actamat.2018.01.005>
- Speranza G, Vinciguerra S, Di Genova D, Romano C, Vona A, Mollo S, Iarocci A (2013) New insights on the rheological properties of a rocksalt. In: *AGU fall meeting abstracts, vol 2013*, pp MR13A–2233
- Speranza G, Vona A, Vinciguerra S, Romano C (2016) Relating natural heterogeneities and rheological properties of rocksalt: new insights from microstructural observations and petrophysical parameters on messinian halites from the Italian peninsula. *Tectonophysics* 666:103–120. <https://doi.org/10.1016/j.tecto.2015.10.018>
- Spiers C, Peach C, Brzesowsky R (1989) Long-term rheological and transport properties of dry and wet salt rocks: final report. Office for Official Publications of the European Communities
- Staudtmeister K, Rokahr R (1997) Rock mechanical design of storage caverns for natural gas in rock salt mass. *Int J Rock Mech Mining Sci* 34(3):300.e1–300.e13. [https://doi.org/10.1016/S1365-1609\(97\)00199-8](https://doi.org/10.1016/S1365-1609(97)00199-8)
- Teubner M (1991) Level surfaces of gaussian random fields and micro-emulsions. *Europhys Lett (EPL)* 14(5):403–408. <https://doi.org/10.1209/0295-5075/14/5/003>
- Thiemeyer N, Habersetter J, Peinl M, Zulauf G, Hammer J (2015) The application of high resolution x-ray computed tomography on naturally deformed rock salt: multi-scale investigations of the structural inventory. *J Struct Geol* 77:92–106. <https://doi.org/10.1016/j.jsg.2015.05.014>
- Thiemeyer N, Zulauf G, Mertineit M, Linckens J, Pusch M, Hammer J (2016) Microfabrics and 3D grain shape of gorleben rock salt: constraints on deformation mechanisms and paleodifferential stress. *Tectonophysics* 676:1–19. <https://doi.org/10.1016/j.tecto.2016.02.046>
- Torquato AS, Haslach JHW (2002) Random heterogeneous materials: microstructure and macroscopic properties. *Appl Mech Rev* 55:B62–B63. <https://doi.org/10.1115/1.1483342>
- Van-Hassel B (1991) Évaluation qualitative du rôle de la texture dans le fluage du sel bressan. PhD thesis

- Wang T, Yang C, Ma H, Li Y, Shi X, Li J, Daemen J (2016) Safety evaluation of salt cavern gas storage close to an old cavern. *Int J Rock Mech Mining Sci* 83:95–106. <https://doi.org/10.1016/j.ijrmms.2016.01.005>
- Wang T, Yang C, Chen J, Daemen J (2018) Geomechanical investigation of roof failure of China's first gas storage salt cavern. *Eng Geol* 243:59–69. <https://doi.org/10.1016/j.enggeo.2018.06.013>
- Wernt B, Tilmann R (2007) Concepts and technologies for radioactive waste disposal in rock salt. *Acta Montan Slovaca* 12:67–74
- Wu Z, Zhou H, Ding J, Ran L, Yi H (2012) Research on permeability testing of rock salt under different permeability pressures. *Yanshixue Yu Gongcheng Xuebao/Chin J Rock Mech Eng* 31(SUPPL. 2):3740–3746
- Xu Y, Liu J, Xu H, Li T, Xiang G, Deng C, Wu C (2016) Experimental study on acoustic emission characteristics of salt rock with impurities under uniaxial compression. *Sichuan Daxue Xuebao (Gongcheng Kexue Ban)/J Sichuan Univ (Eng Sci Ed)* 48(6):37–45:37–45. <https://doi.org/10.15961/j.jsuese.2016.06.006>
- Yang C, Wang T, Qu D, Ma H, Li Y, Shi X, Daemen J (2016) Feasibility analysis of using horizontal caverns for underground gas storage: a case study of yunying salt district. *J Nat Gas Sci Eng* 36:252–266. <https://doi.org/10.1016/j.jngse.2016.10.009>

Publisher's Note Springer Nature remains neutral with regard to jurisdictional claims in published maps and institutional affiliations.